Strong Field Ionization of Atoms and Molecules: Electron-Ion Coincidence Measurements at High Repetition Rate

Im Fachbereich der Physik
der Freien Universität Berlin
eingereichte Dissertation

von

Sascha Birkner

Berlin 2015

Diese Arbeit wurde am 7.7.2015 gedruckt.

1. Gutachter: Prof. Dr. M.J.J. Vrakking
2. Gutachter: Prof. Dr. L. Wöste

Tag der Disputation: 18.11.2015

Erklärung der Selbstständigkeit

Hiermit versichere ich, die vorliegende Arbeit selbstständig verfasst und keine anderen als die angegebenen Quellen und Hilfsmittel benutzt sowie die Zitate deutlich kenntlich gemacht zu haben. Die Arbeit ist weder in einem früheren Promotionsverfahren angenommen noch als ungenügend beurteilt worden.

Berlin, den 7. Juli 2015 Sascha Birkner

Contents

-

Introduction

Almost everything that we know about structure, function and dynamics of matter on the microscopic level we do know from spectroscopic investigation of light-matter interaction. Hence, the underlying principles of how photons and light fields interact with matter is a core objective in physics. The development of quantum mechanics at the beginning of the 20th century provided a new quality in the explanation of spectroscopic observations. The quantum mechanical model of the hydrogen atom developed by Heisenberg and Schrödinger in 1925/26 [1, 2] was capable of reproducing all known spectral lines and thus advanced the theoretical understanding of light-matter interaction. Nonetheless, a complete quantum-mechanical description remains feasible only for very simple systems. The advance in theory goes along with the advance in spectroscopy and vice versa.

The invention of the laser in 1960 [3] provided a new powerful tool for spectroscopy. Pulsed ultrashort laser sources allowed the time-resolved investigation of dynamics in atomic and molecular systems as well as in condensed matter on their natural timescale. Shortly after the invention of the laser, sources with pulse durations in the picosecond regime ($1\,\mathrm{ps} = 10^{-12}\,\mathrm{s}$) became available [4]. These are the timescales of rotational motion of molecules as seen for example for the rotational relaxation of large molecules in solution [5]. In order to observe these dynamics, so-called pump-probe scheme were developed: Dynamics are initiated by a first pulse, the pump pulse. It generates a coherent superposition of excited states, which form a wave packet. The temporal evolution of the system is probed by a delayed second pulse, the probe pulse. This may be realized by absorption to higher excited states or by ionization. Varying the delay between the two pulses samples the dynamics of the triggered process.

As in classical photography, the time resolution of a measurement is limited by the shutter speed[1]. Applied to the pump-probe technique, the shutter speed is given by the duration of the pump and the probe pulses. In the late eighties of the 20th century the pulse duration reached the femtosecond regime ($1\,\mathrm{fs} = 10^{-15}\,\mathrm{s}$) accessing also vibrational timescales of small molecules[2]. In the Zewail group bond breaking was observed for the first time in a time-resolved fashion [6], later awarded with the Nobel prize. This was the birth of femtochemistry, bringing chemists closer to their dream of manipulating the breaking and making of bonds by controlling the wave packet motion.

Femtochemistry experiments are typically described within the so-called Born-Oppenheimer approximation [7], which assumes that the nuclear and electronic motion can be separated due to their different timescales. In this approximation, the electrons adjust instantaneously to any nuclear motion. Solving the Schrödinger equation for different positions of the nuclei

1 Today, cameras exist that have a time resolution on the order of a few μs.

2 Hydrogen has the highest vibrational frequency of neutral diatomic molecules with a period of 7.6 fs.

leads to a potential energy surface, on which the wave packet, generated by the pump pulse, propagates. This approximation is valid as long as the gap between the potential energy surfaces is large compared to the energy in the nuclear degrees of freedom. If the energy gap is comparable, the Born-Oppenheimer approximation breaks down, since both - the electronic and nuclear - motion proceed on comparable timescales. This breakdown is rather the rule than the exception in the photochemistry of polyatomic molecules [8], as for example seen in long-range electron transfer in biomolecules [9]. When the breakdown leads to a coupling of electronic and nuclear motion, the electronic motion slows down to femtosecond timescales. However, recent theoretical investigations [10, 11] on larger molecules recognized the importance of electronic dynamics on attosecond timescales ($1\,\mathrm{as} = 10^{-18}\,\mathrm{s}$) for photo-induced nuclear processes on much longer timescales. The creation of an electron hole by sudden ionization of Glycine leads to a migration through the entire molecule within a few fs [12]. Hence, in order to understand this charge migration driven by multi-electron interactions, investigations of ultra-fast electron dynamics on timescales of attoseconds are necessary. The investigation of these ultra-fast dynamics, called attosecond spectroscopy, can be addressed in two ways.

As a natural extension of the pump-probe scheme, one approach is to decrease the pulse duration of both pulses to attosecond timescales. The relation between pulse duration and spectral bandwidth is given by the Fourier-transformation, which can be expressed by the time-bandwidth product $\Delta t \cdot \Delta E \approx 1.8\,\mathrm{fs{\cdot}eV}$ with the duration Δt of the pulse and the spectral energy bandwidth of ΔE. Accordingly, an attosecond pulse with a duration of 100 as requires at least a bandwidth of 18 eV. A bandwidth like this is only supported in the extreme ultra-violet (XUV) part of the electromagnetic spectrum (or in a part with even higher frequencies). The generation of XUV radiation can be done by so-called high harmonic generation (HHG) [13]. HHG is a highly non-linear process that is driven directly by the strong electric field of an intense IR laser pulse interacting with a gas. Because of symmetry reasons, this interaction generates light only at odd multiples of the driving laser field. However, due to the low conversion efficiency, the photon flux currently achieved with HHG is low and pump-probe experiments at attosecond timescales can hardly be performed [14]. Recently, an XUV-pump-XUV-probe experiment has been carried out to investigate double ionization of xenon [15], but with a time-resolution of 1 fs.

An alternative approach uses intense few-cycle laser pulses with their strong electric field directly. The interaction of these intense pulses with matter opened the field of strong field physics with many new phenomena that provide new tools to investigate (electron) dynamics in laser-induced processes. Among those phenomena are above-threshold ionization (ATI) [16], laser-induced electron diffraction (LIED) [17, 18] and high harmonic generation, as already described above. ATI describes a process where an atom or molecule ionizes by absorbing more than the minimum number of photons that are necessary to overcome the ionization potential. LIED is the scattering of ionized electrons at their parent ion guided by the ionizing laser field.

The models developed to describe strong field processes show that already intense few-cycle laser pulses give access to time information on the attosecond timescale due to the highly non-linear interaction. Many of the common models use the single-active-electron (SAE) approximation [19]. It assumes that only the weakest bound electron is involved in the

interaction. A further approximation commonly used is the strong-field approximation (SFA) [20–22], which treats the propagation of the released electron classically taking into account only the oscillating field of the laser and neglecting any influence of the potential of the remaining ion. Corkum [23] combined these approaches and suggested the very simple, but yet very successful, three-step-model to explain the strong field processes ATI and HHG mentioned above. In this model, atoms are treated as electron sources that release electrons at certain phases of the laser field due to tunnel ionization using the SAE approximation. The different times of emission lead to different trajectories of the electron in the laser field, calculated in the SFA. Some of the trajectories lead to a return of the electron to the ion core. These electrons can recombine leading to emission of photons with energies given by the energy gained during the motion in the laser field and the ionization potential. Alternatively to recombination, the electron can also scatter from the ion and be accelerated further in the laser field, reaching significantly higher kinetic energies. It is important to note that the trajectories of the electrons are synchronized to the electric field of the IR laser and only a small part of the trajectories, restricted to a small fraction of the IR cycle, lead to a recollision with the ion core. Since the emission of a particular energy of high energy photons and electrons is restricted to a particular trajectory, the detected energy of the photon or electron contains sub-cycle temporal information on attosecond timescales. The total control of the electric field of few-cycle laser pulses, including the carrier-to-envelope phase[1], additionally allows to influence the electron motion for example during fragmentation [24]. A deeper explanation of strong field processes and the models used to describe them will be given in the next chapter.

Although, initially largely seen only as an alternative to XUV-pump-XUV-probe experiments, it turned out that strong field ionization, HHG and LIED have a remarkable potential and will remain key spectroscopic tools in attosecond physics. The three-step model in its simple way is astonishingly powerful in explaining many phenomena of the light-matter interaction in the strong field regime. However, it relies on several simplifications and applying this model to larger molecules gives unsatisfying results. For example, the single active electron approximation already fails in molecules with two atoms and even more in the case of polyatomic molecules due to the fact that in molecules a few electrons occupy states with similar binding energies [25, 26]. Hence, there is not just one electron taking part in the interaction with the laser field. An increase of the significance of spectroscopic strong field methods requires an extension towards polyatomic molecules and a better understanding of the influence of multi-electronic dynamics in strong field ionization of polyatomic molecules.

A different process showing the involvement of multiple electrons is non-sequential double ionisation first suggested by L'Huillier in 1983 for strong-field double ionization of xenon [27]. Investigations of the ionization yield for helium as a function of laser intensity showed a difference of more than one order of magnitude from predictions of sequential models [28, 29]. These models assume a sequential or cascade-like ionization in double ionization by strong laser fields, i.e. the electrons are liberated independently one after the other. Non-sequential models have been proposed based on a three step mechanism: The ionized

1 This is the phase between the carrier wave of a pulse and the maximum of the pulse envelope.

electron is accelerated in the field and finally rescatters inelastically at the ion. Further experiments with circularly polarized light [29, 30] indicated that the recollision step plays a major role in non-sequential double ionization. By the analysis of the correlation between both photoelectrons several different regimes for non-sequential double ionization have been identified [31].

Many results obtained in attosecond physics are based on the detection of the photoelectrons or ionic particles generated during the light-matter interaction. Unfortunately, the laser interaction with an atomic or molecular target triggers several different processes, e.g. single and double ionization. One is usually not able to distinguish between different channels by the exclusive detection of one charged particle type (electrons or ions) if the process of interest has very low probability.

This problem is not specific for attosecond science and has been encountered in many other research fields. Bothe and Geiger invented in 1924 the very powerful tool of coincidence detection to investigate events of light-matter interaction with low probability among events with high probability. In their detection scheme the scattered photons and electrons are detected in coincidence to explore the Compton effect[1][32]. Brehm and von Puttkamer [33] transferred this scheme 40 years later to photoelectron-photoion-coincidence (PEPICO) spectroscopy, which allows to measure the kinetic energy of the photoelectron and the mass of the ion simultaneously, to investigate the photoinduced fragmentation of methane. The photoelectron spectra for different fragment channels could thereby be measured for each channel individually.

Reaction microscopes provide the ultimate coincidence capability, since they extend the PEPICO scheme to full three-dimensional momentum coincidence detection of all charged particles. Hence, this apparatus gives an exceptionally detailed insight into kinematics of atomic or molecular ionization/fragmentation dynamics providing not only channel-resolved electron spectra but also angular information. However, coincidence techniques rely on the ability to separate individual events (e.g. ionization of an atom/molecule), which is strongly affected by the limited detection efficiency of (particle) detectors used in coincidence schemes. The limited detection efficiency gives rise to so-called false coincidences. A false coincidence is, for example, the coincident detection of an ion and electron that emerged from different ionization events. If the detector does not detect all ionized particles, such a false coincidence can not be identified. Therefore, every laser pulse must ionize at most one particle at a time, otherwise one cannot correctly determine if the ions and electrons detected originate in the same interaction.

The probability for a particular number of ionization events per pulse is given by the Poisson distribution[2]. This distribution is determined by the average number of ionization events per pulse. When the average number of ionization events per pulse is one, the probability to ionize two particles per pulse is half as high as for the ionization of a single particle. Thus, experiments using a coincidence detection run typically at an average number

1 Compton effect is the inelastic scattering of photons at electrons leading to a decreased energy of the photon.

2 The Poisson distribution can be used to describe independent events.

of ionization events on the order of 0.1. In this way events with two or a higher number of ionizations are strongly reduced to about 5% of the number of events with a single ionization.

The duration of a measurement is given by the average number of particles per laser pulse, the repetition rate of the laser, the relative probability of that specific process under investigation (e.g. ratio between double ionization to single ionization) and the total number of events to be recorded. Up to now, most laser systems generating strong few-cycle pulses operate at a repetition rate of 1-10 kHz. Typically a number of $10^6 - 10^{10}$ registered events is used in order to achieve a high statistical confidence level. The angle and momentum differential measurements of the reaction microscope can require even higher numbers. With these numbers, the requirements of an average event rate well below one ($\sim$0.1) induces a long measurement time up to several days with kHz-laser systems. Performing a time-resolved measurement as for example a pump-probe scan described above with a reaction microscope will easily take weeks depending on the necessary number of different delays between pump and probe pulse.

For such a long measuring time, huge efforts are needed to maintain stable experimental conditions. An intuitive way to decrease the overall duration of a measurement is to increase the repetition rate. However, the conventional laser design based on chirped pulse amplification (CPA) [34] is always a trade-off between pulse energy and repetition rate limited by the thermal properties of the gain medium. In addition, intense pulses from conventional laser systems are limited to a few tens of fs pulse duration. In order to achieve intense few-cycle pulses, they require additional pulse-compression schemes using for instance an external spectral broadening in hollow-core fibres [35]. In contrast, optical parametric amplification (OPA) is a different amplification scheme that uses a wave-mixing process and supports the amplification of few-cycle pulses with virtually no heat load in the gain medium. In the OPA process a weak seed pulse is amplified by transferring energy from another so-called pump pulse, overlapping in time and space, mediated by a non-linear crystal. This will be explained in more detail in chapter two. Although this scheme was already described in 1992 [36], until recently it was not applicable for the generation of intense pulses due to its limits in the achievable average power of the pump lasers. But recent developments in gain media technology and high power laser diodes to pump the gain medium led to commercially available fibre pump lasers that allow to build table-top OPA systems producing intense laser pulses at high repetition rates.

With the aim to give the coincident detection scheme a larger impact on the multi-electron processes as for example involved in SFI of polyatomic molecules, the idea arose to combine a high-repetition few-cycle OPA system with a reaction microscope.

This thesis deals with the implementation of this unique combination. The main focus of my thesis is on the reaction microscope built within the frame of this work. But in this thesis also aspects of the setup of the OPA system spearheaded by Federico Furch are discussed. The system is then used to investigate strong field ionization of polyatomic molecules and double-ionization of xenon.

The structure of the thesis divided into five chapters is as follows: in the first chapter the most relevant aspects of light-matter-interaction in strong laser fields are summarized. Chapter one is concluded by a short discussion about conditions of coincidence detection.

In chapter two a description of the complete setup consisting of the laser system and the reaction microscope is given. It starts with the necessary basics of the properties and generation of ultra-short laser pulses and describes the constructed OPA system. The design and construction of the reaction microscope have been my main task. An introduction into general aspects of a reaction microscope and technical details of the reaction microscope built within the framework of the thesis is given in the second part of chapter two. After a brief presentation of the general working principle, the vacuum system, the molecular beam, the spectrometer and the particle detectors are described in more detail. The next section of this chapter shows the analogue and digital signal processing and discusses the influence of the high repetition rate on the trigger scheme. The chapter is concluded with an explanation of the analysis and momentum reconstruction of the measured data.

In chapters three and four, experimental results are presented obtained with the new system. The experiment described in chapter three acts as a performance test of the system in order to understand its properties. Strong field ionization of argon is used as a reference. Based on the results from the argon experiments, chapter three continues with the theoretical investigation of the possibility to retrieve the population of Rydberg states of neutral argon after the interaction with an intense few-cycle IR-pulse. Finally, the application to triple coincidence events using the example of (non-sequential) double ionization of xenon is studied.

First results on strong field ionization of polyatomic molecules are presented in chapter four, showing the potential of the system to study the fragmentation of these molecules. The channel-resolved angular-resolved electron spectra retrieved in this measurement hint to different ionic states for different detected fragments.

Finally, in chapter five a conclusion and an outlook are given.

1 Background

1.1 Strong Field Physics

This section introduces phenomena concerning the interaction of atoms with strong laser fields. The term strong refers to a situation in which the electric field of the laser approaches the strength of the fields that exists within an atom. At a distance of the Bohr radius a_0 the electron in a hydrogen atom feels an electric field whose strength is $5 \times 10^{11}\,\mathrm{V/m}$. A laser field that reaches 1% of this interatomic field has an intensity of $3.5 \times 10^{12}\,\mathrm{W/cm^2}$.

Several strong field phenomena can be understood using the so-called three step model introduced by Corkum [23]. This model divides the process leading to strong field phenomena, as e.g. HHG, into three steps. The first step describes the ionization of an atom leading to a liberated electron. In the next step this electron propagates in the laser field and can return to the ion or not. The last step deals with the interaction of the electron with its ion if the electron returns.

An understanding of the motion of a photoelectron in the field of a laser pulse helps to explain different phenomena seen in photoelectron spectra that accompany strong field ionization. Therefore this is described first. Then, different regimes of the ionization process of an atom depending on laser parameters are discussed. The description of strong field phenomena, should provide the reader with a foundation, from which he or she may understand the investigations carried out in this thesis. The basic information of strong field interaction discussed in this section also supports the interpretation of photoelctron spectra obtained by strong field ionization as seen in the experiments of this thesis. Although the following is discussed in the context of atomic ionization, many properties introduced here can be transferred to molecular ionization as well.

1.1.1 Electron Motion in the Laser Focus

After ionization the electron will propagate under the influence of the laser field. In the context of the three step model, the electron is described classically as a point charge. The force of the laser field is given by the Lorentz force $\vec{F}_L$:

$$\vec{F}_L(r,t) = -q_e \left(\vec{E}(r,t) + \vec{v} \times \vec{B}(r,t) \right) \tag{1.1}$$

with q_e the electron charge, $\vec{v}$ the velocity of the electron, $\vec{E}$ the electric field and $\vec{B}(r,t)$ the magnetic field of the laser field. The electric field can be written as:

$$\vec{E}(r,t) = -\nabla \Phi(r,t) - \frac{\partial \vec{A}(r,t)}{\partial t} \tag{1.2}$$

with $\Phi(r,t)$ the scalar potential and $\vec{A}(r,t)$ the vector potential of the field.

For the following derivation four approximations are made:

- The excursion of the electron during the laser pulse is small compared to the focus spot size. Hence, the electric field is position independent and the scalar potential in eq. 1.2 can be neglected.
- The magnetic field is neglected to simplify the calculation. This can be done up to an intensity of $10^{17}\,\mathrm{W/cm^2}$. Beyond this intensity, the excursion of the electron due to the magnetic component reaches atomic dimensions.
- The laser pulse is linearly polarized. Hence, the problem is reduced to one dimension.
- The amplitude of the pulse envelope $h(t)$ changes slowly compared to the optical period of the pulse.

The electric field can then be written as:

$$E(t) = E_0 h(t) \sin(\omega t) \qquad \xrightarrow{h(t)\approx 1} \qquad E(t) = E_0 \sin(\omega t) \tag{1.3}$$

with E_0 the maximum amplitude of the electric field and ω the laser frequency. The time-dependent envelope $h(t)$ is set to zero due to the last of the four assumptions and approximations given above. The vector potential $A(t)$ is then:

$$A(t) = -\frac{E_0}{\omega} \cos(\omega t) \tag{1.4}$$

The momentum p of an electron in classical mechanics is given by

$$p = p_0 - q_e \int_{t_0}^{t} E(t')dt' = p_0 + e\left[A(t) - A(t_0)\right] \tag{1.5}$$

The first assumption of a position independent electric field made above allows the last equality in eq. 1.5.

Equation 1.5 shows that the instantaneous momentum contains three terms: a possible initial momentum due to the ionization process, an oscillatory part determined by the current vector potential and a drift part depending on the point in time t_0 when the electron is created. However, detection of an electron typically occurs with a detector that is placed outside the laser field, where $A(t) = 0$. Thus, the detected momentum, according to eq. 1.5 with $t \to \infty$, is

$$p_\infty = p_0 - q_e A(t_0). \tag{1.6}$$

Hence, the detected momentum shows the sum of the initial momentum and the momentum due to the drift term. From this one can calculate the final kinetic energy of the electron by:

$$E_{\mathrm{kin}} = \frac{p_\infty^2}{2m_e} = T_0 + 2U_\mathrm{p} \cos^2(\omega t_0) + \sqrt{8U_\mathrm{p}T_0} \cos(\omega t_0) \tag{1.7}$$

with the initial kinetic energy of the electron $T_0 = \frac{p_0^2}{2m_e}$ and the ponderomotive potential

$$U_\mathrm{p} = \frac{q_e^2 E_0^2}{4m_e\omega^2} = \frac{q_e^2}{8\pi m_e \epsilon_0 c^3} I\lambda^2 \tag{1.8}$$

where I is the intensity and λ is the wavelength of the laser. The ponderomotive potential is the cycle averaged energy of the oscillatory motion of an electron in the laser field.

By integrating eq. 1.5 over time, one can obtain the position of an electron in the laser field as a function of time:

$$x(t) = x_0 - \underbrace{\frac{q_e E_0}{m_e\omega^2}\left(\sin(\omega t) - \sin(\omega t_0)\right)}_{\text{oscillation}} + \underbrace{\left(v_0 + \frac{q_e E_0}{m_e\omega}\cos(\omega t_0)\right)(t - t_0)}_{\text{drift}} \tag{1.9}$$

with t_0 the time when the electron enters the laser field, v_0 the initial velocity and x_0 the initial position of the electron at t_0. In the case of an electron originating from the ionization of an atom, x_0 is the position of the atom and can be set to zero. This equation contains an initial term, an oscillatory term and a drift term.

Eq. 1.7 in combination with the trajectories calculated with eq. 1.9 contains rich information on the dynamics after ionization. Figure 1.1 shows electron trajectories for different ionization times. It can be seen that the time of ionization strongly influences the electron trajectory. The electron either leaves the vicinity of the ion core or can revisit the ion core. Equation 1.7 shows that the maximum energy for an electron not revisiting the ion core can reach an energy of $2\mathrm{U_p}$ assuming no initial momentum. This is also clearly seen in strong field ionization experiments as for example by Walker *et al.* on the strong field ionization of helium [29].

The maximum energy achievable on return to the ion core at x_0 is 3.17 U_p (indicated by the thick black trajectory). The ionization time for this trajectory corresponds to a phase of 18° after the first field maximum as shown in fig. 1.1.

1.1.2 Electron Interaction with the Ion

When the electron is driven back by the laser field to the ion, several different processes may happen:

The returning electron can recombine with the ion. Thereby a photon is emitted with an energy corresponding to the sum of the ionization potential and the energy gained by the electron during the motion in the laser field. As described above the maximum energy at recollision due to the quiver motion is $3.17U_\mathrm{p}$. Hence, the maximum observable photon energy in this process is:

$$h\nu_{max} = IP + 3.17U_\mathrm{p} \tag{1.10}$$

Every half-cycle of the pulse can liberate electrons, as long as the field strength within that half-cycle is strong enough to ionize the atom. Since this happens every half-cycle, a fraction of the electrons recombines every half-cycle with the ion. The light bursts that are created during each half-cycle form a pulse-train with a pulse-to-pulse distance of half the period of the strong laser field. The spectrum of the emitted light connected via Fourier

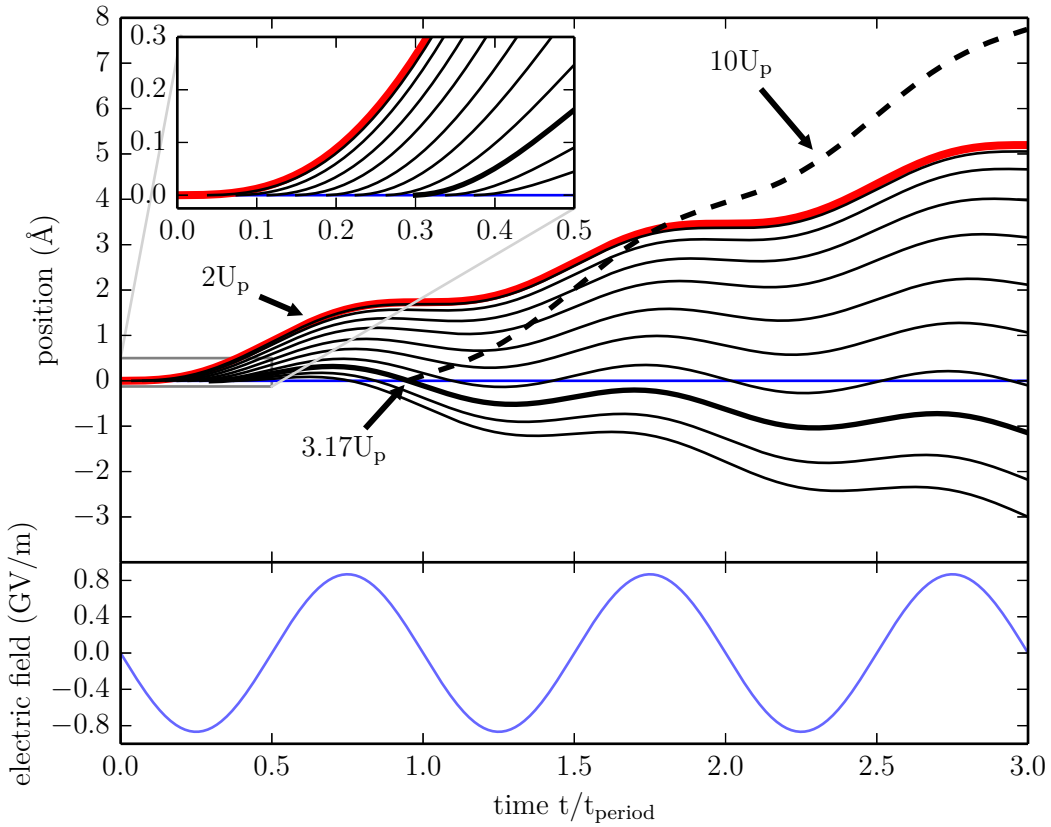

Figure 1.1: Trajectories of electrons liberated at different times during the laser cycle under the influence of the laser field. The scale of the abscissa is given in multiples of the laser cycle period. The red trajectory belongs to the $2\,U_p$ limit of direct electrons. The black solid line marks the trajectory with the highest recollision energy of $3.17\,U_p$. When this electron scatters by 180° it will gain the highest possible drift energy of $10\,U_p$ by the laser field (dashed line).

transformation consists of several peaks with a distance of two times the photon energy of the fundamental pulse. The spectral position of these peaks is at odd harmonics of the frequency of the strong laser pulse due to inversion symmetry of an atomic gas. This process is called correspondingly high harmonic generation (HHG)[1]. Experimental results of HHG prove the correctness of Corkum's model as they for instance reproduce the cut-off law of eq. 1.10 [38].

A second possible process upon recollision of the electron is inelastic scattering at the ion. Thereby the electron transfers a part of its energy to the ion and possibly liberates a second electron. This process called non-sequential double ionization is explained in more detail in

1 For more details on HHG the reader is referred to [37].

section 3.5.1.

The last process is elastic scattering. In this process the electron changes its direction but keeps its already gained energy. If it is scattered by 180°, the electron will again gain energy from the laser field, resulting in a maximal kinetic energy of $\approx 10U_\mathrm{p}$. This is the maximum energy observed in electron spectra [39].

1.1.3 Single Ionization in Strong Fields

According to the photo-electric effect, ionization takes place if the photon energy exceeds the binding energy. Typically, one assumes a single photon absorption. But with increasing intensity the probability of a two or more photon absorption increases as well.[1] Thus, also photons with a photon energy $h\nu$ below the ionization potential can ionize the atom if a sufficient number of photons is absorbed. This process is called multi-photon ionization. As long as the electric field of the laser is small compared to the intra-atomic field this process can be described by perturbation theory.

For intensities at which the electric field cannot be treated as a small perturbation of the atomic system, a different picture describes the ionization process. Here, the electric field of the laser directly leads to ionization of the atom due to the strong bending of the atomic potential. Figure 1.2 shows these different ionization pictures. In his paper [20] Keldysh has described a way to determine which picture describes the ionization process better.

Keldysh Parameter

Keldysh assumed a maximum laser frequency ω_t up to which the tunneling probability depends only on the instantaneous field strength E_0:

$$\omega_t = \frac{q_e E_0}{\sqrt{2 m_e IP}} \tag{1.11}$$

with IP the ionization potential. ω_t can also be seen as the inverse of the tunnelling time. At higher frequencies, the tunnelling probability gets frequency dependent. Hence, the ratio of the actual laser frequency and the frequency ω_t is a measure to choose the appropriate picture. This ratio is known as the Keldysh parameter:

$$\gamma = \frac{\omega}{\omega_t} = \frac{\omega\sqrt{2 m_e IP}}{q_e E_0} \tag{1.12}$$

the last step uses eq. 1.8.

If γ is $\ll 1$, the external field varies slowly compared to the tunneling time defined by Keldysh. Or the ponderomotive potential is much stronger than the binding potential. Therefore the tunneling picture is an adequate description.

1 This was discussed for the first time already in 1931 by Göppert-Mayer [40] long before the invention of the laser.

If γ is $\gg 1$, the oscillation of the laser is faster than the tunneling time and a perturbation picture describing multi-photon ionization is valid. The ponderomotive potential is a small perturbation of the binding potential.

For $\gamma \approx 1$, a mixed multi-photon and tunnel ionization takes place. For this range, Yudin and Ivanov developed a time-resolved description [41].

Multi-Photon Ionization

At a Keldysh parameter $\gamma \gg 1$, the ionization process can be treated by perturbation theory [42].

Following perturbation theory, the MPI ionization rate Γ_{if} from an initial state i to a final state f is given by

$$\Gamma_{if} = \sigma_{if}^{(n)} I^n \tag{1.13}$$

with $\sigma_{if}^{(n)}$ the n-photon cross-section of this process and n the number of required photons.

Tunnel Ionization

At a Keldysh parameter $\gamma \ll 1$, a quasi-static picture is appropriate. The superposition of atomic potential and electric field creates a new effective potential. This new potential has a barrier with a finite width depending on the field strength. Known from basic quantum mechanics, this raises the possibility for the electron to tunnel through the barrier. The tunnelling rate Γ_{tunnel} for a static DC field, which is a good representation at a Keldysh parameter below one, was derived by Ammosov, Delone and Krainov, known as ADK-theory[44], to (in atomic units):

$$\Gamma_{\text{tunnel}} \propto \exp\left[-\frac{2}{3}\frac{IP}{\sqrt{I}}\sqrt{2IP}\right] \tag{1.14}$$

with I the intensity or $\sqrt{I}$ the field strength of the laser.

Barrier Suppression Ionization

As the intensity increases, the atomic potential is bent more strongly. At some point, where the barrier height matches the energy level of the electrons in the ground state, the electrons can escape the potential directly as shown in fig. 1.2. This point can be calculated classically by using the superposition of a Coulomb potential and a constant electric field:

$$V_{\text{eff}}(r) = -\frac{Z q_e^2}{4\pi\epsilon_0 r} - q_e E r \tag{1.15}$$

Finding the maximum of this potential and setting it to -*IP*, the minimum intensity for barrier suppression ionization is given by

$$I_{\text{BSI}} = \frac{c\epsilon_0 \left(4\pi\epsilon_0\right)^2}{32 Z^2 q_e^6} IP^4 \tag{1.16}$$

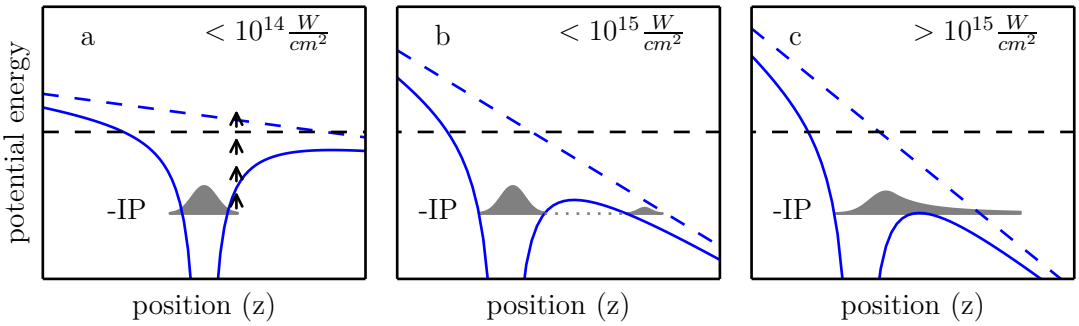

Figure 1.2: Superposition of laser field and Coulomb potential for different laser intensities. (a)At low intensities, the ionization is dominated by multi-photon processes. (b)As the intensity increases, the potential is more affected by the laser field and creates a sufficient finite barrier. The tunneling ionization becomes dominant. (c) At even higher intensities, the potential barrier is completely suppressed allowing the electron to escape freely. The intensities given are a rough indication when each mechanism becomes dominant. Adapted from [43].

with Z the charge state of the residual ion.

1.1.4 Above Threshold Ionization

Above threshold ionization (ATI) is explained intuitively using the multi-photon picture, although it also occurs in the tunnelling regime as seen later. If an atom is ionized by a multi-photon process, it is also possible that the electron absorbs more photons than the number necessary to reach the continuum. This process was observed for the first time in [16]. ATI looks surprising since the absorption of a photon by a free electron is not possible. However, as long as the electron is still under the influence of the Coulomb field of the atom, it can absorb photons due to the coupling with the atom.

As described in the beginning of this chapter,in a laser field, a free electron has a quiver energy that is given by the ponderomotive potential U_p (eq. 1.8). This additional energy has to be considered to calculate the ATI peak position in the photoelectron energy spectrum:

$$E = n \cdot h\nu - (IP - U_\mathrm{p}) \tag{1.17}$$

ATI can also be understood in the tunnelling regime. A long pulse with several cycles produces photoelectrons with a broad energy distribution at each half cycle. Hence, an electron pulse train is produced. Fourier transformation of this pulse train yields a broad frequency distribution which is modulated as also explained for the high harmonic generation.

But in contrast to the HHG spectrum, the peaks in the energy spectrum of the ATI spectrum are spaced by the photon energy. This is attributed to the fact that one can distinguish electrons ionized in the first or second half of a laser cycle. Therefore, one has to Fourier transform two pulse trains with a time pattern given by the laser cycle period. Thus, the energy distance of the peaks in the spectrum is the photon energy $h\nu = \frac{h}{T}$.

1.1.5 AC Stark Shift and Freeman Resonances

An alternating electric field affecting a free electron does also affect the bound states of an atomic system. Their levels become shifted due to the induced polarization. The strength and sign of the energy shift of a bound state depends additionally on the state itself. Rydberg states which are bound only by a fraction of an eV can be treated almost as a free electron. Deeply bound electrons are bound by many eV and separated from neighbouring states by a similar amount. Therefore, their quiver motion will be much smaller than that of a free electron and correspondingly the shift of that state will be smaller as well.

Quantitatively, Eberly and Javanaien [45] derived the ponderomotive potential of a bound state based on the Lorentz model [1]. The ponderomotive potential for a bound state is written as

$$U'_{\mathrm{p}} = \frac{q_e^2}{4m_e\left(\omega^2-\omega_0^2\right)}E^2 = \frac{q_e^2}{2m_e\epsilon_0 c}\frac{I}{\left(\omega^2-\omega_0^2\right)} \tag{1.18}$$

with ω_0 the eigenfrequency of this state as given by the Lorentz model. A deeply bound electron has a higher frequency than a weakly bound electron corresponding to their spring constant in that model.

Written as a ratio between both cases (eq. 1.18 and 1.8)

$$\frac{U'_{\mathrm{p}}}{U_{\mathrm{p}}} = \frac{\omega^2}{\omega^2-\omega_0^2} \tag{1.19}$$

In most cases, the ground state of an atom has a high eigenfrequency, $\omega_0 \gg \omega$. Hence, the ground state shows almost no shifting due to the alternating field, whereas Rydberg states shift like free electrons.

The different scaling of the ponderomotive shift for different states with intensity generates interesting features in the ATI spectra.

One example are freeman resonances [46]. Figure 1.3 depicts the principle of freeman resonances schematically. While the intensity at the leading edge of the pulse is increasing, the energy levels of the Rydberg states get up-shifted. At a certain point in time a Rydberg state becomes resonant with a multi-photon excitation increasing the probability of this excitation by many orders. From this state further ionization can happen, either one- or multi-photon depending on the photon energy and the Rydberg state.

Let us assume two Rydberg states 1 and 2 that get into resonance with an n-photon transition at intensities $\mathrm{I}^{(1)}$ and $\mathrm{I}^{(2)}$ and further assume that one photon is sufficient to ionize from both Rydberg states, then the drift energies of the electrons are:

$$\begin{aligned} E_D^{(1)} &= h(n+1)\nu - (IP + U_{\mathrm{p}}^{(1)}) \\ E_D^{(2)} &= h(n+1)\nu - (IP + U_{\mathrm{p}}^{(2)}) \end{aligned} \tag{1.20}$$

The difference between both energies is precisely the difference in the ponderomotive shift due to the different intensities at which the states get resonant. This is also exactly the energy

1 The Lorentz model considers the electron harmonically bound to the nucleus.

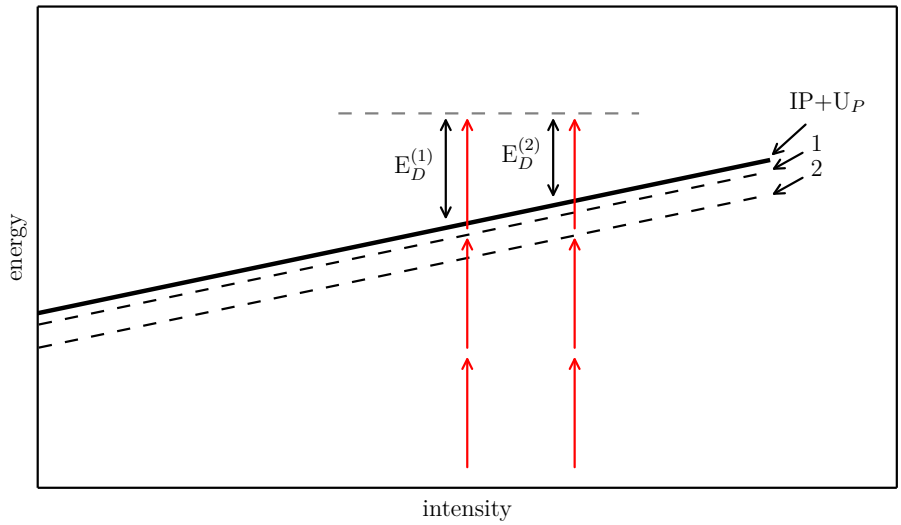

Figure 1.3: Freeman resonance: with increasing intensity Rydberg states shift into multi-photon resonances. By the absorption of a further electron the population is transferred into the continuum. Due to the resonantly excitation step this path is strongly enhanced.

difference between both Rydberg states. Hence, the typical non-resonant ATI spectrum can be superimposed with a Rydberg series of the atom. In contrast to non-resonant ATI peaks, the position of the Freeman resonances is independent of the peak intensity of the laser. A change of the peak intensity shifts only the point in time during the pulse when a Rydberg state is resonant with a multi-photon excitation. The required intensity for a specific Rydberg state of an atom to be resonant stays always the same. The position of ATI peaks instead shifts with U_p.

1.2 Coincidence Detection

This section will discuss statistical and mathematical aspects of the coincidence detection method. It should serve as a basis for later chapters in which the following derived numbers are mentioned as a reason for chosen conditions.

Coincident detection schemes are one of the most powerful techniques in terms of information content. As described in the introduction, they allow to gain insight into laser-induced dynamics providing vast amounts of information. But they have a very strong restriction.

In order to avoid ambiguities, there must be at most one event per laser shot. Assuming a theoretical detector with 100 % detection efficiency situations with two events per trigger can be identified. But a real detector with a limited detection efficiency gives rise to false coincidences.

False coincidences are coincidence events in which particles from different events (e.g. ionization of two atoms) are correlated. Due to the limited detection efficiency these coincidence events can look like a true coincidence. However, false coincidences can be

avoided or at least their number can be reduced by lowering the event rate[1].

Stert *et al.* [47] and Mikosch and Patchkovskii [48] have explained this in quantitative terms utilizing a ion-electron coincidence Gedankenexperiment. For the following example, any mass distribution of the ions and any energy distribution of the electrons are neglected. It is only important if a particle is detected or not.

For a gas target in which all particles are independent and do not influence each other, as for example in a super sonic jet, the probability to ionize n particles leading to pairs of one ion and ion electron per laser pulse is given by a Poisson distribution:

$$p^{(\bar{n})}(n) = \frac{\bar{n}^n}{n!}\mathrm{e}^{-\bar{n}} \tag{1.21}$$

where $\bar{n}$ is the average number of ionization events.

The number of detected ions and electrons is determined by the transmission of the flight tubes which might be reduced due to field-defining meshes, and the efficiency of the detector resulting in an overall efficiency of ξ_i, respectively ξ_e. Hence, the average number of detected particles is

$$w_{i,e} = \xi_{i,e}\bar{n} \tag{1.22}$$

If the laser pulse created n ion (electrons), the detection probability for k of them is given by the binominal distribution:

$$p_{i,e}(n,k) = \binom{n}{k}\xi_{i,e}^k(1-\xi_{i,e})^{n-k} \tag{1.23}$$

In order to get the probability of detecting exactly one ion and one electron per pulse at a given number of ionization events n, one has to multiply the individual probability of each detector with the Poisson distribution: $p_i(n,1)p_e(n,1)p^{\bar{n}}(n)$. The overall probability of detecting a coincidence is given by summing over all n[47]:

$$w_{11} = \xi_i\xi_e\bar{n}\left[1+\bar{n}(1-\xi_i)(1-\xi_e)\right] \times \exp\left[-\bar{n}+\bar{n}(1-\xi_i)(1-\xi_e)\right] \tag{1.24}$$

This will contain true as well as false coincidences. If a laser pulse produces n ion-electron pairs, the probability to detect one ion and one electron from the same pair is $1/n$. Hence, the probability for a true coincidence for a certain n is obtained by $p_i(n,1)p_e(n,1)p(n)/n$. Summing over all n gives the probability of true coincidences:

$$w_{11}^{(\mathrm{true})} = \xi_i\xi_e\bar{n}\exp\left[-\bar{n}+\bar{n}(1-\xi_i)(1-\xi_e)\right] \tag{1.25}$$

Subtracting the latter from the former defines the probability of false coincidences:

$$w_{11}^{(\mathrm{false})} = \xi_i\xi_e\bar{n}^2(1-\xi_i)(1-\xi_e)\exp\left[-\bar{n}+\bar{n}(1-\xi_i)(1-\xi_e)\right] \tag{1.26}$$

Figure 1.4 shows these three probabilities as a function of the average number of events.

1 Number of events per laser pulse

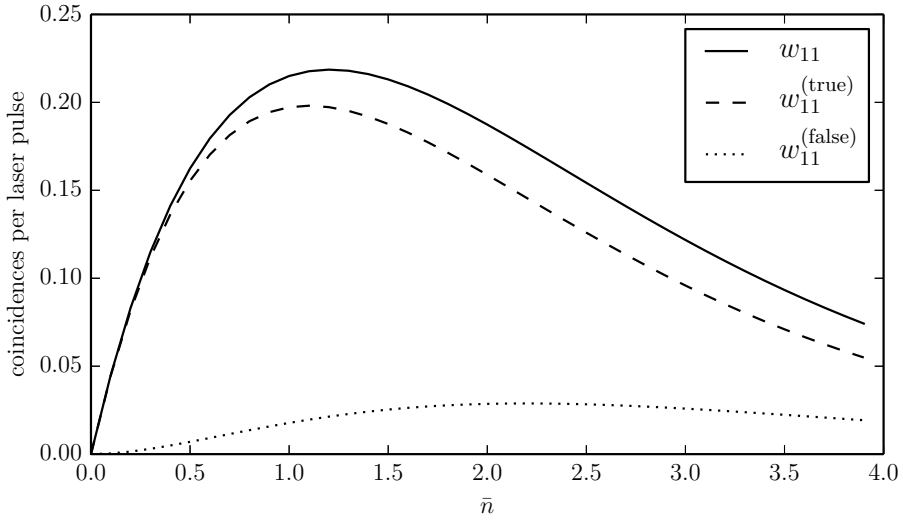

Figure 1.4: Rates of true, false and total coincidence rates for detection efficiencies of ξ_i=0.7 and ξ_e=0.7 as a function of the average number of produced ion-electron pairs per laser pulse.

The total coincidence rate increases with increasing average event rate. At some point it reaches its maximum and decreases afterwards as all rates do, because multi particle events become more frequent, which are discarded.

The true and false coincidence rates peak at different position due to the different minimum number of required ion-electron pairs. False coincidences need at least two ion-electron pairs.

Beside the pure probability of the true coincidences, it is also important to consider the influence of statistical and systematic error. The number of coincidences $Coinc$ is a so-called random Bernoulli variable that can only assume the values 1 (coincidence) and 0 (no coincidence). $Coinc$ has a mean of w_{11} and a variance of $w_{11}(1 - w_{11})$. The absolute statistical error of the measurement is given by the standard deviation of the sample average:

$$SD_{Coinc} = \sqrt{\frac{\mathrm{Var}(Coinc)}{N}} \tag{1.27}$$

with $\mathrm{Var}(Coinc)$ the variance of $Coinc$ and N the number of measured laser shots. With this the relative statistical error is deduced to [48]:

$$R_{\text{stat}} = \frac{SD_{Coinc}}{Coinc} = \left(\frac{1 - w_{11}}{N w_{11}}\right)^{\frac{1}{2}} \tag{1.28}$$

It can be reduced by increasing the number of laser shots.

The systematic error is defined as the ratio of false to true coincidences:

$$R_{\mathrm{sys}} = \frac{w_{11}^{(false)}}{w_{11}^{(true)}} \tag{1.29}$$

For a certain systematic error R_{sys}, an upper limit of the event rate can be calculated by

$$\bar{n}_{\mathrm{max}} = R_{\mathrm{sys}} \left[(1-\xi_i)(1-\xi_e)\right]^{-1} \tag{1.30}$$

For a given R_{sys}, one can calculate the number of necessary laser shots to obtain a certain statistical error:

$$N = \frac{1}{R_{\mathrm{stat}}^2} \frac{1 - w_{11}(\bar{n}_{\mathrm{max}})}{w_{11}(\bar{n}_{\mathrm{max}})} \tag{1.31}$$

with $\bar{n}_{\mathrm{max}}$ from eq. 1.30.

Assuming detector efficiencies of ξ_i,ξ_e ~ 0.7 and a desired systematic error of 1% so that false coincidences can be neglected, eq. 1.30 gives a maximum event rate of 11%. A statistical error of 1% needs $\sim 2 \cdot 10^5$ laser shots. This sounds quite low, but as mentioned in the beginning of this section neither a mass distribution of the ions nor an energy distribution of the electrons have been considered.

These equations also give the possibility to obtain the detection efficiency of a given apparatus and the average number of events per laser pulse (More details are given in appendix A.2).

2 Experimental Setup

This chapter describes the setup that has been built within the framework of this thesis. The setup consists of two main parts, the laser system (sec. 2.1) and the reaction microscope (sec. 2.2). The strong field experiments put certain requirements on both parts of the setup. The intended experiments need few-cycle laser pulses with a sufficiently high pulse energy to reach an intensity on the order of $10^{14}\,\mathrm{W/cm^2}$ by reasonable focussing conditions. As mentioned in the section 1.2, a high repetition rate is beneficial for coincidental detection schemes to reduce the total duration of a measurement. Hence, the laser source should also provide a high repetition rate of several hundred kHz. Besides the repetition rate, the coincidence detection put constraints on the combination of spectrometer and laser source. The atomic/molecular density of the target must be adapted to the ionization probability of the laser pulses in order to achieve an average event rate of $\sim 10\%$. The spectrometer itself needs a very low background pressure on the order of 10^{-10} mbar in order to provide a good signal-to-noise ratio. Thus, the design of each component plays an important role for the overall performance of the setup. The data analysis is covered in section 2.3.

2.1 Laser System

Before presenting the design of the laser system, some information about the generation of ultra-short laser pulses is given.

2.1.1 Laser Pulses: Generation and Properties

In order to reach field strengths sufficient for the experiments of this thesis, a laser source producing pulses with fs pulse duration has been used. Therefore, it is appropriate to give a brief description of the mathematical representation, properties and generation of ultra-short laser pulses. This section is partially based on [49–51], where a more in depth description can be found. The following section concentrates on the basic concepts. Specific topics will be explained during the description of the actual laser setup.

Mathematical description

A laser pulse is a coherent superposition of a multitude of monochromatic waves with a well defined phase relation. Its electric field description is in general depending on position and time (here for one monochromatic wave) [50]:

$$\vec{E}\,(\vec{r},t) = E_0(\vec{r},t)\cos(\vec{k}\vec{r} - \omega t + \phi_0) = \frac{1}{2}\left[E^-(r,t) + E^+(r,t)\right] \tag{2.1}$$

using

$$E^+(r,t) = E_0(r,t)e^{-i(\vec{k}\vec{r}-\omega t+\phi_0)} = E^-(r,t)^* \tag{2.2}$$

with $E_0(\vec{r},t)$ the amplitude, $\vec{k}$ the wave vector defining the propagation direction, ω the frequency and ϕ_0 the phase offset at $t = 0$. $\vec{k}$ and ω are connected by $|\vec{k}| = k = \frac{n(\omega)\omega}{c}$ with $n(\omega)$ the wavelength-dependent refractive index. For the following discussion, one could use the real representation by the cosine term. But for mathematical convenience, the discussion will use the complex representation and focusses only on the complex $E^+(r,t)$ component, since the relation 2.2 gives complete information about the real, measurable quantity $\vec{E}\,(\vec{r},t)$ of eq. 2.1[1].

Typically, one is interested in the field strength at a certain position in space. Therefore, $\vec{k}\vec{r}$ is set to zero. As stated before, a laser pulse is a superposition of several monochromatic light waves. This laser pulse can be described by a time dependent envelope $h(t)$ and a carrier wave if the bandwidth $\delta\omega$ is small compared to the carrier frequency ω_c [50]:

$$E^+(t) = E_0 h(t)e^{-i(\omega_c t+\phi(t))} \tag{2.3}$$

with $\phi(t)$ an in-general time-dependent phase. If ϕ_t is time-independent, then it defines the relative phase between the envelope and the carrier frequency. This is called Carrier-Envelope-Phase (CEP). The CEP becomes relevant for few cycle pulses where the change of the CEP has a large influence on the shape of the field below the envelope. It decides, for example, whether the maximum of the field is reached twice (sine pulse) or only once (cosine pulse).

So far the description of the laser pulse was based on a time representation of the electric field, but one can also use a frequency representation. The link between time and frequency is given by the Fourier transformation [50]:

$$\tilde{E}(\omega) = \frac{1}{2\pi}\int_{-\infty}^{\infty} E(t)e^{-i\omega t}dt = \frac{1}{2\pi}E_0\int_{-\infty}^{\infty} h(t)e^{-i(\omega-\omega_c)t}dt \tag{2.4}$$

The temporal shape of laser pulses can often be described by a Gaussian envelope $h(t) = \exp[-t^2/2\tau^2]$ with τ defining the width of the Gaussian envelope. τ is related to the Full-Width-Half-Maximum (FWHM) by $\Delta t_{1/2} = 2\sqrt{2\ln(2)}\tau$. The Fourier transformation with a Gaussian envelope in a temporal representation produces a Gaussian envelope in a spectral representation as well:

$$\tilde{E}(\omega) = \frac{E_0}{\omega_w\sqrt{2\pi}}e^{-\frac{(\omega-\omega_c)^2}{2\omega_w^2}}e^{i\phi(\omega)} \tag{2.5}$$

with $\omega_w = 1/\tau$ and $\phi(\omega)$ the spectral phase. One can define the minimum time-bandwidth-

1

product using the FWHM of the pulse envelope in both representations as

$$\Delta t_{1/2}\Delta\nu_{1/2} = 2\frac{\ln 2}{\pi} \approx 0.441 \qquad \text{for a Gaussian envelope} \tag{2.6}$$

with $\Delta\nu_{1/2} = 2\sqrt{2\ln(2)}\omega_w/2\pi$. This relation shows the minimum bandwidth which is required to obtain a (Gaussian) pulse with a pulse duration $\Delta t_{1/2}$.

If a laser pulse fulfils eq. 2.6, it is called *transform-limited*. In reality laser pulses are mostly not transform-limited. Although the measured spectrum of a pulse would yield a certain pulse duration due to eq. 2.6, the frequency-dependent phase of eq. 2.4 can lead to a longer pulse duration. If one assumes for the phase a quadratic time dependence $\phi(t) = \alpha t^2$ with α a constant, the central frequency gets time dependent:

$$e^{i(\omega t+\phi(t))} = e^{i\overbrace{(\omega+\alpha t)}^{\omega(t)}t} \tag{2.7}$$

If α is positive, the central frequency increases with time and the pulse with such a phase has a so-called up-chirp. This is the case when a transform limited pulse has passed a medium with normal dispersion (e.g. glass). A normal dispersion has a larger refractive index for the blue part of the spectrum than for the red part. The high frequencies are more retarded than the low frequencies of the spectrum.

Therefore, eq. 2.6 gives only a lower limit of the pulse duration.

Gaussian Beams

This paragraph summarizes a few important relations concerning Gaussian beam optics without their explicit derivation[1].

The instantaneous intensity is defined as

$$I(t) = \frac{1}{2}\epsilon_0 cE(t)E^*(t) \tag{2.8}$$

From this equation one can see, that the information about the (carrier-envelop-)phase is lost.

For laser beams geometric optics is not the appropriate way to describe their propagation. Laser beams propagating in the z-direction have typically a Gaussian intensity distribution across the beam profile with the radial coordinate $\rho = \sqrt{x^2+y^2}$:

$$I(\rho,z) = I_0(z)\exp\left[-2\frac{\rho^2}{w(z)^2}\right] \qquad \text{with } I_0(z) = \frac{2P_{tot}}{\pi w(z)^2} \tag{2.9}$$

where P_{tot} is the total power of the beam and $w(z)$ is the beam waist at $1/e^2$ of the intensity

1 An elaborate derivation is given in standard text books e.g. [50]

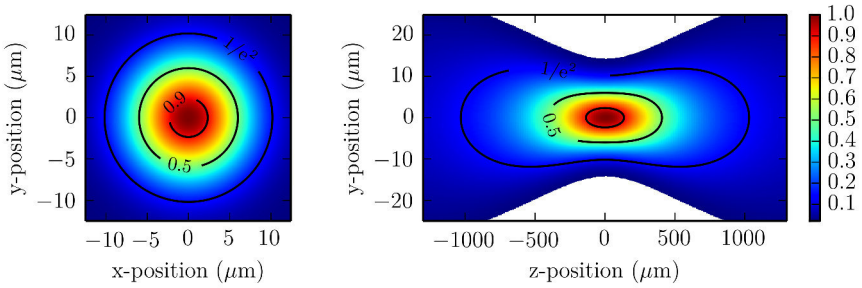

Figure 2.1: Intensity distribution of a laser focus according to eq. 2.9 with beam parameters: wavelength $\lambda = 800\,\text{nm}$ and beam waist $w = 10\,\mu\text{m}$. These parameters correspond to the situation when focussing a collimated beam with 4 mm beam diameter by a 80 mm focal length lens. Sub-plot (a) shows the radial distribution across the beam profile. Sub-plot (b) shows the axial distribution along the propagation direction. The intensity is given in fractions of I_0. Lines of a constant intensity are indicated by solid lines. The marked intensities are 0.9, 0.5 and $1/e^2$ of the peak intensity.

defined as:

$$w(z) = w_0\sqrt{1 + \frac{z^2}{z_0^2}} \tag{2.10}$$

where w_0 is the beam waist for $z = 0$ and z_0 is the Rayleigh length $z_0 = \frac{\pi w_0^2}{\lambda}$. It denotes the length at which the intensity drops by a factor of two. Figure 2.1 shows the radial and axial intensity distribution of a laser beam defined by eq. 2.9.

When a laser beam with a waist of w_L in front of a lens is focused, the focal spot size can be calculated by

$$w_0 = \frac{\lambda}{\pi}\frac{f}{w_\text{L}} \tag{2.11}$$

with f the focal length of the lens or focussing mirror. Hence, the intensity in the focus at the centre is

$$I_0(0) = 2\pi P_{tot}\frac{w_\text{L}^2}{\lambda^2 f^2} = \frac{\pi}{2}P_{tot}\frac{d^2}{\lambda^2 f^2} \tag{2.12}$$

with $d = 2w_\text{L}$.

This is the intensity in the centre of the focus at $z = 0$ and $\rho = 0$. Of course, it is not possible to achieve an interaction of the laser and the molecules only at this intensity due to the radial and axial intensity distribution of the laser beam. Hence, one can expect to get contributions from lower intensities as well. Fortunately, in the case of strong field ionization(see section 1.1) the ionization probability scales highly non-linearly with the intensity. Therefore, the contribution from low intensities are only marginal. In addition, by confining the molecular beam one can minimize any intensity averaging along the laser

beam axis, if the molecular beam width is a fraction of the Rayleigh length.

In order to understand processes in strong field physics which are in general strongly non-linear, knowledge of the exact intensity is of great importance. However, the accurate determination of laser peak intensity in the exact location where the interaction takes place is challenging, because it is sometimes hard to measure the beam profile and determine the pulse temporal shape in the interaction region. But the physical processes driven by a laser field provide themselves possibilities to measure the intensity as well. Two will be mentioned here:

Ratio of Double to Single Ionization Yield: The probability to single or double ionize an atom scales differently with the intensity. Hence, the ratio gives a measure of the intensity. Many experiments have been performed accurately measuring the yield of single and double ionization as a function of intensity of rare gas atoms. A quite comprehensive work is given in [52]. However, this method also requires a very precise measurement of the yield for single and double ionization as a function of intensity since the shape of both relations is very similar.

$2U_p$ Cutoff: As explained by the classical motion of an electron in an linearly oscillating field in section 1.1.1, the maximum energy gained by an electron in the laser field after ionization is two times the ponderomotive potential. Higher kinetic energies can only be reached by scattering at the ion core. But since scattering has a low probability the rate of electrons produced beyond $2U_p$ drops strongly leading to a kink in the energy distribution of the photoelectrons. In practice this method is not as exact as the classical calculation suggests.

However, for the determination of the intensity of the presented experiments, the geometrical approach and the $2U_p$ cutoff are used to cross check each other.

Generation of Strong Ultra-Short Laser Pulses

This section will describe how ultra-short laser pulses are generated and amplified. The term *ultra-short* refers usually to pulse durations below 1 ps.

As shown in eq. 2.6, the spectrum of a laser pulse needs to be large in order to achieve a short pulse duration. Since the amplification of light in a laser cavity happens during several round trips, only waves, that create standing waves between both mirrors of the cavity, interfere constructively and can be amplified. These waves are called longitudinal modes. The frequencies ν_m of these modes have to satisfy the condition:

$$\nu_m = m\frac{c}{2L} \tag{2.13}$$

with c the speed of light, m an integer and L the (optical) cavity length.

The electric field of a laser will oscillate on several adjacent longitudinal modes (typical several thousand). In general, these modes oscillate with a random phase relation between each other. Phase refers to the phase offset as defined in eq. 2.2. A random phase relation lead to a near-constant output intensity since the interference of several thousand modes tend

to average. If all modes oscillate at a particular phase relation, all modes can periodically interfere constructively leading to a pulsed intensity output. This implies two requirements on the oscillator:

- The gain medium must support a large spectral bandwidth containing multiple longitudinal modes.
- The oscillator must provide a mechanism to lock the phase of many modes to generate a short pulse.

Any mode locking principle is based on the idea that the cavity must provide a lower loss for modes with a fixed phase relation, i.e. pulsed operation mode, than for modes oscillating at random phases, i.e. continuous-wave operation mode.

The most commonly used gain medium for pulsed lasers in the fs-regime is sapphire doped with Titanium atoms (TiSa). It provides a large emission bandwidth (670-1070 nm)[53] as well as a passive mode locking mechanism. In order to exploit such a large bandwidth, it is necessary to carefully control the spectral dispersion inside the cavity. By using a pair of prisms or chirped mirrors, one can compensate the dispersion induced by the gain medium and other optical elements of the cavity.

The passive mode locking mechanism is Kerr lens mode locking [54]. It is based on an intensity dependent index of refraction:

$$n(\omega,I) = n_0(\omega) + n_2(\omega)I(r) \tag{2.14}$$

with n_0 the linear and n_2 the non-linear refractive index. The most intense part of a Gaussian laser beam is the central part. Thus, the central part experiences a larger refractive index than the transverse beam wings. In the case of a plane-parallel crystal, this produces the same situation as a common convex lens where the central part of the wave front is retarded and leads to focussing. Since the refractive index is intensity dependent, the laser pulse will experience a stronger focussing than the continuous-wave mode. With a proper design, for example by using apertures, the losses of the continuous-wave mode exceed those of the pulsed mode.

A typical length of a TiSa oscillator cavity is 1.8 m. According to eq. 2.13 this oscillator produces a pulse train with a repetition rate of ≈ 80 MHz. The energy per pulse is typically a few nJ with a pulse length of a few tenth of fs down to a few fs. Depending on the desired pulse duration, the average output power is in the range from a few hundred mW up to a few W. By tight focussing one can achieve an intensity on the order of 10^{11} W/cm^2 which is too little for strong field experiments.

Although oscillator designs exist that have much longer cavities increasing the pulse energy by lowering the repetition rate, they are mechanically less stable and do not support few-cycle pulses. Increasing the pulse energy while maintaining ultrashort pulse durations is a difficult task due to the extremely high peak intensities that can result in optical damage of the laser components. To increase pulse energies without the risk of optical damage, Strickland and Mourou adapted an amplification scheme for Radar pulses to the optical regime [34]. In this approach the pulse is stretched in time to decrease the instantaneous intensity. A

combination of two prisms or gratings is used to obtain the desired stretching in a controlled way by changing their distance to adjust the dispersion [55].

The stretched pulse is amplified by one of two common schemes. Either one can use a regenerative amplifier [56] which basically consists of a further cavity with a gain medium, or a multi-pass amplifier [57] which consists of a gain medium without a cavity. In both cases a pulse picker (e.g. Pockels cell) selects one pulse from the oscillator pulse train and sends it into the amplifier and thereby lowering the repetition rate.

The regenerative amplifier keeps the pulse for a few round trips inside the cavity. The pulse will extract energy from the gain medium at each round trip. When the gain medium is almost depleted, the pulse is coupled out of the cavity again by a pulse picker. In a multi-pass system the pulse will also pass the gain medium several times, but under different angles to the gain medium due to a mirror arrangement. After amplification a grating pair or chirped mirrors are used to recompress the pulse in time.

Both amplification schemes are limited in the achievable pulse duration due to gain narrowing and higher order dispersion by terms of higher order(neglected in eq. 2.14). Gain narrowing is a combined effect of the finite amplification bandwidth of the gain medium and the high gain per pass. This leads to multiple folding of the gain spectrum amplifying the centre of the pulse's spectrum more than its wings resulting in a smaller spectral FWHM. Hence the pulse duration becomes longer according to eq. 2.6. CPA systems deliver pulses down to 20 fs at a repetition rate from single shot to a few tens of kHz with up to several mJ of pulse energy.

In summary, the methods for intense laser pulse generation explained so far are not suited for a high repetition rate laser source as required in this thesis. Before the laser source is described (in section 2.1.2), that generates such strong pulses at high repetition rates, a few common methods to measure and to characterize ultra-short pulses are introduced.

Pulse Characterization

The characterisation of ultra short pulses in the fs-regime is not trivial due to the much lower temporal resolution of electronic devices (several ps). Typically one uses instead correlation methods in which replica or two or more different pulses overlap in a medium with non-linear response. The next pages will introduce three commonly used methods. For a larger overview, the book by Diels [51] is recommended.

Autocorrelation: The most frequently chosen method is the second harmonic autocorrelation. Here, two replica enter a non-linear crystal under a small angle. The second harmonic generation is detected along the angle bisector by a photo diode. Delaying one pulse with respect to the other, one measures a signal proportional to the convolution of the intensities:

$$S(\tau) = \int_{-\infty}^{\infty} I(t) \cdot I(t-\tau) dt \tag{2.15}$$

with the delay τ. However, this method requires the knowledge of the pulse shape to retrieve a correct pulse duration. For a Gaussian pulse shape, the retrieved pulse width τ_{AC} relates

to the real pulse duration as

$$\tau = \frac{\tau_{\mathrm{AC}}}{\sqrt{2}} \tag{2.16}$$

Frequency Resolved Optical Gating: If the autocorrelator as described above measures the spectrum of the second harmonic instead of the intensity by replacing the photo diode by a spectrometer, the pulse shape can be retrieved as well. This method is called frequency resolved optical gating (FROG). It uses an iterative algorithm to retrieve the amplitude and phase information of the pulse [58]. It starts with an initial guess for the electric field E(t) of the pulse and generates the FROG trace for this pulse. With this calculated trace, the algorithm calculates the error between the measured and the calculated FROG trace. Next, the algorithm generates a new guess for E(t) and starts the whole process again. In this way, it tries to find a best pulse by minimizing the error.

Spectral Phase Interferometry for Direct Electric-Field Reconstruction: Another method to retrieve the amplitude and phase of the laser pulse is Spectral Phase Interferometry for Direct Electric-field Reconstruction (SPIDER) [59]. It is experimentally more challenging but the retrieval is direct without iterative procedures.

The pulse under investigation is split into three replica. One of them is stretched in time to a multiple of its original duration by introducing a chirp. All three replica are then overlapped in a non-linear crystal. The two unstretched replica are delayed by τ with respect to each other, but their temporal separation stays within the pulse duration of the stretched third replica.

Hence, each of the short replica is superimposed with a different spectral slice of the stretched pulse due to the chirp. The sum-frequency generation process[51] will produce slightly different spectra according to:

$$\omega_{\mathrm{SG}} = \omega_{\mathrm{chirped}}^{(1,2)} + \omega_0 \tag{2.17}$$

with the new generated frequency ω_{SG}, the frequency ω_0 of the unstretched replicas and the instantaneous frequency $\omega_{\mathrm{chirped}}^{(1,2)}$ of the stretched replica at temporal overlap with replica 1 or 2, respectively. The interference of these two generated pulses measured with a spectrometer produces a interference pattern in the spectrum $S(\omega)$ containing information to reconstruct the spectral phase:

$$\begin{aligned} S(\omega) =& (E(\omega) + E(\omega+\delta\omega)e^{i\omega\tau})^2 \\ =& \left|E(\omega)\right|^2 + \left|E(\omega+\delta\omega)\right|^2 + 2\left|E(\omega)E(\omega+\delta\omega)\right| \times \cos\left(\phi(\omega+\delta\omega) - \phi(\omega) + \omega\tau\right) \end{aligned} \tag{2.18}$$

where $E(\omega)$ is the upconverted unknown pulse, $\delta\omega$ is the difference in frequency seen by one of the replica during the sum frequency generation, $\phi(\omega)$ is the spectral phase and $\omega\tau$ the phase introduced due to the delay between both short replicas. This signal $S(\omega)$ is Fourier transformed. From this transformed signal the DC terms and one side band are filtered. By subsequent back transformation of the filtered signal the phase term is retrieved. $\omega\tau$ can

be determined and removed from this by a calibration measurement beforehand. Finally, together with the spectrum of the pulse its temporal shape can be calculated.

2.1.2 Implementation of the High Repetition Laser System

In this section, the high repetition laser system will be described. An extensive description is given in the thesis of Freek Kelkensberg [60] and reference [61].

A commonly used system to generate few-cycle laser pulses is the combination of an oscillator-amplifier chain using chirped pulse amplification (CPA) to produce fs-laser-pulses with energies in the mJ-range. Pulse durations from these CPA systems based on laser amplifiers are typically limited to a few tens of fs due to gain narrowing. Therefore, the production of few-cycle laser pulses with those systems needs an additional step in which self-phase modulation [62] is used to broaden the pulse spectrum. Most commonly this is done by propagating the amplified pulse through a gas-filled hollow-core fibre[63] or by focussing the amplified pulse into a gas cell to produce a filament [64]. Recompression of these pulses leads to ultra-short pulses approaching the single cycle limit [35].

However, the repetition rate of these systems is typically a few kHz. Raising the repetition of these systems to hundred of kHz or more is not possible, since the TiSa-crystal will experience a tremendous heat load due to the difference of absorption wavelength to emission wavelength[1].

A different approach that is used in the present setup is Optical Parametric Amplification (OPA) in which few-cycle pulses from an oscillator are amplified by a non-linear effect in a crystal. The process itself transfers energy from a pump pulse with higher photon energy to a seed pulse with lower photon energy during an instantaneous interaction inside the crystal. The excess energy is also emitted as a so-called idler photon. Therefore, there is no heat load on the crystal.

But indeed, this shifts the thermal limitation from the amplifier to the pump source which involves itself a CPA scheme. However, the pump laser for an OPA has no strict requirements on its bandwidth as shown later. Hence, a narrowband source with good thermal characteristics can be chosen as well. A good alternative to Ti:Sa-CPA systems is therefore diode-pumped Yb-based CPA systems [65].

A small sketch of the setup is depicted in fig. 2.2. The setup consists of a Ti:Sa oscillator, a Yb-doped fibre amplifier and a non-collinear optical parametric amplifier. Each component is described in the following sections.

Oscillator

The laser oscillator is a commercial Ti:Sapphire oscillator from Venteon[2] (model type Pulse:ONE). It produces sub-6 fs laser pulses. The laser operates at a repetition rate of 80 MHz with pulse energies of 2 nJ. The wavelength is centred around 800 nm with a bandwidth of > 400 nm (@10 dB). The full bandwidth covers a complete octave allowing

1 Known as Stoke shift[50].
2 VENTEON Femtosecond Laser Technologies GmbH (http://www.venteon.com/)

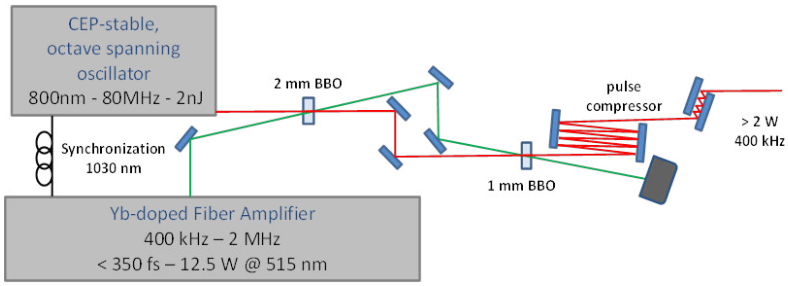

Figure 2.2: Schematic sketch of the laser system described in the text.

carrier-envelope-phase stabilization with an internal f-to-2f interferometer without the need of an additional spectral broadening. Furthermore, the large bandwidth covers also the spectral region where the pump laser (see next section) operates. Hence a small fraction with a bandwidth of 10 nm centred at 1030 nm is coupled out to seed the pump laser.

Pump Laser

The pump laser for the OPA is the commercial fibre CPA system 'Tangerine' from Amplitude Systèmes[1] with a custom-made modification. Instead of using an Yb-doped-fibre-based oscillator as the seed, the amplifier is seeded by out-coupled pulses around 1030 nm from the Ti:Sa-Oscillator as described in the preceding paragraph. After amplification of the seed pulses in an Yb-doped fibre based CPA, the laser pulses pass a frequency-doubling stage producing pulses at 515 nm with a duration <350 fs at a maximum average power of 12.5 W. The repetition rate of this laser is adjustable between 400 kHz and 2 MHz. A repetition rate of 400 kHz was chosen, to achieve relatively high pulse energies. Thus, pump pulses with 30 μJ were available for the amplification process.

Non-collinear Optical Parametric Amplification

The amplification of the short laser pulses in the present setup is done by Optical Parametric Amplification (OPA) [66] also known as difference frequency generation. In order to support a large bandwidth, this process is done in a non-collinear geometry as explained further below. The section starts with a description of the properties of OPA. At the end, it will summarize the key properties of the presented non-collinear OPA setup.

If light passes through a medium with electric field strengths small compared to inter-atomic fields, the polarization response is linear to the electric field strength. But at high intensities, when the electric field strength of the laser approaches fractions of intra-atomic field strengths, this picture changes and the polarization shows a non-linear response to the electric field. The polarization P of a medium can be written in a Taylor series with different

1 AMPLITUDE SYSTEMES (http://www.amplitude-systemes.com)

orders of the electric field:

$$P = \epsilon_0 \chi^{(1)} E + \epsilon_0 \chi^{(2)} E^2 + \epsilon_0 \chi^{(3)} E^3 + \cdots \tag{2.19}$$

Where χ^n is called the n-th order susceptibility of the medium. Classical linear optics is described by the first term that is linear in E. All other terms with a higher order in E can be ordered in accordance with the n-th order of the susceptibility and lead to a wave-mixing process of n+1-th order.

OPA is described by the second order susceptibility and is called a third order wave-mixing process. This can be seen by inserting electrical waves of two different frequencies into the second order term of the polarization:

$$E = E_1 \cos(\omega_1 t) + E_2 \cos(\omega_2 t) \tag{2.20}$$

gives

$$\begin{aligned} P_2 = \epsilon_0 \chi^{(2)} E^2 = & \epsilon_0 \chi^{(2)} \cdot \\ & \left[\frac{E_1^2}{2} \cos(2\omega_1 t) + \frac{E_2^2}{2} \cos(2\omega_2 t) \right. \\ & + E_1 E_2 \left(\cos[(\omega_1 + \omega_2)t] + \cos[(\omega_1 - \omega_2)t] \right) \\ & \left. + \frac{1}{2} \left(E_1^2 + E_2^2 \right) \right] \end{aligned} \tag{2.21}$$

In this equation, frequency components show up which are the sum and difference of the initial frequencies: $2\omega_1$, $2\omega_2$, $\omega_1 + \omega_2$, $\omega_1 - \omega_2$. The OPA process is a special case of difference frequency generation $\omega_1 - \omega_2$. Here, the lower frequency has a lower intensity and is referred to as *signal* and the strong beam as *pump*. The outgoing third photon $\omega_3 = \omega_1 - \omega_2$ is called *idler*. The labelling of idler and signal is arbitrary and can be swapped but in the common convention the lower frequency is called idler.

Besides the energy conservation $\hbar\omega_{pump} = \hbar\omega_{signal} + \hbar\omega_{idler}$, momentum conservation $\vec{k}_{pump} = \vec{k}_{signal} + \vec{k}_{idler}$ has also to be fulfilled in this process. A phase mismatch Δk can be defined by transposing all $\vec{k}$ on one side:

$$\Delta\vec{k} = \vec{k}_{pump} - \vec{k}_{idler} - \vec{k}_{signal} \tag{2.22}$$

If $\Delta\vec{k} \approx 0$, momentum conservation is achieved. This is also referred to as *phase matching*.

Phase matching can be achieved basically in two geometries: collinear and non-collinear propagation of the laser pulses in the non-linear medium. Figure 2.3b shows this schematically.

In a collinear configuration (left sketch of fig. 2.3b), the vectorial eq. 2.22 simplifies to a scalar equation with $|\vec{k}| = k = \frac{n(\omega)\omega}{c}$:

$$\Delta k = \frac{1}{c} \left(n(\omega_{pump})\omega_{pump} - n(\omega_{idler})\omega_{idler} - n(\omega_{signal})\omega_{signal} \right) \tag{2.23}$$

If the frequencies involved in the wave-mixing process are not close to any resonance of

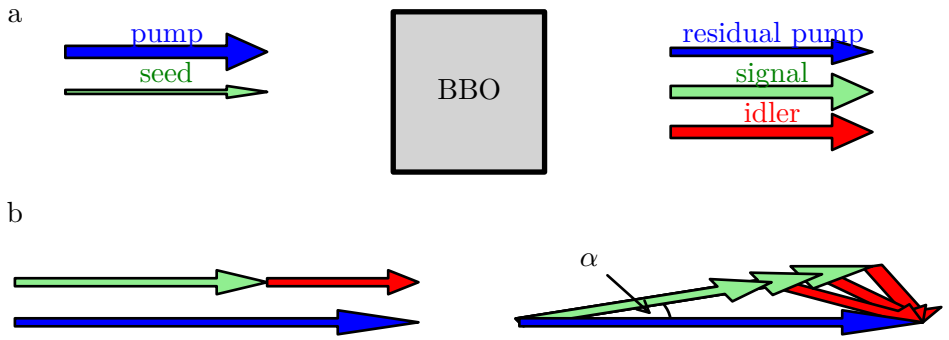

Figure 2.3: (a) General picture of the OPA process: pump beam and seed beam overlap in the crystal where energy from the pump pulse is transferred to the signal pulse producing an idler pulse following energy conservation.
(b) Two possible phase matching geometries: left figure shows collinear superposition, right figure shows non-collinear superposition. In both cases, the phase matching condition can be fulfilled but the non-collinear superposition fulfils it for a larger spectral bandwidth (for more detail see text and fig. 2.4).

the medium, the refractive index will show normal dispersion. Hence, the refractive index increases with frequency and therefore, as can be seen in formula 2.23, it is typically impossible to achieve phase matching in most of the wave-mixing processes. In contrast, when using a birefringent crystal phase matching can be achieved for different frequencies since the refractive index depends on the polarization of the light. In uni-axial[1] birefringent crystals one distinguishes two different refractive indices for different polarization of the laser light. The first refractive index, called ordinary (n_o), applies for a polarization parallel to the plane defined by the optical axis of the crystal and the k-vector of the light. A second refractive index, called extra-ordinary (n_e), is used in the case of a perpendicular orientation of the polarization with respect to the plane defined by the optical axis and the k-vector. The angle θ between optical axis and propagation axis k defines the value for the extraordinary refractive index n_e:

$$n_e^2(\theta) = \left[\frac{\sin^2(\theta)}{n_{e,90°}^2} + \frac{\cos^2(\theta)}{n_o^2} \right]^{\frac{1}{2}} \tag{2.24}$$

with n_o the ordinary refractive index and $n_{e,90°}$ the extraordinary refractive index at an angle θ of 90°. Using a negative uni-axial crystal ($n_{e,90°} < n_o$) one can achieve phase matching with a extraordinary pump beam and ordinary signal and idler beams by adjusting θ. This choice of polarisations is called type-I eoo phase matching.

However, phase matching for a broad range of wavelengths is not possible in a collinear

1 An uni-axial crystal has a single optical axis

configuration as can be seen in fig. 2.4a. Figure 2.4a plots the phase mismatch given by eq. 2.23 as a function of signal wavelength and angle between optical axis and pump-k-vector for a given pump wavelength of 515 nm. It is possible to achieve phase matching over a large signal wavelength region, but not at the same time for all wavelengths. Hence, the collinear geometry does not support amplification of ultra-broadband pulses needed for few-cycle laser pulses.

In the non-collinear configuration (shown in the right sketch of fig. 2.3b) the phase mismatch Δk transforms to:

$$\Delta k = \sqrt{k_{signal}^2 + k_{pump}^2 - 2k_{signal}k_{pump}\cos\alpha} - k_{idler} \tag{2.25}$$

with α the angle between pump and signal k-vector. Now it is possible to find a set of angles θ, α, where Δk is minimized for a larger wavelength region as shown in fig. 2.4b. The figure shows the same plot as fig. 2.4a, but for a non-collinear configuration of the beams at a non-collinear angle α of 2.5°. Clearly, for a certain angle (≈24.4° in this case) between crystal axis and pump-k-vector, phase matching is achieved for a large bandwidth. From fig. 2.3b one sees that the non-collinear geometry produces a strongly dispersed idler beam.

So far only the conditions for phase-matched parametric amplification have been discussed. But it is also important to know, how large the energy transfer is from pump to signal.

As derived in reference [67], the amplified intensity of the signal beam[1] is:

$$I_s(z) = I_s(0)\cosh^2 gz \qquad \text{for } gz \gg 1 \qquad \approx I_s(0)\frac{1}{4}e^{2gz} \tag{2.26}$$

with z the propagation distance in which pump and signal beam overlap. When the gain is high ($gz \gg 1$), $\cosh x$ can be approximated by $\frac{1}{2}e^x$. Hence the amplified intensity simplifies to

$$I_s(z) \approx I_s(0)\frac{1}{4}e^{2gz} \tag{2.27}$$

The gain coefficient g for the energy transfer from the pump pulse to the signal pulse is given by:

$$g = \sqrt{{\chi^{(2)}}^2 \frac{\omega_s\omega_i I_p(0)}{2\epsilon_0 n_s n_i n_p c^3} - \left(\frac{\Delta k}{2}\right)^2} \tag{2.28}$$

where $I_p(0)$ is the pump beam intensity at the beginning of the interaction. n_x is the refractive index of the crystal for signal, idler and pump photons, respectively. ω_s and ω_i are the frequencies of idler and signal photons. These equations show that the phase mismatch influences the amount of amplification.

Besides the phase matching, timing issues have to be considered as well. Since OPA is an instantaneous process, amplification only takes place, if pump and signal pulse overlap temporally in the crystal. The ratio between the pulse duration of both pulses determines the amplification efficiency as well as the pulse duration after amplification. Unfortunately,

1 with the approximation of no-pump-depletion, i.e. that the intensity of the pump pulse is constant during the amplification.

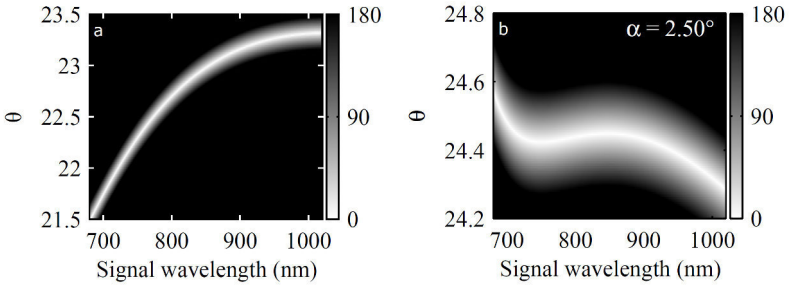

Figure 2.4: Phase mismatch for 515 nm pump pulse and the phase matching angle θ for (a) collinear configuration and (b) non-collinear configuration with a non-collinear angle α of 2.5° in a BBO crystal. It is clearly visible that the non-collinear configuration supports a larger spectral bandwidth during amplification. Both plots from [60]

one cannot optimize both. If one gets better, the other gets worse. It is a trade-off between amplification efficiency and pulse duration. For a high amplification efficiency, both pulse durations should match completely. If the seed pulse is shorter, parts of the pump pulse are not used for amplification. This matching is typically achieved by stretching the seed pulse, introducing a chirp. Hence, different parts of the seed pulse spectrum are present at different times of the pump pulse. Equation 2.28 shows that the gain depends on the instantaneous intensity of the pump pulse. Thus, with a chirp seed pulse, each part of the seed pulse spectrum is amplified by a different pump pulse intensity. This leads to a stronger amplification of the central part of the spectrum, if seed and pump pulse have the same duration. The effect is the same as described as gain narrowing for a CPA-system. The pulse duration gets longer due to the narrower spectrum.

If the seed pulse is shorter than the pump pulse and both pulse maxima coincide, the change in pump peak intensity along the seed spectrum is minimized. This provides a more uniform amplification of the seed pulse maintaining the achievable pulse duration.

The discussed properties show that the non-collinear geometry is a good choice for the amplification of few-cycle pulses at a high repetition rate. The present non-collinear OPA setup, shown in fig. 2.2, uses two BBO[1] crystals with different sizes for the amplification steps. Both amplification steps are based on type-I phase matching.

In the first step seed and pump are focused into a 2 mm thick BBO crystal with a non-collinear angle inside the crystal of 2.2° reaching an intensity of 200 $\mathrm{GW/cm^2}$. The beam divergence of seed and pump are similar and the beam sizes are 220 μm (pump) and 260 μm (seed). The seed beam is incident normal to the crystal surface to avoid angular dispersion.

After collimation both beams are focused into a second 1 mm thick BBO-crystal with slightly smaller beam size (30 %). The non-collinear angle is again set to 2.2°.

The broad bandwidth of the seed pulse already experiences a strong chirp due to dispersion in air while propagating towards the first OPA stage. This makes a further stretching of the

1 Beta Barium Borate (β-BaB_2O_4)

seed pulse unnecessary. The ratio at this point between seed(80 fs) and pump(300 fs) pulse is 0.25. Material dispersion of the BBO crystals leads also to a further stretching of the pulse. Therefore, one bounce on a pair of chirped mirrors is needed to restore the pulse duration ratio of seed to pump pulse before amplification in the second BBO crystal. After passing through the second BBO-crystal, the amplified beam is recompressed by eight bounces on chirped mirrors. At this point, a pulse energy of 5 μJ at 400 kHz is measured.

The temporal characterization was done using a SPIDER[1] specifically designed for few-cycle pulses. Figure 2.5 shows the reconstructed pulse with its spectrum (a) and its temporal shape (b). From this, the pulse duration is determined to be below 6-fs. But it also shows strong post pulses containing 65% of the overall pulse energy. Thus the energy in the main pulse is 2 μJ at 400 kHz repetition rate.

Measurements of the beam profile revealed a slight astigmatism of the beam exiting the non-collinear OPA [61]. The beam is resized by a reflective telescope in front of the reaction microscope. By a carefully adjusted angle between the mirrors of the telescope, the astigmatism is minimized. Additionally to the telescope, a periscope has been used to rotate the linear polarisation parallel to the spectrometer axis. The reshaped beam enters the reaction microscope through a 4 mm thick window[2] with a beam diameter of $\sim$5 mm, passes the interaction region collimated and is focused onto the molecular beam by a spherical mirror (f=80 mm) mounted inside the chamber. Position and tilt of the mirror can be controlled from the outside to maximize the overlap between the laser focus and the molecular beam.

The expected intensity can be calculated in the case of a collimated beam by[50]:

$$I = \frac{2W_{\text{pulse}}}{\pi\tau w^2} \tag{2.29}$$

with W_{pulse} the pulse energy, τ the pulse duration with w the focussed beam waist:

$$w = \frac{\lambda f}{\pi w_0}, \tag{2.30}$$

λ the laser wavelength and w_0 the beam waist of the collimated beam.

Using the measured values from above, the calculated intensity in the focus is in the order of 10^{14} $\mathrm{W/cm^2}$ assuming a central wavelength of 800 nm.

1 FC Spider from A · P · E Angewandte Physik & Elektronik GmbH (http://www.ape-berlin.de)
2 Propagation through the entrance window was taken into account for pulse characterization.

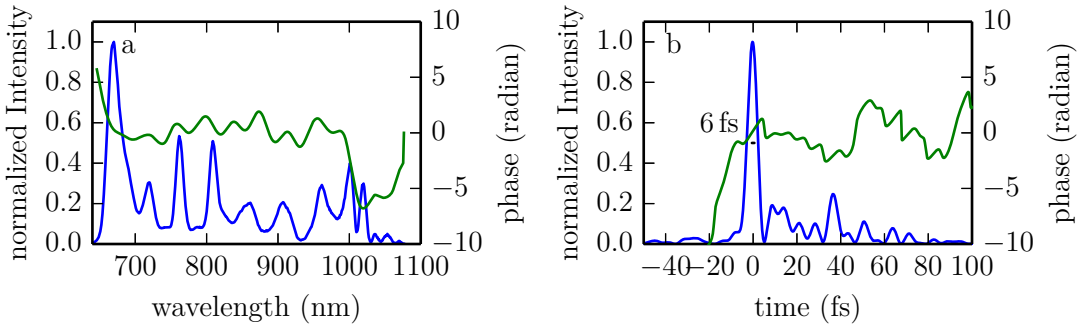

Figure 2.5: Reconstructed pulse measured by a SPIDER.
Figure a shows the spectral intensity in blue and the spectral phase in green.
Figure b shows the square of the reconstructed pulse envelope in blue and the temporal phase in green.

2.2 Reaction Microscope

The principle of the reaction microscope used in this thesis evolved historically from a technique called **R**ecoil **I**on **M**omentum **S**pectrometer (RIMS). First RIMS experiments studied the collision of very heavy, highly charged ions with atomic systems to measure multiple ionization and capture cross sections with angular resolution [68]. In order to obtain the transverse momentum transfer to the projectile these experiments detected the transverse momentum of the recoil ion, because the deflection of the projectile due to the collision was to small to be detected.

However, in this experiments the target atom was at room temperature. Therefore it has already such a large initial momentum spread that typical momenta of the recoil ions gained in the collision are largely covered by the target thermal motion at room temperature. For example, considering a helium target at room temperature following a Maxwell-Boltzmann distribution for the velocity of the gas atoms along one axis

$$f(v) = \sqrt{\frac{m}{2\pi k_B T}} e^{-\frac{mv^2}{2k_B T}} \tag{2.31}$$

gives a velocity spread of 1860 m/s (FWHM). Thus, the momentum resolution was restricted due to the thermal motion of the target to about 6 a.u. ($1.2\times10^{-23}\,\frac{\mathrm{kg\,m}}{\mathrm{s}}$) dependent on the target species[1]. Increase of the momentum resolution to the order of 1 a.u. was achieved by cooling the gas cell in a first step [69] and later an effusive gas jet [70] was used. A big step in terms of momentum resolution was taken by the usage of a supersonic expansion of the target beam. The supersonic expansion produces cold target beams with a few tens of mK translational temperatures[71] achieving a momentum resolution of 0.01 - 0.07

1 A higher mass results in a worse momentum resolution. The velocity spread scales with $m^{-\frac{1}{2}}$, but the momentum scales linear in m.

a.u. This apparatus is therefore called **COL**d **T**arget **R**ecoil **I**on **M**omentum **S**pectrometer (COLTRIMS).

COLTRIMS apparatuses are also used to measure electron momenta as well, but the acceptance angle is rather small compared to the acceptance angle of the ions. This drawback has been overcome by the use of a magnetic field along the spectrometer axis by Moshammer *et al.* [72, 73]. With this modification, it was not only possible to detect electrons within a solid angle of 4π but also to decouple transversal and longitudinal momentum resolution for the electrons. The name reaction microscope can be deduced from the fact that it is possible to adjust the momentum resolution as needed. Since then the reaction microscope was used for many different systems [74], for example: the study of electron correlations in double ionization processes [75], the observation of photo induced nuclear motion [76] as well as fundamental quantum questions [77].

In a typical reaction microscope, a molecular beam and a laser beam cross in the centre of a vacuum chamber. In this crossing region photo-induced reactions take place leading to the formation of ions and electrons. These charged particles are guided by an electric and a magnetic field towards position-sensitive detectors. From the time-of-flight and impact position, the full 3-dimensional momentum vector of the particle is calculated. The coincident measurement of all involved particles provides the option to look at different reaction channels in one measurement. An illustration of the actual setup is depicted in fig. 2.6.

The following sections describe each individual component of the spectrometer. It starts with the vacuum system in section 2.2.2. Section 2.2.3 describes the molecular beam which is produced by supersonic expansion of the target gas. This leads to a very cold beam providing a small initial velocity spread of the molecules. A narrow velocity spread increases the accuracy of the subsequent momentum reconstruction. In section 2.2.4 the spectrometer design is described in detail. Section 2.2.5 shows the design of the coils for the magnetic field. Section 2.2.6 explains the principle of the time- and position-sensitive detectors, followed by section 2.2.7 describing the processing of the measured signals.

2.2.1 Estimation of Vacuum Requirements

In this short paragraph, the vacuum requirements are estimated, since they determine the signal-to-background ratio. The signal-to-background ratio is given by the number of particles ionized in the molecular beam to the number of particles ionized in the background gas.

This signal rate and background rate $\dot{N}$ are given by:

$$\dot{N}_{\mathrm{mb,bg}} = R n_{\mathrm{mb,bg}} V \tag{2.32}$$

with the interaction volume V between laser and molecular beam or background, $n_{\mathrm{mb,bg}}$ the number density of molecular beam and background and the ionization rate R:

$$R = \sigma^{(n)} \frac{I^n}{\hbar\omega}. \tag{2.33}$$

Here, $\sigma^{(n)}$ is the n-photon cross section. Unfortunately, there is no large database available

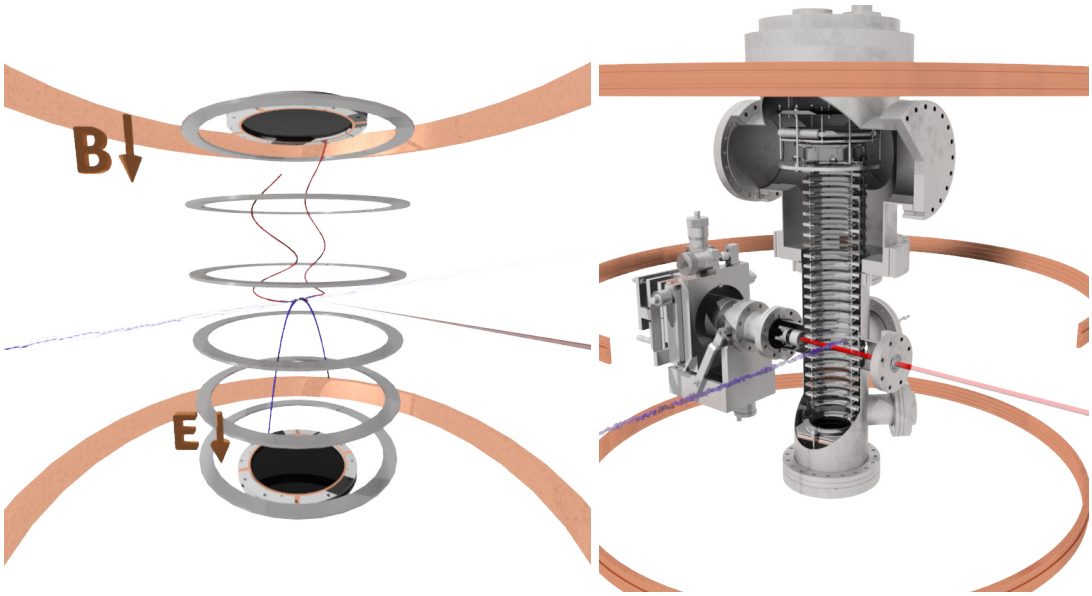

Figure 2.6: (a)Working principle of the reaction microscope: A laser beam is crossed with a molecular beam to excite and to ionize the target species of that beam. The surrounding electrodes produce an electric field to guide all ions towards the lower and all electrons to the upper detector, respectively. Additional coils generate a homogeneous magnetic field which mainly affects the electron trajectories to increase the acceptance angle for high energetic electrons. The detection of the time-of-flight and the impact position of each particle provides the information to calculate its initial momentum.
(b)Actual design: Here, the actual design (CAD drawing) of the spectrometer chamber is shown. The laser beam (red line) is focused by a mirror mounted inside of the chamber into the molecular beam (blue line). The ions are detected at the bottom detector whereas the electrons fly to the upper detector.

that provides the multi-photon cross sections for an arbitrary photon number and species. To get an estimation of the signal rate, the rate is approximated by a theoretical calculation.[1] More specifically, the calculation gives the probability P_{calc} that an atom will be ionized by the laser pulse. Multiplication by the repetition rate f_{rep} of the laser and the number of atoms in the interaction volume provides the signal rate:

$$\dot{N} = P_{\mathrm{calc}} \cdot f_{\mathrm{rep}} \cdot n \cdot V = R \cdot n \cdot V \tag{2.34}$$

If one takes into account a maximum signal rate of 0.11 ionization events per laser pulse as derived in section 1.2, the signal rate is $\dot{N} = 0.1 f_{\mathrm{rep}}$. Hence, the necessary number density is $1.3{\times}10^{9}\,\mathrm{cm}^{-3}$ using an interaction volume of $1.7{\times}10^{3}\,\mu\mathrm{m}^{3}$ and probability of 0.049 derived from the calculation for the ionization of argon with a 6-fs laser pulse at an intensity of

1 This is done by a time-dependent Schrödinger equation calculation as explained in a later chapter. For the estimation the details of the calculation are not important and therefore not explained at this point.

$10^{14}\,\mathrm{W/cm^2}$ and a central wavelength of 800 nm.

With the assumption of the same cross section for the background gas, one sees that the signal-to-background ratio is directly proportional to the ratio of the densities of molecular beam and background gas and the ratio of both volumes:

$$\frac{\dot{N}_{mb}}{\dot{N}_{bg}} = \frac{n_{\mathrm{mb}}}{n_{\mathrm{bg}}}\frac{V_{\mathrm{mb}}}{V_{\mathrm{bg}}} \tag{2.35}$$

Using a ratio of 10 (which means 10% of the signal stems from the background) and a background volume of $1.1\times10^5\,\mu\mathrm{m}^3$ results in a required background number density of $2.1\times10^6\,\mathrm{cm}^{-3}$. The background volume has been approximated by a cylinder with the same diameter as the focus and a length of twice the Rayleigh length. By using $p = nk_bT$, it gives a necessary background pressure on the order of 1×10^{-10} mbar. Since the ionization probability has been taken constant for the entire background volume, although the intensity is changing by a factor of two within the Rayleigh length, the derived background pressure is lower than actual necessary.

2.2.2 Vacuum Chambers

High efforts are needed to reach such low pressures as deduced in the previous section. All materials have to be ultra high vacuum (UHV)-compatible ensuring low outgasing rates and clean and smooth surfaces. Furthermore, due to the magnetic field, which is generated outside the chamber but must be homogeneous in the centre of the apparatus, all materials must have a low magnetic susceptibility. The most common choice for the chambers is stainless steel. Due to the requirements of a low magnetizability, only alloy type 1.4429 (DIN EN 10088-3) is suitable. This alloy has undergone the so called electro-slag remelting process (ESR)[1]. If an electrical insulation is needed, PEEK[2], ceramic, and Kapton are used.

The pump system is divided into two separate circuits, one for the molecular beam and its differential pumping stage and the second one for the main spectrometer chamber and the beam dump of the molecular beam. An overview of the pump circuits is depicted in fig. 2.7.

Turbo molecular pumps are used as the main pump type. They can operate in a wide pressure range starting at a few mbar down to 10^{-10} mbar. In addition, they have a high compression ratio[3]. Typical compression ratios for nitrogen and hydrogen are 10^9 and 10^7 [78], respectively.

To reach the necessary pressure (pre-vacuum) at which turbo molecular pumps can start to operate, one uses typically scroll pumps or membrane pumps. Additionally, these types of pre-vacuum pumps have the advantage that their mode of operation is oil-free which avoids possible back stream into the main chamber.

Scroll pumps having a high pumping speed of a few m^3/h are best suited for applications with a high gas load like molecular beams. Therefore, the backing pumps of the system

1 The ESR process cleans the steel alloy from impurities and gives it a small magnetic susceptibility μ_r
2 Polyether ether ketone
3 The compression ratio is the ratio of the outlet pressure to the intake pressure of a pump for a certain gas.

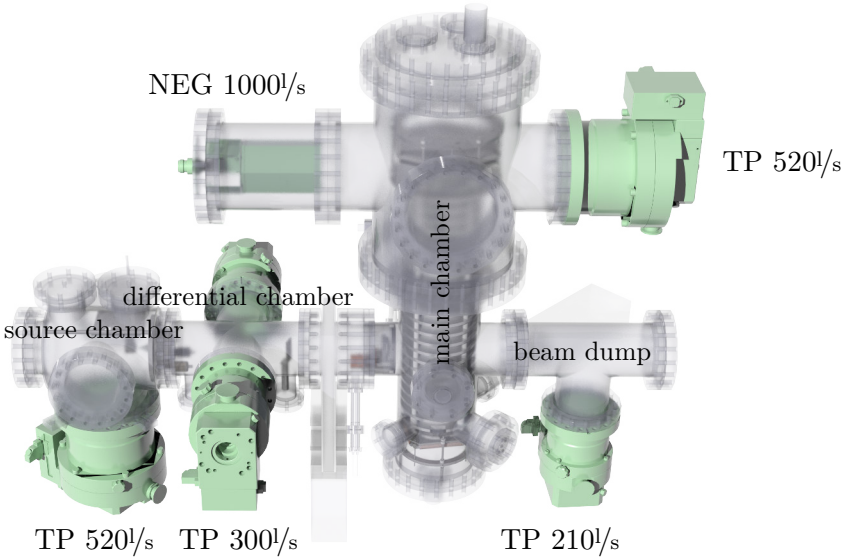

Figure 2.7: Vacuum system: The vacuum system contains two independent circuits with separate backing pumps. One circuit handles the high gas load due to the molecular beam and its differential pumping stage producing a low pressure. It consists of three turbo pumps. The second circuit produces a very high vacuum needed in the interaction region having only a low gas load and the vacuum of the beam dump. It consists of two turbo pumps and a special non-evaporative getter pump. Corresponding pumping speeds are shown in the figure. TP - turbo pump, NEG - non-evaporative getter pump

consists of a scroll pump for each pump circuit. Their final pressure is on the order of 10^{-2} mbar.

With this pressure and the above given compression ratios, one can estimate the final pressure in the vacuum chamber achieved by the turbo pumps to be on the order of 10^{-9} mbar. This is sufficient for the operation of the molecular beam,. But to reach the necessary pressure of 10^{-10} mbar in the main chamber of the spectrometer, an additional pump is needed to increase the compression ratio. Therefore, a small turbo pump called booster is inserted between the scroll pump and the turbo pump. This improves the pressure at the outlet of the turbo pump to 10^{-4} mbar.

The principle of operation of turbo pumps is based on momentum transfer between the rotating blades and the gas molecules. For this reason, light gases such as helium and hydrogen are pumped less efficiently by turbo molecular pumps, as can be seen already from the given compression ratios above.

Normally one uses ion getter pumps which pump these gases efficiently. However, ion getter pumps use a strong magnetic field to increase their efficiency. This magnetic field will disturb the homogeneous magnetic field needed for the electron detection in this setup.

Hence, ion getter pumps cannot be used.

In recent years, non-evaporative getter (NEG) pumps have been developed using special materials containing zirconium and titanium. These materials have the property to adsorb active gases (like H_2, N_2,O_2,H_2O, etc.) by chemical reactions. Since these pumps adsorb the gases instead of transporting them to the outside, they can saturate and loose their pump ability. The time frame for this depends on the sorption rate which is dependent on the actual pressure. Therefore, a NEG pump can only be operated at pressures of 10^{-7} mbar or better. Once activated, by heating the material to high temperatures for a short time, the material starts pumping without any further power consumption. In particular, the very high pumping speed for hydrogen (even at low pressures) make this kind of pumps very advantageous for UHV applications.

When a chamber is pumped starting at atmospheric pressure, the gas of the chamber volume will be evacuated relatively fast. Most of the remaining pumping time to reach a final pressure is determined by the desorption of molecules and atoms from the chamber walls. The main contribution of the adsorbed molecules is typically water. A common procedure to increase the desorption rate is to heat the vacuum chamber. This reduces the time to reach the final pressure significantly. The temperature level determines the time of heating for a certain target pressure; the higher the temperature the shorter the necessary time of heating. However, heat sensitive parts of the setup limit the applicable temperature. In the present setup, the temperature is limited to about 110°C by the optical window through which the laser pulses enter the chamber. The optical window is glued to the flange by a special adhesive[1] and temperatures above 120°C would loosen the adhesive.

Great care has been taken to achieve a homogeneous temperature of all vacuum parts to avoid a condensation of the desorbed water at a different location in the chamber. Therefore the frame for the entire spectrometer except for the molecular beam can be closed with heat isolation panels. All remaining protruding parts are covered with aluminium foil.

The final pressure achieved with this procedure is 2×10^{-10} mbar in the main spectrometer chamber. Since only the main chamber is heated during the bake-out procedure, the source chamber of the molecular beam and the differential pumping stage have a higher pressure. The source chamber has a base pressure of $\sim1\times10^{-6}$ mbar and the differential pumping stage $<1\times10^{-8}$ mbar.

2.2.3 Molecular Beam

A molecular beam is produced by the expansion of a gas at high pressure through a small orifice into the vacuum. The characteristics of the dynamics in this beam can be described by the Knudsen number:

$$K_n = \frac{\Lambda}{d} \tag{2.36}$$

Λ is the mean free path of the particles and d the diameter of the orifice. One distinguishes two different cases of molecular beams (with corresponding Knudsen number): effusive beams (also known as Knudsen beams) and supersonic expansion beams.

1 Torr Seal Vacuum Equipment High Vacuum Epoxy from Varian

The former is produced if the Knudsen number is ≥ 1. In this situation, the mean free path of the molecules is larger than the size of the orifice and almost no molecular collisions happen. The velocity distribution along the beam axis of an effusive beam is given by the one-dimensional Maxwell-Boltzmann distribution and determined by the initial temperature (see eq. 2.31).

But for a reaction microscope a source providing a narrow distribution is needed, which is given by a supersonic source having a Knudsen number $\ll 1$.

In this situation, the mean free path of the molecules is much smaller than the diameter of the orifice. The dynamics during expansion are mainly given by the intra-molecular collisions and leads to the production of a cooled, directed beam.

A high momentum resolution is crucial in the experiments. The initial velocity distribution of the target beam influences the momentum resolution of the spectrometer strongly.

In more detail (following [79]): If the expansion is considered as adiabatic and isentropic, then the sum of enthalpy H and kinetic energy of a particle with the gas flow velocity v, called stagnation enthalpy, is constant:

$$H_{stag} = H + m\frac{v^2}{2} = \text{constant} \tag{2.37}$$

The gas flow velocity prior to expansion is zero. Hence, the stagnation enthalpy is equal to the enthalpy H. When the gas expands, the flow velocity increases. This will decrease the enthalpy to conserve the stagnation enthalpy. Thus the expansion leads to cooling.

For an ideal gas the relation of a change in enthalpy H to a change in temperature T is given by

$$dH = C_p dT \tag{2.38}$$

with the specific heat capacity C_p. Using eq. 2.37 and the assumption of constant C_p over the range of T_0 to T, one gets for an ideal gas after integration over T the final velocity v:

$$v = \sqrt{2C_p(T_0 - T)/m} \quad \text{with} \quad C_p = (\gamma/\gamma - 1)(k_B/m) \tag{2.39}$$

with γ the adiabatic index, k_B the Boltzmann constant and m the mass of the species. The adiabatic index is defined as the ratio between the heat capacity at constant pressure C_p and the heat capacity at constant volume C_V which is also related to the degrees of freedom f of an atom or molecule:

$$\gamma = \frac{C_p}{C_V} = \frac{f+2}{f} \tag{2.40}$$

In the limit of a substantial cooling, T$\rightarrow$ 0 K gives the final velocity in the isentropic limit of:

$$v_{max} = \sqrt{2\frac{\gamma}{\gamma - 1}\frac{k_B}{m}T_0} \tag{2.41}$$

In the case of a seeded beam, consisting of two different components with a large difference in the number density $n_{1,2}$, the mass $m_{1,2}$ of eq. 2.41 is approximated by an averaged mass

m_{ave}[80]:

$$m_{ave} = m_1 \left[n_1/(n_1+n_2)\right] + m_2 \left[n_2/(n_1+n_2)\right]. \tag{2.42}$$

Equation 2.39 can be rearranged into a convenient form using the speed of sound $a = \sqrt{\gamma k_b T/m}$, the Mach number $M = v/a$ and the isentropic relations of an ideal gas [81]:

$$\left(\frac{P}{P_0}\right) = \left(\frac{\rho}{\rho_0}\right)^{\gamma} = \left(\frac{T}{T_0}\right)^{\gamma/(\gamma-1)} = \left(1+\frac{\gamma-1}{2}M^2\right)^{-\gamma/(\gamma-1)} \tag{2.43}$$

A simple relation between the Mach number M and the downstream distance x has been developed by Ashkenas *et al.* [82]:

$$M(x) = A\left(\frac{x}{d}-B\right)^{\gamma-1} - \frac{\left[(\gamma+1)/(\gamma-1)\right]}{2A(x/d-B)^{\gamma-1}} \tag{2.44}$$

where d is the diameter of the orifice and constants $A = 3.26$ and $B = 0.075$.

With M determined all relevant thermodynamic properties of the source can be calculated at any position.

As already mentioned before, the cooling effect is a result of the high molecular collision frequency. At some point along the expansion, this frequency decreases substantially leading to a transition from continuum flow to free molecular flow. This region of free molecular flow is called *zone of silence* due to the lower local speed of sound than the actual speed of the particles.

Due to the decrease of collision frequency, the energy transfer per collision also becomes smaller since the velocity difference between the particles decreases. This decrease in energy transfer affects the relaxation order of different degrees of freedom of the particles because the magnitude for a quantum of energy differs for different degrees of freedom. The quantum of energy of a vibrational degree is larger than that of a rotational degree followed by the translational degree. Hence, the vibrational degrees of freedom fall out of this cooling process at first, followed by the rotational degree of freedom. Finally, in the free molecular flow regime, the collision rate has dropped by such an amount that even translational equilibration will stop. Each degree of freedom will have a different final temperature, called vibrational, rotational or translational temperature.

The final translational temperature parallel to the beam is given by the final Mach number. Perpendicular to the beam, the temperature of the molecules continues decreasing since it is a pure geometrical effect. The fast particles will leave the beam faster than the slower particles.

So far the background pressure in the chamber has been neglected or has not played a role in the description of the expansion. But this is only true for the first part of the expansion as long as the pressure of the beam is much higher than the background pressure. When the beam pressure approaches the background pressure, the number of collisions between background and beam molecules increases and the velocity distribution gets disturbed. This leads to two shock zone boundaries in the case of a free expansion into the vacuum shown in fig. 2.8. These boundaries enclose the zone of silence. One boundary is cylindrically

symmetric centred around the beam axis - called barrel shock - and second a flat boundary terminates this barrel perpendicular to the beam axis called Mach disk. The position of the Mach disk is given by [79]:

$$x_{disk} = 0.67d\sqrt{\frac{p_0}{p_b}} \tag{2.45}$$

with d the orifice diameter, p_0 the stagnation pressure and p_b the background pressure of the source chamber. Typical Mach disk distances are on the order of a few mm to cm.

In this inner region, the molecular beam is "well behaving" and can be described by eq. 2.43. But as soon as the beam enters the shock zone behind the Mach disk, the properties of the molecular beam described above are destroyed. By reduction of the background pressure, the distance between orifice and Mach disk increases. A lower background pressure can be achieved by a high pumping speed of the source chamber[1] or - even more advantageous - by placing a skimmer at the position of the Mach disk slightly protruding into the zone of silence. A skimmer is a funnel with a specific form to avoid particles of the molecular beam hitting the skimmer to be backscattered into the beam again. Skimming the beam provides further advantages. First, since the skimmer produces a differential pumping situation, the pumping speeds needed in the chamber behind the skimmer are lower and a higher vacuum can be reached easily. Second, due to the free molecular flow at the skimming position, the molecular beam can be cut geometrically. This allows a high control over the beam width by using specific apertures or adjustable slits downstream of the beam. The divergence of the beam is given only by the cone angle between orifice and skimmer or skimmer and second aperture, respectively. Additionally, the distance between skimmer and second aperture as well as their sizes restrict the transverse velocity distribution of the beam. The maximal perpendicular velocity is given by (approximately) by

$$v_\perp = \frac{D_a}{d_{sa}} v_\parallel \tag{2.46}$$

with D_a the diameter of the last aperture, d_{sa} the distance between skimmer and aperture and $v_\parallel$ the velocity in the beam direction.

The dimensions of the present molecular beam setup are sketched in the lower half of fig. 2.9b.

The beam source is a small aluminium block with a Swagelok tube connector on the back and a 2 mm hole on the front. A small flexible PEEK tube connects the beam source with the external gas reservoir via a vacuum sealed feedthrough. The hole on the front side is covered by a small thin stainless steel pin hole plate[2] which is sealed with indium and a clamp ring pressing the plate with Indium in between against the main aluminium body. The entire source is moveable in all three dimensions to find the optimal position for throughput in terms of nozzle-skimmer distance and lateral overlap between nozzle and skimmer aperture.

The diameter of the pinhole in the experiment is 10 μm. Behind this nozzle a 300 μm-

1 The source chamber contains the nozzle through which the gas is expanding.
2 CVI Melles Griot

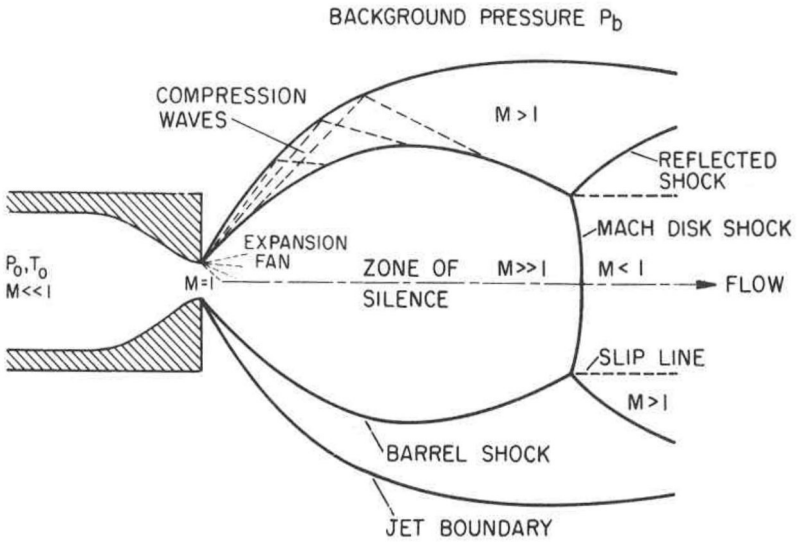

Figure 2.8: Zones in a supersonic expansion as described in the text. Figure from [79]

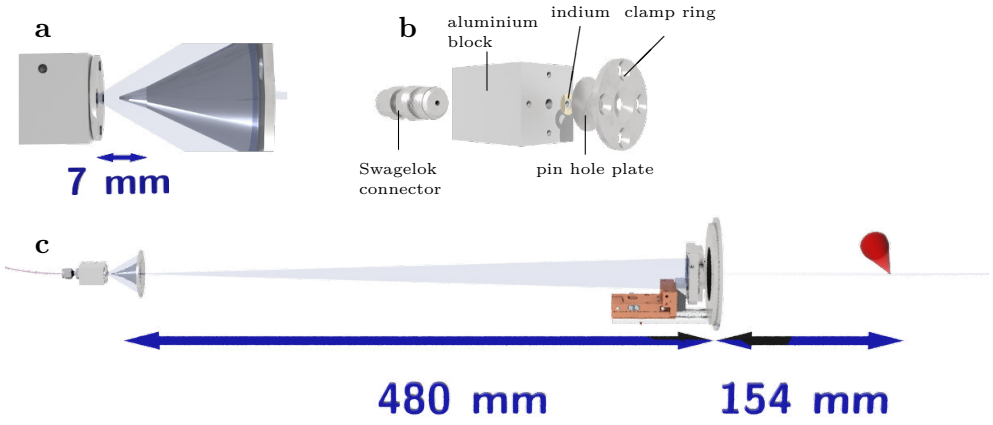

Figure 2.9: dimensions of the molecular beam: **(a)**Distance between nozzle and skimmer **(b)**Expanded view of nozzle
(c) Distances between skimmer and piezo slit and between slit and interaction point.

skimmer from Beamdynamics[1] is mounted at a distance of 7 mm on an adjustable mount. The source chamber separated by the skimmer mount is followed by a differential pumping stage. In this stage, a beam flag and a piezo-driven slit are installed for further manipulation of the molecular beam. The beam flag is a small plate mounted on a rotary feedtrough to manually block the molecular beam while in operation. This allows to measure the background in the main chamber without shutting down the beam. The installed piezo-driven slit from Piezosystem Jena[2] has a slit range from 8 μm to 300 μm. An orifice of 1 mm connects this stage with the main chamber of the spectrometer. The molecular beam crosses the laser focus 80 mm behind the orifice. After passing the main chamber, the beam is collected by a beam dump consisting of a further orifice with a 10 mm hole and a small tube pumped by a molecular turbo pump. In this way a large gas flow into the main chamber is prevented.

The stagnation pressure in the performed experiments is typically 1 bar. This leads to an increase of pressure in the source chamber to 10^{-3} mbar and in the differential pumping stage to 10^{-7} mbar. The pressure of the main chamber is increasing to $\sim 1 \times 10^{-9}$ mbar depending on the gas species. When closing the beam flag, the pressure in the main chamber decreases only by $\Delta p \approx 2 \cdot 10^{-10}$ mbar. Shutting off the beam completely leads to a reduction of the pressure to the base pressure of $2 \cdot 10^{-10}$ mbar. This increase points towards the fact that not only the molecular beam enters the main chamber but also diffuse gas from the differential stage leaks into the main chamber.

From the distance between nozzle and interaction point shown in fig. 2.9, one calculates the Mach number M (eq. 2.44) to be 4800. Given a stagnation pressure of 1 bar at room temperature using $n = p/kT$ and eq. 2.43 gives a density of the beam at the intersection with the laser beam of $\approx 1.4 \times 10^9\,\mathrm{cm}^{-3}$.

2.2.4 Spectrometer

In this subsection, the spectrometer shown in fig. 2.6 is described in detail. The main purpose of the spectrometer is to guide charged particles from the interaction region to the detectors. This has to happen in a controlled way to be able to reconstruct the initial momentum vectors of the particles with high accuracy. Accordingly, the electric and magnetic fields must be homogeneous by accurate design and assembly of the electrodes and coils. By using a classical time-of-flight (TOF) technique, the momentum of the particles can be reconstructed as explained in a later section. Since the time-of-flight technique is well known and used for a long time, many fully developed methods for compensation of non-ideal initial conditions like different starting positions (Wiley-McLaren TOF spectrometer [83]) or initial energy spread (Reflectron[84]) are available.

Nevertheless, these methods increase the effort of producing a homogeneous extraction field and/or destroy the momentum information due to the more complex setup. Furthermore, the Wiley-McLaren configuration needs sharp potential steps to achieve spatial focussing. Thus, metal meshes with typical 80-90 % transmission would need to be used to separate

1 for specification see http://www.beamdynamicsinc.com/skimmer_specs.htm Model 2
2 model type: PZS1 V1

the regions of different fields. Therefore, if one can reduce the number of used meshes, the overall detection efficiency of the spectrometer increases. Fortunately, due to the small laser focus (see section 2.1) used to ionize the target beam, a Wiley-McLaren configuration is not necessary. For this reasons, the current design discards the use of this method.

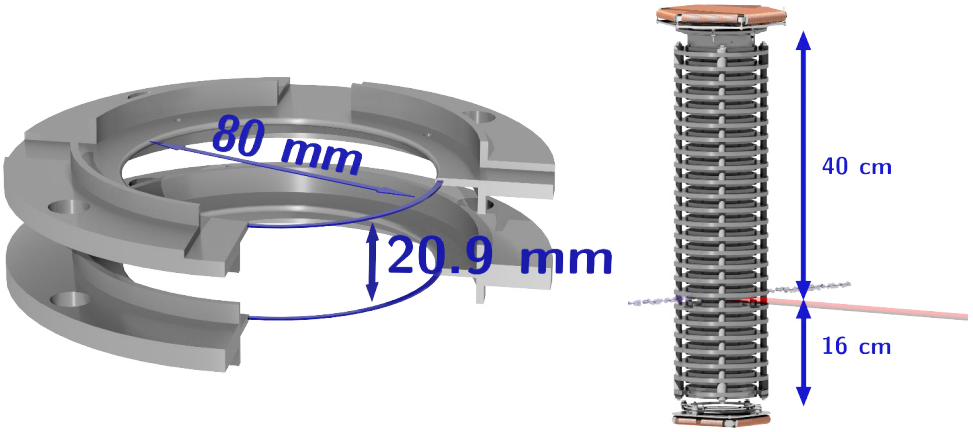

Figure 2.10: The left figure shows the dimensions of a single electrode. The upper electrode shown has cut-outs to avoid clipping of the laser beam and molecular beam. The right image shows the dimensions of the complete electrode stack.

The electrical field is produced by a stack of 25 stainless steel rings as shown with their dimensions in fig. 2.10. Small ceramic tubes insulate all adjacent electrodes and keep the distance between two adjacent electrode from centre to centre at 20.9 mm. By this symmetric and periodic layout, a high degree of homogeneity is achieved especially in the inner region around the interaction zone where laser beam and molecular beam cross each other. To maintain this high electric field homogeneity, great care has to be taken to screen any high voltage applied in the vicinity of the particles paths to the detector to avoid distorting their trajectories. Therefore, the electrodes have a high rim at a larger diameter closing the opening between the electrodes to 5 mm to avoid penetration of external fields. Small cut-outs in the electrode next to the interaction region of the laser beam and the molecular beam allow both beams to pass the electrodes without clipping. Simulations with SIMION[1] shows a negligible influence on the homogeneity of the electric field by these cut-outs as shown in fig. 2.11. The cut-outs will influence the homogeneity of the electric field in the region around the intersection between laser beam and molecular beam. During the acceleration towards the detectors, the ions and electrons will be still close to the centre of the spectrometer axis in the close vicinity of the interaction point. Therefore, fig. 2.11 shows the relative deviation of the electric field strength at the centre along the spectrometer axis for electrodes with and without cut-out.

1 http://simion.com/

At the lower end of the electrode stack facing the ion detector, a gold mesh (18.5 μm wire thickness, 344 μm spacing, 90% transmission) is mounted above the detector to shield the high operation voltage of the micro-channel-plate (MCP). On the opposite side (electron detector), no mesh is used because the MCP side facing the electrodes is close to ground potential (as will be explained in the detector section) and therefore a good matching in potential is possible. However, the gap between the upper electrode and the electron detector is surrounded by stainless steel since external fields in this region have to be shielded as well.

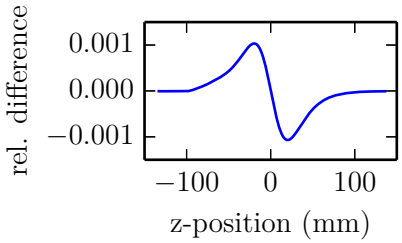

Figure 2.11: Relative difference between the electric field produced by electrodes with and without cut-outs in the region around the intersection of laser and molecular beam. This intersection is at 0 mm. The z-position is along the centre line of the spectrometer.

Voltage is applied to each electrode individually using Kapton insulated wires connected to a multi-pin vacuum feedthrough. Each pin is supplied with its voltage by an external resistive voltage divider which consists of 24 resistors of 50 kΩ in series and additionally one potentiometer with the same maximal resistance at each end of the chain (see appendix A.3.2 for more details). Due to the voltage divider, only two voltages are applied to produce the electric field. The field strength can be calculated by

$$E(\Delta U) = \frac{\Delta U}{N_R l_p} \tag{2.47}$$

with ΔU the difference between both applied voltages, N_R the number of used resistors and l_p the distance between two adjacent electrodes. The actual values of both voltages can be freely chosen since the voltage divider is floating.

The wiper contact of one of the potentiometers is used to apply an adjustable voltage to the gold mesh. This is necessary, because the distance between the last electrode and the gold mesh is different from the distance between two electrodes. The correct voltage was determined by simulation with SIMION.

The flight distance from the interaction point to the detector is 16 cm for the ions and 40 cm for the electrons.

2.2.5 Magnetic Field Coils

By applying a magnetic field parallel to the electric field the acceptance angle for electrons can be increased while keeping the electric field strength constant. Electrons with a perpendicular velocity move on a helical path defined by the Lorentz force. The Lorentz force is directly proportional to the (perpendicular) velocity $\vec{\mathbf{v}}_\perp$ and the magnetic field strength $\vec{\mathbf{B}}$:

$$\vec{\mathbf{F}}_L = q \cdot \left(\vec{\mathbf{v}}_\perp \times \vec{\mathbf{B}}\right) \tag{2.48}$$

With a known magnetic field strength, the initial velocity components and thus the momentum can be calculated from the detected position on the MCP. As for the electric field, also a

homogeneous magnetic field is essential for an accurate calculation.

Commonly, a pair of Helmholtz coils are used to generate a homogeneous magnetic field due to their simple design. The Helmholtz configuration consists of two equal coils placed symmetrically along a common axis separated by a distance equal to their radii. A current with the same strength and direction leads to homogeneous field which can be calculated with:

$$B(z) = \frac{\mu_0 I N R^2}{2} \left(\left[\frac{1}{R^2 + \left(\frac{d}{2} - z\right)^2} \right]^{\frac{3}{2}} + \left[\frac{1}{R^2 + \left(\frac{d}{2} + z\right)^2} \right]^{\frac{3}{2}} \right) \tag{2.49}$$

where I, N, R, d are the current, the number of windings, the coil radius and the distance between both coils. Eq. 2.49 shows that doubling the current or doubling the number of windings will double the magnetic field in both cases. Thus, in what follows the term current is used referring to the product of current and windings.

The main drawback of the Helmholtz geometry is the large space needed for the coils producing a homogeneous field only in a relatively small volume. However, as described in [85], an uniform field can be generated by a coil system that fulfils one of the following conditions:

1. same current in all coils but variation of radii and distance
2. identical radii but variation of current and distance
3. coils whose radii and positions are slices of one sphere with adjusted currents

The setup presented uses the second way consisting of three coils with identical radii but different currents as shown in fig. 2.12.

For this geometry, the conditions for an uniform field are:

$$\frac{d_{outer}}{r_{coil}} = 0.760051 \qquad \text{and} \qquad \frac{I_{centre}}{I_{outer}} = 0.531463 \tag{2.50}$$

where d_{outer} denotes the distance of the outer coils to the centre one, r_{coil} the radius of all coils, and I the current through the outer or centre coil, respectively.

The radius of the coils was chosen to be 50 cm which results in a separation of the outer coils to the centre of 38 cm. For the sake of simplicity in terms of the operation, all three coils are connected in series. To match the current ratio (eq. 2.50), 13 windings for the centre coil and 25 windings for each outer coil were used. The wound wire of the coils is a enamelled copper wire with a rectangular profile of 2 mm $\times$10 mm. The current source is a ZAS 1000/50/20 from Zentro-Elektrik which delivers up to 50 A at 20 V. Figure 2.12 shows the relative homogeneity of the magnetic field produced by this 3-coil-system.

The homogeneity of the field is not only affected by the design of the coils itself but also by unwanted external magnetic fields and the magnetic susceptibility of the materials used for the spectrometer. The magnetic susceptibility has to be as low as possible and is influenced by the choice of material as already mentioned in section 2.2.2.

The unwanted external fields consist of the earth field and of magnetic fields produced by other electrical devices producing magnetic fields. While the electrical devices can be

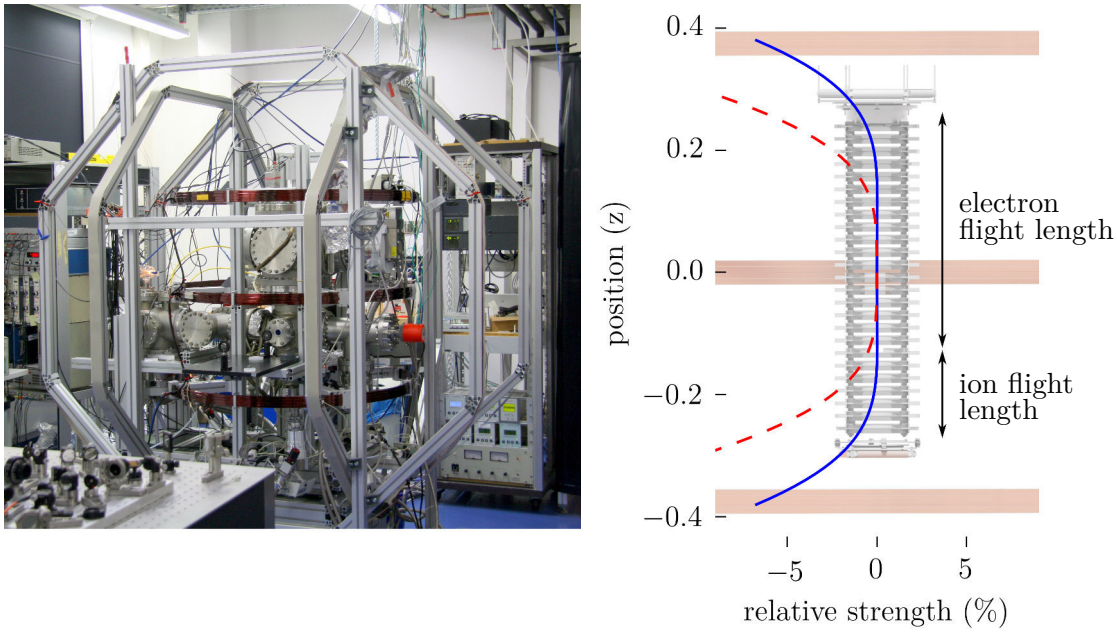

Figure 2.12: **(a)** Picture of the reaction microscope with the magnet coils for the main magnetic field and octagonal Helmholtz coils for compensation of the earth magnetic field. **(b)** Homogeneity of the magnetic field along the spectrometer axis. The plot shows the relative change of the magnetic field with respect to the centre of the field. The solid line is the field of the three coil system. The dashed line shows the field of a Helmholtz pair with the same radii.

switched off or placed at large distances, the earth magnetic field cannot. Although the earth magnetic field is homogeneous on the length scales of the spectrometer, it has typically not the same orientation as the spectrometer axis. An easy way to get control over the earth field is to apply an additional magnetic field which adds to the earth field and cancels unwanted components by the right choice of settings. This is implemented in the current setup by two pairs of additional Helmholtz coils surrounding the spectrometer (see fig. 2.12). They are built by an octagonal frame with diameter of 1.75 m and 1.6 m respectively supporting a ribbon cable.

2.2.6 Position-Sensitive Detectors

The purpose of the detectors is to record the time-of-flight and the position at which ions and electrons impinge. Each detector consists of two parts as shown in fig. 2.13: A micro-channel plate (MCP), which amplifies the impact of an particle to produce the time-of-flight-signal, and a so-called delay-line anode which provides the position information. The delay-line

anode is placed behind the back side of the MCP to detect the position of a hit on the MCP.

Micro-Channel Plates

MCPs are a few mm thick plates made of a glass material. The entire surface is covered by a regular pattern of channels having a diameter of a few microns (5-25 μm). The inner walls of these channels consist of a semiconductor material. When applying a high voltage difference of approx. 800 V between both sides of this plate, each channel acts as an electron multiplier. A particle hitting one of these channels, produces secondary electrons. These secondary electrons get amplified by a factor of typically 10^3 due to many further collisions with the walls inside the channel. The electrons are drawn by the electric field of the applied voltage towards the back of the MCP where they exit the channel. These channels are slightly tilted with respect to surface normal to increase the collision probability. High multiplication factors can only be achieved by actively dragging the electrons away from the MCP back once they left the channel. Otherwise the electron cloud gathering at the back would prevent an effective amplification.

This large number of electrons removed in a short time from the MCP increases the current rapidly, which in turn produces a voltage pulse. By using a capacitive decoupler, the voltage pulse can be retrieved and gives the time information of a particular hit.

Combining two (Chevron stack) or three (Z-stack) MCPs allows increasing the amplification factor up to 10^7. In these configurations each MCP is rotated by 180° with respect to the adjacent plate to avoid ion feedback[1]. The necessary voltage, at which an amplification sets in, increases with the number of MCPs. Each MCP in a stack needs a potential difference between 500 V and 800 V leading to an overall voltage applied on the stack of 2 kV and more. The preferred operation mode is at the highest voltage. Then, the amplification saturates and a signal with constant height is delivered independent of the impact energy of the detected particle.

A stack of three MCPs is used in the present setup for each detector. They are 86.7 mm in diameter with a useful diameter of 78 mm. The total thickness is 3 mm when stacked in a Z-stack. The pore size of the channels is 12 μm with a centre to centre spacing of 15 μm resulting in an open-area ratio of 70%. The channels have a bias angle of 20°. The resistance of each stack is 100 MΩ.

Due to the high number of individual channels the information of the detected particle's impact position is preserved.

Delay-Line Anode

There are several ways to extract the position information from the electron cloud leaving the back of the MCP. Very often a combination of a phosphor screen and a camera is used.

1 The increasing electron avalanche can ionize atoms from residual gas in the channel or adsorbed atoms on the channel wall. The ions then are accelerated by the MCP voltage towards opposite direction. These free, moving ions are called ion feedback. They can again produce a second electron avalanche when hitting the wall. These second signal disturbs the measurement and can also lead to a destruction of the MCP over time.

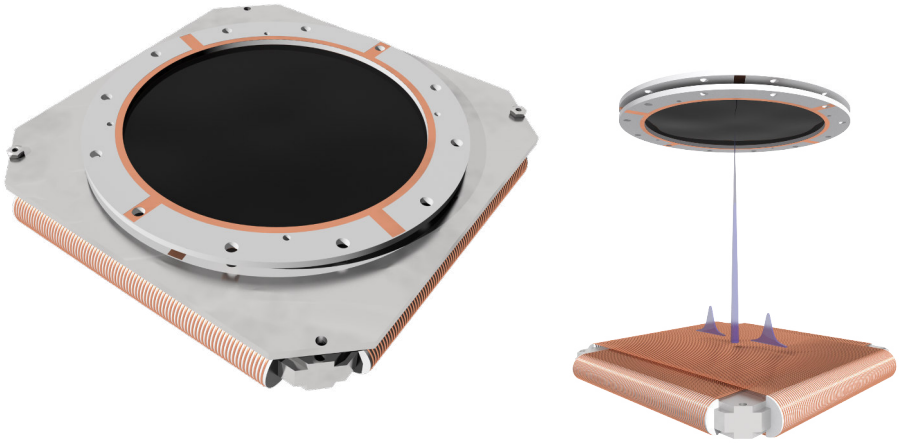

(a) (b)

Figure 2.13: **(a)** Structure of a delay-line detector: A chevron or z-stack MCP is placed in front of the delay-line anode. The distance between MCP back side and the anode is a few mm.
(b) Principle of operation of a delay-line detector: After impact of an particle the produced electrons are amplified in the corresponding channel of the MCP and exit the MCP at the back. This large electron cloud is collected by the anode producing two signals which propagate towards each end of the collecting wire pair. By measuring the time difference of both signals, the position can be calculated. (The distances between MCP and delay-line anode in figure b is overstated for visualization purposes.)

Due to the fluorescence lifetime and the speed of the camera, this combination is limited to low repetition rates if information of individual events is necessary. It can not be used to resolve a multiple hit in time.

With a delay-line anode (DLA), this problem can be overcome delivering high spatial and high temporal resolution. Delay-line anodes consist typically of two or three layers of a thin wire pair. Figure 2.13a shows a delay-line anode with two layers. These wire pairs are wounded around a plate with a pitch of 1 mm isolated by ceramic parts from the plate. The two wires of one pair are electrically isolated from each other and called reference and signal wire. A positive voltage (ΔU = +300 V) with respect to the MCP back is applied on both wires to attract the electron cloud from the back of the MCP. The signal wire has a slightly higher voltage (ΔU = +50 V) than the reference wire to preferentially collect the electrons.

After collecting the electrons, the deposited charge will start to propagate along the wire in both directions (fig. 2.13b). This current pulse can be detected at each end of the wire. The wire pair configuration has the advantage that one can use the difference signal between signal and reference to reduce the noise. By measuring the propagation time to each end, it

is possible to retrieve the position in one axis. To get the two dimensional position at least a second layer rotated by 90° is necessary. Typically, a spatial resolution below 100 μm is reached for these detectors when using fast electronics to measure the time differences.

The high resolution of 100 μm compared to the wire spacing of 1 mm is surprising. The reason is the following: the electron cloud leaving the MCP expands during its flight to the anode wires and as a result several wires collect electrons from this cloud. Determining the centre of mass of the resulting signal pulse gives a higher resolution than one would expect from the wire spacing.

Another important aspect of a delay-line anode is their multi-hit capability, i.e. the ability to detect and distinguish several events within a short time. The capability to detect several hits is limited by intrinsic dead times of the detector and dead times of the subsequent electronics. The dead time of a single MCP channel is on the order of a few ms, but a MCP has a few million independently operating channels. Due to the low probability to hit the same MCP channel, this dead time can be neglected for a two hit event. Typical dead times for the signal detection electronics are 10 ns [86] which is the bottle neck for the signal detection since the width (FWHM) of the analogue signal of the MCP is usually smaller. In the case that two particles hit the detector with a two layer delay-line anode within this dead time window of 10 ns, the impact time can be reconstructed, nevertheless, if the signals of the delay-line anode wires differ more than 10 ns. But as soon as the signals of the delay-line anode of one layer get into this dead time window, the electronics can not distinguish the hits any more. This leads to a blind area in a shape of a cross around a first hit for a simultaneous second hit as shown in fig. 2.14a.

An improvement is achieved using three layers with a rotation of 60°. This provides redundant information which is helpful in the case of multi-hit events. The redundant information leads to a reduction of the blind area to a small spot around the first hit position (see fig. 2.14b). Every time two particles hit the detector at the same impact time at least two layers will deliver position timing signals which are different for both particles except for the case hitting exactly the same place.

The current setup uses a detector with a two layer delay-line anode for the ion detection since even in fragmentation processes a multi-hit event within a time window of few ns is very rare. Additionally, due to the requirements for coincidence detection (see section 1.2) with a high ratio of good to bad coincidences, events with ionization of more than one particle hardly happen.

The electron detector uses a three layer delay-line anode since double ionization will most probably occur as well at the laser intensities used.

All applied voltages to the detectors are provided by iseg power supplies[1]. Since the voltages of the delay-line anode wire pair have a constant absolute difference between both wires (reference and signal), a special circuit has been assembled to use only one power supply output but having two voltage outputs with a specific voltage difference. This circuit is described in appendix A.3. For the sake of completeness the applied voltages to all components of the detector are summarized in table 2.1.

1 iseg Spezialelektronik GmbH (http://www.iseg-hv.com/) model type: NHQ 204M

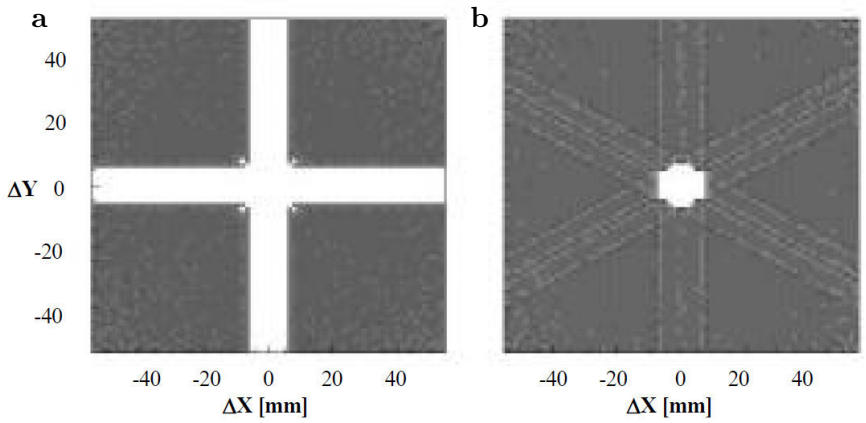

Figure 2.14: Monte-Carlo simulation of the blind regions for two particles. It shows the relative position on a (a) square delay-line anode with two layers and (b) a hexagonal delay-line anode with three layers. In the white region the detector is blind for the second particle position.(from [86]).

detector	**component**	**voltage [V]**
ion	MCP front	−2400
	MCP back	0
	holder	100
	DLA reference	260
	DLA signal	300
electron	MCP front	70
	MCP back	2470
	holder	2570
	DLA reference	2710
	DLA signal	2770

Table 2.1: voltages applied to detectors

2.2.7 Signal Processing

Signal processing needs several steps as signal decoupling, amplification and discrimination of the decoupled signals and finally digital processing. Figure 2.16 summarizes the entire circuit of the signal processing in a diagram. The following describes each component in this diagram in more detail.

Each particle impact produces several current pulses which are used to retrieve the time-of-flight and impact position. But before these signals can be used for the analysis, they must be decoupled from the channel plates and delay-line anodes carrying high voltages. In the case of the MCP, this is done by a high-pass filter consisting of a capacitor and a resistor. The capacitor guarantees the separation of the high voltages applied to the detector,

but transmits the fast signal of the voltage pulse. The resistor is variable to achieve an impedance matching to the cable connected with the subsequent electronics. The signal can be retrieved from front and back of the MCP. Hence, both sides are connected to a decoupling circuit. If one picks the signal from the front side, the decoupler from the back is connected to ground (and vice versa). The resistors of both decoupling circuits must be adjusted minimizing the impedance mismatch to avoid reflections.

Signals from the delay-line anode are decoupled in a different way. Here, also a galvanic separation of the high voltages is needed, but in addition the difference signal of reference and signal wire is decoupled. As a result the signal decoupled is free of external noise.

Then, all signals (MCP and delay-line anode) must be amplified for further processing. In this amplification step, great care has to be taken to preserve the time resolution. Consequently, the electric amplifier has to provide a large bandwidth supporting the fast rise of the signal pulse's leading edge which is 7 ns[1]. All signals are amplified with devices from RoentDek. The amplifier model type for the electron signals is FAMP8 and the ion signals are amplified by a ATR19.

The next step is the conversion of these signals into standardized NIM[2]-logic-signals. This step has the advantage of producing a signal which is less sensitive to external noise. To get a high precision for the time information, a constant fraction discrimination (CFD) is used, which produces an output always at a certain relative height of the signal pulse. Thus, the time information is independent of the pulse height. Figure 2.15 shows the working principle of a CFD. In short, the CFD produces an inverted attenuated copy of the original signal which is delayed by 80% of the rise time. Recombining both signals creates a zero-crossing which triggers the new NIM-signal. Compared to threshold based discriminators, the CFD does not degrade the time resolution due to different signal heights. The model used for the ion signals is the ATR19, which is a combined amplifier and discriminator, and the model for the electron signals is the CFD8c.

After conversion all NIM-signals are fed into two time-to-digital converter (TDC) PCI cards (one for each detector) based on the HPTDC chip from CERN [88]. Both TDCs are synchronised to an external clock. Each card has eight channels which record the arrival time of the signals with a time resolution of 25 ps with respect to a common trigger signal. Each individual channel has a dead time of < 10 ns (typically 5 ns). The maximum number of hits distributed over all channels of one card is $2 \cdot 10^6$ hits per second without a dead time due to read out since new data is already acquired during a readout. This last point makes this TDC particularly useful for high repetition rate systems.

Beside the signals from both particle detectors, the TDC records a laser pulse time signal as well. This laser time information is collected by an avalanche-photo diode using a weak reflection of the laser pulses at the entrance window to the spectrometer. After amplification by a fast pre-amplifier from Phillips Scientific (model 6954) the signal is discriminated by a leading edge discriminator (Fast ComTec Model type: 7011) which is possible because the signal height of the detected laser pulses is not varying more than 5-10% from pulse to pulse.

1 Rise time from 10% to 90% of the signal height.
2 nuclear instrument module standard

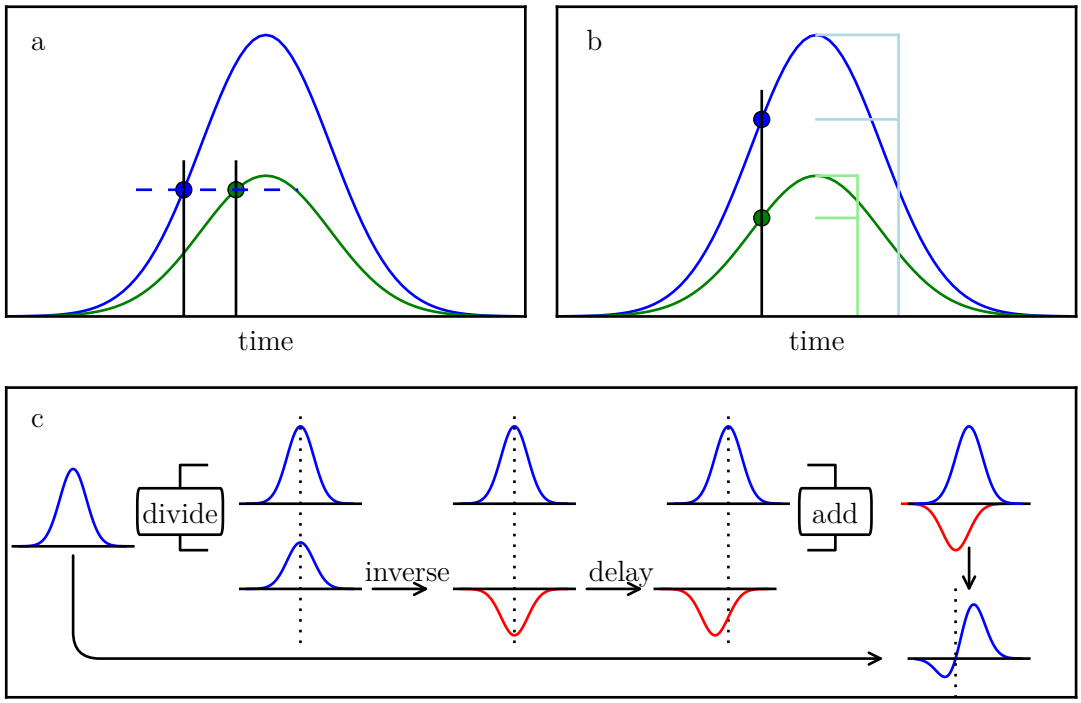

Figure 2.15: Idea of a constant fraction discriminator: Instead of using a threshold to measure the pulse arrival time which leads to inaccurate time information for strongly fluctuating pulses (shown in **(a)**), constant fraction discriminators use the time at which the ratio between pulse maximum and current signal is a constant value (shown in **(b)**).
(c) Realisation: This principle is realized by producing a copy of the signal which is inverted, delayed and finally superposed with the original signal. When this combined signal crosses zero the discriminator triggers. a and b adapted from [87]

The recorded times from the TDC cards are saved to a file in an event based manner by a commercial acquisition software (COBOLD), provided also by RoentDek.

Trigger Scheme

In order to retrieve the full information of a hit, the measured times need a common time zero as a reference. Typically the laser trigger defines this common time zero, since it starts the photo-induced process under investigation. However, in the present situation with a high repetition rate laser, triggering on the laser pulse leads to complications in the data evaluation.

When triggering on the laser pulse, it is convenient that all ionized particles arrive at the detector before the next laser pulse triggers a new event. Otherwise these later particles will be registered as particles of the new event but with a reduced time-of-flight. The detected

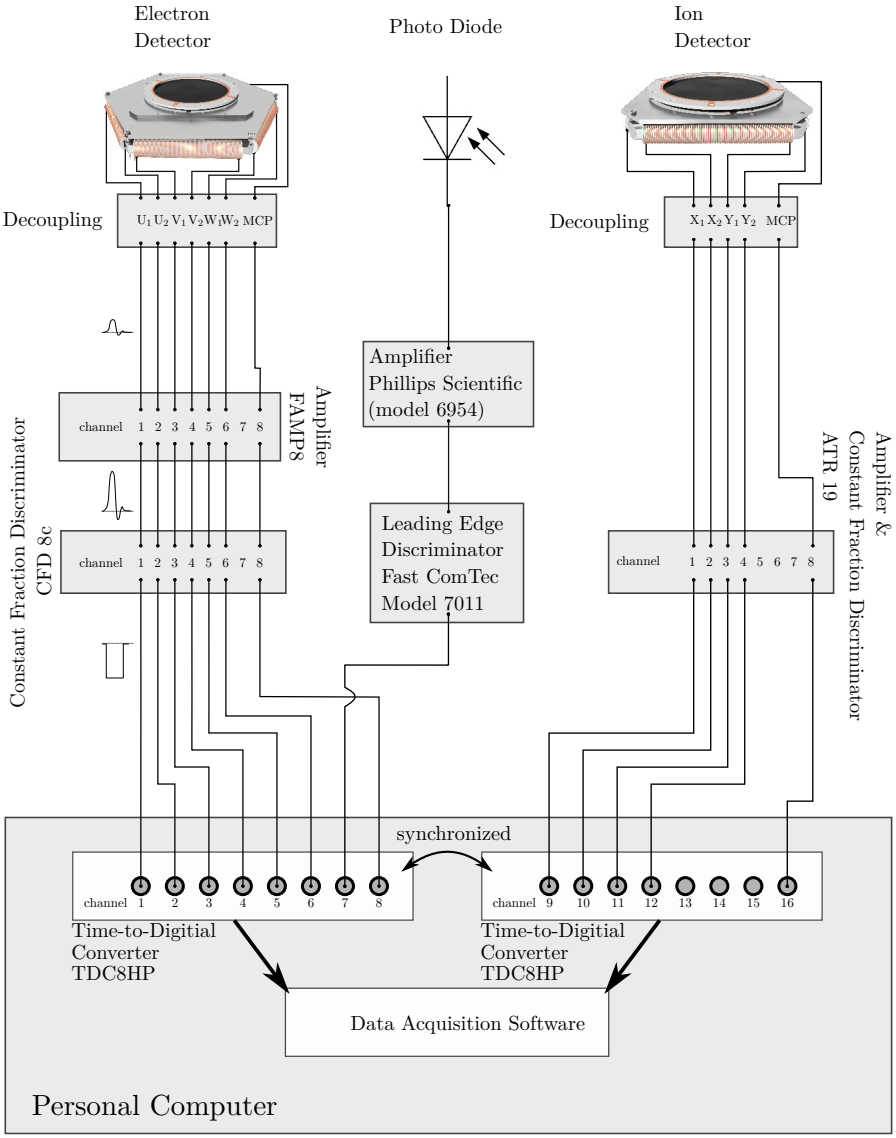

Figure 2.16: Signal processing: The MCP signal of the electron detector triggers a detection event and all other signals are registered with respect to that time.

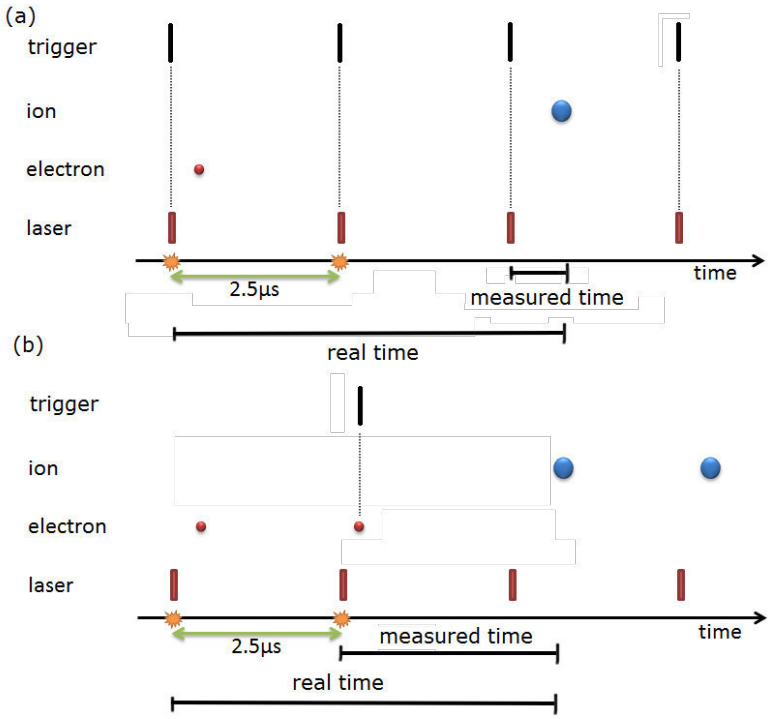

Figure 2.17: TOF folding: (a) The laser pulse arrival to the photo diode is used as trigger signal. This produces a folding of the real time-of-flight into the laser repetition period. **(b)** A signal from the electron MCP is used as trigger. This produces in most cases a detection of the real time-of-flight. But in some cases when an electron is missed but a second electron is detected the measured time is shifted by a multiple of the laser repetition period. Since this case is most probable for species with main contribution to the ion time-of-flight signal, only shifted peaks for this mass show up.

time-of-flight is given by the actual time-of-flight modulo the repetition period of the laser. Thus the mass spectrum would be folded into a time window given by the repetition period. Figure 2.17a shows this folding. In the present setup this period is 2.5 μs at a 400 kHz repetition rate and the time-of-flight of the main mass contribution is on the order of 10 μs. In addition, the actual signal rate is about 10% of the repetition rate and therefore, a lot of events are triggered and stored, in which neither an ion nor an electron was detected.

In order to avoid the time-of-flight folding and to reduce the amount of stored information, the electron MCP signal is used to trigger the TDC, since the flight time of the electrons is below the laser repetition period. This enables the assignment of the electron to the corresponding laser pulse.

Unfortunately, triggering on the electron not completely avoids problems related to the high repetition rate which can be seen in the following example depicted in fig. 2.17b. When two laser pulses within the time-of-flight of the main mass contribution produce an ionization event, it can happen that the first ionization does not trigger a new event. This might

happen if the first electron hits the detector within the trigger dead time[1] or if the first electron is not detected. Both cases lead to a false time information for one of the detected ions. Normally, the main mass contribution is dominant. Therefore, a false time-of-flight will show up in the time-of-flight spectrum as a small so-called ghost-peak shifted by a multiple of the laser repetition period from the main mass peak depending on how many laser pulses are between ionization event and trigger event. The amount of these ghost-peaks is determined by the actual signal rate and the detection efficiency of the spectrometer for electrons. Thus, the amount of visible ghost-peaks is another indicator for the ratio between true and false coincidences. The higher the ghost-peak contribution in the TOF spectrum, the higher is the ratio of false to true coincidences.

In addition to the choice of the trigger channel, one has to define a time window which is recorded after a trigger is detected. This window starts 500 ns before the trigger. The end time depends on the time-of-flight of the species under investigation. The negative start time is necessary to detect the laser pulse that initiated the ionization. For later data evaluation, all measured times will be shifted by the difference between trigger and the first laser signal at negative times to set the reference to this laser pulse.

2.3 Data Analysis

This section describes the processing of the recorded raw data containing time stamps to obtain the momenta of each detected particle. For this transformation a few steps are needed:

- calibration of each detector
- extraction of impact position and tof from raw data
- determination of time offsets
- momentum calculation

The steps necessary to extract the correct time and position information are described in section 2.3.1. Section 2.3.2 explains briefly how the software deals with events containing timing information of several hits. In section 2.3.5 the momentum calculation is described. Each measurement produces large amounts of data, thus, an elaborated data handling is needed which is described in section 2.3.6.

For the analysis, it is necessary to define a coordinate system which is depicted in fig. 2.18. The origin is located at the intersection between molecular beam and laser focus. The x-axis goes along the molecular beam towards the beam dump. The y-axis coincides with the pointing vector of the laser beam after reflection on the focussing mirror. Thus, the y-axis is pointing towards the entrance window for the laser beam. The z-axis is then determined by the cross product of the x- and y-axis leading to a z-axis parallel to spectrometer axis pointing towards the ion detector.

1 The trigger dead time can be set in the acquisition software.

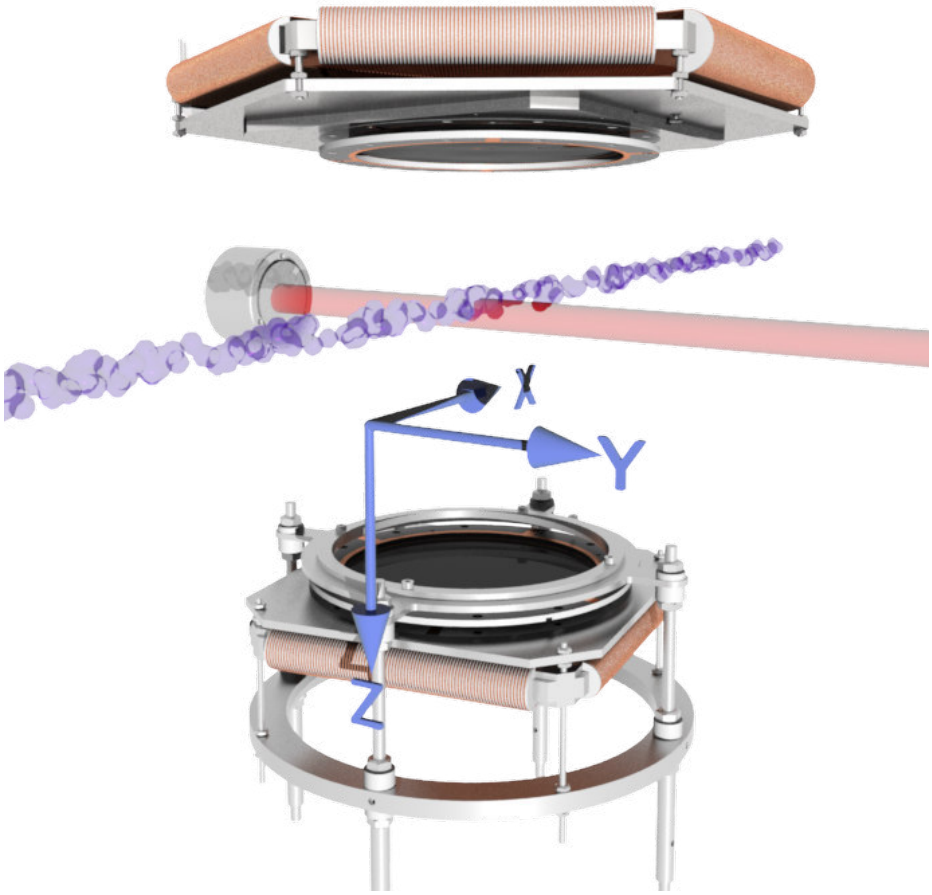

Figure 2.18: illustration of the used coordinate system: the x-axis coincides with the direction of the molecular beam, the y-axis points in the same direction as the laser beam after reflection on the focussing mirror and the z-axis points towards the ion detector.

2.3.1 Calibration

As described briefly in section 2.2.6, the position information from the delay-line anode is retrieved from arrival time differences at both ends of a wire pair. Obviously, the signal travel-time depends on the cable length and has to be calibrated for a proper position determination.

For a delay-line anode with two layers orientated 90°with respect to each other, the position is given by

$$\begin{aligned} x &= v_x \cdot (t_{x1} - t_{x2}) + x_0 \\ y &= v_y \cdot (t_{y1} - t_{y2}) + y_0 \end{aligned} \tag{2.51}$$

with $v_{x,y}$ the signal velocity perpendicular to the winding, t the signal time for each wire end (1,2) of layer x or y and x_0/y_0 an arbitrary offset.

In the case of a delay-line detector with three layers where the layers have an angle of 60°, one defines three coordinates u,v,w for each layer. The position calculation for each layer is the same as above:

$$\begin{aligned} u &= v_u \cdot (t_{u1} - t_{u2}) \\ v &= v_v \cdot (t_{v1} - t_{v2}) \\ w &= v_w \cdot (t_{w1} - t_{w2}) + w_0 \end{aligned} \tag{2.52}$$

But due to the angle between the layers, the obtained positions u,v,w have to be transformed into Cartesian coordinates:

$$\begin{aligned} x_{uv} &= u + x_0 \\ y_{uv} &= \frac{1}{\sqrt{3}}(u - 2v) + y_0 \\ x_{uw} &= x_{uv} \\ y_{uw} &= \frac{1}{\sqrt{3}}(2w - u) + y_0 \\ x_{vw} &= (v + w) + x_0 \\ y_{vw} &= \frac{1}{\sqrt{3}}(w - v) + y_0 \end{aligned} \tag{2.53}$$

The equations 2.53 show also the redundancy of the position calculation using the Hexanode. Although two layers are sufficient to determine the position, the third layer gives redundant information for cases in which a signal is missing.

The perpendicular signal velocity in equations 2.51 and 2.52 depends on the size of the delay-line anode. It can be roughly estimated to be 1 mm/ns for a two layer delay-line anode and 1.4 mm/ns for a three layer delay-line anode. However, the real value for each layer differs since each layer has a slightly different size. To obtain the actual value for the signal velocity, one uses a shadow mask. This mask is a thin disc with a pattern of holes having a defined diameter and defined distances between them. Putting this mask in front of each detector and illuminating it with an alpha-source gives data which can be used for calibration. For the two layer delay-line anode, the velocity factor for each layer is changed iteratively until the dimensions of the retrieved pattern matches the dimensions of the shadow mask. The three layer delay-line anode provides the possibility of an auto-calibration due to its redundant layer.

For the reconstruction of the coordinates for a particle hit with an incomplete set of times, further calibration steps are needed. Whereas the difference between the arrival times encodes the position, the sum of both times is constant for each layer. This time sum helps to reconstruct particle positions for these incomplete sets. In order to do this, the detectors are illuminated without a mask to obtain an uniform exposure of each detector from which

the parameters needed for the reconstruction algorithm are retrieved. These parameters are different but characteristic for each layer. They include the maximal signal travel-time, the average time sum of both signals, the width of the time sum and a deviation map of the time sum dependent on the impact position.[1]

Finally, the axes of both detectors in general will not coincide with the chosen lab frame. Thus, it is necessary to rotate each detector image. To get the right rotation angle, it is useful to measure the impact position of ionized molecules from the molecular beam with both detectors. The molecular beam axis defines the x-axis and can be used as a reference. In addition, since both detectors face each other, the image of the ion detector has to be flipped to match the y-axis.

2.3.2 Reconstruction Algorithm

The signal travel-time on the anode layers is on the order of 100 ns, but multiple hits occur typically within a shorter time. Hence, the signals on each layer of these multiple hits will mix up. Fortunately, the analysis software has the capability to sort these mixed signals. The algorithm works as follows[89]:

The software searches for combinations of anode signals and MCP signals fulfilling certain criteria. These criteria are:

- the time sum for each layer must be within the tolerance window which is the time sum width determined during the calibration of the detectors.
- the position which is calculated using the first two layers must be close to the position which is calculated by the third layer and another layer.
- the resulting position on the detector must be within the active area of the MCP.

Initially the algorithm starts with the attempt to find a full set of six anode signals and one MCP signal. If this signal set does not fulfil the criteria described above, the algorithm reduces the number of required signals searching for five anode signals and one MCP signal. The reduction of required signals continues until the algorithm searches for only three anode signals without a MCP signal.

Signals which can not be assigned to any combination are discarded. The algorithm differentiates 18 situations as listed in appendix A.5.

2.3.3 Time-Offset Calibration

At this point, the position information from the detectors is calibrated and also sorted, but the time information still contains some unknown offsets. The offsets of all time signals originate from different cable lengths for the cables connecting the detector through all electronics with the TDC. Additionally, different electronic devices are used for the timing signals of both detectors and the laser. These devices have internally different transit times.

1 For more detail see the manual *Software of the RoentDek Hexanode* by RoentDek [89].

The way to determine the time offsets for both detectors differs. The offset of the ion time-of-flight is determined from two largely separated but known masses in the time-of-flight spectrum. The mass m can be calculated from the time-of-flight t by:

$$m = \gamma(t - t_0^{(\mathrm{ion})})^2 \qquad \text{with} \quad \gamma = \frac{qE}{2s} \tag{2.54}$$

in which q is the charge of ion, E the electric field strength and s the length of the spectrometer. t_0 is the unknown offset. By using two masses one defines the ratio:

$$\frac{m_1}{m_2} = \frac{(t_1 - t_0^{(\mathrm{ion})})^2}{(t_2 - t_0^{(\mathrm{ion})})^2} \tag{2.55}$$

Solving for t_0 one obtains:

$$t_0^{(\mathrm{ion})} = \frac{\sqrt{m_2}t_1 - \sqrt{m_1}t_2}{\sqrt{m_2} - \sqrt{m_1}} \tag{2.56}$$

The offset calibration for the electron detector is different, since the method for ion cannot be applied. The magnetic field which affects the electron trajectories helps to determine this offset. The direction of the Lorentz force (eq. 2.48) is determined by the cross product between the velocity of the electron and the direction of the magnetic field. Therefore, it acts perpendicular to the field and to the direction of motion. Since the magnetic field is parallel to the z-axis, an electron with a velocity component perpendicular to the magnetic field direction moves on a circle in the xy-plane.

By equating the magnitude of the Lorentz force and the centripetal force:

$$qv_\perp B = \frac{mv_\perp^2}{r} \tag{2.57}$$

with r the radius of the circle, one can determine the cyclotron period T_{cyc} by using the circulation frequency $f = \frac{v_\perp}{2\pi r} = 1/T_{\mathrm{cyc}}$:

$$T_{\mathrm{cyc}} = \frac{2\pi m}{qB} \tag{2.58}$$

The cyclotron period is the time an electron needs to travel one turn on its path. This relation shows that the cyclotron period is independent of the velocity and therefore the same for all electrons at a given magnetic field.

Since all electrons start at the same point in time and space, all electrons will concentrate at a same point after a period of T_{cyc}. Figure 2.19 shows that one can extrapolate the real time zero by plotting the impact position of the electrons versus the time-of-flight if the time-of-flight covers at least two nodes.

The time offsets have been determined to be $t_0^{(\mathrm{ion})}$=30 ns and $t_0^{(\mathrm{elec})}$=21.5 ns.

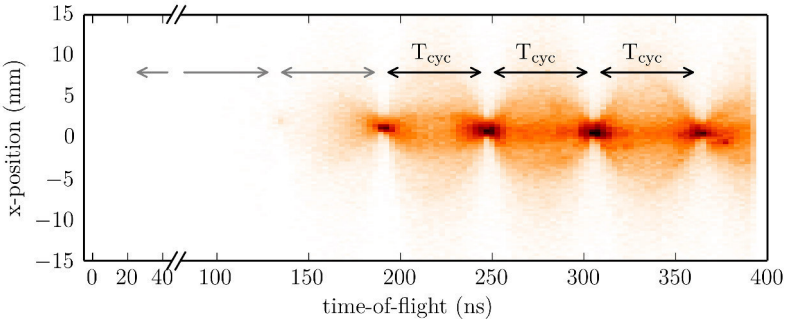

Figure 2.19: Wiggle Spectrum: plot of the electron impact position for one axis versus the time-of-flight. From this plot two things can be obtained. First, the distance between two nodes is the cyclotron period of the electrons. This period provides the strength of the magnetic field. Second, by extrapolating the cyclotron period towards zero one determines the time offset to the real time zero.

2.3.4 Magnetic Field Calibration

By retrieving the cyclotron period from the wiggle spectrum in fig. 2.19, one can calculate the magnetic field strength using eq. 2.58. A calibration of the applied magnetic fields has been performed by measuring the cyclotron period as a function of applied current to the coils. Eq. 2.58 suggest a mapping function of the from:

$$(T_{\mathrm{cyc}}(I))^{-1} = I \cdot a + b = f_{\mathrm{cyc}}(I) \tag{2.59}$$

Figure 2.20 shows this function fitted to data sets of coil current and cyclotron period. The

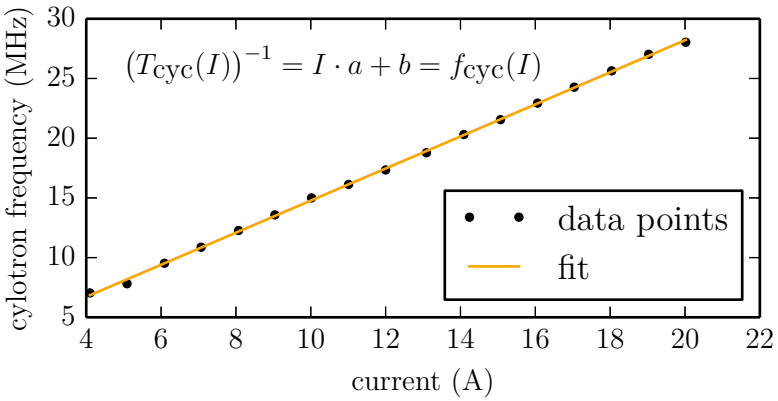

Figure 2.20: Magnetic field calibration: Each dot represents a pair of coil current and measured cyclotron period. By fitting eq. 2.59 to these points one obtains the parameters a and b.

parameters a=1.343×10^6 Hz/A and b=1.349×10^6 Hz are retrieved from this fit and are used later to retrieve the momentum of the detected particles.

2.3.5 Momentum Calculation

In this section and also in later chapters, the term time-of-flight relates to the true time-of-flight obtained after subtracting the time offsets of sec. 2.3.3. The momentum calculation of each particle is based on the equation of motion for charged particles in an electric and magnetic field. For this calculation, two assumptions are made: First, each molecule has only an initial momentum due to the translational temperature of the molecular beam. Second, the momentum transfer from the photon to the molecular system is negligible. The momentum of a photon with 800 nm wavelength is 0.0004 a.u.(8×10^{-28} kg m/s). A typical momentum of ions and electrons produced in a photo-ionization process is ∼1a.u.. Even in a 10-photon ionization, the momentum of the photons is only a few per mill of the resulting electron and ion momenta.

Starting with the equation of motion:

$$\vec{F} = m\vec{a} \tag{2.60}$$

the vector equation can be separated into motion parallel to the electric and magnetic field (z-axis) and perpendicular to them (xy-plane).

Momentum Component Parallel to the z-Axis

The parallel component is only affected by the electric field since the cross-product of the Lorentz force vanishes for parallel vectors. Hence the acceleration $a_\parallel$ is given by

$$a_\parallel = \frac{q}{m}E \tag{2.61}$$

with q the charge of the particle, m its mass and E the electric field strength. Integrating twice yields the distance s

$$s = \frac{1}{2}\frac{qE}{m}t^2 + v_{z0}t + s_0 \tag{2.62}$$

with v_{z0} the velocity along the z-axis of the particle gained during the reaction process. The integration constant s_0, which is the point of interaction between laser and molecular beam, will be set to zero. Using $p_\parallel = mv_0$, one obtains for the time-of-flight:

$$t = -\frac{p_\parallel}{qE} + t_0\sqrt{1 + \frac{p_\parallel^2}{2\,m\,s\,q\,E}} \qquad \text{with} \quad t_0 = \sqrt{\frac{2sm}{qE}} \tag{2.63}$$

where t_0 is the time-of-flight of a particle with the same mass and an initial velocity of zero. Obviously, it is not possible to solve this equation for $p_\parallel$. But if the initial energy is small

compared to the energy gained by the acceleration in the electric field ,

$$\frac{p_{\parallel}^2}{2\,m} \ll s\,q\,E, \tag{2.64}$$

the root will be approximately one. Thus, the equation can be solved for $p_{\parallel}$:

$$p_{\parallel} = q\,E\,(t_0 - t) \tag{2.65}$$

Due to the high mass of the ions compared to that of the electrons, this approximation is only valid for the calculation of the ionic momenta. Calculating the momenta of the electrons in the same way will produce an error since the initial energy is not negligible any more.

To calculate the right momentum, one has to find the root for

$$f(p_{\parallel}) = -\frac{p_{\parallel}}{qE} + t_0\sqrt{1 + \frac{p_{\parallel}^2}{2\,m\,s\,q\,E}} - t \tag{2.66}$$

This is done in the analysis software using Newton's method (also known as the Newton-Raphson method) [90]. By using the calculated momentum from formula 2.65 as the initial value, the method approaches the root by calculating the intersection of the tangent at that position with the abscissa. This is done iteratively until the new momentum differs less than 0.01 a.u. from the momentum of the previous iteration.

$$p_{\parallel}^{(i+1)} = p_{\parallel}^{(i)} - \frac{f(p_{\parallel}^{(i)})}{f'(p_{\parallel}^{(i)})} \tag{2.67}$$

Momentum Components in the xy-Plane

The calculation of the perpendicular momentum differs from the calculation described above. In the xy-plane, the trajectories of the particles are not affected by the electric field but by the magnetic field. Due to momentum conservation the momenta of electron and ion have the same magnitude (in the case of single ionization without subsequent fragmentation). Since ions have a few-thousand times higher mass than electrons, their velocity is smaller by the same factor than the velocity of the electrons. Hence, also the Lorentz force is smaller. This is also shown by eq. 2.58. Using typical values for the magnetic field of 0.5 mT gives a cyclotron period for electrons of 71 ns. This is the same order or even shorter than the typical time-of-flight of the electrons. With the same magnetic field helium ions have a cyclotron period of 522 μs, which is much longer than their time-of-flight on the order of a few μs. Hence, the trajectories of the ions are almost not affected by the magnetic field, and the motion in the xy-plane can be treated as force free leading to simple equations for the momenta in x and y:

$$p_x = m \cdot \frac{x - x_0}{t} \tag{2.68}$$

$$p_y = m \cdot \frac{y - y_0}{t} \tag{2.69}$$

with x_0 and y_0 offsets that correct two effects. The interaction point of laser and molecular beam will not be perfectly centred above the ion detector. This shifts the position in the x- and y-direction. In addition, the ions have an initial momentum induced by the molecular beam velocity distribution which leads to an offset on the x-axis. These offsets can be determined from fig. 2.21, showing a spatial image of the impact position.

For the electrons, the motion in the xy-plane is affected by the Lorentz force as discussed in section 2.3.1 and above briefly. From eq. 2.57, one can deduce the dependence of the perpendicular momentum on the radius of the helical path by substituting $mv_\perp = p_\perp$:

$$p_\perp = qrB \tag{2.70}$$

Hence, by determining the radius r, the perpendicular momentum can be calculated. The magnetic field strength is obtained during the calibration.

However, the radius r is not directly accessible from the detector image itself but it can be determined from the impact position by incorporation of the time-of-flight, the cyclotron period and the starting position as depicted in fig. 2.22.

In the plane of the detector (xy-plane), the electrons will move on a circle with an angular frequency of $\omega_{cyc} = 2\pi/T_{cyc}$. Hence, the angle α in fig. 2.22b is given by the time-of-flight t.

$$\alpha = \frac{2\pi}{T_{cyc}} t \tag{2.71}$$

The radius of the circle is given by:

$$r = \frac{R}{2\sin\left(\frac{\alpha}{2}\right)} \tag{2.72}$$

with R the distance from the starting point to the impact point in the plane of the detector. Now, $p_\perp$ can be calculated by eq. 2.70. However, one still has to transform the direction of the transversal momentum into Cartesian coordinates.

$$p_x = p_\perp \cdot \cos\phi \tag{2.73}$$

$$p_y = p_\perp \cdot \sin\phi \tag{2.74}$$

where $\phi = \theta - \alpha/2$ according to fig. 2.22. By combining all equation from above and using subtraction theorem for sine and cosine eqs. 2.73 and 2.74 can be rearranged for a more

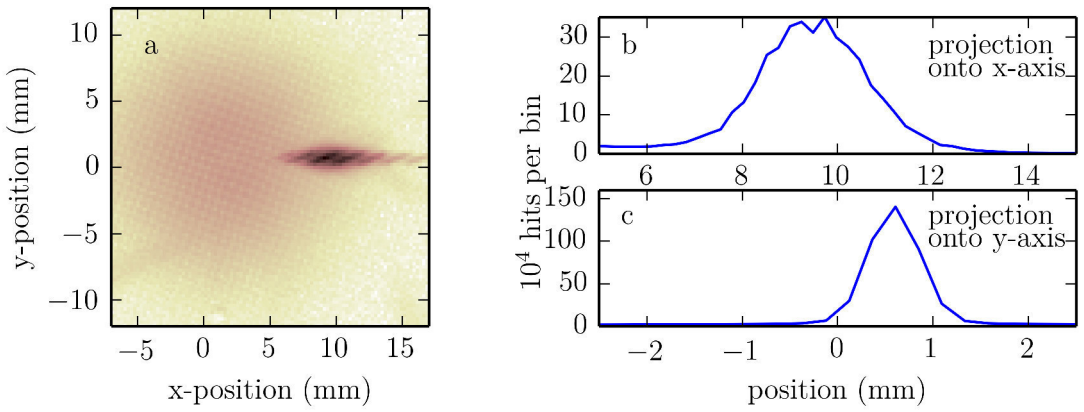

Figure 2.21: Determination of the spatial offset: **(a)**spatial image of the impact position of the ions. The dark spot on the right belongs to ions coming from the molecular beam. **(b)** Projection of the data onto the x-axis. **(c)** Projection of the data onto the y-axis. From the projections one retrieves the offset of x and y, respectively.

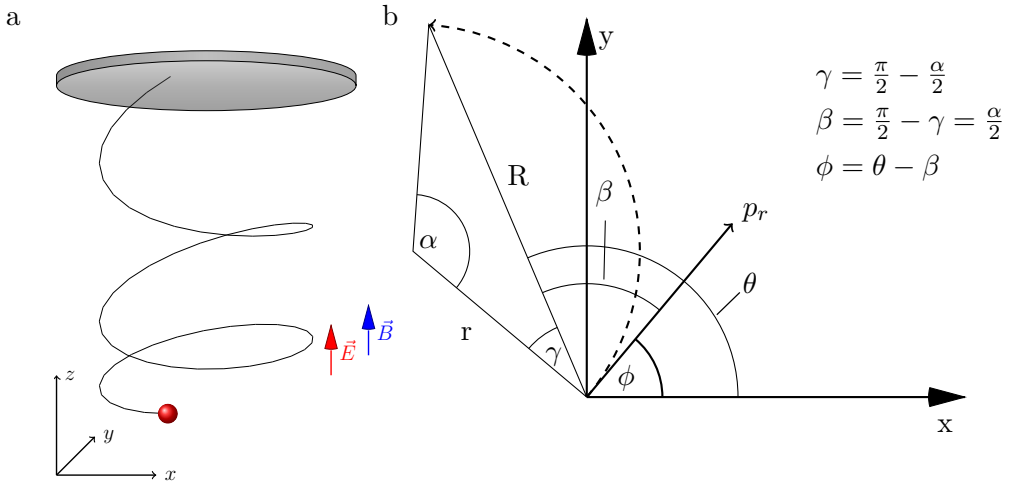

Figure 2.22: **(a)** Trajectory of an electron with a perpendicular momentum. **(b)** Projection of the trajectory on the electron detector: The projection of the trajectory describes a circle on the detector. With the knowledge of the time-of-flight, the start position and the impact position, the perpendicular momentum can be calculated as described in the text.

convenient form containing x and y instead of R:

$$p_x = \zeta \left[x \cos\left(\frac{\alpha}{2}\right) + y \sin\left(\frac{\alpha}{2}\right) \right] \tag{2.75}$$

$$p_y = \zeta \left[y \cos\left(\frac{\alpha}{2}\right) - x \sin\left(\frac{\alpha}{2}\right) \right] \tag{2.76}$$

where

$$\zeta = \frac{m\pi}{T_{cyc} \sin\left(\frac{\alpha}{2}\right)} \tag{2.77}$$

It is important to note that the sign of the magnetic field is determining the sign of α which describes whether the electrons are turning clockwise($\alpha < 0$) or counter-clockwise($\alpha > 0$). In the present setup, the electrons turn clockwise in the detector plane ($\alpha < 0$).

In the analysis, the special case of $\sin\left(\frac{\alpha}{2}\right) \approx 0$ must be considered. This case occurs when the time-of-flight is close to an integer multiple of the cyclotron period T_{cyc}. As shown in fig. 2.19, at this times all electrons, independent of their perpendicular momentum, hit the detector at the same position. Therefore, the perpendicular momentum resolution is lost for these times. However, by a proper adjustment of the electric field E and magnetic field B, one can set the time-of-flight of the electrons to a time window between two of these nodes.

Maximum Detectable Momentum

With the eqs. of section 2.3.5, one can calculate the maximum momentum of an electron detectable for a given geometry of the spectrometer. As before, one has to distinguish between maximum perpendicular and parallel momentum. The parallel momentum is restricted by the distance between the interaction point and the ion detector, labelled as d_{ion}. In a homogeneous electric field, an electron starting towards the ion detector can have a maximum parallel initial kinetic energy corresponding to

$$E_{\text{kin}\parallel}^{(\max)} = q_e E d_{\text{ion}} \tag{2.78}$$

with q_e the electron charge and, E the electric field strength. With a higher kinetic energy, the electron would hit the ion detector and would be lost. Having a lower kinetic energy, the electron turns around before it hits the ion detector.

The perpendicular momentum is treated differently. According to eq. 2.70 the radius of the helical path of the electron for a given magnetic field scales with the momentum. The maximum detectable perpendicular electron momentum is therefore restricted by the free space of the electrodes or the MCP diameter, depending on which dimension is smaller. If the momentum becomes too large, the electron will hit the electrodes or might miss the detector and will be lost. In the present setup, the MCP diameter is the smaller value with d_{MCP}=75 mm. Assuming the interaction point perfectly centred on the spectrometer axis, the maximum diameter of the helical path of an electron is therefore half of d_{MCP}. Hence, the maximum perpendicular momentum is given by:

$$p_{\perp}^{(\max)} = q_e B \frac{d_{\text{MCP}}}{4} \tag{2.79}$$

With a magnetic field of B=5×10^4 T and a electric field of E=500 $^{\mathrm{V}}/_{\mathrm{m}}$, which are typical values, the maximum detectable parallel energy is $E_{\mathrm{kin}\parallel}^{(\mathrm{max})}$=80 eV and the perpendicular momentum is $p_{\perp}^{(\mathrm{max})}$=0.75 a.u. corresponding to an energy of $E_{\mathrm{kin}\perp}^{(\mathrm{max})}$= 7.7 eV.

2.3.6 Data Handling

The high repetition rate of the laser produces a high data rate during a measurement. To avoid any data loss due to data transfer bandwidth limitations, the acquisition software COBOLD does only collect the time information for each TDC channel and saves it to a event based file structure called list-mode-file(LMF)[1]. During a measurement the software shows only basic information as for example the time-of-flight of the ions to reduce CPU load.

A typical event rate with a 400 kHz laser repetition rate is on the order of $10^4\,\mathrm{s}^{-1}$ (assuming a signal rate of 10% of the repetition rate). Assuming the unrealistic case of detecting only one electron and one ion per event, each event consists of five time values for the ion, seven time values for the electron and one for the laser pulse. Each time value uses 4 byte of memory resulting in 52 byte for one event assuming only one hit per detector. Typical measurements contain between 10^7 and 10^9 events to achieve a good signal to noise level. The duration of the experiment may vary between 30 minutes and 24 hours. During this time, depending on the actual signal rate a data set of 1 to 100 GB are produced.

The following describes the computational steps to proceed from the raw data saved by COBOLD to the physical meaningful momentum data.

After data acquisition has been completed, COBOLD is used again to calculate the time and position information for each hit from the times saved in the LMF. During this calculation, COBOLD will apply the corrections described in section 2.3.1 on the raw data, as aligning the coordinate system of both detectors, multiple hit reconstruction and non-linearity compensation. Also, the reference time zero is shifted to the first laser pulse. The calculated positions and times are stored in a different file format (called SLMA[2]) due to library incompatibilities between COBOLD and the later used ROOT framework[3].

Since COBOLD is a commercial software and the developer can not anticipate all possible setups, the software gives the possibility to modify some of its routines to adapt it to the user's needs. Therefore all user accessible routines are put into dynamic link libraries also provided in source code form.

From the data saved in the SLMA file the momenta are calculated as described in section 2.3.5 and saved to a ROOT tree file type, which supports parallel data access. Only those particle hits are stored in the ROOT tree which used a reconstruction method below

1 For more information on the actual format see http://www.roentdek.com/manuals/CoboldPC UserManual (6.2.90.2).pdf

2 SLMA is an acronym for Sorted List Mode Archive. Sorted means that the multiple hit algorithm has processed the data and sorted all multiple hits. The source code form defining the SLMA format can be found in Appendix A.4.

3 ROOT is a analysis framework developed at CERN to handle large sets of event based data. http://root.cern.ch

15. A reconstruction method of 15 and above has no redundancy (see appendix A.5) due to the high number of missing signals and will lead most probably to false position and/or time.

Parallel data access with multiple CPUs is necessary because each time a particular physical quantity (e.g. angularly resolved energy distribution) should be visualized from the saved momenta the program has to process every event to build a histogram. That results in a long processing time in case of single core data access. The program for the momentum reconstruction was adapted to the setup from a source code which was already used at the Max Born institute by Manschwetus [91].

Beyond the technical aspects of the software, it is crucial how one processes the momentum information of each measured event. The coincident detection of all particles, allows a filtering of the data which is not feasible with other detection principles. It is possible for example to reduce the background signal by applying a spatial filter to the data.

Figure 2.23 shows the effect of the spatial filtering in a dataset corresponding to strong field ionization of Ar. The filter restricts the analysis to events which contain a particle hit in a specified area of the ion detector indicated by the rectangle in fig. 2.23a. Ions from the molecular beam have a non-vanishing initial mean velocity[1] in x-direction due to the gas expansion. In contrary, the background gas has a vanishing mean velocity because its velocity distribution is isotropic. Hence, ions of the molecular beam will be detected displaced from ions of the background gas (see fig. 2.23b). The speed of an argon beam in the isentropic limit is 552 m/s (see eq. 2.41). With a time-of-flight of 15.4 μs, the argon ions hit the detector displaced by 8.5 mm. This correlates quite well with the observed x-position of 1 mm for the background signal and 9.5 mm for the spot of the molecular beam (see fig. 2.23a). By choosing the right position and size of the spatial filter, ions mainly from the molecular beam can be selected. As seen in fig. 2.23c, this leads to a strong reduction of background contribution whereas the main signal is hardly affected. Even though the mean velocity of the background gas is zero, it has a high average speed. Thus, a small fraction of the background gas has the same velocity as the molecular beam and hits the detector at the same position producing a remaining signal of the background gas. Figure 2.24 shows Δp for strong field single ionization of argon investigated in chapter 3.

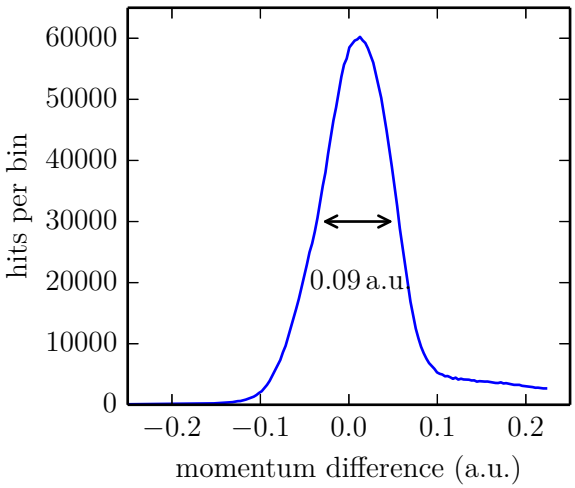

Figure 2.24: Sum of the momenta of ion and electron along the spectrometer axis.

Another common filter method is to apply momentum conservation. The sum of the momenta of all involved particles produced in the same event must be zero. In single ionization without fragmentation, two particles, ion and electron, can be detected. Hence,

1 velocity is a vectorial quantity whereas speed describes only the norm of the velocity

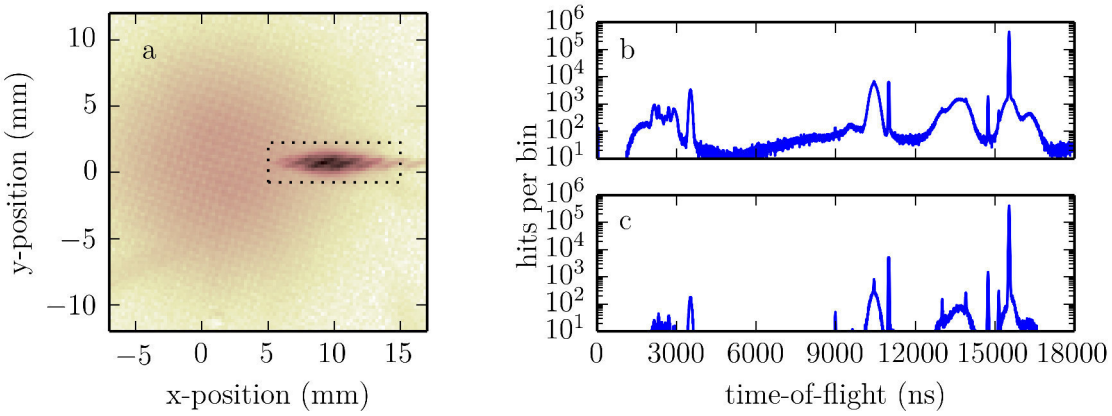

Figure 2.23: spatial filter (a) impact position of detected ions on the MCP. The elongated spot is the impact position of ions originating in the argon beam. The rectangle marks the region of hits accepted by the filter. (b) unfiltered time-of-flight spectrum from strong field ionization of an argon beam. (c) Spatially filtered time-of-flight spectrum. The most obvious change is the reduction of the background contribution (broad pedestals) whereas the signal from the argon beam (narrow peaks) is unaffected.

the momentum conservation is:

$$\Delta p = p_{\text{ion}} + p_{\text{electron}} \simeq 0 \tag{2.80}$$

Thus, it is possible to filter out some of the false coincidences by imposing the momentum conservation. The strength of this filter can be chosen by setting the permitted momentum mismatch.

From the width of Δp one can also retrieve information about the momentum resolution. Since it is the sum of electron and ion momentum it contains the momentum spread of both particles. As written in the beginning of section 2.2 the resolution is mainly limited by the velocity spread of the molecular beam. Ions and electron produced in an interaction will have this initial spread. However, since the momentum is mass dependent, the ions will have much larger momentum spread than the electrons. Therefore, the width of the Δp is virtually the momentum spread of the ions.

Many other filter possibilities exist to take advantage of the coincidence detection in order to extract information from the measured data. These possibilities will be explained in detail in the following chapters where the results for argon, hydrocarbon chains are presented.

3 Strong Field Ionization of Atoms with Few-Cycle Pulses

3.1 Introduction

Many fundamental key experiments in strong field physics have been performed on rare gases. This is related to the fact that they are gaseous in a large range of pressures and temperatures and that gaseous targets are experimentally easy to handle. Whereas this is also true for many other species e.g. nitrogen, rare gases are in contrast mono-atomic by nature. Additionally, atomic spectroscopy has a long history and hence, is very well-understood.

Much work has been done investigating rare gases with plenty of different conditions in terms of laser settings, detection configuration and so forth, they serve as a good reference when testing new spectrometers.

For the current setup, argon has been chosen due to the available literature with similar experimental settings. This provides a reliable source to calibrate the system and offers the possibility to analyse the performance of the entire system.

The measurements presented in the first part of this chapter involve two different laser systems, one with long pulses of about 100 fs and low repetition rate and the newly built high repetition rate laser system with short pulses of ∼6 fs. This approach was necessary to distinguish effects due to the spectrometer and effects caused by the newly built laser system. In addition, long pulses have been studied more often while for short pulses the literature is sparse.

The results and discussion of the measurements are presented separately for each laser system. The findings of the measurement with the OPA system are investigated in more detail with the help of a TDSE calculation. As a result of the analysis presented at the end of this chapter, a new experiment is proposed to extend quantum state holography[92] to electron wave packets prepared through strong field ionization.

In the last section of this chapter the target species was changed to xenon in order to investigate double ionisation. This is interesting in two aspects. First, in contrast to lighter rare gases, double ionization of xenon has so far not been studied in great detail, although it is interesting in the view of electron correlation of this multi electron system. Second, this experiment serves as a test for the capabilities of the setup for detecting triple coincidences.

3.2 CPA System

The laser system used in the first set of measurements is the commercial Ti:Sa CPA laser system 'Red Dragon' from Kapteyn Murnane Labs. It delivers 15 W of output power at a central wavelength of 790 nm with a repetition rate of 10 kHz. It consists of a prism-compensated Ti:Sa oscillator (20 fs, 80 MHz) followed by a grating stretcher and a three-stage

amplifier operating at 10 kHz. After pulse compression with a grating compressor, the output power amounts to 15 W (1.5 mJ energy per pulse) with pulses as short as 40 fs.

An autocorrelation measurement of the laser pulses is depicted in fig. 3.1 showing a FWHM of 180 fs. This corresponds to a pulse duration of 128 fs assuming a Gaussian temporal pulse shape. Three different intensities have been used during the experiment by changing the angle of a $\lambda/2$-wave-plate in combination with a polarizer. The pulse energies utilized are 22 μJ, 30 μJ and 60 μJ.

The extraction fields have been set to an electric field of 514 V/m and a magnetic field of 2.88×10^{-4} T by sending a current of 5 A through the main magnetic field coils. According to equations 2.78 and 2.79 on page 73, any produced electron can therefore be detected up to a momentum of 0.41 a.u. perpendicular to the spectrometer axis and 2.44 a.u. parallel to the spectrometer axis. The stagnation pressure of the molecular beam was set to 0.8 bar.

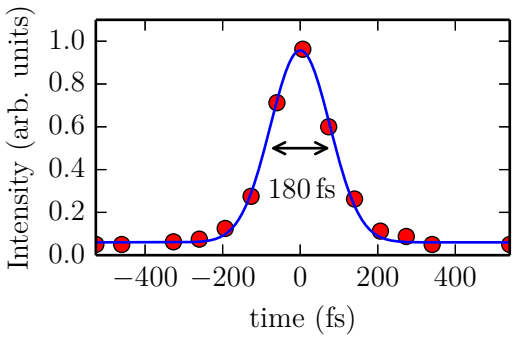

Figure 3.1: Second harmonic autocorrelation trace of pulses from the CPA system. Assuming a Gaussian pulse shape the measured pulse duration of the laser pulse corresponds to 128 fs according to eq. 2.16

Results are presented in two sections. The first section shows the ion time-of-flight data and the second section shows the electron spectra. Then, in the following sections the electron spectra are discussed in more detail.

3.2.1 Ion Spectra

Figure 3.2 plots the time-of-flight spectrum obtained when the laser is focussed into the empty chamber without a molecular beam. The base pressure was 2.5×10^{-10} mbar. This reveals the contribution of the residual gas to the later measurements. It can be seen that the residual gas mainly contains hydrogen, water, oxygen, carbon monoxide and carbon dioxide. The peaks around 1 u are produced by the dissociation of molecular hydrogen mainly due to bond softening [93]. The width of the shown peaks is caused by the broad velocity distribution of the residual gas at room temperature.

Figure 3.3 shows the ion time-of-flight spectrum when argon is sent into the chamber. A strong peak is visible around 15500 ns in fig. 3.3 which corresponds to the time-of-flight of argon. All other contributions are small and only visible due to the logarithmic scale.

The most striking feature of the spectrum besides additional peaks is the small width of the argon peak compared to the peaks of the residual gas. This is an effect of the low perpendicular velocity distribution of the molecular beam and a signature of a very small (point-like) ionization volume.

Beside the mentioned species present in the residual gas, some additional peaks are visible. These additional peaks mainly stem from impurities of the molecular beam. In particular, one can identify molecular nitrogen and molecular oxygen as narrow peaks on top of the broad peaks around 13500 ns. In addition, at the water peak a small sharp tip is visible on

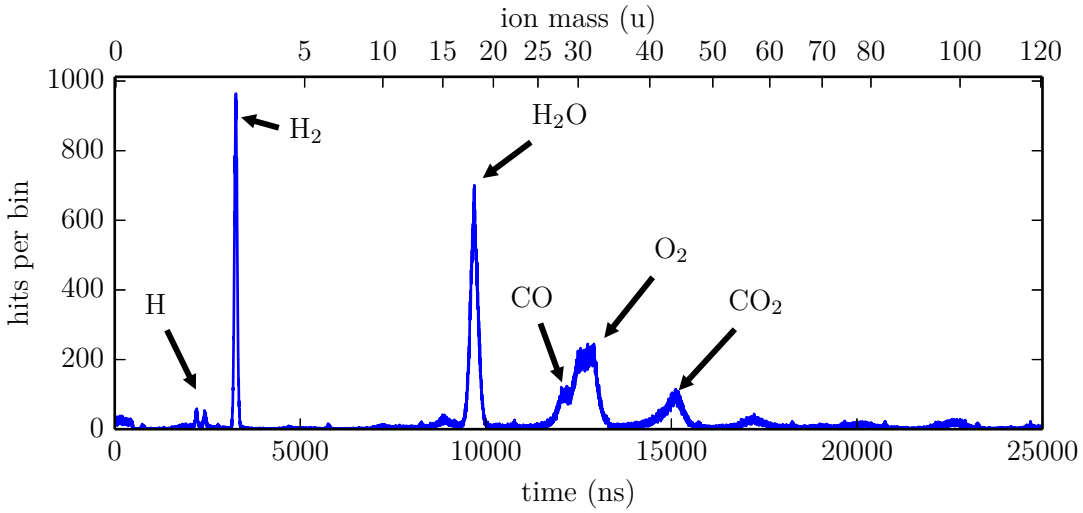

Figure 3.2: Time-of-flight spectrum obtained by strong field ionization of the residual background gas of the vacuum chamber without a molecular beam. The laser parameter are: $\lambda = 790$nm, pulse duration $\Delta t = 128$ fs, intensity $I = 1.9 \times 10^{14}\,\mathrm{W/cm^2}$. The chamber pressure is 2.5×10^{-10} mbar. The main constituent parts of the background gas are H_2, H_2O, CO and CO_2

top suggesting that the molecular beam contains some small fraction of water as well.

The sharp peak at mass 36 u and 38 u correspond to the stable isotopes of argon. The ratios of argon isotopes ($Ar_{36}/Ar_{40} \approx 3.4{\times}10^{-3}$ and $Ar_{38}/Ar_{40} \approx 6 \times 10^{-4}$) are consistent with their natural abundance [94] of $3.3{\times}10^{-3}(Ar_{36})$, $6.29{\times}10^{-4}(Ar_{38})$ and $0.996(Ar_{40})$.

Next to the broad water peak, a small peak rises at 20 u. This is doubly charged argon produced by double ionization. The ratio between doubly charged and single charged argon suggests an intensity of $2{\times}10^{14}\,\mathrm{W/cm^2}$[52]. This is only a rough estimation which gives the order of magnitude. A better estimation will be obtained from the electron spectra.

3.2.2 Electron Spectra

Due to the simultaneous measurement of the mass spectrum and the electron spectrum, it is possible to filter the electron spectrum mass specific. This filter works similar as described for the spatial filter in section 2.3.6. By the choice of a certain time window for the ion time-of-flight, one can filter for events belonging to the ionization of argon. Only those events are filled into a histogram which fall into the time window around the argon peak. The time window has been chosen to be between 15540 ns and 15620 ns.

Figure 3.4 shows the energy distribution of the detected electrons accompanied by the coincident detection of an argon atom for the measurement with a pulse energy of 30 μJ. One clearly sees a periodic pattern up to a kinetic energy of 50 eV with peaks separated by the energy of one photon. These are ATI-peaks and are discussed in more detail later. At

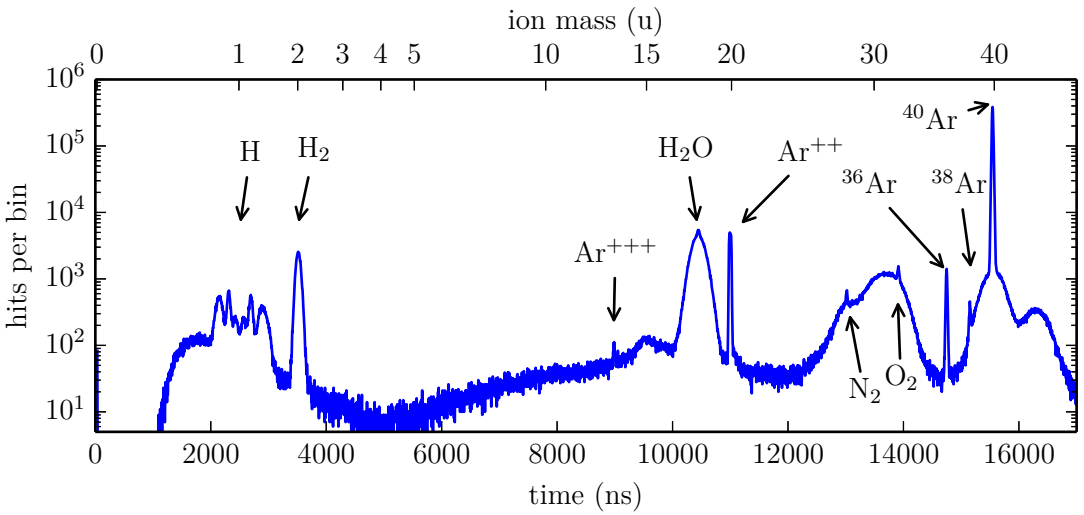

Figure 3.3: Time-of-flight spectrum produced by SFI with a molecular beam. Argon is clearly dominating the spectrum. As discussed in the text, narrow peaks indicate their origin in the molecular beam. Thus, the molecular beam consists mainly of argon with some minor contribution from N_2, O_2, H_2O. The isotopes ^{38}Ar and ^{36}Ar are visible as well. The laser parameters are: $\lambda = 790$nm, pulse duration Δt =128 fs, intensity $I = 1.9 \times 10^{14}\,\mathrm{W/cm^2}$.

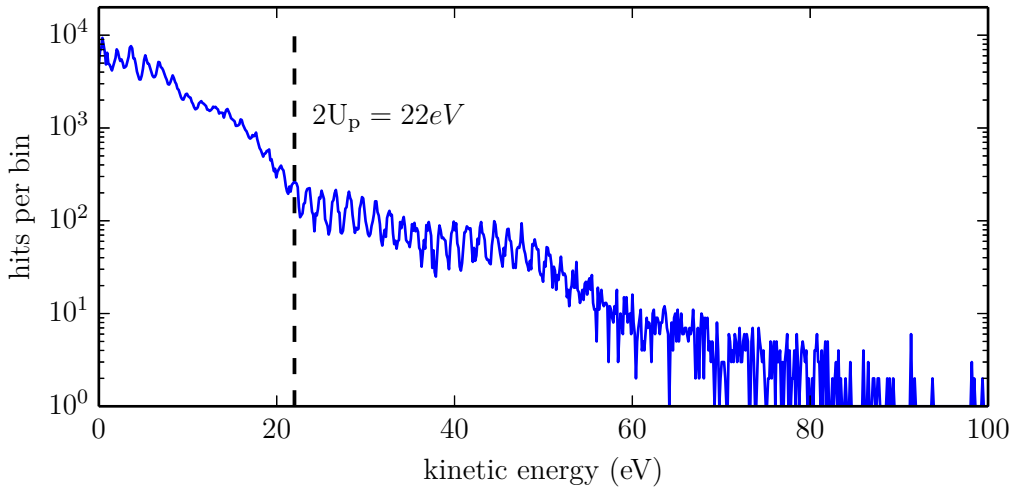

Figure 3.4: Kinetic energy distribution of photoelectrons along the polarization axis of the laser. The $2U_p$ kink at which the main contribution changes from direct to scattered electrons is clearly visible(dashed line). The observed kink energy corresponds to an intensity of $1.9 \times 10^{14}\,\mathrm{W/cm^2}$.

22 eV one notices a kink which is attributed to the $2U_p$-kink as discussed in section 2.1.1 The $2U_p$-kink is marked by the dashed line. A $2U_p$-energy of 22.2 eV corresponds to a laser field intensity of 1.9×10^{14} W/cm^2. In that way the intensities for each measurement have been determined.

Figure 3.5 depicts the momentum maps of the photoelectrons detected corresponding to singly ionized argon atoms, at different intensities. A momentum map shows the angular resolved momentum distribution of the photoelectrons as a function of parallel and perpendicular momentum. The reference axis is the laser polarization axis, parallel to the spectrometer axis in these measurements. As described in subsection 2.1.2 on page 39, the laser polarization axis is parallel to the spectrometer axis which coincides with the z-axis. Therefore, the momentum p_z is parallel to the polarisation and p_r is perpendicular to it (with $r = \sqrt{x^2 + y^2}$). A momentum map as in fig. 3.5 shows the number of detected electrons $N(p_z,p_r)$ per bin $dp_z dp_r$. During the data processing, the retrieved momenta are calculated in Cartesian coordinates. In principle, one has to apply the Jacobian factor for the transformation to polar coordinates. However, commonly this Jacobian is neglected throughout the literature when momentum maps are shown. To simplify the comparison, this factor is also neglected in this thesis. This procedure pronounces the contribution perpendicular to the laser polarisation because $N(p_z,p_r)$ is proportional to $|\Psi(p_z,p_r)|^2 p_r$.

The momentum maps (except the map of fig. 3.5c) show a fan-like structure consisting of roughly seven rays pointing radially outwards. At total momenta higher than 0.25 a.u., the rays transform into several diffuse features.

Intensity Dependence and Coincidence Rate

As described in section 1.2 one can calculate the detection efficiency of the spectrometer for ions and electrons from the number of total laser pulses, detected electrons, detected ions and coincidences. The numbers for each measurement are shown in table 3.1. The table shows two effects of the intensity on the measurement performance. First, increasing the intensity naturally increases the rate of ions and electrons (each laser pulse produces more charged particles). Second, at the same time this does not increase the number of coincidences, defined as the events where only one singly-charged ion and one electron are detected. A higher intensity gives a higher average number of detected particles. This leads to more events in which more than one ion-electron pair is produced according to eq. 1.21.

Increasing the intensity influences also the photoelectron distribution shown in the momentum maps of fig. 3.5: The length of the radial rays of the fan-like structure increases towards higher momenta which is explained by a higher ponderomotive potential at higher intensities. At the highest intensity, the momentum map shows an asymmetric distribution towards negative parallel momenta. In addition to the asymmetry, also the visibility of the radial rays as well as the diffuse features have degraded strongly.

The asymmetry seems to be caused by the high number of ionized particles per laser pulse. A high number of detected electrons leads to a mixing of their time signals on each delay-line anode channel, since the differences in the time-of-flight of the photoelectrons is typically smaller than the travel-time of their signals on the anode layers. The mixed data is sorted by the reconstruction algorithm described in section 2.3.2. Figure 3.6 shows the histograms

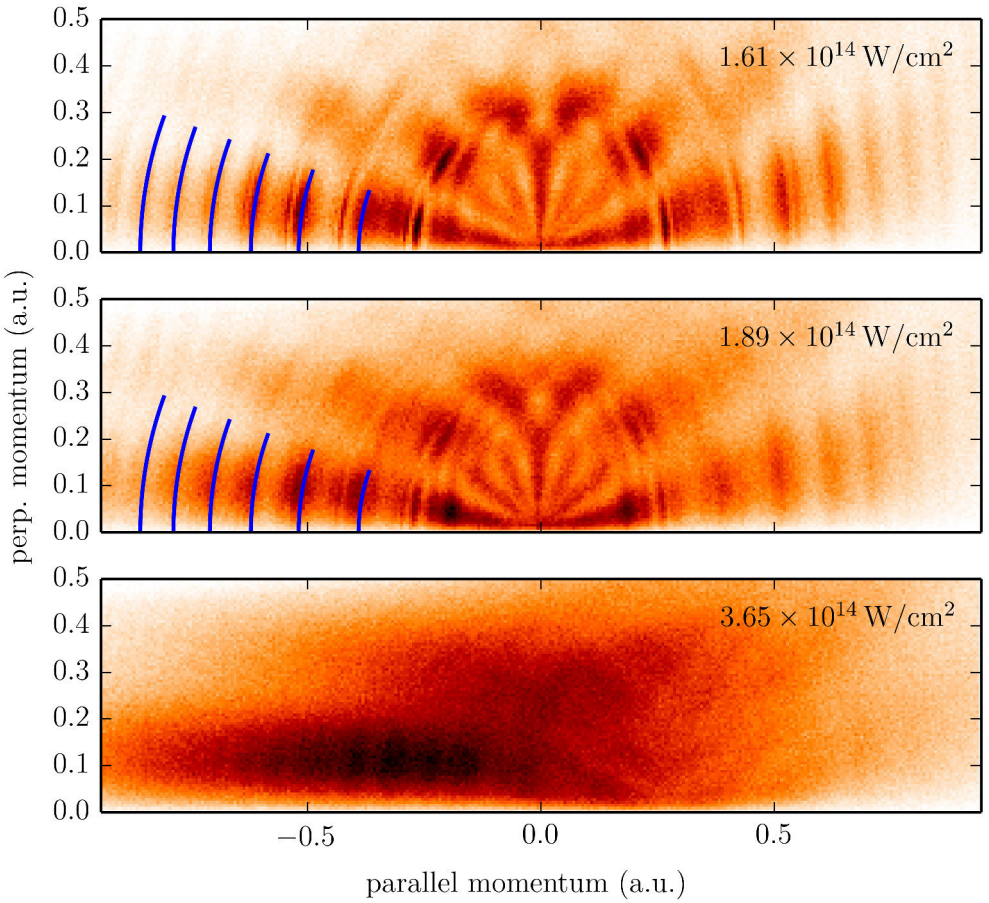

Figure 3.5: All three plots show the momentum map of photo electrons produced by strong field ionization of argon atoms. Each plot shows the number of detected electrons $N(p_z,p_r)$ per bin $dp_z dp_r$ for different intensities as noted. The increase in intensity produces an asymmetry of the electron distribution along the p_z-axis. The reason for this is a too high event rate as described in the text. The colour scale is linear. The scale uses white as the smallest value and increases via yellow, orange, red to black for the highest value.

of the different reconstruction methods used for the argon measurements with an intensity of $1.6 \times 10^{14}\,\mathrm{W/cm^2}$ and $3.7 \times 10^{14}\,\mathrm{W/cm^2}$. This comparison shows that many hits have produced incomplete signal sets in the measurement with the highest intensity. It shows also that many of these incomplete signal sets miss their MCP signal (reconstruction method 7-13).

The lack of MCP signals is most probably caused by the dead time of the MCP detector (and subsequent electronics). From table 3.1 one sees, when comparing the number of laser pulse with the number of detected electrons, that each laser pulse generates on average two electrons at the highest intensity. If the second electron hits the detector within the

	number of				from this follows			
I(W/cm²)	**pulses**	**electrons**	**ions**	**coinc.**	ξ_{ion}	ξ_{electron}	$\overline{n}$	**signal rate**
1.6×10^{14}	85624000	9288830	4443630	3232330	38.6%	80.6%	0.13	5.4%
1.9×10^{14}	36348900	10470000	5270760	2921590	36.1%	71.8%	0.4	27.5%
3.7×10^{14}	10113000	23736100	15594100	448310	-	-	-	98.8%

Table 3.1: Determination of detection efficiencies: From the number of detected ions, electrons, coincidences and laser pulses, the detection efficiency and the average number of ionized particles per pulse can be retrieved according to the equations of section 1.2. Only events with one ion and one electron are counted as a coincidence. The number of laser pulses has been calculated by the duration of the measurement and the repetition rate of the laser. The column labelled as signal rate shows the ratio of the number of triggered events to the number of laser pulses. The calculation is explained in more detail in appendix A.2. Besides the detection efficiency, this table also shows that the signal rate should be below 5% of the laser repetition rate to achieve the desired conditions for a low false coincidence rate.

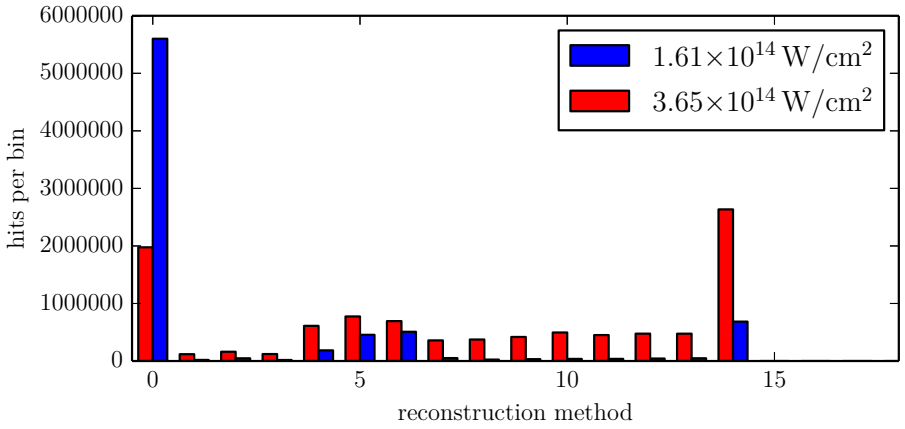

Figure 3.6: Used reconstruction methods for two different measurements as labelled. The high intensity measurement shows many events in which high number reconstruction methods have been used. A high number means that the number of missing signals is high as well (see appendix A.5). Since for methods above 14 the program cannot check if a signal combination is valid these signal combination are not used. Although they are not shown in the plot, it can be presumed that the number of signal combinations using a reconstruction method above 14 increases for the higher intensities as well.

dead time after the first hit, it will not be detected. Electrons emitted towards the electron detector arrive at the detector earlier than electrons in the opposite direction. The former have a negative z-momentum the latter a positive according to the coordinate system used. Hence, electrons with a negative momentum are less affected by the dead time resulting in a higher detection probability. This shifts the photoelectron distribution towards negative momenta.

Fan-like Structure

The origin of the fan-like structure are interferences between different electron trajectories with the same final momentum. For a particular final momentum, different times during the laser pulse exist that lead to that particular momentum of the photoelectron. The trajectories with the same final momentum have different probabilities and phases. The coherent addition of all paths will lead to interference structures in the probability distribution (momentum distribution).

Beyond this purely quantum interferometric interpretation of the fan-like structure in the low momentum region of the momentum distribution, Arbo *et al.*[95] have suggested a more qualitative interpretation based on the dominant angular momentum. The electrons will have a distribution of the angular momentum l depending on the number of absorbed photons. This distribution peaks at a dominant angular momentum l_0. The number of rays in this fan-structure at low momenta k correlates to the dominant angular momentum of the electrons. It can be estimated by the following formula as derived in [95]

$$L(k) = \sqrt{\alpha^2 k^2 + 2\alpha} \tag{3.1}$$

with $\alpha = E_0/\omega^2$. k is the value of the total momentum which describes a half circle in the momentum map. E_0 is the field strength of the laser pulse and ω is the laser frequency. All quantities are in atomic units. L is the classical angular momentum which is connected to the angular momentum l by

$$L = l + 1/2. \tag{3.2}$$

The wave function of an electron with an angular momentum of l has l nodes. These nodes show up as the minima in the fan-like structure of the momentum distribution.

With the given intensities of $1.6 \times 10^{-14}\,\mathrm{W/cm^2}$ and $1.9 \times 10^{-14}\,\mathrm{W/cm^2}$ and a wavelength of 800 nm, eq. 3.1 gives for k=0.1 a.u. a classical angular momentum L of 6.8 and 7, respectively. Thus, l is 6.3 and 6.5, which fits to the six minima seen in the momentum maps.[1]

Above Threshold Ionization

Superimposed on this fan-like structure, one can identify ATI peaks. They have been already seen in fig. 3.4. For the proper picture to describe the ATI peaks, one usually calculates the Keldysh parameter. With the intensities given, the Keldysh parameter is in the range

1 The apparent minima parallel and close to the abscissa with an almost vanishing perpendicular momenta is an artefact of the missing Jacobian factor.

of 0.6 for the highest intensity and 0.9 for the lowest intensity. These values belong to the mixed regime of multi-photon and tunneling picture. In this regime, a sub-cycle resolved description is necessary when dealing with few-cycle laser pulses with a fixed CEP. Yudin and Ivanov developed an analytical expression of the ionization rate as a function of the instantaneous laser phase for arbitrary values of the Keldysh parameter [41].

In the present case, the laser pulse is far from being in the few-cycle regime. Hence, the description by a multi-photon or tunneling picture based on laser cycle-averaging is a good approximation. Furthermore, as described in section 1.1.4, both pictures can qualitatively explain the structure of an ATI spectrum. The following discussion will therefore use the multi-photon picture.

The ATI peaks appear at positions (indicated by blue lines in fig. 3.5) shifted by a multiple of the photon energy starting from an offset given by the difference between the number of absorbed photons ($n \cdot h\nu$) and the ionization potential shifted by the ponderomotive potential ($IP + U_\mathrm{p}$) as describe by eq. 1.17. The peak distance correspond to a photon energy of 1.57 eV. A shift of the ATI peak positions between $1.6 \times 10^{14}\,\mathrm{W/cm^2}$ and $1.9 \times 10^{14}\,\mathrm{W/cm^2}$ is not visible, since the difference between the ponderomotive potential $\mathrm{U_p}$ (eq. 1.8) of both intensities is 1.6 eV which is approximately the photon energy.

Freeman Resonances

On top of these two processes, a third phenomenon is visible in the momentum distribution. The narrow features in the momentum maps below a momentum of 0.35 a.u. correspond to Freeman resonances. This resonances are a dynamical effect due to the light field. The changing instantaneous intensity shifts Rydberg states of the atom/molecule into multi-photon resonance followed by a one-photon excitation into the continuum. As described in more detail in section 1.1.5, the position of the Freeman resonances does not depend on the intensity. This can be seen in the upper plots of fig. 3.5. While the intensity is changing, the position of the Freeman resonance at 0.25 a.u. is the same in both plots.

Comparison with Literature

The measurements utilizing the commercial CPA system was intended to check the performance of the reaction microscope. Therefore it is helpful to see if the results match previously published data of similar experiments.

Figure 3.7 depicts the results of Rudenko *et al.* [96] using 25 fs laser pulse with a wavelength of 795 nm at an intensity of $5{\times}10^{14}\,\mathrm{W/cm^2}$ to ionize argon and of von Veltheim *et al.* [97] using 25 fs laser pulses with a wavelength of 800 nm at an intensity of $2{\times}10^{14}\,\mathrm{W/cm^2}$. Both experiments used a reaction microscope to record the momentum distribution of the photo electrons.

They show a very similar distribution as recorded with the CPA laser system of the present thesis.

The number of rays in the fan structure is the same in all plots, but in fig. 3.7a they are less pronounced. This change is also visible in the data of fig. 3.5 in which the measurement with an intensity of $1.9 \times 10^{14}\,\mathrm{W/cm^2}$ shows also less pronounced rays. Whereas the ATI

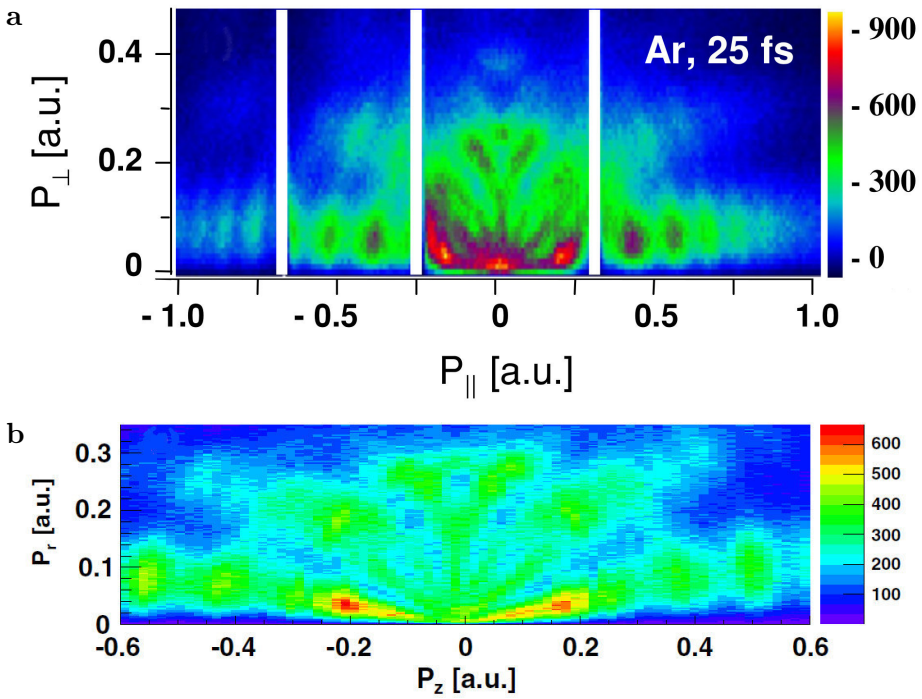

Figure 3.7: Photoelectron momentum distributions from strong field ionization of argon atoms by (a) Rudenko *et al.*[96] and (b) by von Veltheim *et al.*[97]. Both experiments used laser pulses with similar properties (pulse duration: 25 fs for both, wavelength: 795 nm(a) and 800 nm(b) intensity: 5×10^{14} W/cm^2(a) and 2×10^{14} W/cm^2(b)).

peaks are also reproduced, no Freeman resonances are visible. This is attributed to the much coarser binning of the plots in fig. 3.7.

3.3 OPA System

The following section presents the performance test of the entire apparatus consisting of the high repetition OPA system and the reaction microscope. The laser system used in this part is the OPA system described in section 2.1. The repetition rate was 400 kHz. The pulse duration was less than 6 fs and the pulse energy was 5 μJ at a central wavelength of 800 nm. The extraction field and the magnetic field as well as the molecular beam have been set to the same values as in the experiments with the CPA laser system.

3.3.1 Ion Spectra

Figure 3.8 shows the time-of-flight spectrum for the ionization of a molecular argon beam with the OPA system.

The most obvious difference to the spectrum shown in fig. 3.3 is the appearance of several

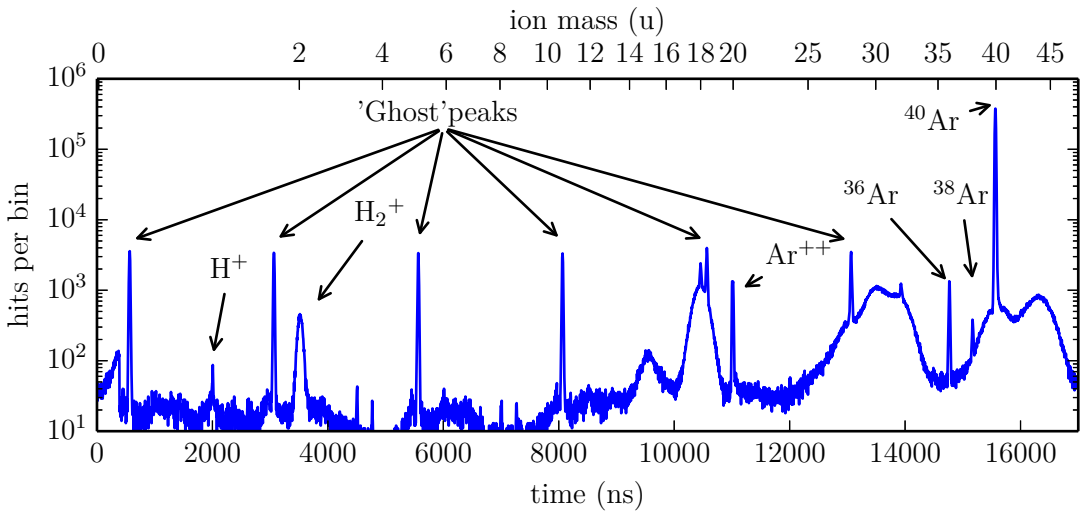

Figure 3.8: Time-of-flight spectrum from strong field ionization of argon using laser pulses from the OPA system. The most visible difference in the spectrum compared with the spectrum produced by the CPA laser system is the appearance of ghost-peaks. The laser parameters are: central wavelength $\lambda = 800\,\text{nm}$, pulse duration $\Delta t = 6\,\text{fs}$, intensity $I = 1.6 \times 10^{14}\,\text{W/cm}^2$.

peaks with the same height which are not present in the spectrum taken with the CPA laser system. The peaks are equally spaced in time by 2.5 μs. This corresponds to the repetition rate period of the laser system at 400 kHz. As described earlier in fig. 2.17 of section 2.2.7, this is the so-called ghost-peak effect.

All other peaks correspond to masses already seen with the CPA laser system. Only a minor difference is visible for the ratio of atomic hydrogen to molecular hydrogen. The amount of atomic hydrogen has decreased, since bond softening decreases with shorter pulse duration.

3.3.2 Electron Spectra

Figure 3.9 shows the kinetic energy spectrum and fig. 3.10 the corresponding momentum map for singly ionized argon obtained with the OPA system. Also for this electron spectrum, the $2U_p$ kink in the distribution is noticeable. The kink position at 18.9 eV gives an intensity of $1.6{\times}10^{14}\,\text{W/cm}^2$. This is in good agreement with the theoretical estimation of 10^{14} W/cm^2 using the focussing conditions and beam characteristics such as beam size, energy per pulse, pulse duration, central wavelength and focal length as described on page 39.

Above Threshold Ionization

In the results obtained with the OPA system, the ATI peaks seem to be missing. This is recognizable in both, the momentum map (compare figures 3.5 and 3.10) and the kinetic

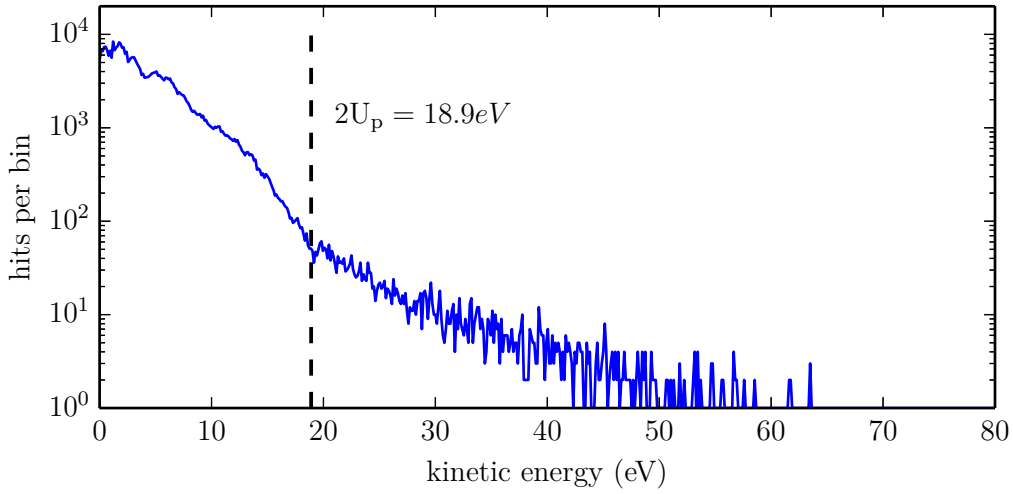

Figure 3.9: Kinetic energy distribution of photoelectrons along the polarization axis. From the $2U_p$-kink at 18.9 eV, an intensity of 1.6×10^{14} W/cm^2 is estimated. The ATI peaks seen in the measurement with the CPA system are not visible here due to the large bandwidth of the short laser pulses.

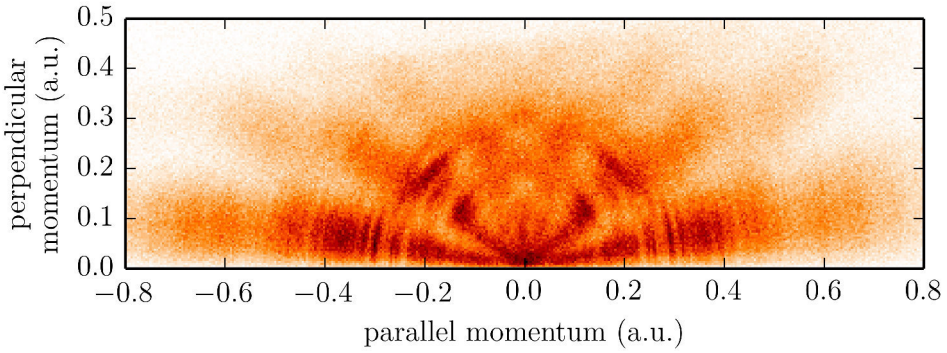

Figure 3.10: Momentum map of photoelectrons produced by strong field ionization of argon atoms by 6 fs laser pulses from the OPA system. It shows unexpected narrow features in each ray of the fan-like pattern.

energy distribution (compare figures 3.4 and 3.9). The intensity of this measurement gives a Keldysh parameter of 0.9. This is again the mixed regime of multi-photon and tunneling regime. But this time the laser pulse has only a few cycles.

In contrast with the observation described, one would expect a periodic ATI-like structure as seen in the work of Lindner *et al.*[98], where they see a periodic pattern in the electron spectrum at kinetic energies above 10 eV. The spectrum below 10 eV shows no pattern.

The origin of the pattern is explained by an interference between electrons from different sub-cycles of the pulse similar to the explanation of the ATI peaks in the tunnel picture(compare sec. 1.1.4). The visibility of this interference is influenced by the CEP of the pulses. Lindner *et al.* change the electric field of the pulse from a pulse with one major field peak to a field with two equally strong peaks by varying the CEP. The change in the electron spectra is interpreted by Lindner *et al.* with a double slit analogon. Two equally strong field peaks act as a double slit in time producing a high visibility of the interference fringes. One single field peak is a single slit with no interference pattern.

However, the current experiment does not use CEP stabilized pulses. Hence, each laser pulse has a different field distribution leading to different electron spectra. The detected spectrum will be an average over all spectra and might lead to a blurring of the ATI structure. Additionally, Lindner has seen these modulation at kinetic energies above 10 eV. This corresponds to a momentum of 0.85 a.u. where the signal is low for the data presented in fig. 3.10.

Fan-like Structure

A fan-like structure is also visible in the momentum map in the case of few-cycle pulses. The rays reach out towards 0.6 a.u. and are diffuser than with the longer pulses produced by the CPA laser system. For small parallel momenta around zero and perpendicular momenta above 0.1 a.u. the fan is diffuse and fades out. With eq. 3.1, one can again determine the classical angular momentum to $L = 6.8$ of this electron momentum distribution at a momentum $k = 0.1$. Hence, l is close to 6 which should result in six minima. This can hardly be seen due to the diffuse part.

Freeman Resonances

At first glance, all narrow features in fig. 3.10 could be assigned to Freeman resonances. But usually they are visible only for the first ATI peak, since multi-photon absorption or ATI has a lower probability compared to a one-photon ionization from this Rydberg state. Hence, the observable photoelectron energy of the features should be below $\hbar\omega$ and only hardly visible for higher energies due to the decreasing probability.

In addition, with this short pulse duration, the photon energy bandwidth is broad. The bandwidth of the pulse from the OPA system is 0.26 eV. The ionization step from the Rydberg state uses one photon from this bandwidth. Therefore, one would expect to see also diffuse freeman features with a width on the order of the photon bandwidth. At a momentum of 0.2 a.u., the photon bandwidth corresponds to a momentum bandwidth of 0.04 a.u.. However, the narrow features seen have a smaller bandwidth. Hence, a different

reason must be the cause of these features.

The SPIDER measurement of the OPA pulse of fig. 2.5b shows a few small post-pulses after the strong main pulse. These post-pulses might influence the ionization process and lead to the narrow features.

3.4 Theoretical Calculations

Theoretical calculations have been carried out to clarify the role of the post pulses. To study the interaction of light with atoms, one starts with the time-dependent Schrödinger equation(TDSE):

$$i\hbar\frac{\partial}{\partial t}\Psi(t) = \hat{H}\Psi(t) \tag{3.3}$$

with $\Psi(t)$ the time-dependent wave function of the quantum system and $\hat{H}$ the Hamiltonian. The form of the Hamiltonian depends on the actual problem. The Hamiltonian of an electron in a potential $V(r)$ under the influence of a laser field with a vector potential $\mathbf{A}(t)$ is given by:

$$\hat{H} = \frac{1}{2m_\mathrm{e}}(\mathbf{p} - q\mathbf{A}(t))^2 + V(r) \tag{3.4}$$

with $\mathbf{p}$ the momentum, m_e the mass of the electron and q its charge.

For a system with more than two particles, no analytical solution exists for this problem without any approximation. However, due to the availability of high CPU power, one can nowadays solve this equation by numerical methods.

Before details of the calculations are described in section 3.4.4 and 3.4.5 the following paragraph explains briefly the methods used for the numerical calculation. First the simplification of the, in principal multiple particle, problem by a single active electron approximation is explained followed by a schematic description of the algorithm.

3.4.1 Potential Representation

For the sake of completeness, this paragraph describes the atomic potential used in the calculation. Extending eq. 3.4 to a multi-particle system consisting of a number of nuclei N and a number of electrons n, the Hamiltonian is written as a sum of each single particle Hamiltonian and the interaction potential between all particles:

$$\hat{H}(R_1,...,R_N,r_1,...,r_n,t) = \sum_{\alpha=1}^{N}\frac{1}{2m_\alpha}(\mathbf{p}_\alpha - Z_\alpha\mathbf{A})^2 + \sum_{i=1}^{n}\frac{1}{2m_i}(\mathbf{p}_i - q\mathbf{A})^2 + V(R_1,...,R_N,r_1,...,r_n) \tag{3.5}$$

with Z the charge of the nuclei. The subscript α denotes the nuclei and the subscript i the electrons. The term $V(R_1,...,R_N,r_1,...,r_n)$ describes the Coulomb interaction between all particles in this system and is given by:

$$V(R_1,...,R_N,r_1,...,r_n) = \sum_\alpha\sum_{\beta\neq\alpha}\frac{Z_\alpha Z_\beta}{|R_\alpha - R_\beta|} + \sum_\alpha\sum_i\frac{Z_\alpha q_e}{|R_\alpha - r_i|} + \sum_i\sum_{j\neq i}\frac{q_e^2}{|r_i - r_j|} \tag{3.6}$$

From this equation, one sees that, even for a few particle system, the calculation becomes multidimensional and complex.

Since the present calculation deals with an atom, the complexity is naturally reduced to an n-particle problem. Further simplifications can be made due to the fact that in many cases of photo-ionization only a few or even only one electron is involved in the interaction of the atom with an external field. All other electrons produce an effective potential which influences the single electron under investigation. This approximation is called accordingly single active electron approximation (SAE).

The argon potential used in the calculations is given in the SAE approximation by a screened Coulomb potential [99]:

$$V(r) = \left[1 + Ae^{-Br} + (17 - A)e^{-Cr}\right]/r \tag{3.7}$$

with the constants A=5.4, B=1 and C=3.682 (All in atomic units). The eigenenergies of an electron bound in this potential reproduce quite well the binding energies of the singly excited states [100].

3.4.2 Numerical Method

The numerical calculation has been performed using a program originally written by H.G. Muller [101]. The code solves the TDSE based on a space-time grid. Spherical coordinates are chosen for the space grid due to the spherically symmetric potential. Therefore the wave function is represented by spherical coordinates as well:

$$\Psi(r,\theta,\phi,t) = \sum_{l=0}^{L_{max}} \sum_{m=-L_{max}}^{L_{max}} c_{nlm}(t)\frac{1}{r}\psi_{nlm}(r)Y_l^m(\theta,\phi) \tag{3.8}$$

with ψ_{lm} the radial part and Y_l^m the spherical harmonics. $c_{nlm}(t)$ is a time dependent coefficient, which determines the contribution of each state with the quantum numbers n,m,l. The variable r is discretized as $r_n = n \cdot \delta r$. Since we are only interested in linearly polarized light and the potential has azimuthal symmetry with respect to the laser polarization axis, the quantum number $m = 0$ is conserved and the second sum is absent.

The calculation starts with the field-free solution of the atom which is well known. The entire time evolution is discretized in several small time steps δt as well. The wave function propagates by calculation of

$$|\Psi(t_n + \delta t)\rangle = e^{-i\hat{H}_n \delta t}\,|\Psi(t_n)\rangle \tag{3.9}$$

where $\hat{H}_n$ is the Hamiltonian at the time $t_n + \delta/2$. This step is handled via the Crank-Nicolson method [102] to solve partial differential equations. A more detailed explanation can be found in [99, 101]. Accuracy and convergence of the calculation is determined by the choice of the parameters. The following paragraphs describe the available parameters listed in table 3.2.

One can specify two individual pulses with a $\cos^2$-envelope which approximate a Gaussian

Parameter	Function
E_0	electric Field strength of laser pulse
ω_0	central frequency of laser pulse
n_{cyc}	number of field cycles per pulse
ϕ_0	carrier envelope phase
τ	delay between both pulses measured from peak to peak
n_{grid}	number of radial grid points
n_{abs}	number of grid points used for the absorbing boundary
δr	radial grid step size
L_{max}	the maximum angular momentum used in the calculation
n_{time}	number of time steps
δt	time step size (is calculated from n_{time} and the total time given by the pulse definition)

Table 3.2: Input parameters of the calculation

pulse. The $\cos^2$-envelope assures that the laser field is zero at the beginning of the calculation. Using the more realistic shape of a Gaussian pulse would lead to errors due to the non-vanishing field at any time produced by the exponential function.

Each laser pulse is characterized by a maximum field strength E_0, a centre frequency ω_0, the number of cycles n_{cyc} and the carrier envelope phase ϕ_0. The number of cycles gives the total width of the pulse. The second pulse additionally has a parameter for the time delay between both pulses centres. Mathematically, this gives

$$E(t) = E_0 \cos(\omega_0 t + \phi_0) \cdot \cos^2\left(\frac{\omega_0}{2n_{cyc}} t\right) \qquad \text{for} \qquad -\frac{\pi n_{cyc}}{\omega_0} \leq t \leq \frac{\pi n_{cyc}}{\omega_0} \tag{3.10}$$

The space grid is specified by the total number of grid points and the step size δr per grid point. The step size influences the maximal observable energy. A particle with higher energy has a higher momentum and therefore a smaller de Broglie wavelength. In order to map the highest momentum on the space grid, the step size δ_r must be at most $\frac{\lambda_B}{2}$ with $\lambda_B = \frac{h}{p}$.

A high oscillation of the wave function exists also close to the nucleus. Hence, an exact calculation of the wave function at the core would need a very fine space grid introducing numerical problems. In order to avoid this, a core radius $R_C = 0.5$ bohr is defined [99]. At this radius R_C, a boundary condition is imposed to the wave function of $\Psi(R_C) = 0$. All time calculations have been performed outside of this core.

However, filtering in that way disturbs the energy levels, since parts of the wave function have originally a contribution in this core region. Therefore, a counteracting potential is

added in the range of $R_C < r < R_x$:

$$W(r) = F\left([(R_x - r)/G]^5 - [(R_x - r)/G]^4\right) \tag{3.11}$$

with $R_x = 3$, $F = 2.5$ and $G = 2.01785$ (all in atomic units), which weaken the effects of the boundary condition. The ionization process and subsequent processes occur outside of R_x and should therefore not be affected by this approximation.

The grid space defined above has additionally an absorbing boundary to avoid interference by reflected parts of the wave function at the boundary. However, this absorbing boundary only weakens the reflections. Strong contributions of the wave function still produces a partial reflection of the wave function. Hence, the total grid size has to be chosen carefully to prevent the fastest part of the wave function to reach the boundary. This choice depends on the total time, that is defined as the period from the beginning of the first pulse to the end of the second pulse.

The number of maximal angular momentum L_{max} for the calculation must be large enough to cover the whole process. If a strong contribution of multi-photon excitation and ionization is expected, this value must be high since each absorption can increase the total angular momentum quantum number by one. In the case the maximum number of angular momentum is exceeded, the representation of the wave function by eq. 3.8 is no longer sufficient.

The last parameter that can be chosen is the number of time steps for the entire calculation. This number is influenced by the highest frequency ω_0 and the time delay between both pulses. A higher frequency and a larger delay need a higher number of time steps. From the total time and the number of time steps, the time step size δt can be calculated. This δt should be small enough to have a good sampling of the electric field. Additionally, one should pay attention to the distance that the fastest part of the wave function is propagating in δt. If the time step δt is chosen large, so that the fastest part of the wave function propagates in δt a larger distance than δr, numerical errors will occur.

3.4.3 Intensity and CEP Averaging

A theoretical calculation with the above mentioned method gives a result for a single intensity at a certain CEP. But due to the radial intensity distribution of a Gaussian laser beam, different intensities are present in a real laser matter interaction. Additionally, a measurement consists of the sum of many single laser matter interactions. If the laser is not CEP-stable, each laser pulse has a different CEP and the result is an average over all CEP values. These two effects have to be incorporated in the simulation of the experiment.

The CEP-averaging is done by taking 21 different CEP values equidistantly distributed in the range of zero to 2π. Then all results are summed up to the CEP-averaged result for a particular intensity.

The averaging of the intensity distribution is a bit more complicated. According to eq. 2.9, the beam intensity is changing across the beam profile and along the beam axis. Since the molecular beam is much smaller than the Rayleigh length of the focus, only the radial Gaussian intensity distribution has been considered in the simulation. In order to perform the

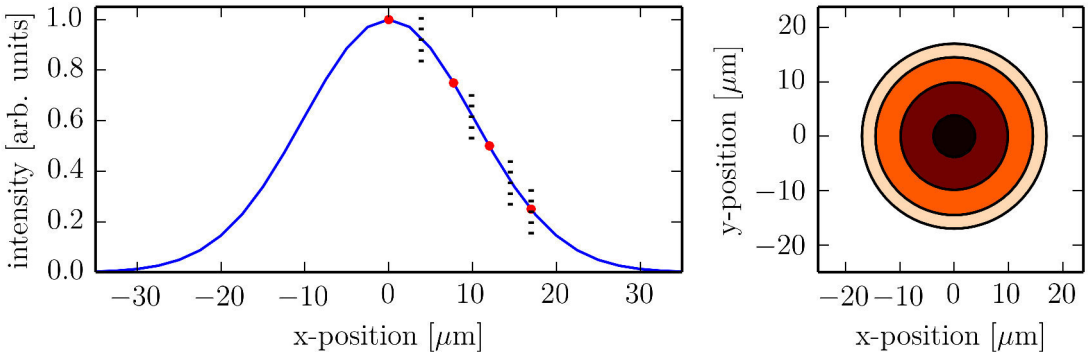

Figure 3.11: Principle of intensity averaging. The left figure shows the radial intensity distribution of a Gaussian beam. The red dots mark the different intensity used in a calculation. The dashed line indicate the radii R_{inner} and R_{outer} for the calculation of the area as described in the text.
The right figure shows the corresponding area of each intensity used. The weighting of each intensity is given by the ratio of its area to the total area.

intensity averaging, the intensity profile has been divided into eight intensities. Figure 3.11 shows this schematically for four different intensities. The value of the lowest intensity is chosen such that it produces less than a per mill of the electron yield produced by the highest intensity. For each intensity I_n, a radial position r_n is calculated by

$$r_n = w\sqrt{-\frac{1}{2}\log\left(\frac{I_n}{I_0}\right)} \tag{3.12}$$

with I_0 the maximum intensity at r=0 and w the beam waist defining the width of the radial intensity distribution as given by eq. 2.9. Then, to each intensity I_n, an area A_n is assigned given by a disc with a central hole described by

$$A_n = \pi R_{outer}^2 - \pi R_{inner}^2 \tag{3.13}$$

with

$$R_{inner} = (r_{n-1} + r_n)/2 \tag{3.14}$$

and

$$R_{outer} = (r_n + r_{n+1})/2 \tag{3.15}$$

If n is equal to one, indicating the first intensity, the inner radius R_{inner} is set to zero. If n indicates the last intensity, the outer radius R_{outer} is set to r_n. In that way the area of the last intensity is underrated, but since its total yield is less than a per mill of the highest intensity, the error introduced is negligible.

The final result is obtained by weighting each CEP-averaged result by the area as described above and by summing them all up.

3.4.4 Calculation of a Single Pulse with and without a Post-Pulse

In order to understand the role of satellite pulses in the temporal shape of the laser E-field on the photoelectron momentum distribution, one can compare momentum distributions produced by a single pulse against a distribution produced by a single pulse plus a weak post-pulse. Weak pre-pulses may be neglected since they don't have enough intensity to lift the atom out of the ground state.

Figure 3.12 shows the result of the calculation for a single pulse with a wavelength of 800 nm and five field cycles ionizing argon at an intensity of $1.6 \times 10^{-14}\,\mathrm{W}/cm^2$. Five field cycles correspond to a FWHM pulse duration of 6.6 fs at a wavelength of 800 nm. The pulse parameters are summarized in table 3.3 labelled as main pulse. The results of te calculation show the same general structure as the experimental data. One identifies a fan-like structure and also ATI peaks above a momentum of 0.2 a.u.. The number of rays in the fan matches the experimental data in fig. 3.10, which is a strong indication that the intensity chosen is in good agreement with experimental results. In the experimental momentum spectrum, no ATI peaks are discernible whereas the calculation shows diffuse ATI peaks. The most obvious difference to the measured spectrum are the narrow features. They also cover the ATI peaks visible in the calculated spectrum.

To mimic the experimental settings better, one post-pulse was added. The parameters of the post pulse labelled are summarized in the lower part of table 3.3. Figure 3.13 shows the calculated angular momentum distribution of photo electrons obtained by the TDSE code using the parameters of table 3.3 including a post pulse. Adding a post pulse produces narrow features on top of the distribution obtained by a single pulse. This looks very similar to the experimental observation.

A comparison between the populations of Rydberg states after interaction with both different pulses reveals the origin of these features. Figure 3.14 shows these populations. The dashed line in fig. 3.14 represents the population of shells up to a quantum number of $n = 15$. The population of the shells n=1-3 populated by the ground state of argon is suppressed for the sake of visibility. After the main pulse is gone, non-zero population in

	parameter	**value**
main pulse	intensity	$1.6\times10^{14}\,\mathrm{W/cm^2}$
	frequency	374 THz ($\widehat{=}$ 800 nm)
	number of cycles	5
	carrier envelope phase	$0\ldots2\pi$
post pulse	intensity	$3.2\times10^{13}\,\mathrm{W/cm^2}$
	frequency	374 THz ($\widehat{=}$ 800 nm)
	number of cycles	5
	carrier envelope phase	$0\ldots2\pi$
	delay	15 fs

Table 3.3: Input parameters of the TDSE calculation for the ionization of argon with the laser pulse from the OPA system. The step size $\Delta\phi$ for the carrier envelope phase range is 0.3. In each individual calculation, main pulse and post pulse have the same CEP.

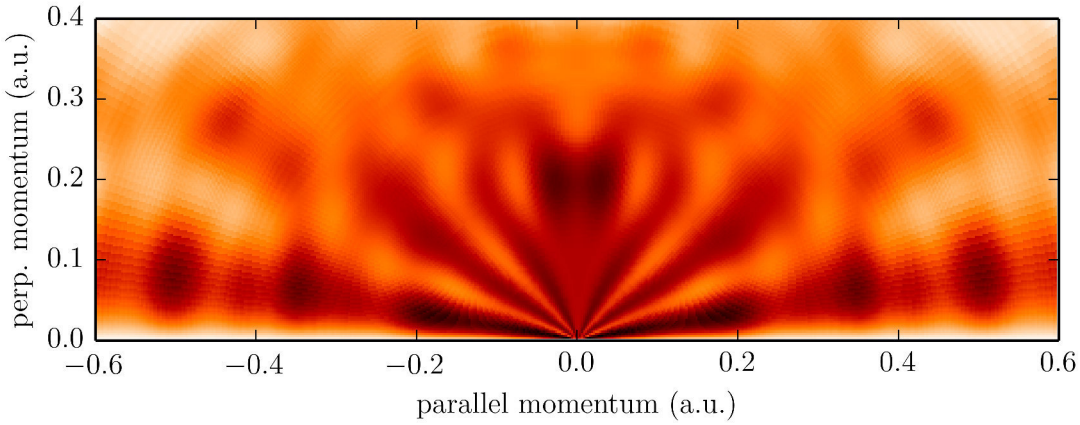

Figure 3.12: Calculated photo electron momentum map of strong field ionization of argon atoms by a 6.7 fs laser pulse with a wavelength of 800 nm at an intensity of $1.6{\times}10^{14}$ W/cm². It shows a similar electron distribution with a fan-like structure as the momentum map obtained with OPA laser system. However, it shows no narrow features like the ones observed experimentally.

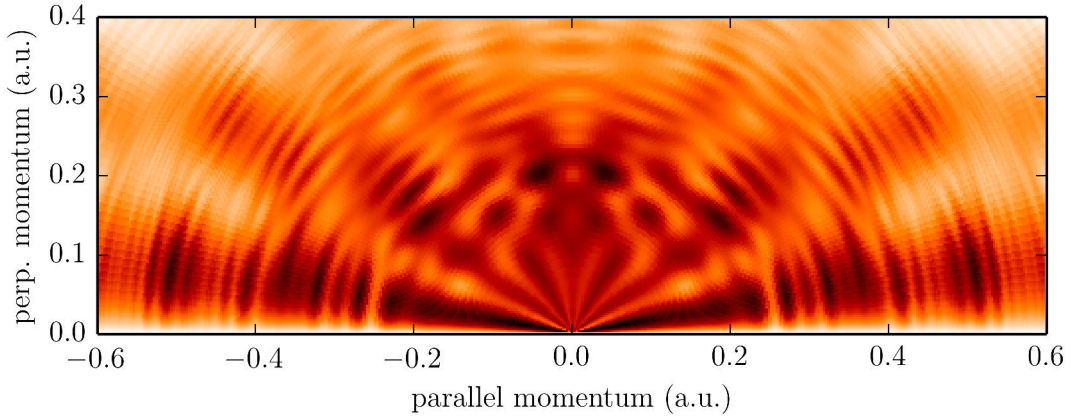

Figure 3.13: Calculated photoelectron momentum map for the strong field ionization of argon by a 6.7 fs laser pulse followed by a weaker delayed post pulse. This calculation reproduces the experimental data including also narrow features on top of diffuse features.

Rydberg states is left over. The consecutive post-pulse does not have a strong influence on the population distribution as it can be seen in the plot. Nevertheless, the difference between both populations shows the small changes induced by the post pulse (shown by the solid line). This small population shift gives a hint about the possible mechanism that causes the narrow features in the momentum map. The post pulse seems to ionize Rydberg states excited by the main pulse. These photoelectrons will then interfere with direct photoelectrons with the same kinetic energy produced by the main pulse.

3.4.5 Quantum State Holography

The process described in the previous section reminds one strongly on the experiments and calculations by Klünder *et al.*[92] and Mauritson *et al.*[103]. In these experiments, they have investigated the population of neutral atomic states by a pump probe measurement. Mauritson *et al.* have used a single isolated attosecond pulse for the pump step and a few cycle IR pulse for the probe step. They used helium atoms as target. Figure 3.15 sketches the principle of their experiment. The XUV pulse spectrum is centred around the ionization potential in order to excite population with a part of the spectrum into Rydberg states below the ionization potential and at the same time to also ionize into continuum states. The delayed few-cycle IR probe pulse ionizes the populated Rydberg states into the continuum. These two paths from the bound ground state into the continuum, called direct and indirect, interfere. Of course, this interference depends on the phase accumulated along these paths:

$$\begin{aligned} \phi_{direct} &= \phi_{XUV} + \phi_{continuum} \\ \phi_{indirect} &= \phi_i + \phi_{IR} + \phi_{Rydberg} \end{aligned} \tag{3.16}$$

with ϕ_{XUV} and ϕ_{IR} the phases due to the ionization process, $\phi_{continuum}$ and $\phi_{Rydberg}$ the phases for the time progression of the free and bound wave packet, respectively, and ϕ_i the initial phase of the Rydberg state. $\phi_{continuum}$ and $\phi_{Rydberg}$ are given by $\frac{E\tau}{\hbar}$ with E the energy of the continuum state or, E_i the energy of the Rydberg state and τ the delay between pump and probe pulse.

The interference structure is determined by the phase difference between direct and indirect path:

$$\Delta\phi = \phi_{direct} - \phi_{indirect} = (E - E_i)\,\tau/\hbar + \phi_i + \delta\phi \tag{3.17}$$

with $\delta\phi = \phi_{XUV} - \phi_{IR}$ and E_i the energy of the Rydberg state i.

It is assumed that the phase contribution due to the ionization process by the XUV or IR is independent of the state and energy. Therefore $\delta\phi$ is a constant phase offset and set to zero. An interference minimum is obtained if $\Delta\phi$ is a multiple of π. Thus, the eq. 3.17 can be rewritten as

$$E = E_i + (n\pi - \phi_i)\,\hbar/\tau \tag{3.18}$$

with n an integer.

In a diagram with the kinetic energy E as a function of τ, this equation gives a family of

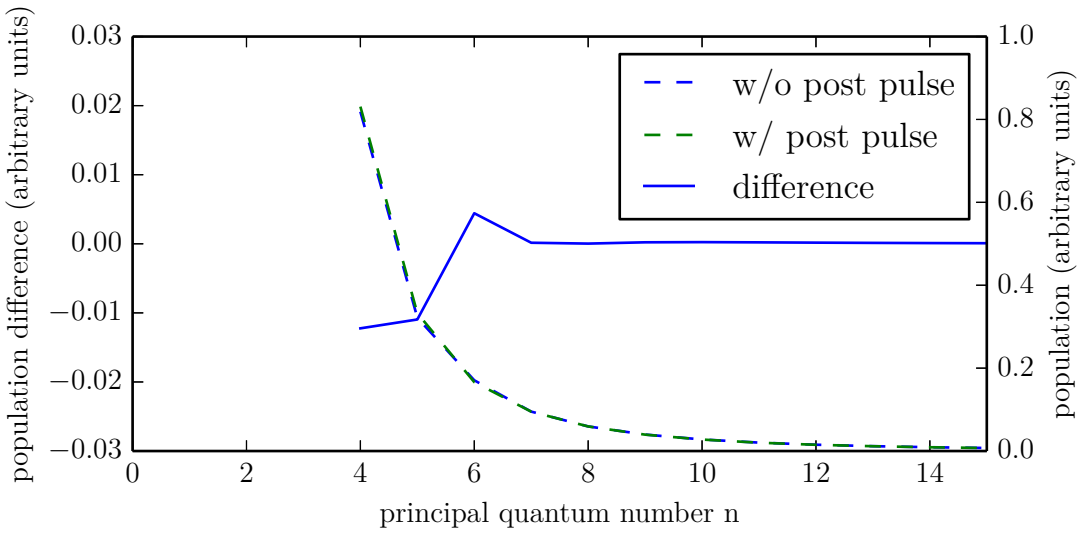

Figure 3.14: The dashed line shows the population after interaction with the single laser pulse for different principal quantum numbers. The population for n = 1-3 is suppressed. These principal quantum numbers belong to the ground state of argon and have the highest population. Even by suppression of these states, slight differences can only be hardly seen. The difference (solid line) of the population shows these changes more clearly. It suggests an ionization of excited states by the post pulse.

hyperbolic curves that get closer with increasing delay τ. Figure 3.16a shows a simulated photoelectron spectrum for helium where the hyperbolic curves are clearly visible.

In addition, from eq. 3.17 one can also see that the electron yield at a given energy E oscillates with the frequency:

$$(E - E_i)/\hbar \tag{3.19}$$

By applying a Fourier transformation to the pump probe scan for each kinetic energy E, the contribution of all present 'frequencies' is obtained. These frequency components will appear as lines tilted by 45° in the Fourier space (kinetic energy versus frequency) as it can be seen from eq. 3.19. The intersection with the abscissa gives the bound state energies. The relative strength shows the contribution of each bound state to the signal. Figure 3.16b shows the Fourier transformation of the spectrum shown in fig. 3.16a.

Transition from an XUV to an IR Pump Pulse

Although it seems that the interference between a direct photoelectron and a photoelectron via a Rydberg state is also the reason for the fringes seen in the calculation of section 3.4.4, it is unclear at first sight, if it is possible to retrieve the same information from a measurement with an IR pump pulse instead of the XUV pump pulse. To investigate this scheme with an IR few-cycle pump pulse, the TDSE calculation has been repeated with different laser parameters and also different delay times. The transition from an XUV pump pulse to an IR

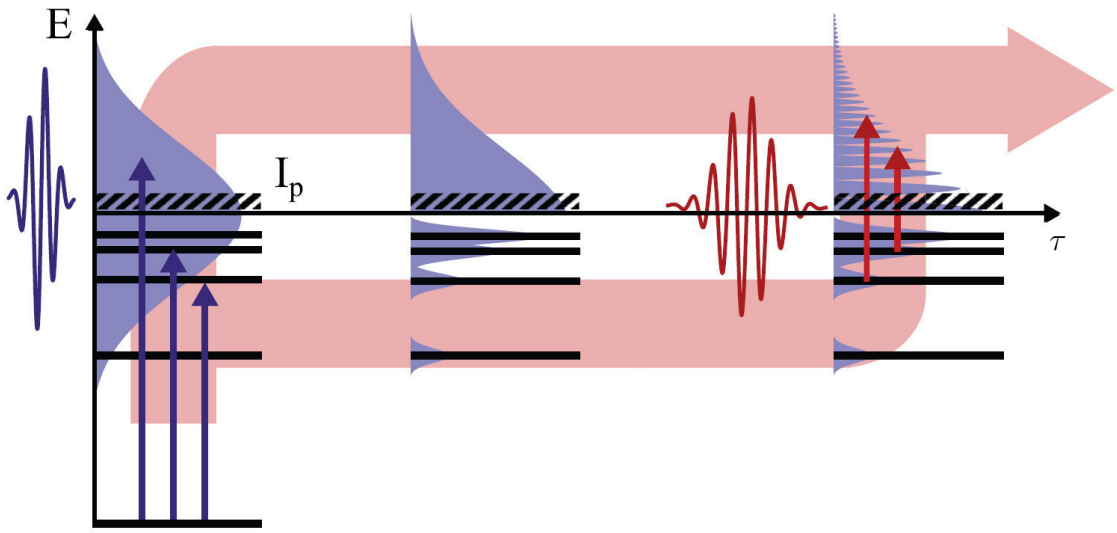

Figure 3.15: Principle of the attosecond electron interferometer as described in [92]. A wave packet in a Rydberg state is created by the absorption of an XUV photon. Simultaneously, a continuum reference wave packet is created. Both wave packets evolve freely in time until, after a delay τ, the bound wave packet is ionized using a synchronized IR probe pulse. At this point, quantum-mechanical interference arises between the two (direct and indirect) pathways that produce the continuum electrons. Figure from [92]

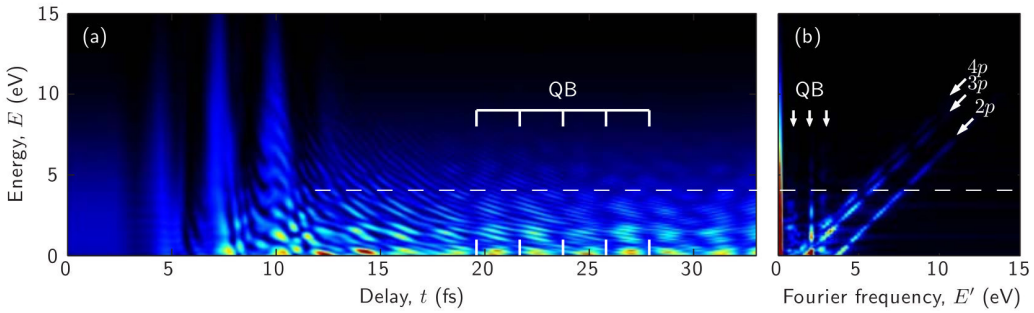

Figure 3.16: Results of [103] (a) Calculated photoelectron spectra in He as a function of delay between the XUV and the IR pulse. Interference fringes are clearly seen where the XUV pulse precedes the IR probe pulse. (b) Fourier transformation of the photoelectron spectrum showing the states forming the bound wave packet.

pump pulse has been made in a stepwise manner to keep track of the changes induced by the change of the wavelength. Since the argon IP is lower than that of helium, an adjustment of the central frequency of the XUV pulse is required to achieve the same energetic conditions of a pulse spectrum overlapping with Rydberg states and continuum states at the same time.

As an intermediate step, a calculation with a fraction of the XUV photon energy was performed to investigate a few-photon excitation in the UV region. Finally, the last scan utilizes a few-cycle IR pulse for the pump pulse.

In all scans, a few-cycle IR pulse with a moderate intensity of $3.5{\times}10^{12}\,\mathrm{W/cm^2}$ is used for the probe step. In a first set of calculations, no intensity or CEP averaging has been done, which would be necessary to simulate an experiment more realistically. Table 3.4 summarizes the most important parameters of each simulation.

Figures 3.17-3.19 show the results of each pump probe scan. As expected, the results of the XUV-IR pump probe scan shown in fig. 3.17 look very similar to the results shown in fig. 3.16 [103]. The similarity is not surprising, since the main difference is the different energy levels of the bound states of argon and helium.

When both pulses overlap at delay times around 0 fs, one can see large changes in the kinetic energy. The change in kinetic energy is given by the vector potential of the laser pulse at the time of ionization (see eq. 1.5). At delay times of 10 fs and beyond, where both pulses are separated, the previously described hyperbolic lines are visible. Since several Rydberg states contribute to the interference pattern, the corresponding hyperboles overlap and the hyperbolic pattern in the pump-probe scan looks distorted.

After Fourier transformation of the photoelectron spectrum, the diagonal lines can be assigned to Rydberg states of argon as labelled in fig. 3.17. The vertical lines stem from interference between different Rydberg states. This can be seen from eq. 3.17. With two different Rydberg states the phase difference becomes:

$$\Delta\phi = \phi_1 - \phi_2 = (E_i - E_k)\,\tau/\hbar + \phi_i + \phi_k + \delta\phi \tag{3.20}$$

with $\phi_{1,2}$ the phases of the two different indirect ionization pathways. Eq. 3.20 shows that the oscillation of the interference with time is independent of the observed photoelectron

	parameter	**XUV**	**UV**	**IR**
pump pulse	intensity ($\mathrm{W/cm^2}$)	$3.5{\times}10^{12}$	$5.6{\times}10^{13}$	$5.6{\times}10^{13}$
	photon energy (eV)	17	4.63	1.56
	number of cycles	5	5	5
	carrier envelope phase	0	0	0
probe pulse	intensity ($\mathrm{W/cm^2}$)	$3.5{\times}10^{12}$	$3.5{\times}10^{12}$	$3.5{\times}10^{12}$
	photon energy (eV)	1.56	1.56	1.56
	number of cycles	5	5	5
	carrier envelope phase	0	0	0
	delay (fs)	$-5\ldots55$	$-5\ldots55$	$-5\ldots55$
	delay step size (fs)	0.1	0.1	0.1

Table 3.4: Parameter of the TDSE calculation for different pump pulse frequencies.

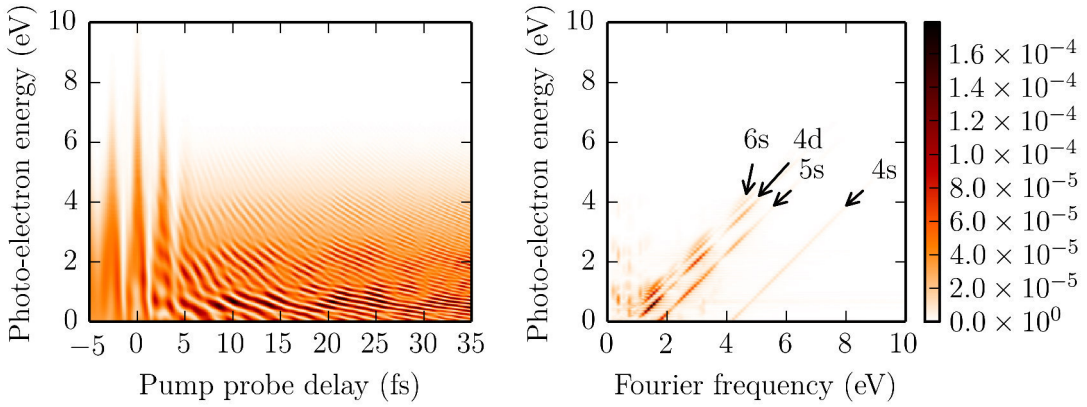

Figure 3.17: TDSE simulation using XUV pulse and IR probe pulse

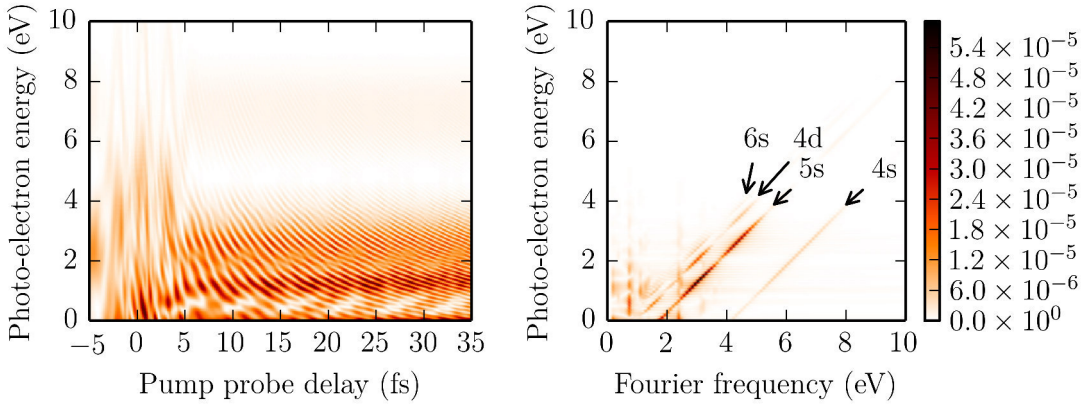

Figure 3.18: TDSE simulation using UV pulse and IR probe pulse

kinetic energy:

$$\omega_{ik} = (E_i - E_k)/\hbar \tag{3.21}$$

with E_i,E_k the energy of the involved Rydberg states i and k. Hence, Fourier transformation results in vertical lines. This type of interference is called quantum beating. The visible quantum beating corresponds to the interference between electrons from 6s and 7s (0.36 eV), 5s and 6s (0.75 eV) and 5s and 7s (1.1 eV).

Figure 3.18 shows the results of the UV-IR pump-probe calculation. Due to the lower photon energy the pump step needs a three photon absorption to reach the ionization threshold . This change of the ionization to a three step process does not distort the main pattern of the hyperbolic fringes. Only two minor changes are visible in the pump probe scan. In the time range when both pulses overlap (-5 fs to 5 fs), a richer structure is visible. The pump probe scan shows two regions at a photoelectron energy of 2.4 eV and 7 eV. These

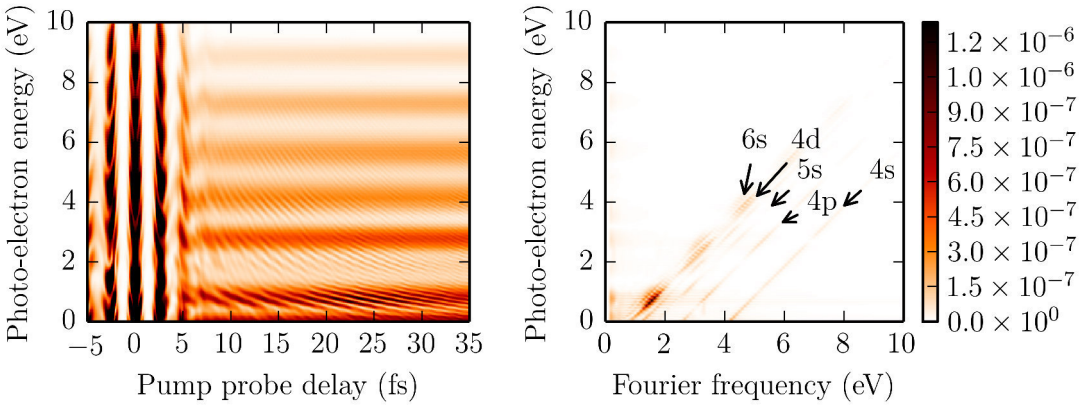

Figure 3.19: TDSE simulation using IR pump pulse and IR probe pulse with a CEP of 0° and a single intensity of $5.6 \times 10^{13}\mathrm{W/cm^2}$

regions correspond to the first and second ATI peak produced by the 4.6 eV UV pulse. The second has a much lower intensity, since the probability to produce photoelectrons in that energy region is lower due to the necessary two-photon ionization. This separation into two regions is also visible after Fourier transformation. The line of the 5s state shows a weak line at 7 eV photoelectron energy.

Figure 3.19 shows the results of the IR-IR pump-probe calculation. Now, the pump step is changed to a multiple photon ionization. Again, the pump-probe scan shows hyperbolic fringes, but the kinetic energy distribution of the photoelectrons differs substantially from those of the XUV-IR and UV-IR pump-probe scans. Now, one identifies several ATI peaks which also show up clearly after Fourier transformation.

The transition from high photon energies(XUV) to low photon energies(IR) increases the number of necessary absorption steps to reach the ionization potential. This higher number of steps with a smaller photon energy leads to a higher population of lower Rydberg states.

Averaging Influence

Although this simulation shows that the quantum state holography works with a strong field excitation as well, it is not clear at first sight whether this is true under real experimental conditions. The pump-probe simulations presented so far have neglected any intensity or CEP averaging.

Therefore, the simulation for the IR-IR pump-probe scan has been repeated with intensity averaging and fixed CEP and with averaging over both intensity and CEP as described in section 3.4.3. Fig. 3.20a and fig. 3.21a show the electron yield of the pump-probe scans for these two cases. The most remarkable observation is that the main features persist almost unchanged. The hyperbolic interference pattern is still visible and also the ATI peaks show up. Only small differences can be seen between the scans with and without intensity averaging shown in fig. 3.19 and 3.20. Also, the differences due to CEP averaging comparing fig. 3.20 and 3.21 are small. In both cases, the averaging decreases the ATI modulation of the kinetic energy distribution. This decrease is also visible in the Fourier transformed spectra. The different intensities have different maximal electric field strengths and also the different CEP values change the maximum value of the electric field of the pulse. According to eq. 1.6, the instantaneous vector potential at the moment of ionization determines the final momentum of the electron. Hence, different maximal field strength lead to different energy distributions.

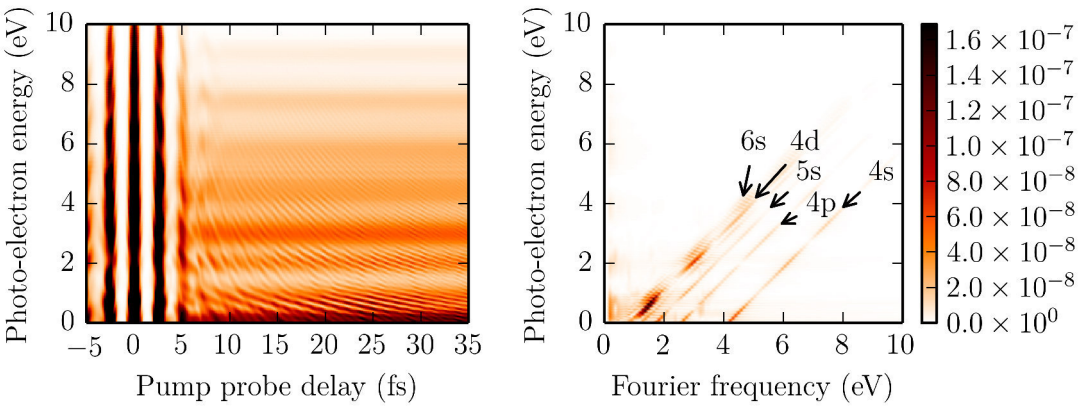

Figure 3.20: TDSE simulation using IR pump pulse and IR probe pulse with a defined CEP of 0Â° and intensity averaging over ten different intensities

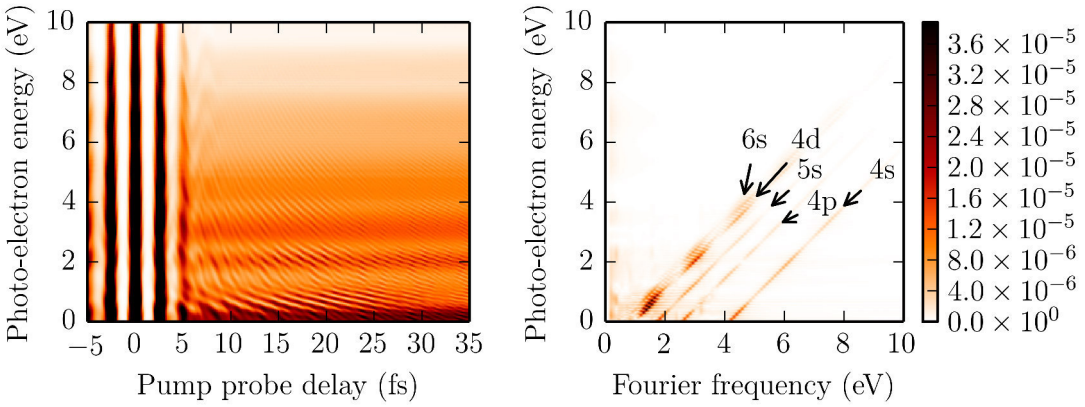

Figure 3.21: TDSE simulation using IR pump pulse and IR probe pulse with CEP averaging and intensity averaging over ten different intensities

3.5 Strong Field Double Ionisation of Xenon

3.5.1 Motivation

In the preceding part of this chapter, strong field ionization leading to singly charged atoms has been investigated and the results have been discussed in the single active electron picture. But as described in the main introduction, strong field ionization shows several phenomena that cannot be understood within the SAE picture [31]. One of these phenomena is non-sequential double ionization showing strong correlations between both ejected electrons. These correlations show large differences in the momenta distribution of both photoelectrons at different laser intensities implying diverse ionization mechanisms. A sketch of the different mechanisms are shown in fig. 3.22 ordered by decreasing ponderomotive potential. The corresponding momentum distributions are shown in fig. 3.23.

The first mechanism (fig. 3.22a) belongs to the sequential regime. At high intensities, the atom is ionized via 'over the barrier' ionization, i.e. both electrons can leave the ion core over the barrier. All following mechanisms belong to non-sequential mechanisms.

The second mechanism for double ionization is explained by a direct impact ionization. The first electron is released by tunnelling and accelerated in the laser field. When driven back by the field, the electron scatters inelastically with the atom and transfers its energy partially to the atom. If the transferred energy is higher than the IP for double ionization, a second electron can leave the ion core. The electron gains the highest recollision energy of 3.17 U_p if it is liberated close to the field maximum (see sec. 1.1.1). Since the recollision with 3.17 U_p happens at a zero crossing of the electric field, the second electron gains also high kinetic energy. Therefore, the momentum of both electrons will be similar leading to a typical V-shape structure in the momentum correlation map (fig. 3.23a).

However, even at intensities which do not provide enough recollision energy to remove a second electron a higher double ionization yield is obtained than expected by sequential

models. This third mechanism is explained by a process called recollision-excitation with subsequent ionization (RESI). Here the first electron recollides with the atom and excites the second electron. Then, at the next field maximum the second electron can tunnel into the continuum. Hence, one expects to see a correlation between an electron with a non-vanishing and an electron with a vanishing momentum (fig. 3.23b).

A fourth double ionization process exists in which the recolliding electron has just enough energy to excite a second electron into a higher state. Thereby it looses kinetic energy and is recaptured by the atom producing a doubly excited state. This state is then ionized by over the barrier ionization with in the next laser half cycle [104]. Therefore, both electrons will leave the atom almost simultaneously leading to a similar momentum with the same direction. A small difference in the ionization time of both electron produces the deviation of momentum of both electrons (fig. 3.23c).

These correlations maps have been investigated using reaction microscopes for many different rare gases as He, Ne, Ar [75, 107, 108]. Due to the different electronic structure of these atoms, the electron-electron correlation observed differ. Especially, if an intermediate state as in case c and d of fig. 3.22 is involved, signatures of these states are expected to be present in the correlation.

In these experiments, typically the momentum of the doubly charged ion and the momentum of only one electron is measured since the detection probability is the square of the detection probability for a single electron (typically 0.7). The momentum of the second electron has to be calculated by momentum conservation of all three particles. However, the detection of all three particles (triple coincidence) gives the complete information. But, as written above, the detection of two electrons in one event has a probability of the squared efficiency for a single electron detection. This reduction of probability increases the total time of the measurement. The setup presented in this thesis facilitates this kind of measurements due to the high repetition rate.

Xenon has been chosen as the target species since the available laser intensity of the OPA system was appropriate to double ionize xenon by SFI. A rare gas atom with a higher IP as for example argon would lead to very long measurement times even at 400 kHz. A second reason for the choice of xenon is that, up to the point that this experiment was done, published studies concentrated on lighter rare gas atoms and no correlation maps exist for high-Z rare gases as xenon . So far, the studies published [109–111] only showed that a non-sequential process plays a role in the formation of doubly charged xenon by SFI. The correlation of the ejected electrons has not been addressed.

Beyond the challenge of detecting triple coincidences, another difficulty is the high number of isotopes of xenon. Xenon has eight stable isotopes and one long-lived isotope. Table 3.5 shows that the abundance of seven isotopes varies from 4% to 26%. Therefore, it is necessary to measure approximately seven times longer to achieve a similar statistical confidence for each isotope as for argon or helium with only one main isotope each.

The next section summarizes the experimental settings. Thereafter, the results are presented.

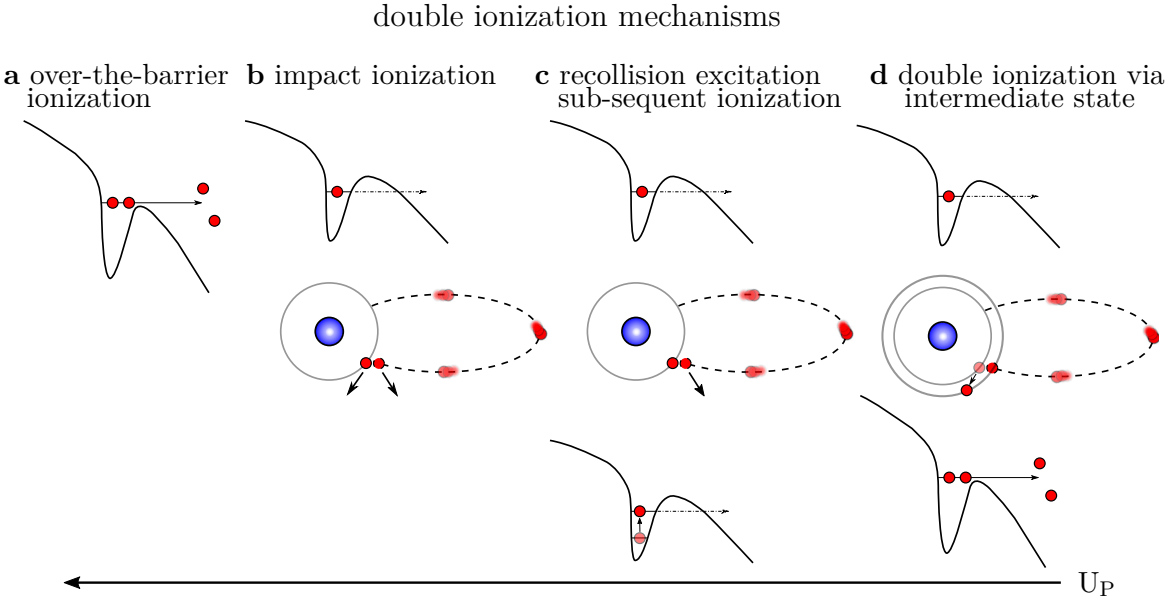

Figure 3.22: NSDI mechanisms adapted from [31].
(a) sequential regime: the laser is strong enough to liberate two electrons by over the barrier ionization.
(b) direct impact ionization: The first electron tunnels at a field maximum and is driven by the laser field. On recollision with the ion, the electron transfers energy leading to a release of a second electron.
(c) recollision-excitation-tunnelling: As case b but the first electron has too less energy for a direct release of a second electron by recollision. Instead, the second electron is excited and will tunnel in a subsequent laser cycle.
(d) double ionization through doubly excited intermediate state: The first electron is captured by the ion and thereby excites also a second electron leading to a doubly excited state. This state will subsequently decay and release two electrons.

Isotope	**abundance**[112]	**measured abundance**
^{124}Xe	9.5×10^{-4}	not observed
^{126}Xe	8.9×10^{-4}	not observed
^{128}Xe	0.019	0.026
^{129}Xe	0.26	0.26
^{130}Xe	0.040	0.044
^{131}Xe	0.21	0.21
^{132}Xe	0.27	0.26
^{134}Xe	0.10	0.10
^{136}Xe	0.09	0.09

Table 3.5: stable isotopes of xenon from [112]. ^{136}Xe has a half-life of 2.165×10^{21} years and can be considered as stable.

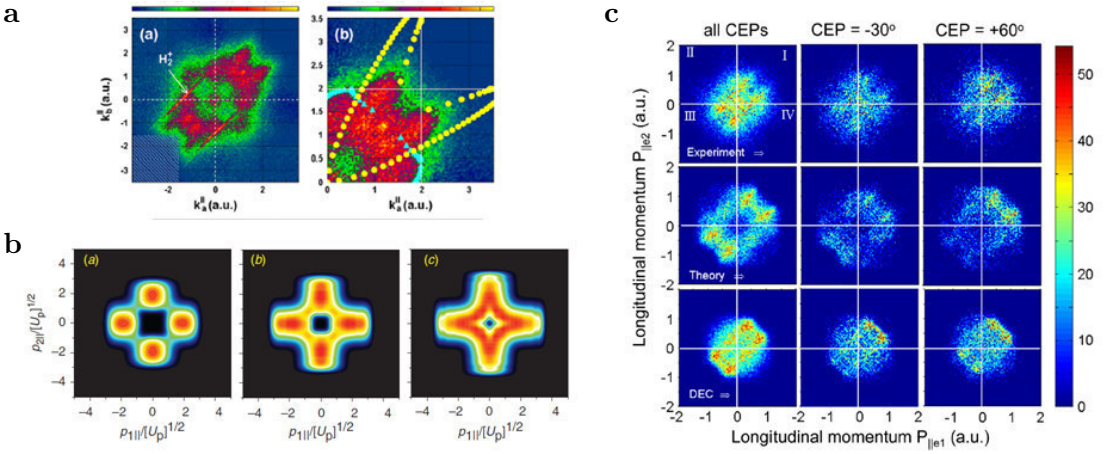

Figure 3.23: Correlations between both electrons produced by double ionization mechanisms as shown in fig. 3.22.
(a) Direct impact ionization: The second electron is released due to recollision at a field crossing. Both electrons fly in the same direction with a similar momentum leading to a V-shape pattern. From [105]
(b)RESI: The first electron will have high a momentum gained in the field. Since the second electron tunnels at a subsequent field maximum, it will have a small initial momentum close to zero. From [106]
(c) Double ionization through doubly excited state: Since both electrons are released in the same laser cycle, they have the same direction. Small differences of the tunnelling point of time of each electron let both electrons be released at different fields leading to slightly different final momenta. From [104]

3.5.2 Results

To achieve a sufficient but not too high count rate, the xenon gas had to be diluted in helium (ratio 1:100). Due to its high ionization potential helium was not ionized by the laser, which would have produced unwanted signal otherwise. The stagnation pressure has been 1 bar. The intensity in the focus was $1.5\times10^{14}\,\mathrm{W/cm^2}$. Seeding in helium leads to a higher average velocity of the xenon atoms in the molecular beam than that achieved with a pure xenon beam. The extraction field has been set to $428\,\mathrm{V/m}$. At this extraction field, the xenon ions hit the ion detector close to its edge. The magnetic field was set to $5.3\times10^{-4}\,\mathrm{T}$ at a current of 10 A. The accepted maximum momentum for the electrons was therefore 2.2 a.u. parallel and 0.74 a.u. perpendicular to the spectrometer axis. The laser pulses had a duration below 7 fs at a central wavelength of 800 nm with an energy of 3.55 μJ per pulse. 10^8 events have been recorded by the measurement software in a time of 2 hours. The average event rate was therefore 4.1 % of 400 kHz.

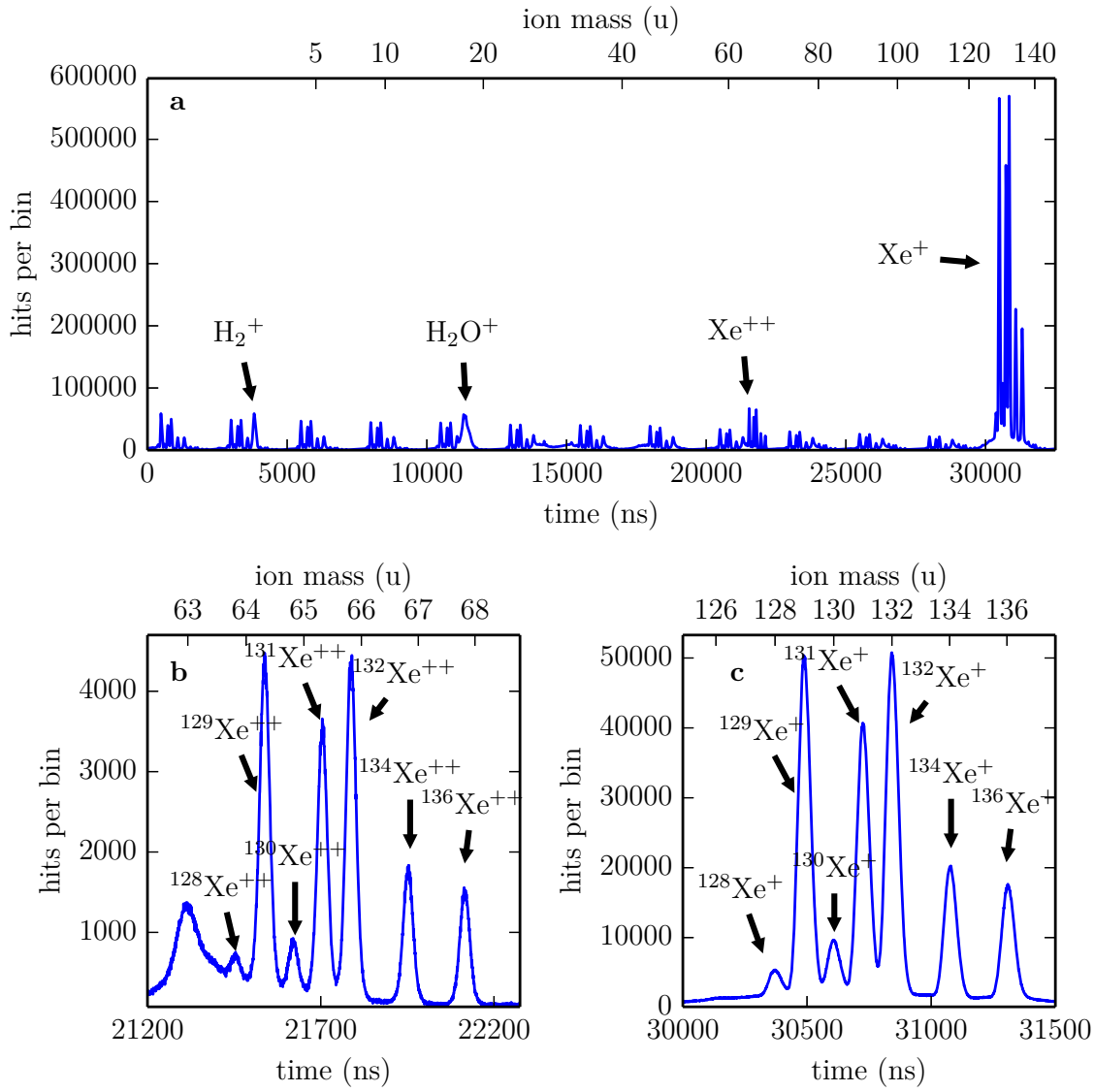

Figure 3.24: Time-of-flight spectrum of strong field ionization of xenon.
(a) complete time-of-flight spectrum
(b) zoom on doubly charged isotopes: $^{128}Xe^{++}$ overlaps with a part of a ghost-peak.
(c) zoom on xenon isotopes. Seven out of nine stable isotopes are visible as labelled.

Ion Time-of-Flight Spectra

In fig. 3.24 a, the time-of-flight mass spectrum of the strong field ionization of xenon is shown. Xenon can be identified as the main contribution around 30000 ns. Doubly ionized xenon (21500 ns), water (11400 ns) and H_2 (3800 ns) are visible as well. All other peaks are the so-called ghost-peaks (see section 2.2.7).

Figure 3.24 b and c show a zoom onto the Xe^+ and Xe^{++} peaks. In this zoom, seven of the nine natural isotopes of xenon are visible. The relative occurrences matches the natural abundance. Table 3.5 gives a comparison of the measured and tabulated abundances.

Unfortunately, the $^{128}Xe^{++}$-signal (fig. 3.24 b) is overlapping with a ghost-peak of $^{136}Xe^+$. All other peaks are unaffected noticeable from the relative height reflecting the natural abundance.

In order to check the momentum conservation of photoion and photoelectron, each isotope has to be treated individually to calculate their momenta. After momentum calculation, the momentum histogram of each isotope can be filled into one common histogram since the configuration of the nucleus has no noticeable effect on the photo-ionization. Thus, the momentum distribution is the same for each isotope.

Electron Spectra

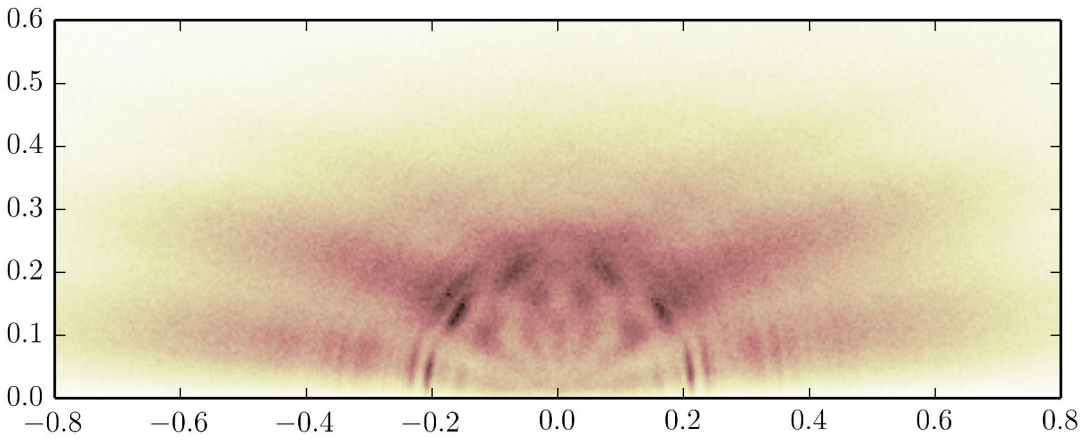

Figure 3.25: Momentum map of photoelectrons produced by strong field ionization of xenon atoms by 6 fs laser pulses.

Before the correlation maps for double ionization are shown, the electron momentum map of singly charge xenon is presented for the sake of completeness in figure 3.25. It shows a similar structure as the momentum map of argon in fig. 3.10. One can identify several rays of a fan-like structure as also seen for argon. On top of the rays, small narrow features are visible. Most probably, the origin is the same as in the case of argon. The post pulses of the laser pulse ionize excited Rydberg states of xenon which leads to interference with directly ionized photoelectrons. But in comparison to the argon measurement, the interferences have a weaker occur-

rence.
During the time elapsed between the argon and the xenon measurements, the temporal pulse shape of the OPA has been improved leading to weaker post-pulses.Thus, the interferences are less pronounced.

The following part will briefly present the information obtained from the electron time-of-flight data coincident with a doubly charged ion. As written in the motivation, the correlation maps of both electrons are typically produced by calculating the momentum of the second electron due to momentum conservation between all three particles. In that way, the correlation map in figure3.26 was created. The figure depicts the correlation of the momentum parallel to the laser polarization axis between the first (detected) electron and the second (calculated) electron with the simultaneous detection of a doubly charged xenon atom. One sees a distribution with a maximum at zero momenta for both electrons. This was also seen very recently in a publication by Sun *et al.* [113].

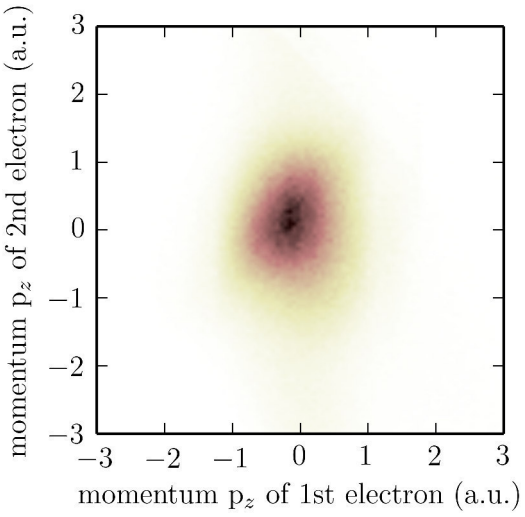

Figure 3.26: Correlation map with calculated momenta for the second electron when only one electron is detected accompanying a doubly charged xenon atom.

However, by calculating the second momentum due to momentum conservation, the error of the momentum of the ion degrades the momentum resolution of the correlation map. The ion momentum resolution of the reaction microscope is on the order of 0.1 a.u. as seen in figure 2.24 of section 2.3.6. The momentum resolution of the electrons is on the order of 0.01 a.u. as seen from the sharpest features of the momentum map in figure 3.10. Hence, if one uses events in which both electrons of the double ionization have been detected, the correlation map should show a higher momentum resolution.

Figure 3.27 depicts the correlation of the momenta parallel to the laser polarization of both detected electrons for all events with two detected electrons and one doubly charged xenon ion. It shows two distributions which touch each other but seem to be separated along a distinct line.

Unfortunately, the reason for this line is an artificially increased dead time (30 ns)

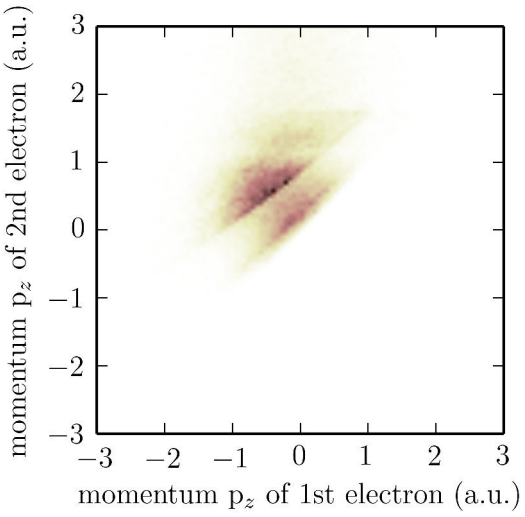

Figure 3.27: Correlation map of p_z of two detected electrons for all doubly ionized xenon isotopes

caused by wrong settings of the constant fraction discriminator. Therefore, an interpretation of the data is far from being reliable. It was not possible to repeat the experiment with corrected settings because a laser upgrade was planned right after these measurements in the schedule of the project. This upgrade caused a down-time, which reached beyond the period of my thesis.

Despite the technical flaw, this experiment demonstrated the potential of a high repetition rate in order to detect triple coincidences by investigating exemplary NSDI of xenon. The setup is capable of detecting 104555 triple coincidences in 2 hours at 400 kHz repetition rate. In terms of stability and reliability this period does not put high demands on any setup, which would look different for a common 10 kHz laser system.

For future experiments on NSDI of xenon, this first measurements have shown a few things to be improved: All settings of the electronics has to be chosen such, that the smallest dead times will be provided. Additionally, since a dead time of about 10 ns of the MCP will persist, it is advantageous to extract the electrons with a weak extraction field. This increases the time difference for a given momentum difference of two electrons.

A low electric field will induce two problems to keep in mind. The time-of-flight difference of different masses/isotopes increases and a change of the extraction field also shifts the signal of the doubly charged ions with respect to the singly charged ions. The ghost-peaks copy the strongest contribution of the mass spectrum which is in general the singly charged ion. They appear always shifted by a multiple of the laser repetition period. Therefore, a decrease of the extraction field leads easily to an overlap of the doubly charge xenon ions and the ghost-peaks.

This adverse effect can be weakened or limited by either lowering the repetition rate - which increases the distance between the ghost-peaks - or by diluting the molecular beam to lower the event rate. But, both actions will increase the duration of measurement.

3.6 Summary

In the first part of this chapter, the performance of the newly constructed reaction microscope and its interplay with the new OPA high repetition laser system has been investigated. The performance analysis of the reaction microscope proved the proper operation of the apparatus on the basis of strong field ionization of argon. Recent literature results have been reproduced by these measurements. From the measurements, a very good detector efficiency of 80 % for the electron detection and of 38.6 % for the ion detection was retrieved.

The momentum resolution was estimated to be ≤ 0.01 a.u. from the sharpest features in the electron momentum maps, since it is not clear whether the width of this feature is determined by the energy resolution of the apparatus or by the process causing this feature. The momentum resolution could be even better. In order to achieve a better estimation, one should perform a measurement on an atomic target (e.g. helium) with a light source which provide a single photon ionization.

The importance of a proper choice of the event rate has been shown in this chapter, as well. A too high event rate produces a high number of false coincidences and also unwanted ghost-peaks which could cover information. But more important is the asymmetry observed in the photoelectron momentum distribution along the polarization axis of the laser at

high event rates. This asymmetry will distort or even ruin results obtained with CEP stabilized pulses, where waveform induced asymmetries in the momentum distribution has to be measured.

In the second part of this chapter, the role of post pulses from the OPA laser system in the strong field ionization of argon have been studied by means of TDSE calculations. The results of the calculations have shown that a post pulse ionizes Rydberg states populated by the main pulse leading to interference in the kinetic energy distribution of the photoelectrons. This led to consecutive TDSE calculations studying an IR-pump-IR-probe scheme to investigate the population of neutral states after strong field interaction. The calculations suggest that such an experiment is feasible. Moreover, since the observed interference fringes are robust against intensity and CEP averaging, no high demands exist for the required laser system.

4 Strong Field Ionization of Hydrocarbon Molecules

4.1 Introduction

A comprehensive understanding of strong field physics in polyatomic molecules is a prerequisite for the establishment of strong field spectroscopy in these molecules. As briefly discussed in the introduction, strong field phenomena as HHG, LIED and ATI have shown to be versatile spectroscopic methods to investigate attosecond dynamics. The interpretation of these experiments largely uses the three step model which is based on approximations as for instance strong field approximation and single active electron approximation. These approximations work well for atomic systems. However, it has been recognized that in molecules the picture of only the weakest bound electron taking part in HHG has to be changed. Experiments by McFarland *et al.* on investigation of HHG with aligned nitrogen molecules [114] and theoretical investigation of HHG in aligned carbon dioxide molecules by Smirnova *et al.* [115] have shown fingerprints of several molecular orbitals participating in HHG. At the same time Akagi *et al.* [26] have observed tunneling from lower-lying orbitals in HCl. Therefore, the application of methods of strong field spectroscopy on molecules requires a deeper understanding of the contribution of multiple electronic orbitals. An important step in this context was done by Boguslavskiy *et al.* [116] showing purely experimentally that strong field ionization of poly-atomic molecules directly populates excited ionic states. This can be seen as a breakdown of the single-active electron approximation, since the ionization of the most weakly bound electron would lead to the population of the ionic ground state only. But, the ionization led additionally to excited states which means that also lower bound electrons have been ionized.

From synchrotron experiments on 1,3-butadiene [117] and n-butane [118] it is well known, that for these molecules only the ionic ground state is stable. All excited states of the ion fragment via unimolecular fragmentation.[1] Additionally, some of the produced fragments correlate mainly to a specific excited ionic state for these molecules. Boguslavskiy *et al.* used this circumstance to see if a strong field ionization directly into an excited state took place. But the sole detection of ionic fragments by means of time-of-flight mass spectrometry is not sufficient to distinguish a direct SFI into an excited ionic state from a sequential process via the ionic ground state.

The simultaneous detection of the ion mass spectrum and the electron kinetic energy spectrum allows to unambiguously distinguish the channels. The above threshold ionization

1 Unimolecular fragmentation or unimolecular decomposition is a fragmentation process in which the molecule fragments via a metastable state [119]. After electronic excitation, the electronic energy is converted into vibrational energy by internal conversion or intersystem crossing [120]. The vibrational energy will be redistributed into several vibrational modes, which leads potentially to the breakage of the weakest bond.

(ATI) peaks in the electron spectra are spaced by the photon energy and have an energy offset given by IP and the ponderomotive potential U_P(eq. 1.17). In good approximation, U_P is the same for all fragmentation channels within one measurement[1]. Therefore, the electron spectrum accompanying a fragment can be used to distinguish different ionization potentials. Figure 4.1 sketches the principle. The ATI spectrum of the parent ion, which corresponds to the ionic ground state, acts as a reference. If a detected fragment is produced due to direct ionization followed by fragmentation, the corresponding ATI comb will be shifted by the difference between the (Stark-shifted[2]) IP of the neutral ground state and the excited ionic state modulo the photon energy. If the detected fragment stems from a subsequent excitation, the ATI comb will show no shift with respect to the ATI comb of the parent ion, since in both cases the photoelectron stems from an ionization into the ionic ground state.

Boguslavskiy *et al.* investigated the strong field ionization of 1,3-butadiene by the simultaneous detection of ions and electrons to distinguish between a sequential and non-sequential ionization process. The time-of-flight data sets of ions and electrons have been analysed by the covariance mapping method [121]. This method uses the statistical fluctuations of the count rate to reveal correlations between detected particles. It has the advantage to accept a higher count rate than true coincidence detection, but it is very sensitive to shot-to-shot variations caused by unstable experimental conditions [122]. Figure 4.2 shows the ion mass spectrum for 1,3-butadiene and its correlated ATI spectrum obtained by [116]. A clear offset in the ATI spectra for different fragments is visible, which is the proof of a direct ionization into excited ionic states as explained before.

Since few-cycle laser pulses with a controlled CEP allow to investigate and also to control sub-cycle dynamics, a natural next step for the investigation of strong field ionization of polyatomic molecules is the use of few-cycle pulses. The experiment presented in this chapter extents the work described in [116] by using a reaction microscope. It uses few-cycle pulses but in this first experimental run without CEP stabilization.

Without CEP stabilization, no ATI peaks will be identifiable in the photon electron kinetic energy spectrum due to CEP averaging as seen in the measurements of argon in the previous chapter. Hence, the ATI spectra will not be suited any more to distinguish sequential from non-sequential excitation. However, there is another possibility to see whether the detected fragments stem from different electronic states or not. The angular distribution of the photoelectron spectrum also contains information on the electronic state from which the photoelectron originates. According to Ivanov *et al.* [123], who use the strong field approximation [20–22] to calculate the shape of the electron wavepacket as it appears after ionization, the momentum distribution of the electrons perpendicular to the laser polarization

1 The small difference in IP of ionic states changes the volume of the laser focus which contributes to the signal. For a lower IP a lower intensity is sufficient for ionization, hence ions will be produced in a larger volume. A larger volume means a different average intensity and hence a different U_P. In the present case the differences of the IPs are small compared to their absolute value.

2 see section 1.1.5

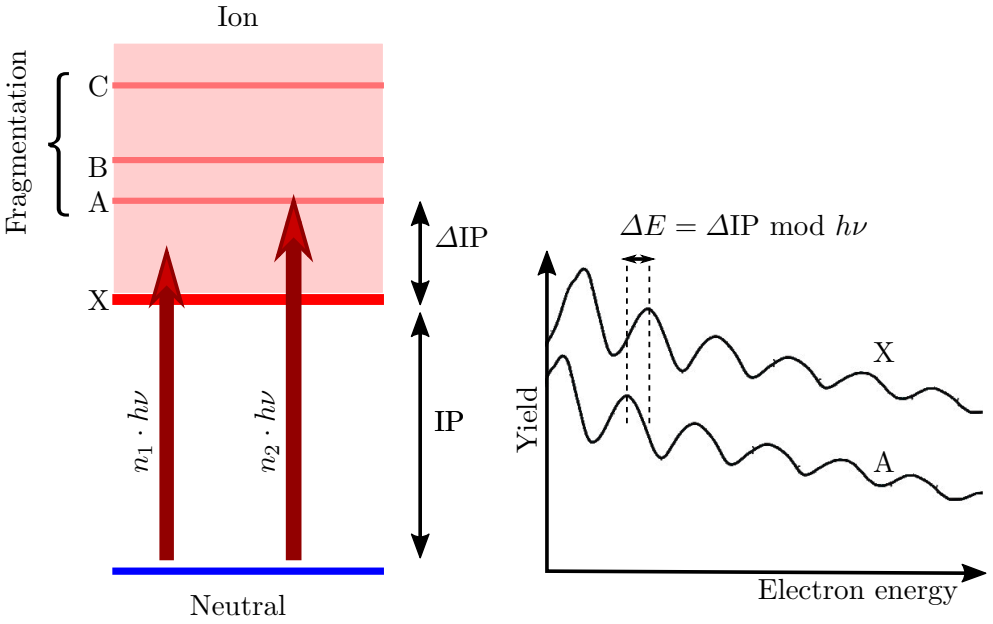

Figure 4.1: Principle of channel-resolved above-threshold ionization: The left figure shows a schematic diagram of electronic states of a molecule. X is the stable ionic ground state. The excited states A,B,C will fragment subsequently after ionization. The detected photoelectrons have peak positions according to eq. 1.17 at $E = n \cdot h\nu - (IP - U_\mathrm{p})$. Hence the offset between the ATI spectra for each individual channel is given by $\Delta E = \Delta\text{IP mod } h\nu$.

$|\Psi_\perp|^2$ depends on the wave function Ψ_0 as follows:

$$|\Psi_\perp|^2 = |\Psi_0|^2 \exp\left(-p_\perp^2 \frac{\sqrt{2IP}}{E}\right) \tag{4.1}$$

with IP the ionization potential and E the field strength of the laser pulse. Different electronic states of a molecule will show different angular resolved electron distributions, because Ψ_0 and the exponential factor changes. Therefore, the reaction microscope at hand is an ideal tool to investigate strong field ionization of molecules, since it provides coincident detection for angular-resolved ion and electron momenta. The coincident detection gives the ability to obtain electron spectra for different ion species (channels) at the same time, thus, under the same experimental settings.

In a different publication, Xu *et al.* [124] investigated not specifically electron dynamics but the fragmentation process of doubly excited 1,3-butadiene. Their particular interest was the study of proton migration within molecules due to strong field interaction as seen also in

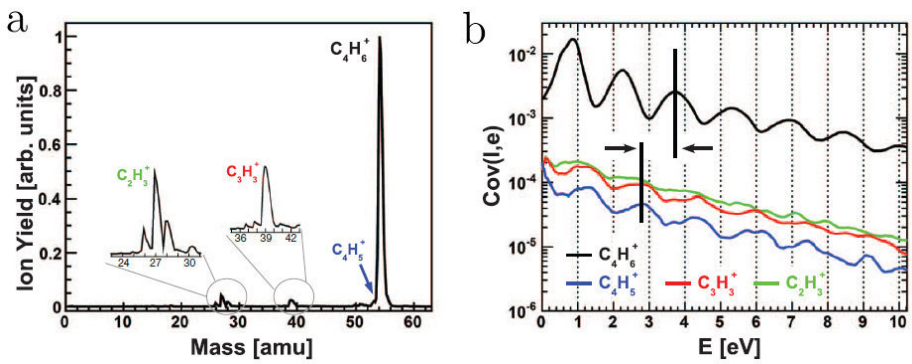

Figure 4.2: Top row: Strong-field ionization of 1,3-butadiene at a peak intensity of $1.9\times10^{13}\,\mathrm{W/cm^2}$.
(a) Mass spectrum with the most prominent peak being the parent ion C_4H_6.
(b) Channel resolved ATI photoelectron spectra correlated with both parent and fragment ions. As indicated by the vertical lines, the fragment ATI combs are shifted in energy relative to that of the parent ion.
Results from [116].

various other hydrocarbon molecules. The proton migration, in which a proton changes its position in a molecule, can lead to rearrangement of chemical bonds. Apart from the pure observation of proton migration, the potential to control chemical bond breaking increased the interest in the investigation of proton migration.

The following experiment described in this chapter will touch also parts of this doubly charged fragmentation process. In the next section, the experimental settings are summarized followed by the presentation and discussion of the results. 1,3-butadiene and n-butane are called butadiene and butane in the rest of this chapter.

4.2 Results and Discussion

As shown in fig. 4.2, a number of fragments are expected in strong field ionization of butadiene. The laser induced fragmentation causes a broadening of the time-of-flight-peaks due to the kinetic energy release[1], which could lead to an overlap of different masses in the time-of-flight spectra. To retrieve fragmentation channel resolved electron spectra in the analysis, the masses of the fragments have to be clearly separated in the time-of-flight spectra. From eq. 2.63 one sees that for large extraction fields the initial momentum (due to the kinetic energy release) becomes negligible and a mass separation is possible as seen in fig 4.2. However, the value of the electric field applied in a reaction microscope cannot be chosen arbitrarily high. Higher fields lead to smaller time differences between particles with different momenta. The extraction field has been set to $3400\,\mathrm{V/m}$ in this experiment, which is restricted by the ratings of the electrical vacuum feedthrough. With a time resolution of

1 Kinetic energy release is the translational energy of fragments resulting from dissociation.

25 ps given by the TDC, the applied field leads to a momentum resolution of 0.01 a.u. for ions and electrons. This is high enough to resolve narrow features in a momentum distribution as seen for example in strong field ionization of argon (chapter 3). The magnetic field was set to 5.3×10^{-4} T by a current of 10 A. This leads to an accepted maximum momentum for the electrons of 6.3 a.u. parallel and 0.74 a.u. perpendicular to the spectrometer axis. The laser parameters are similar to that of the previous chapter: At a repetition rate of 400 kHz, pulses with sub-6-fs duration were produced at a central wavelength of 800 nm with an energy of 3.6 μJ per pulse. The intensity was 1.5×10^{14} W/cm^2(butadiene) and 1.3×10^{14} W/cm^2(n-butane).

Since the ionization potential of xenon (12.1 eV) is only slightly higher than that of butane (10.6 eV) and butadiene (9.1), similar mixing ratios with helium have been chosen for butane and butadiene as well to achieve reasonable count rate. The ratio have been 1:700 (butadiene:helium) and 1:100 (n-butane:helium).

The following part of this section, presenting and discussing the results of the experiment, is divided into two parts. The first part treats the information obtained for the detected ions, the second part deals with the data of the electrons.

4.2.1 Ion Data

Time-of-Flight of Butadiene

Figure 4.3 shows the time-of-flight spectrum obtained for strong field ionization of butadiene on a logarithmic scale. As the top scale, a calibrated mass axis assuming singly charged particles is given. The highest peak can be assigned to the parent ion $C_4H_6^+$, followed by its isotopes in which one or two ^{12}C atoms are replaced by ^{13}C atoms. The measured ratio corresponds to the natural abundance for $^{13}C/^{12}C$ of $\sim$1 %. The probability for having one of the four carbon atoms replaced by a ^{13}C atom is about 4%[1], which is consistent with the time-of-flight spectrum. The replacement of two ^{12}C atoms by ^{13}C atoms has a probability of 0.06% also consistent with the time-of-flight spectrum.

Most of the remaining peaks can be sorted into three groups (areas blue shaded in the figure). Each group corresponds to the signal of fragments having one, two or three carbon atoms and a varying number of hydrogen atoms.

A number of additional mass peaks are also visible in the spectrum. The most prominent one is a narrow peak at 5085 ns. The shape of the peak indicates that it originates from the molecular beam directly and not from a fragmentation, which is always connected to a peak broadening due to the kinetic energy release. Since a time-of-flight mass spectrometer measures the ratio between mass and charge state, doubly charged butadiene appears at the same position as fragment $C_2H_3^+$. Thus, due the sharpness of the peak it is assigned to doubly charged butadiene $C_4H_6^{++}$.

Two additional narrow peaks can be seen at 2180 ns and 4680 ns. These two have a time difference to the peak of the parent ion of a multiple of 2500 ns which is the repetition period of the laser source identifying them as the ghost-peak artefacts (see page 63).

1 The exact value can be calculated with the binomial distribution.

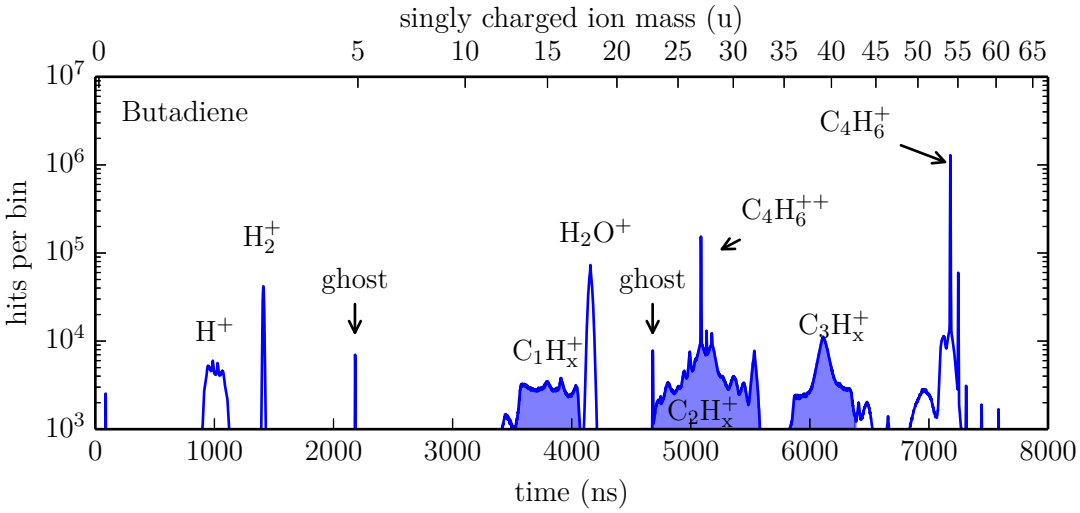

Figure 4.3: Time-of-flight spectrum of strong field ionization of butadiene. Among several narrow mass peaks three broad groups are visible belonging to chemical compounds with a different number of carbon atoms as labelled. For details see text.

The two peaks at 1 u and 2 u belong to atomic and molecular hydrogen ions, respectively. Additionally, a larger peak of water (18 u) shows up which is mainly a background gas contribution. A small sharp peak on top of the water peak indicates a small contamination of the molecular beam with water. A contamination with air is weakly visible at 28 u (nitrogen) and 32 u (oxygen). This suggest a leak in the gas supply line of the molecular beam.

The following takes a deeper look at the fragment groups just mentioned. In order to determine any momentum or energy distribution of the ions, one has to assign a mass to a particular time window of the time-of-flight spectrum. Unfortunately, the groups CH_x and C_2H_x consist of a high number of peaks which makes an assignment difficult. In contrast, the group C_3H_x at 6200 ns has a symmetric shape. This leads to the assumption that this peak contains only one species, which is also supported by the mass spectrum measured by Boguslavskiy *et al.* (see fig. 4.2). Figure 4.4 depicts the impact position of detected C_3H_3 ions at the detector (lower plots) at different time windows as indicated in the upper plot. The impact position corresponds to the momentum or velocity in the plane of the detector (see sec. 2.3.5). The different time windows reveal two different velocity distributions. A first contribution that has a low in-plane velocity distribution at the wings of the time-of-flight distribution (fig. 4.4b). When moving the time window towards the centre peak in the time-of-flight spectrum, the corresponding in plane velocity expands in a concentric ring and shrinks again moving the time window towards the other wing of the time-of-flight distribution. When the time window is close to the centre of the time-of-flight spectrum a second in-plane velocity distribution shows up at x≈ 10 mm and y≈ 0 mm. This second in-plane velocity distributions shows almost no expansion. Both contributions have an isotopic distribution. The position plots d-f show a further signal that is displaced by an

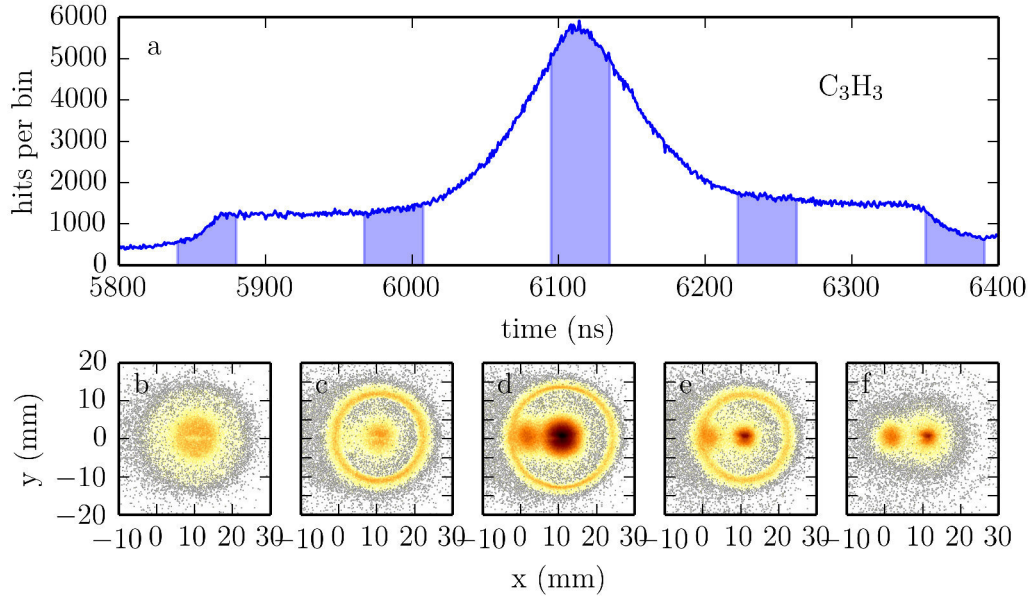

Figure 4.4: In-plane velocity distribution for different time windows of the TOF spectrum. The different time windows are marked by blue shaded stripes. The corresponding position plots (b-f) are plotted on a logarithmic color scale with dark meaning high value and bright meaning a low value.

offset from the centre of both contributions mentioned before. This signal is background gas contribution since it is located at x=0 mm and y=0 mm.

Fig. 4.5 shows the kinetic energy for ions detected in the time range of 5800 ns to 6400 ns using the mass of $C_3H_3^+$. The energy is given by $p^2/2m$ using the detected three-dimensional momentum of the ions. The distribution reveals two peaks at 0.05 eV and at 0.95 eV, respectively. This energy distribution shows the kinetic energy of the single fragment $C_3H_3^+$ which obviously originates in the fragmentation of $C_4H_6^q$ to $C_3H_3^{q'}$ and $CH_3^{q''}$. q specifies the charge state of the particular ion. The total energy release, which is the total energy that is released in the fragmentation, is shared by all fragments. The share in energy obeys momentum and energy conservation. This means that the $C_3H_3^+$-fragment has a about one fourth of the total energy. Three fourth are transferred to the CH_3^+-fragment.

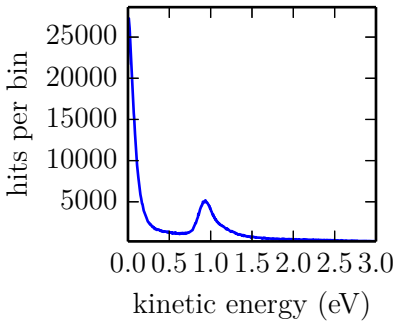

Figure 4.5: Kinetic energy distribution of C_3H_3 ions.

To support the assumption that the wings of the time-of-flight peak are not produced by a superposition of many small peaks of subsequent masses instead of a single mass, a simple simulation was performed additionally. The simulation uses the equation of motion of a

charged particle (see section 2.3.5) in an electric field with two different energy distributions corresponding to the observed energy distributions of fig. 4.5. The results shown in fig. 4.6 clearly reproduce the experimental results quite well. This is a strong indication that the assumption above is valid.

The energy distribution of fig. 4.5 suggests that two different processes exist producing fragments with different kinetic energies. The low energetic part belongs to unimolecular fragmentation that results in a low kinetic energy release due to its statistical character [119]. The appearance of doubly charged butadiene let assume that the high kinetic energy part belongs to fragments originating from the fragmentation of doubly charged butadiene due to Coulomb repulsion. Details will be discussed in a later section. The broad pedestal of the peak groups C_1H_x and C_2H_x hints also to sharp energy distribution at elevated kinetic energies for fragments of these peaks and therefore caused by Coulomb repulsion.

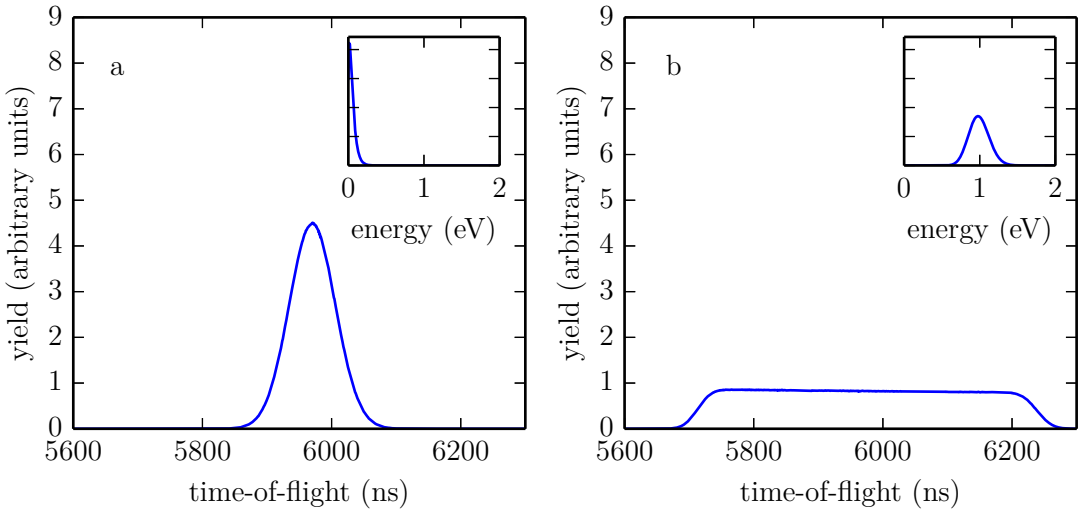

Figure 4.6: Simulated time-of-flight spectra of C_3H_3 fragments using different kinetic energy distributions.
(a) Low kinetic energies produce a narrow peak in the time-of-flight spectrum.
(b) Higher kinetic energies produce a flat plateau-like peak over a large time interval.

Fragmentation Axis of Singly Charged Butadiene

Although figure 4.4 already hints towards an isotropic angular distribution, one can look at the angular distribution of the recoil axis of the fragmentation. This can verify whether the fragmentation happens fast. From the paper of Mikosch *et al.* [125] it is known that the probability to ionize butadiene is twice as high if the laser polarization is parallel to the molecular axis than perpendicular to it. Hence, molecules aligned parallel to the laser polarization axis are ionized more preferentially. If the fragmentation process happens fast, one would expect to see this preference also in the distribution of the recoil axis.

The angular distribution of the recoil axis is determined by calculating the polar angle θ from the momentum vector of the detected fragment. The polar angle is the angle with respect to the z-axis. Since the laser polarization is aligned along the z-axis of the coordinate system, the polar angle coincides with the angle with respect to the laser axis.

Figure 4.7 shows the angular distribution determined from the momenta of C_3H_3 ions with a kinetic energy corresponding to the fragmentation of the singly charged butadiene($E < 0.5\,eV$). Since the polar angle θ ranges from 0° to 180°, the distribution has been mirrored along the horizontal axis. The distribution is isotropic, which verifies the assumption of a statistically driven fragmentation of the singly charged butadiene. Due to the long timescale of the fragmentation, the molecule will rotate prior to fragmentation, which spoils the alignment caused by the selective excitation.

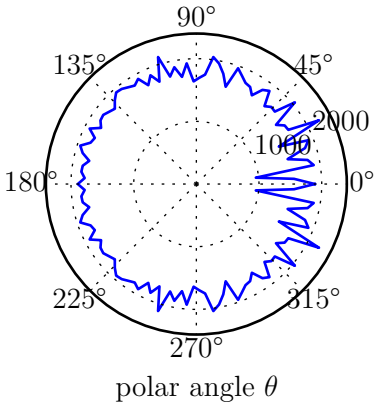

Figure 4.7: Angular distribution of the momentum vector for detected C_3H_3-fragments.

Time-of-Flight of n-Butane

Figure 4.8 shows the time-of-flight for the strong field ionization of n-butane on a linear scale. The highest peak corresponds to the parent ion of n-butane. Also for n-butane three fragment groups with one, two and three carbon atoms and a different number of hydrogen atoms can be distinguished. But this time they are already visible on a linear scale implying a higher fragmentation rate.

The molecular beam contaminations like water, air, hydrogen seen in the butadiene data can be identified as well. Ghost peaks also show up at 2400 ns and 4900 ns. The natural abundance of ^{13}C in n-butane is reproduced by the data as well. With four carbon atoms, n-butane has the same isotopic distribution as butadiene.

In the mass spectrum, a doubly charged parent ion species does not appear. According to quantum chemical calculation done by H.H. Ritze, the doubly charge butane is unstable and fragment by Coulomb explosion [126].

Ion-Ion Correlations

An ion-ion correlation plot depicting the time-of-flight of a first ion versus the time-of-flight of a second ion detected in the same event will reveal any two particle correlation present. Figure 4.9 depicts the ion-ion correlation for butadiene on a linear and logarithmic scale separated along the diagonal of the plot. Before the correlations found in the measurements of butadiene and butane are described in detail, some general features of what can be seen in an ion-ion correlation plot are discussed using fig. 4.9. A fragmentation process producing two charged fragments with a particular energy released in the fragmentation is seen as a narrow line in the correlation map, since the release energy of a fragmentation process is shared among both fragments formed in this process. At the same time, the momenta of all fragments have to obey momentum conservation. Hence, in the case of the fragmentation of

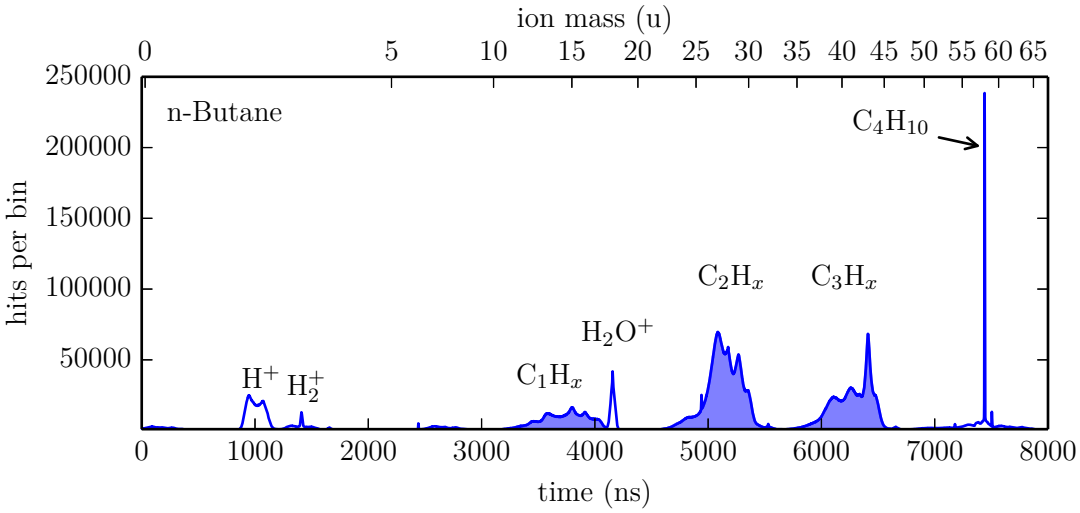

Figure 4.8: Time-of-flight spectrum of strong field ionization of n-butane. n-butane shows a higher rate of fragmentation than butadiene, but it shows the same three fragmentation groups. For details see text

a doubly or higher charged molecule leading to two charged fragments, the time-of-flight of both fragments are correlated via eq. 2.63 and momentum conservation, which causes a narrow line in an ion-ion correlation plot. The slope of the lines is determined by the (negative) charge ratio of both fragments[1]. These narrow lines are clearly visible in the figure as for example in the regions marked I and II.

If the fragmentation process produces three fragments with at least two being charged, additional lines parallel to the narrow lines show up in the ion-ion correlation map. These lines are more diffuse and shifted towards smaller times. The diffuseness is caused by the third particle. The third fragment carries some unknown momentum, which leads to an uncertainty in the momenta of the other fragments. Since three particles are involved, the individual fragments are lighter than in the case of a fragmentation into two particles. Hence, the diffuse lines appear at a smaller time-of-flight. This is visible in the plots b and c of fig. 4.9 marked with an asterisk.

The last features typically visible in ion-ion correlation plots are signals produced due to remaining false coincidences. They can be divided into two appearances. The first is the appearance of straight lines (vertically and horizontally), which appear at times of strong mass peaks of the time-of-flight spectrum due to random correlations with background or noise hits as for example visible at the time-of-flight of 4150 ns corresponding to water or at 7200 ns corresponding to the parent ion. The second type of false coincidences is the correlation between fragments which emerged from fragmentation of two different molecules in the same event. In this way there is no correlation between the time-of-flight of both

1 This relation neglects the influence of the root in eq.2.63 and is based on eq. 2.65 instead.

fragments. The large diffuse areas therefore cover the time ranges of both fragments involved. This can be seen for example at a time-of-flight range of 4800 ns to 5500 ns for the first ion and 3000 ns to 4000 ns for the second ion.

On the linear scale in fig. 4.9, two main correlation lines can be seen. On logarithmic scale, a few more lines are visible. In order to assign the correlation lines to particular fragmentation processes, a simple calculation has been performed: In a first step, the masses of the two fragments have been chosen requiring that the sum of both masses yields the mass of the parent ion. The maximum energy of one of the fragments was retrieved from the energy plot as in fig. 4.5. From this energy the absolute value of the total momentum of the fragment is calculated by

$$|\vec{p}| = \sqrt{2Em} \tag{4.2}$$

The momentum of the second fragment is given by momentum conservation. With eq. 2.63, one obtains the time-of-flight of both fragments. As seen by this equation, the time-of-flight depends only on the z-component of the momentum. The isotropic angular distribution of the fragmentation axis seen in fig. 4.4 and fig. 4.7 means that the z-component of the momentum varies from a negative maximum value to the positive maximum value, since a fragmentation perpendicular to the spectrometer axis will have no initial momentum along the spectrometer axis and a parallel fragmentation will have an initial momentum corresponding to the maximum energy. To account for this, the initial kinetic energy used to calculate the time-of-flight was varied from zero to the chosen maximum value in the range of 1 eV to 3 eV. The time-of-flight is then calculated for the corresponding negative and positive momentum. The results of this calculation are shown in the plots c and b of figures 4.9 and 4.10 by blue lines. It is important to note, that the calculation reproduces only the times of the ion-ion correlation but not the actual distribution. From this calculation the fragmentation channels of the main contribution has been determined to:

$$\begin{aligned} &1) \quad C_4H_6^{++} \Rightarrow C_2H_3^+ + C_2H_3^+ \\ &2) \quad C_4H_6^{++} \Rightarrow CH_3^+ + C_3H_3^+ \end{aligned} \tag{4.3}$$

The weaker lines only visible on logarithmic scale have been assigned to:

$$\begin{aligned} &3) \quad C_4H_6^{++} \Rightarrow CH_2^+ + C_3H_4^+ \\ &4) \quad {}^{13}C^{12}C_3H_6^{++} \Rightarrow {}^{13}C^{12}CH_3^+ + {}^{12}C_2H_3^+ \\ &5) \quad {}^{13}C^{12}C_3H_6^{++} \Rightarrow {}^{13}CH_2^+ + {}^{12}C_3H_4^+ \\ &6) \quad {}^{13}C^{12}C_3H_6^{++} \Rightarrow {}^{13}CH_3^+ + {}^{12}C_3H_3^+ \\ &7) \quad {}^{13}C^{12}C_3H_6^{++} \Rightarrow {}^{12}CH_3^+ + {}^{13}C^{12}C_2H_3^+ \end{aligned} \tag{4.4}$$

The correlation lines at 5000 ns (1st ion) and 3500 ns (2nd ion) belong to two fragments with mass 27 u, but one fragment is doubly charged, emerging from the fragmentation of triply charged butadiene. The correlation lines at 4300 ns (1st ion) and 3500 ns (2nd ion)

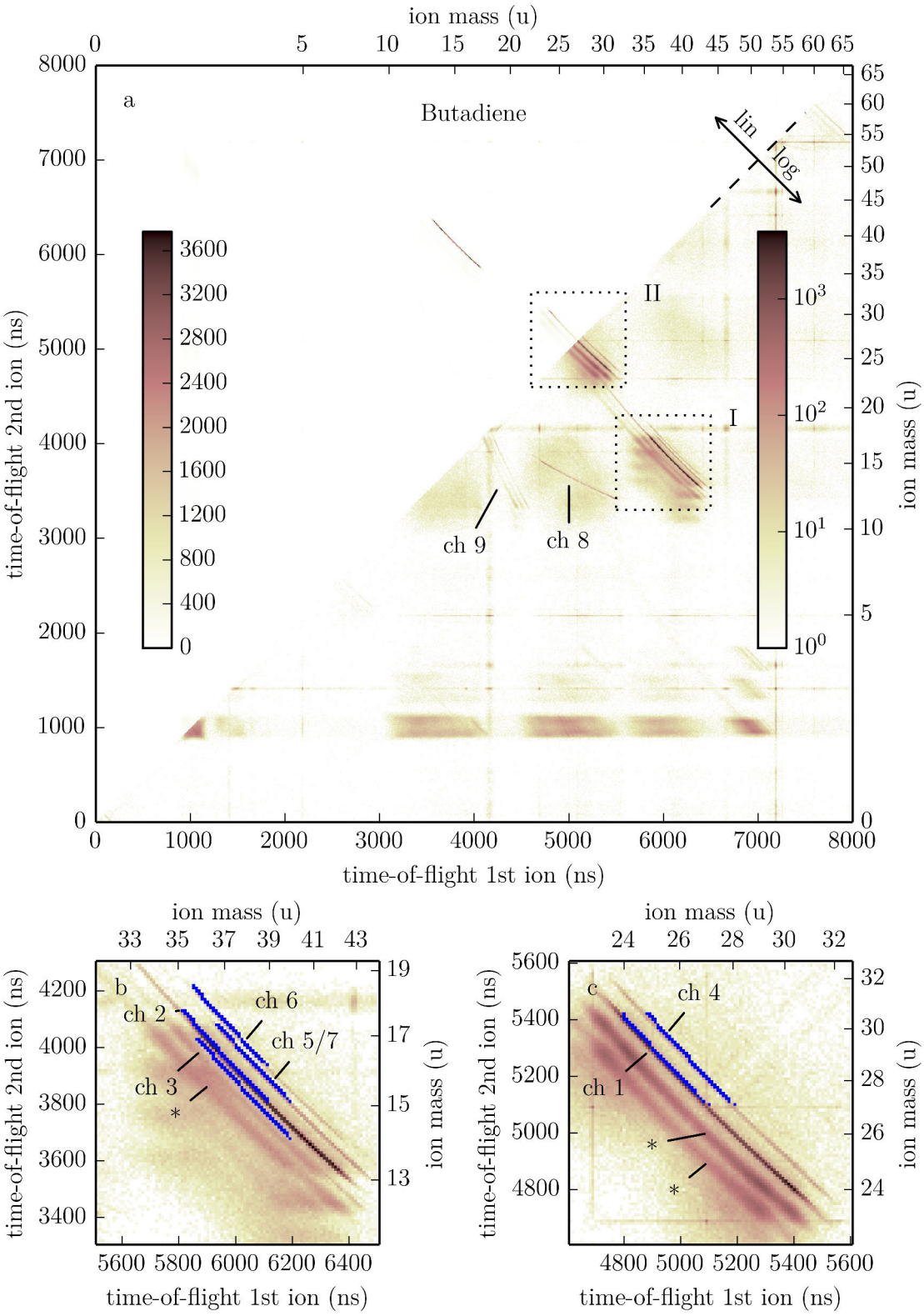

Figure 4.9: Time-of-flight correlation for butadiene.
(a) Overview: the upper triangle shows the correlation on a linear scale. The lower triangle uses a logarithmic scale.
(b) magnification of region I (logarithmic scale): The calculated correlations (blue) are superimposed with the measured correlations. To maintain the visibility of the measured data, each calculated correlations is drawn only partially (see text). Fragmentation channels 2, 3, 5, 6 and 7 are shown. Channel 5 and 7 cannot be distinguished due to the same mass ratio.
(c) magnification of region II (logarithmic scale): It shows the fragmentation channels 1 and 4 of doubly charged butadiene.

corresponds to the fragmentation into singly charged CH_3 (mass 15 u) and doubly charged C_3H_3 (mass 39 u) and their isotopes:

$$\begin{aligned} 8) \quad & C_4H_6^{3+} \Rightarrow C_2H_3^+ + C_2H_3^{++} \\ 9) \quad & C_4H_6^{3+} \Rightarrow CH_3^+ + C_3H_3^{++} \end{aligned} \tag{4.5}$$

Although doubly charged n-butane is not visible in the time-of-flight spectrum, the correlation map of n-butane, depicted in fig. 4.10, reveals its formation in the strong field ionization. On linear scale two main lines are visible, which correspond to the following channels:

$$\begin{aligned} 1) \quad & C_4H_{10}^{++} \Rightarrow C_2H_5^+ + C_2H_5^+ \\ 2) \quad & C_4H_{10}^{++} \Rightarrow C_1H_3^+ + C_3H_7^+ \end{aligned} \tag{4.6}$$

The logarithmic scale shows only one additional narrow line corresponding to the fragmentation of the n-butane isotope with one ^{13}C.

$$3) \quad {}^{13}C^{12}C_3H_{10}^{++} \Rightarrow {}^{13}C^{12}CH_5^+ + {}^{12}C_2H_5^+ \tag{4.7}$$

All remaining correlation lines are much more diffuse than channel 1 to 3 indicating a third particle to be involved. The broad lines parallel to channel 1 shown in fig. 4.10c correspond to a symmetric fragmentation into two charged C_2H_5 molecules that additionally lost atomic or molecular hydrogen during the fragmentation. The same applies for the broad parallel lines in fig. 4.10b but with different masses. Here it is CH_3 and C_3H_7 that also lose hydrogen during fragmentation.

The strong contribution at times of 3800 ns (1st ion) and 5100 ns (2nd ion) seems to stem also from a fragmentation that involves more than two fragments since it has a broad shape. The slope of these lines is $-\frac{2}{3}$ implying a charge ratio of 2:3. The time-of-flights at the centre of these lines correspond to masses 15 u and 28 u and 15 u and 27 u, respectively. In combination with the charge ratio, one can determine the real masses of the detected ions to 30 u and 84 u or 81 u, respectively. The sum of the retrieved masses gives 114 u and 111 u. These masses correspond to C_8H_{18} (octane) and C_8H_{11}. Since the correlation distribution is broad, the fragments stem from complexes with a slightly higher mass. One could think of a butane dimer (mass of 116 u) which is highly ionized and fragments into at least three fragments containing the two detected. Unfortunately, the time window chosen for the time-of-flight spectrum during data acquisition ended at 10000 ns corresponding to a mass of 104 u. Therefore, it is not possible to check, what high mass molecules have been present during the measurement. Finally, also false coincidence correlations of strong contributions show up as vertical and horizontal lines.

Coming back to butadiene, the fragmentation channels observed reveal an interesting process. The molecular structure of butadiene, shown in fig. 4.12, suggests two main

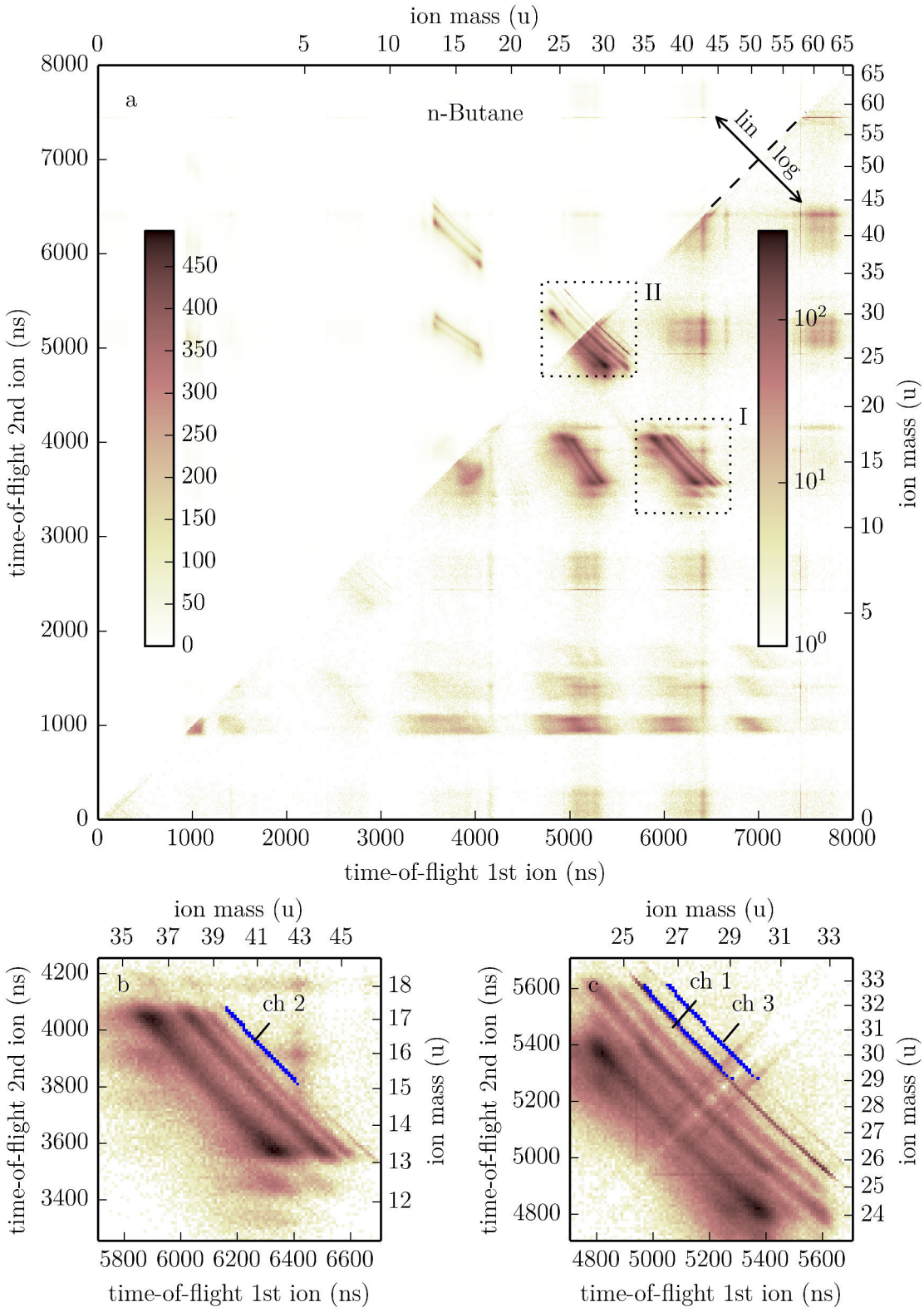

Figure 4.10: Time-of-flight correlation of n-butane:
(a) Overview: the upper triangle shows the correlation on a linear scale. The lower triangle uses a logarithmic scale.
(b) magnification of region I (logarithmic scale): The calculated correlations(blue) are superimposed with the measured correlations. To maintain the visibility of the measured data, each calculated correlations is drawn only partially (see text). To maintain the visibility of the measured data the calculated correlations are only drawn into one direction. Fragmentation channel 2 is shown.
(c) magnification of region II (logarithmic scale): It shows the fragmentation channels 1 and 3 of doubly charged n-butane.

fragmentation channels: Considering a bond breakage only at a bond between two carbon atoms, one would expect to see, for example in the case of butadiene, mainly three different fragments: CH_2,C_2H_3 and C_3H_4. But since a major fraction ends up in fragment C_3H_3, a hydrogen atom must move from one to the other fragment during the break up. This is also described in [124].

The doubly charged fragmentation process explains the observed kinetic energy distribution of the fragments exemplary shown for C_3H_3 in fig. 4.5. The low energetic fraction stems from uni-molecular fragmentation of a single charged ion leading to just a low kinetic energy release. In the case of the doubly (or even triply) charged molecule the fragmentation process might be also statistically driven as in uni-molecular fragmentation. However, after breakage of the bond two particles with the same charge exist close to each other. Hence, they repel each other leading to higher kinetic energy. This Coulomb explosion could also proceed via a completely repulsive state that is populated after ionization. A repulsive state would cause a fast fragmentation. This fast fragmentation after ionization would mean that the atoms of the molecules have no time to rearrange to the new electronic configuration. A fragmentation via a long-lived state would allow this. Assuming that both fragments can be simplified as point charges, one can calculate the distance between them by using the potential energy of two point charges:

$$E(r) = \frac{1}{4\pi\varepsilon_0}\frac{q_1 \cdot q_2}{r} \tag{4.8}$$

with ε_0 the vacuum permittivity, q_i the charge of the point charge i and r the distance between both charges.

If both charges have the same sign, they will repel each other and the potential energy is completely converted into kinetic energy in the limit of an infinite distance between both

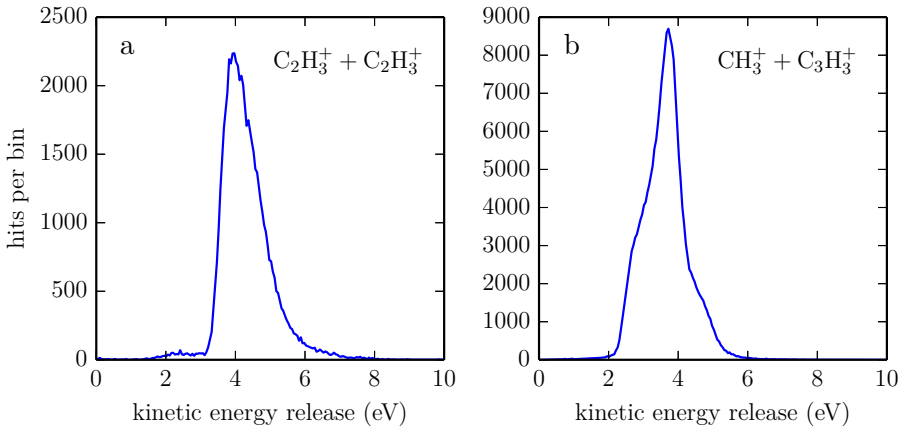

Figure 4.11: Histograms of the total kinetic energy release for channel 1 and 2 of butadiene. The histograms show the sum of the individual kinetic energies of two simultaneous detected ions as labelled.

charges. That is the case when the particles are registered at the detector. Figure 4.11 shows the distribution of the kinetic energy release for the fragmentation channel 1 and channel 2 (see eq. 4.3) of butadiene. The total kinetic energy release is calculated by the sum of the individual kinetic energies of both fragments determined from the measured momenta.

One can see a peak at 4.1 eV for channel 1, which corresponds to a distance of the fragments according to the Coulomb equation (eq. 4.8) of 351 pm at the beginning of fragmentation. The peak at 3.8 eV for channel 2 corresponds to a distance of 379 pm. As shown in fig. 4.12, these lengths correspond roughly to the distance between the outermost carbon atoms. It means that the atoms of the molecule have rearranged before the Coulomb repulsion drives the fragmentation. This lets assume a doubly charged precursor state that has finite fragmentation barrier. Theoretical calculations in [124] support this interpretation. By using density functional theory [128], Xu *et al.* calculated the potential energy curve for different fragmentation channels of doubly charged butadiene. Figure 4.13 shows the potential energy curve for the fragmentation leading to $C_3H_3^+$ and $C_1H_3^+$ with r the reaction coordinate corresponding to the distance between the outermost carbon atom and the neighbouring carbon atom. The potential curve has a barrier approximately at a distance that matches the calculated value of above.

4.2.2 Photoelectron Spectra

So far only the information of the ion data has been considered. The following section will treat the spectra of the photoelectrons and the ion-electron correlation.

In fig. 4.14 the kinetic energy distribution of photoelectrons in coincidence with the detection of the parent ion of butadiene is shown. It reveals, as mentioned in the beginning of this chapter, that with these short pulses no ATI structure can be seen.

Hence, it is necessary to look at the angular distribution to see differences in the electron distributions between different fragmentation channels. Figure 4.15 depicts these angularly resolved electron spectra for butadiene. Due to the possibility of singly and doubly charged fragmentation, one has to filter theses processes. This can be done by selecting a part of the kinetic energy distribution of the considered fragments. The data presented in fig 4.15 uses only events in which the ionic fragment has a kinetic energy below 0.5 eV, which is correlated to fragmentation of singly charged butadiene[1] (compare fig. 4.5). Furthermore, only for the fragment channel with the fragment $C_3H_3^+$ of butadiene it is possible to assign a single mass. For channels involving fragments of the CH_x and C_2H_x groups in the case of butadiene and for all fragment groups of butane, it is difficult to resolve unambiguously the corresponding channel due to the overlap of the time-of-flight spectra. One could in principle also try to separate the masses due to the different impact position on the detector in x-direction. However, due to the velocity spread of the molecular beam, fragments with a mass difference of one or two atomic mass units will still overlap substantially. Therefore, the angular resolved electron spectra have been filled only differentiating between the individual

1 It is not sufficient to choose only events with one detected ion since the detector could miss one particle in a doubly charged fragmentation event.

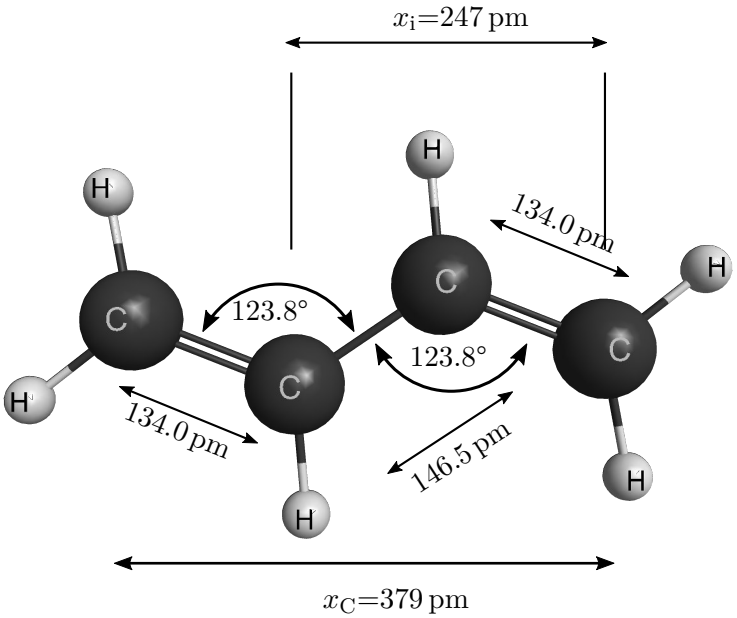

Figure 4.12: Bond lengths and angles of butadiene from [127].x_i denotes the length between the outermost carbon atom and the second next carbon atom in neutral butadiene. x_C denotes the same distance calculated from eq. 4.8 using the total kinetic energy release seen in fig. 4.11b. This means that the Coulomb repulsion starts at a distance larger than the equilibrium distance of the neutral molecule.

fragment groups CH_x, C_2H_x, CH_x and the parent ions. Figure 4.16 depicts these angularly resolved electron spectra for butane.

All plots (for butadiene and butane) show a much more diffuse distribution than the momentum maps of argon in the previous chapter. The momentum map of butane has a more distinct distribution than that of butadiene. In contrast to atoms, the spatial extent of molecules can not be neglected. The distribution seen in an angularly resolved electron spectrum from ionization of molecules depends in general on the orientation of the molecule with respect to the laser polarization axis. Since the molecules have an isotropic distribution, the electron spectra are an average of different orientations.

The difference in blur of the momentum maps for butadiene and butane can be explained by the different bonds in both molecules. Butadiene has two double bonds (see fig.4.12), which form a conjugated system. Hence, the electrons of this π-bond are delocalized over the whole molecule of butadiene, whereas butane has electrons more localized due to the σ-bonds.

All distributions show also a fan-like structure. If one would mirror the distribution along the axis of the parallel momentum, it will resemble the body and the legs of a spider and is therefore in the following referred to as the 'spider structure'. Huismans *et al.* [129] have seen the spider structure for electron momenta up to $2U_p$. They interpreted them

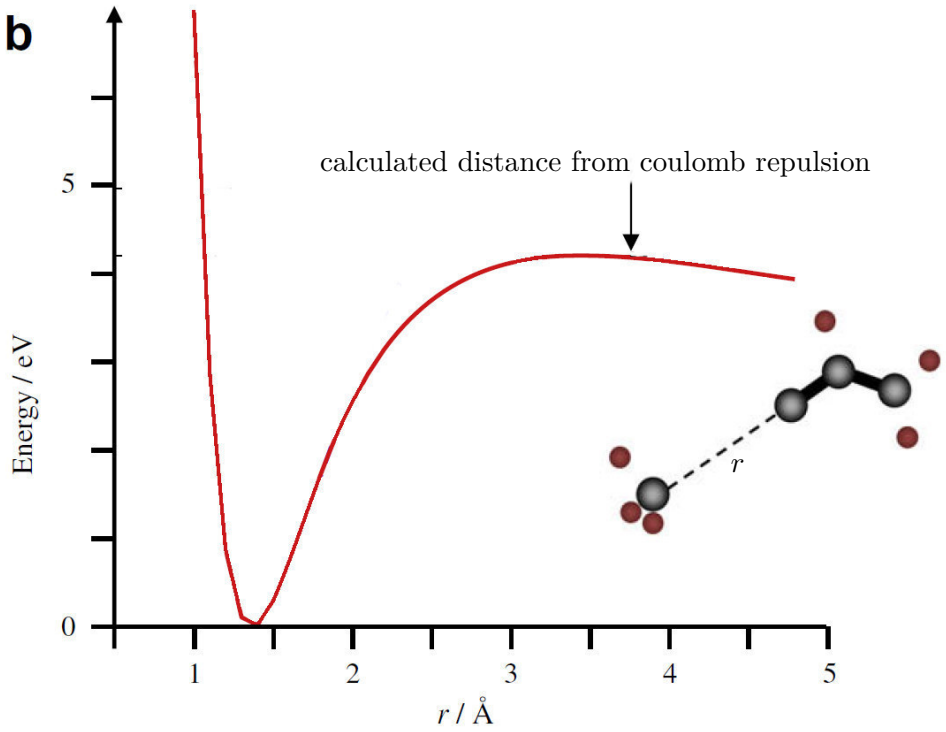

Figure 4.13: Potential energy curve of the doubly charged butadiene for the reaction coordinate along the bond of the outermost carbon atom and its neighbouring carbon atom. Adapted from [124].

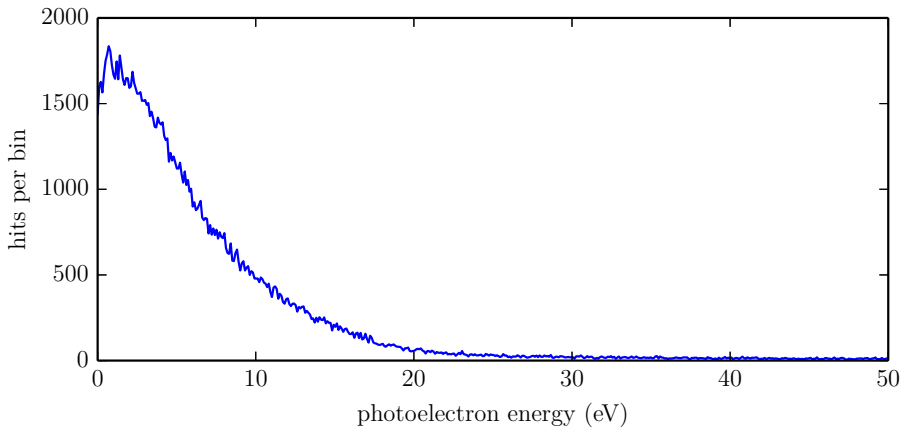

Figure 4.14: Kinetic energy distribution of photoelectrons detected with the parent ion of butadiene. No ATI peaks are visible due to CEP averaging.

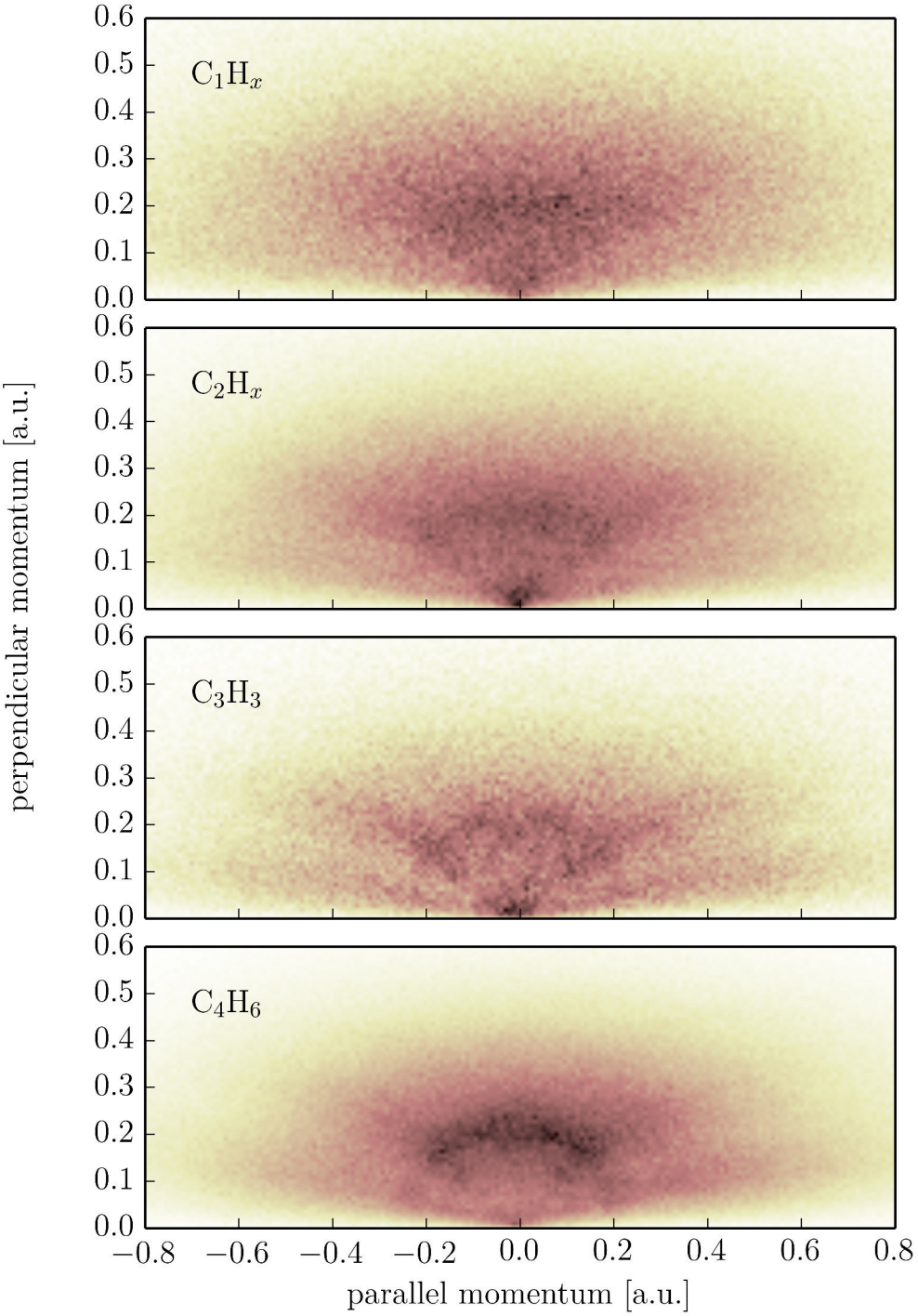

Figure 4.15: Channel-resolved momentum maps of the strong field ionization of butadiene: The label in the upper left corner of each plot indicates the fragment that has been detected in coincidence with the photoelectron. For details see text.

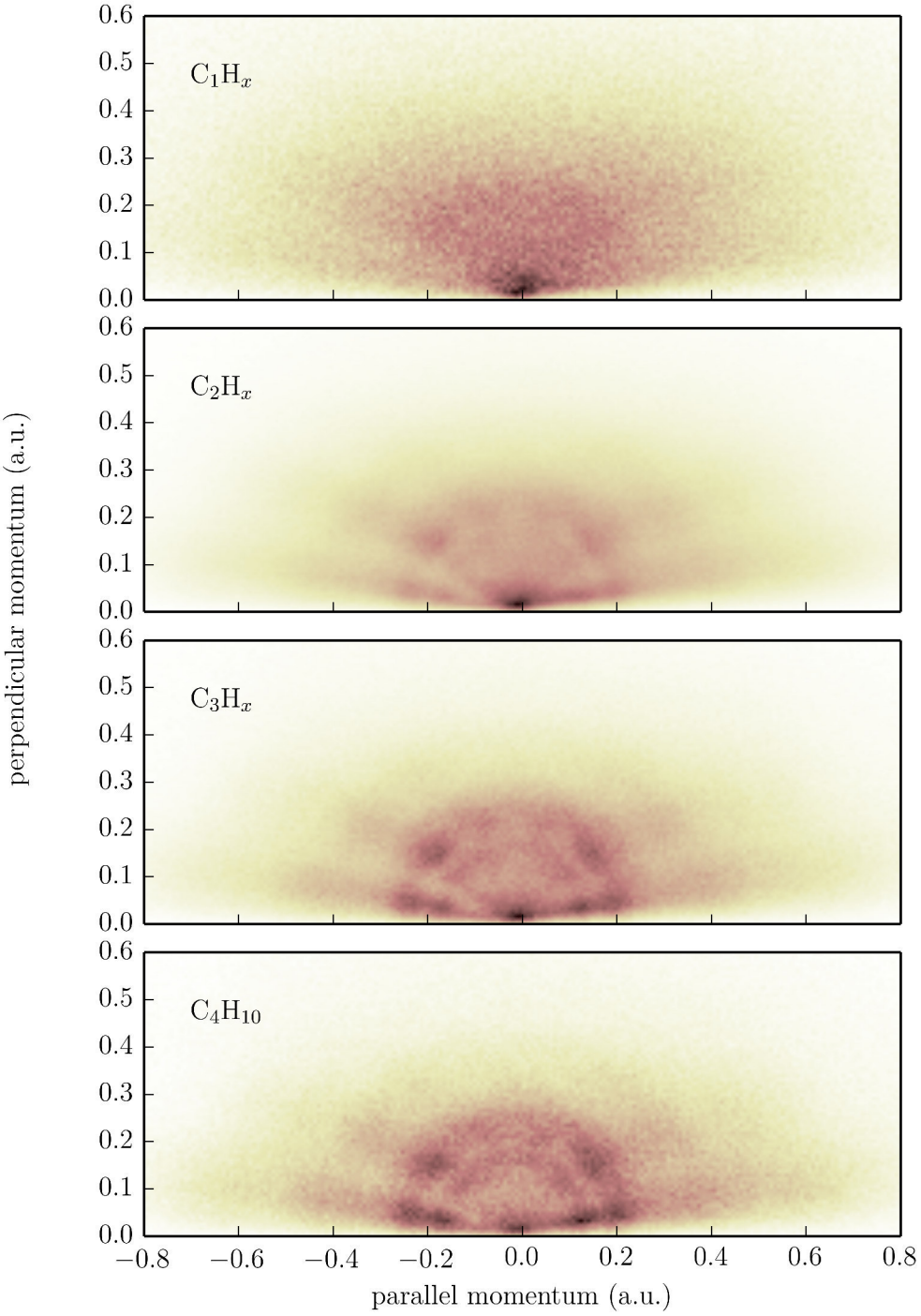

Figure 4.16: Photo-electron momentum map of the strong field ionization of butane: The label in the upper left corner of each plot indicates the fragment that has been detected in coincidence with the photoelectron. For details see text.

as an interference between electrons driven by the laser field recolliding with the ion and those not recolliding. Hickstein *et al.* [130] have observed an additional spider structure at momenta reaching only a small fraction ($\sim \frac{1}{5}$) of U_p. They explained the structure also as an interference between electrons scattered and non-scattered at the ion, but now these electrons have revisited the ion several times before leaving the vicinity of the ion. Their plane-spherical wave (PSW) model introduced in [130] treats the revisiting electron as a plane wave and the scattered electron as a spherical wave. These two waves will interfere at the detector. The phase of the electron determining the interference is given by $e^{-iS/\hbar}$ in the Lewenstein model [131]. S is the quasiclassical action:

$$S(p,t,t_b) = \int_{t_b}^{t} \left(\frac{p(t')^2}{2m_e} + IP \right) dt' \tag{4.9}$$

A result of the PSW model from [130] is shown in fig. 4.17. The intensity and wavelength used in the experiment presented in this thesis give an U_p of 0.33 a.u.. $2U_p$ then corresponds to an energy of 0.66 a.u. which correspond to a momentum of 1.15 a.u.. One fifth of U_p is 0.066 a.u.. The corresponding momentum amounts to 0.36 a.u.. It is not clear to what regime the observed structure belongs to. The lobes as seen for instance in figure 4.15 reach up to a momentum of 0.6 a.u.. Additionally to the spider structure, all distributions have a broad ring with a constant total momentum of $p \approx 0.2$ a.u.. In the case of butane, one additional ring is visible at 0.3 a.u.. The source of the rings is not clear. The energy difference is 0.68 eV, which means that they are not related to an ATI structure. One could think of Freeman resonances leading to the rings observed. However, they show up in the electron spectra accompanying the parent ion of Butane and the fragments C_2H_x and C_3H_x at the same position. At least the parent ion channel and a fragment channel correspond to different ionic states. The Rydberg series for these different ionic states are most probably different. Therefore, one would expect to see a shift of the rings in the electron spectra for the parent ion channel and a fragment channel. In addition, as discussed in the context of the strong field ionization of argon, Freeman resonances are not expected with few-cycle pulses. Another possibility is a coherent excitation of a few ionic states of butane. The energy difference between the IP of the ionic ground state and the first two excited ionic states is ~ 0.2 eV (from [132]). The bandwidth of the laser pulses is ~ 0.26 eV, which covers this energy difference and should allow a coherent coupling.

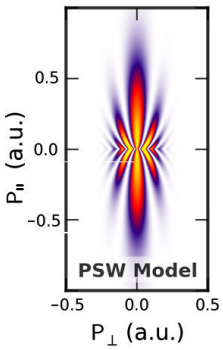

Figure 4.17: Calculation of the PSW model from [130]. For details see text.

The distributions also show an enhanced contribution at low momenta (parallel and perpendicular momentum ~ 0 a.u.). This contribution could stem from field ionization of highly excited neutral states due to the high extraction field of the spectrometer [133]. By comparing with the applied extraction field, one can estimate the minimal quantum number

n of the Rydberg state, which is still field ionized, by [134]:

$$F_{crit} = 6 \cdot 10^8 / n^4 [\mathrm{V/cm}] \tag{4.10}$$

With the applied field of 34 V/cm, the minimal quantum number n is 65. Due to the high number of n the ionization energy of the corresponding Rydberg state can be estimated by the coarse-energy level of hydrogen:

$$E_n = -\frac{13.6}{n^2} \tag{4.11}$$

The energy level for $n = 65$ is 3 meV, which is the maximal energy observable by field ionization in this case. The distribution peak at 0.02 a.u. of momentum. This corresponds to an energy of 5 meV.

Another possibility are so-called low energy structures (LES). LES have been observed the first time by Blaga *et al.* [135] at several eV in the strong field ionization of rare gases and small molecules. Wu *et al.* [136] have observed structures at energies below 1 eV and have called them very low energy structures (VLES). These structures have been attributed to long-range Coulomb effects and forward scattering. However, in the experiment of this chapter, the momentum resolution does not allow to resolve the low energetic part of the spectrum.

Coming back to the question if the direct ionization into excited states of the ion by strong field ionization can also be seen with few-cycle laser pulses, one has to compare the momentum maps for different channels. One might already see slight differences between the channels C_3H_3 and C_4H_6 in theses plots, but theses differences appear more obvious by plotting the difference of the spectra between parent ion and its fragments. Prior to this each spectrum was normalized since the absolute number of hits of each channel varies. Figure 4.18 depicts the difference plots. The fragment channel clearly differs from the parent ion. This is a clear evidence that the strong field ionization directly populates excited ionic states.

As done in section 4.2.1, one could use the three dimensional momentum information of the ions to retrieve the electron spectra in the molecular frame or for different orientations of the molecule with respect to the laser polarization. Although it is not expected to work for the presented data as explained also in section 4.2.1, it will, nevertheless, prove differently the long timescale of the fragmentation. Fig. 4.20 shows the electron spectra for the C_3H_3 fragmentation channel of butadiene for different directions of the detected ions. The energy of the ions is again restricted to be below 0.5 eV to select the fragmentation of singly charged butadiene. Fig. 4.20a depicts the electron spectrum for ions that have a momentum parallel to the polarization axis of the laser within a cone of 22.5°. Fig. 4.20b shows the electron spectrum for ions perpendicular to the polarization axis also within angle of 22.5°. Both figures show the same distribution, which confirms the findings of section 4.2.1.

Up to now, the momentum maps presented belong to the fragmentation of singly charged butadiene. But, the same investigation of the momentum maps can be done for the doubly charged fragmentation as well. Here, one can take advantage of the ion-ion correlation that not only allows to filter for events of doubly charged fragmentation but also allow to filter for

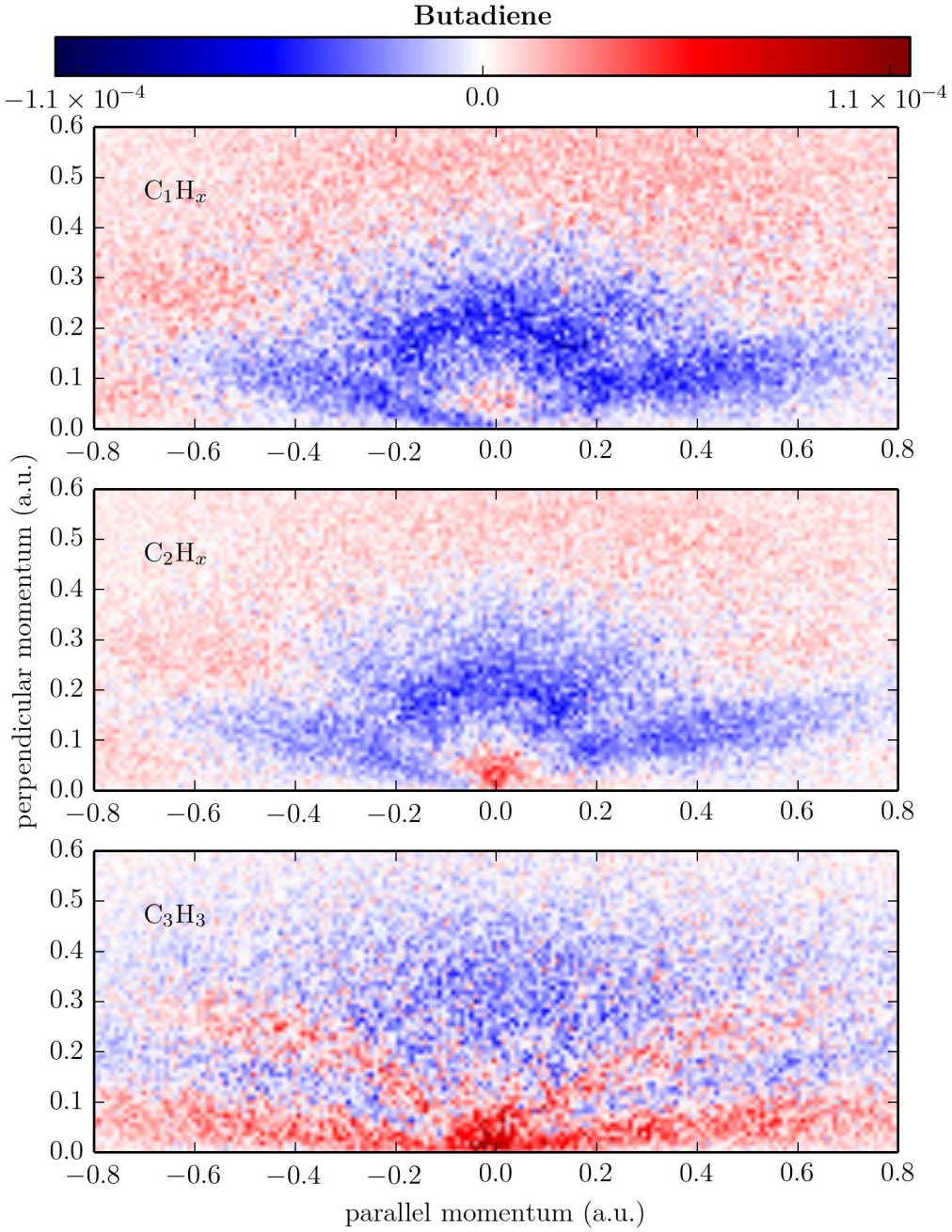

Figure 4.18: Difference of the electron momentum maps of fragment channels as labelled and the momentum map of the parent ion for butadiene. Prior to subtraction the distributions have been normalized. It shows distinct differences map indicating different final states after strong field ionization.

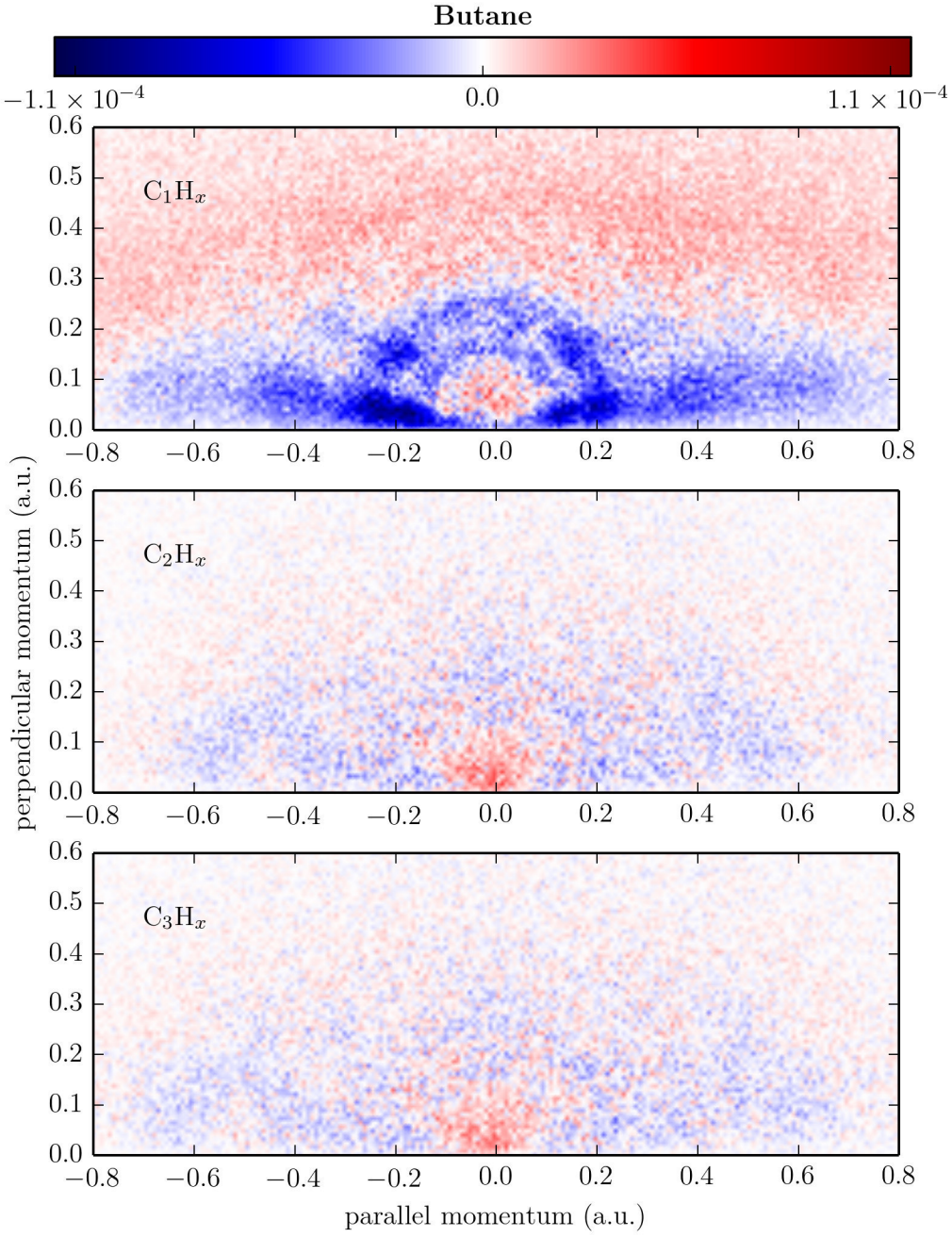

Figure 4.19: Difference of electron momentum maps of each channel with that of the parent ion for butane. Prior to subtraction the distributions have been normalized. Each channels shows a different distribution in its difference map indicating different final states after strong field ionization.

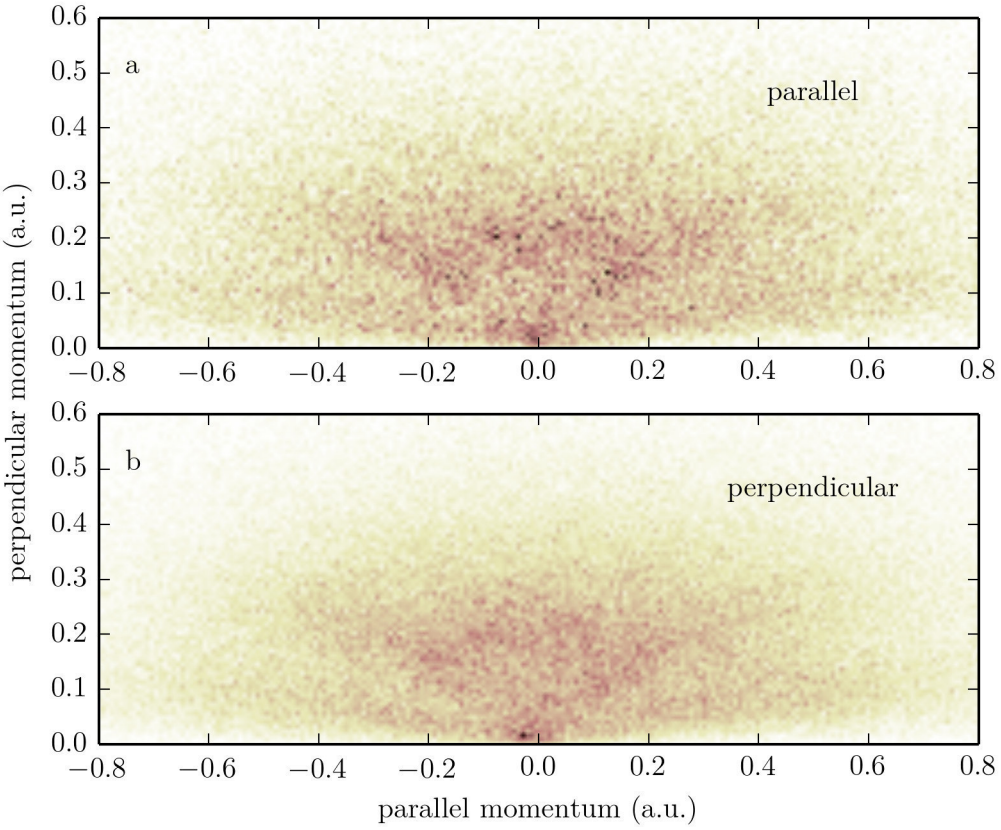

Figure 4.20: Difference of electron momentum maps of each channel with that of the parent ion for butane. Prior to subtraction the distributions have been normalized. Each channels shows a different distribution in its difference map indicating different final states after strong field ionization.

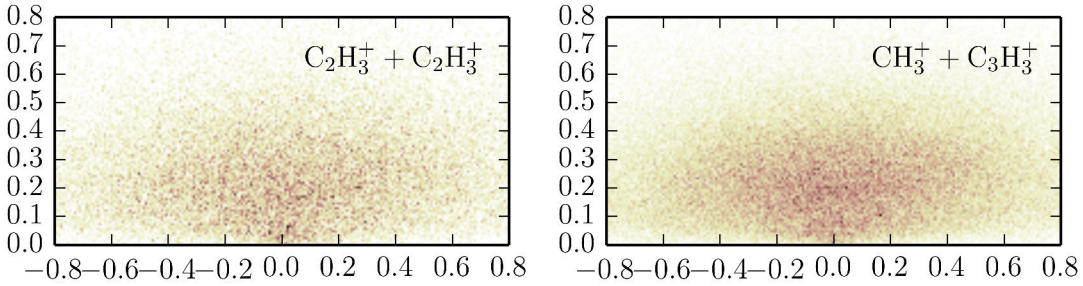

Figure 4.21: Momentum maps of the fragmentation of doubly charged butadiene. The left figure shows the momentum map belonging to the fragmentation channel leading to two $C_2H_3^+$ fragments. The right figure shows the momentum map belonging to the fragmentation channel leading to CH_3^+ and $C_3H_3^+$.

each of the channels. Unfortunately, this reduces the number of events put into a histogram substantially. Therefore, only the result for the two main channels of the fragmentation of butadiene are shown in fig. 4.21. Both distributions look similar except for statistical differences due to the different numbers of events contained in the histograms.

The influence of the post-pulse on the interaction as seen in the previous chapter is uncommented so far. Since the intensity of the post-pulse is a magnitude lower than the main pulse, it is unlikely that the post-pulse will lead to a relevant contribution to the total yield in terms of ionization only due to the post-pulse. Instead one would expect a similar process as for argon. After the interaction with the main pulse probably population in high excited states will be left over. These excited states should be ionized by the post-pulse leading to interference between direct and indirect electrons as well. But as seen in the momentum maps of butadiene and butane this is not visible. Since the number of events used for the momentum maps of butadiene and argon is comparable ($\sim 10^6$), it can be ruled out that any interference pattern is not visible due to statistical fluctuations, which may cover a weak interference pattern. The missing interferences can be explained by a denser excited state distribution in the molecular system than in the atomic system. If the states are energetically close to each other, the interference for each state will overlap in the momentum map. This might lead to a blur of the individual interference paths. But based on the spectra observed no clear statement can be made.

4.3 Summary

In this chapter the strong field ionization of polyatomic molecules with sub-6 fs laser pulses has been investigated using 1,3-butadiene and n-butane as target molecules. The detected fragments emerging from the interaction showed two distinct kinetic energy distributions.

These distributions correspond to two different fragmentation processes of different charge states of the parent ion. The low energetic fragments stem from unimolecular fragmentation of a singly charged ion. In contrast, the high kinetic fragments gained kinetic energy from the Coulomb repulsion when they fragment from a doubly charged ion. The assumption of a doubly charged fragmentation was confirmed by an ion-ion correlation. A calculation supporting the assignment of each observed fragmentation channels identified a process known as proton migration.

The second part of the chapter investigated for the first time channel-resolved and angular resolved electron spectra of SFI of these polyatomic molecules. Since the time-of-flight spectra of the fragments observed in the case of butane overlap strongly, the channels except for the parent ion could not be resolved unambiguously. The momentum maps show a clear difference between different fragmentation channels in the case of butadiene. Hence, it could be shown also with a few-cycle laser pulses that strong field ionization populates directly excited ionic states without sequential excitation.

For a more thorough investigation of the channel and angular resolved momentum maps a higher extraction field would be necessary to separate the fragments more clearly. However, the field required to separate adjacent masses with a kinetic energy as observed in the experiment have to be hundred times higher than applied in the measurement. Such a

high extraction field would spoil any time resolution completely. Hence, one has to find a compromise between channel resolution on one hand and time resolution on the other hand.

The findings of [116], that the SFI into excited states of polyatomic molecules can dominate over the SFI to the ground state, pose the idea that SFI in polyatomic molecules can lead to a laser driven coupling of several electronic states. Theoretical calculations in [116] have shown that the non-adiabatic population of multiple electronic states can make an important contribution to the attosecond molecular response. Shchatsinin *et al.* [137] developed a model that allows one to distinguish SAE excitation from non-adiabatic multi-electron dynamics (NME) by changing the ellipticity. They have shown that, in a case of a excitation purely following SAE, the yield should dependent strongly on the ellipticity whereas a NME process shows only moderate dependence on the ellipticity. Although they have shown this for C_{60}, it might be transferred to smaller polyatomic molecules as 1,3-butadiene and n-butane. To verify this assumption and also investigate experimentally the theoretical findings of [116], one has to repeat the experiment of the present chapter with circularly polarized light.

5 Conclusion and Outlook

In this thesis the potential and benefits of combining a reaction microscope and a high repetition rate OPA-system delivering few-cycle laser pulses to perform strong field ionization experiments has been demonstrated. Due to the high repetition rate, it was possible to measure two-dimensional momentum distributions of photoelectrons from strong field ionization of atoms and polyatomic molecules. In the experiment on strong field ionization of argon intended to check the performance of the setup, a modified version of quantum state holography has been developed theoretically providing the potential to investigate electron dynamics in neutral atoms after strong field excitation. The experiments have shown the capability to measure these distributions for different fragmentation channels simultaneously. It has also been shown, that the setup allows to measure events with a weak probability as triple coincidences in a short time with a sufficient number of counts resulting in low demands on the stability of the entire setup.

These initial experiments have shown that the setup is working properly. Nevertheless, they have also revealed room for further improvement, to be able to use the full capacity of the setup. The xenon measurements(section 3.5.1) revealed the necessity to minimize the dead time of the detectors to increase their multi-hit capacity. This is a prerequisite for future experiments with triple coincidences where e.g. one doubly charged ion and two electrons have to be detected. It will also increase the performance at high ionization rates, since less electrons are lost due to a detection dead time as seen in the SFI of argon by the CPA system (sec. 3.2).

There are also aspects of the OPA system that have to be improved for clean and more sophisticated experiments. A first aspect concerns the purity of the temporal pulse shape. The strong satellite pulses complicate the analysis of any experiment performed. Satellite pulses, especially post pulses, spoil dynamics induced by the main pulse and produce additional contribution to the signal. They are produced by a modulation of the spectral intensity as well as by a non-constant spectral phase. Improving both, leading to a weaker modulation and a more constant phase, will reduce the amount and strength of satellite pulses.

A second aspect concerns the pulse energy. In the experiments with the OPA system presented in the thesis it was not possible to investigate intensity dependent dynamics, because the intensity reached with the available pulse energy was barely enough to ionize the target species. This is addressed by an upgrade of the fibre amplifier which should result in a three times higher pulse energy and is presently pursued in the laboratory. Then, higher intensities will be accessible opening the possibility to perform measurements at different intensities, pump-probe schemes or polarization dependent studies.

By using a different amplifier technique for the pump laser of the NOPA even much higher pulse energies will be accessible. Currently competing technologies are the InnoSlab design [138] and thin-disc amplifiers [139]. Both are also based on Yb-doped materials offering high

average power. This would allow to generate high harmonic radiation at a high repetition rate under reasonable focussing conditions. With this one would be able to do XUV-IR pump probe experiments that give insight into ultrafast dynamics with rich information due to the three dimensional coincidence detection.

Besides technical aspects, the studies presented here led also to new ideas for experiments. The first experiment to be approached is the verification of the quantum state holography presented. As seen from the calculation this experiment will not require a reaction microscope to detect the electrons. A spectrometer providing the kinetic energy distribution of the photoelectrons angularly resolved as e.g. a velocity map imaging spectrometer [140] will be sufficient.

An new experiment, that takes benefit from the reaction microscope and evolves from the measurements on butadiene(chapter 4.1), will investigate the role of multiple strong field ionization channels in laser-driven recollision. Strong field ionization directly leads to different ionic molecular states as described in chapter 4.1. Therefore, one expect to see different contribution to the signal due to recollision as well. To separate these contribution channel-wise the ions have to be detected simultaneously as before, and to separate the scattered from the unscattered electrons one needs also angularly resolved electron spectra. Both is provided by the present reaction microscope. It is expected that the signal due to recollision of different channels behaves differently by changing the ellipticity of the laser pulse.

In summary, although the entire setup is complex and technically difficult, the thesis has shown its potential for SFI experiments. Currently, there is no equivalent technique available providing such rich information obtained in a short period of measurement allowing easily large parameter scans in a coincident measurement.

Bibliography

[1] W. Heisenberg. Quantum-theoretical reinterpretation of kinematic and mechanical connections. *Zeitschrift Fur Physik*, 33:879–893, 1925.

[2] E. Schrödinger. Quantisation as an eigen value problem. *Ann. Phys.-Berlin*, 79(4): 361–U8, 1926.

[3] T. H. Maiman. Stimulated optical radiation in ruby. *Nature*, 187(4736):493–494, 1960.

[4] A. J. Demaria, D. A. Stetser, and H. Heynau. Self mode-locking of lasers with saturable absorbers - (regenerative pulse oscillator bleachable dyes e). *Appl. Phys. Lett.*, 8(7): 174–176, 1966.

[5] Eisentha.Kb and K. H. Drexhage. Measurement of orientational relaxation using picosecond light pulses. *J. Chem. Phys.*, 51(12):5720–5721, 1969.

[6] M. J. Rosker, M. Dantus, and A. H. Zewail. Femtosecond clocking of the chemical-bond. *Science*, 241(4870):1200–1202, 1988.

[7] M. Born and R. Oppenheimer. Quantum theory of molecules. *Ann. Phys.-Berlin*, 84 (20):0457–0484, 1927.

[8] G. A. Worth and L. S. Cederbaum. Beyond born-oppenheimer: Molecular dynamics through a conical intersection. *Annu. Rev. Phys. Chem.*, 55:127–158, 2004.

[9] G. A. Worth and L. S. Cederbaum. Mediation of ultrafast electron transfer in biological systems by conical intersections. *Chem. Phys. Lett.*, 338(4-6):219–223, 2001.

[10] J. Breidbach and L. S. Cederbaum. Universal attosecond response to the removal of an electron. *Phys. Rev. Lett.*, 94(3), 2005.

[11] F. Remacle and R. D. Levine. An electronic time scale in chemistry. *Proc. Natl. Acad. Sci. U. S. A.*, 103(18):6793–6798, 2006.

[12] A. I. Kuleff and L. S. Cederbaum. Charge migration in different conformers of glycine: The role of nuclear geometry. *Chem. Phys.*, 338(2-3):320–328, 2007.

[13] A. McPherson, G. Gibson, H. Jara, U. Johann, T. S. Luk, I. A. McIntyre, K. Boyer, and C. K. Rhodes. Studies of multiphoton production of vacuum ultraviolet-radiation in the rare-gases. *J. Opt. Soc. Am. B-Opt. Phys.*, 4(4):595–601, 1987.

[14] M. Nisoli and G. Sansone. New frontiers in attosecond science. *Prog. Quantum Electron.*, 33(1):17–59, 2009.

[15] P. Tzallas, E. Skantzakis, L. A. A. Nikolopoulos, G. D. Tsakiris, and D. Charalambidis. Extreme-ultraviolet pump-probe studies of one-femtosecond-scale electron dynamics. *Nat. Phys.*, 7(10):781–784, 2011.

[16] P. Agostini, F. Fabre, G. Mainfray, G. Petite, and N. K. Rahman. Free-free transitions following 6-photon ionization of xenon atoms. *Phys. Rev. Lett.*, 42(17):1127–1130, 1979.

[17] T. Zuo, A. D. Bandrauk, and P. B. Corkum. Laser-induced electron diffraction: A new tool for probing ultrafast molecular dynamics. *Chem. Phys. Lett.*, 259(3-4):313–320, 1996.

[18] M. Meckel, D. Comtois, D. Zeidler, A. Staudte, D. Pavicic, H. C. Bandulet, H. Pepin, J. C. Kieffer, R. Dörner, D. M. Villeneuve, and P. B. Corkum. Laser-induced electron tunneling and diffraction. *Science*, 320(5882):1478–1482, 2008.

[19] K. C. Kulander. Multiphoton ionization of hydrogen - a time-dependent theory. *Phys. Rev. A*, 35(1):445–447, 1987.

[20] L. V. Keldysh. Ionization in field of a strong electromagnetic wave. *Soviet Physics Jetp-Ussr*, 20(5):1307–1314, 1965.

[21] F. H. M. Faisal. Collision of electrons with laser photons in a background potential. *Journal of Physics B-Atomic Molecular and Optical Physics*, 6(11):L312–L315, 1973.

[22] H. R. Reiss. Effect of an intense electromagnetic-field on a weakly bound system. *Phys. Rev. A*, 22(5):1786–1813, 1980.

[23] P. B. Corkum. Plasma perspective on strong-field multiphoton ionization. *Phys. Rev. Lett.*, 71(13):1994–1997, 1993.

[24] M. F. Kling, C. Siedschlag, A. J. Verhoef, J. I. Khan, M. Schultze, T. Uphues, Y. Ni, M. Uiberacker, M. Drescher, F. Krausz, and M. J. J. Vrakking. Control of electron localization in molecular dissociation. *Science*, 312(5771):246–248, 2006.

[25] M. Lezius, V. Blanchet, D. M. Rayner, D. M. Villeneuve, A. Stolow, and M. Y. Ivanov. Nonadiabatic multielectron dynamics in strong field molecular ionization. *Phys. Rev. Lett.*, 86(1):51–54, 2001.

[26] H. Akagi, T. Otobe, A. Staudte, A. Shiner, F. Turner, R. Dörner, D. M. Villeneuve, and P. B. Corkum. Laser tunnel ionization from multiple orbitals in hcl. *Science*, 325 (5946):1364–1367, 2009.

[27] A. l'Huillier, L. A. Lompre, G. Mainfray, and C. Manus. Multiply charged ions induced by multiphoton absorption in rare-gases at 0.53 μm. *Phys. Rev. A*, 27(5):2503–2512, 1983.

[28] D. N. Fittinghoff, P. R. Bolton, B. Chang, and K. C. Kulander. Observation of nonsequential double ionization of helium with optical tunneling. *Phys. Rev. Lett.*, 69 (18):2642–2645, 1992.

[29] B. Walker, B. Sheehy, L. F. Dimauro, P. Agostini, K. J. Schafer, and K. C. Kulander. Precision-measurement of strong-field double-ionization of helium. *Phys. Rev. Lett.*, 73 (9):1227–1230, 1994.

[30] T. Auguste, P. Monot, L. A. Lompre, G. Mainfray, and C. Manus. Multiply charged ions produced in noble-gases by a 1-ps laser-pulse at lambda=1053 nm. *Journal of Physics B-Atomic Molecular and Optical Physics*, 25(20):4181–4194, 1992.

[31] C. F. D. Faria and X. Liu. Electron-electron correlation in strong laser fields. *Journal of Modern Optics*, 58(13):1076–1131, 2011.

[32] Walther Bothe. Nobel lecture: The coincidence method, 1954.

[33] B. Brehm and v Puttkamer E. Koinzidenzmessung von photoionen und photoelek ronen bei methan. *Zeitschrift Fur Naturforschung Part a-Astrophysik Physik Und Physikalische Chemie*, A 22(1):8–10, 1967.

[34] D. Strickland and G. Mourou. Compression of amplified chirped optical pulses. *Opt. Commun.*, 56(3):219–221, 1985.

[35] M. Nisoli, S. DeSilvestri, O. Svelto, R. Szipocs, K. Ferencz, C. Spielmann, S. Sartania, and F. Krausz. Compression of high-energy laser pulses below 5 fs. *Opt. Lett.*, 22(8): 522–524, 1997.

[36] A. Dubietis, G. Jonusauskas, and A. Piskarskas. Powerful femtosecond pulse generation by chirped and stretched pulse parametric amplification in bbo crystal. *Opt. Commun.*, 88(4-6):437–440, 1992.

[37] T. Brabec and F. Krausz. Intense few-cycle laser fields: Frontiers of nonlinear optics. *Reviews of Modern Physics*, 72(2):545–591, 2000.

[38] J. L. Krause, K. J. Schafer, and K. C. Kulander. High-order harmonic-generation from atoms and ions in the high-intensity regime. *Phys. Rev. Lett.*, 68(24):3535–3538, 1992.

[39] P. Colosimo, G. Doumy, C. I. Blaga, J. Wheeler, C. Hauri, F. Catoire, J. Tate, R. Chirla, A. M. March, G. G. Paulus, H. G. Muller, P. Agostini, and L. F. Dimauro. Scaling strong-field interactions towards the classical limit. *Nat. Phys.*, 4(5):386–389, 2008.

[40] M. Göppert-Mayer. Elementary file with two quantum fissures. *Ann. Phys.-Berlin*, 9 (3):273–294, 1931.

[41] G. L. Yudin and M. Y. Ivanov. Nonadiabatic tunnel ionization: Looking inside a laser cycle. *Phys. Rev. A*, 64(1), 2001.

[42] H. B. Bebb and A. Gold. Multiphoton ionization of hydrogen and rare-gas atoms. *Physical Review*, 143(1):1–24, 1966.

[43] M. Protopapas, C. H. Keitel, and P. L. Knight. Atomic physics with super-high intensity lasers. *Rep. Prog. Phys.*, 60(4):389–486, 1997.

[44] M. V. Ammosov, N. B. Delone, and V. P. Krainov. Tunnel ionization of complex atoms and atomic ions in a varying electromagnetic-field. *Zhurnal Eksperimentalnoi I Teoreticheskoi Fiziki*, 91(6):2008–2013, 1986.

[45] J.H. Eberly and J. Javanainen. Above-threshold ionisation. *European Journal of Physics*, 9(4), 1988.

[46] R. R. Freeman, P. H. Bucksbaum, H. Milchberg, S. Darack, D. Schumacher, and M. E. Geusic. Above-threshold ionization with subpicosecond laser-pulses. *Phys. Rev. Lett.*, 59(10):1092–1095, 1987.

[47] V. Stert, W. Radloff, C. P. Schulz, and I. V. Hertel. Ultrafast photoelectron spectroscopy: Femtosecond pump-probe coincidence detection of ammonia cluster ions and electrons. *European Physical Journal D*, 5(1):97–106, 1999.

[48] J. Mikosch and S. Patchkovskii. Coincidence and covariance data acquisition in photoelectron and -ion spectroscopy. i. formal theory. *Journal of Modern Optics*, 60 (17):1426–1438, 2013.

[49] Anthony E. Siegman. *Lasers*. University Science Books, Sausalito, Cal., 1986.

[50] I. V. Hertel and C. P. Schulz. *Atoms, Molecules and Optical Physics 2: Molecules und Photons – Spectroscopy and Collisions*, volume 2 of *Springer-Textbook*. Springer, Berlin Heidelberg, 1 edition, 2014.

[51] Jean-Claude Diels and Wolfgang Rudolph. *Ultrashort Laser Pulse Phenomena*. Optics and Photonics. Academic Press, Burlington, San Diego, London, 2 edition, 2006.

[52] S. Larochelle, A. Talebpour, and S. L. Chin. Non-sequential multiple ionization of rare gas atoms in a ti : Sapphire laser field. *Journal of Physics B-Atomic Molecular and Optical Physics*, 31(6):1201–1214, 1998.

[53] Walter Koechner. *Solid-State Laser Engineering*. Springer Series in Optical Science. Springer Berlin Heidelberg, 2006.

[54] D. E. Spence, P. N. Kean, and W. Sibbett. 60-fsec pulse generation from a self-mode-locked ti-sapphire laser. *Opt. Lett.*, 16(1):42–44, 1991.

[55] O. E. Martinez. 3000 times grating compressor with positive group-velocity dispersion - application to fiber compensation in 1.3-1.6 μm region. *IEEE J. Quantum Electron.*, 23(1):59–64, 1987.

[56] K. Wynne, G. D. Reid, and R. M. Hochstrasser. Regenerative amplification of 30-fs pulses in ti-sapphire at 5 khz. *Opt. Lett.*, 19(12):895–897, 1994.

[57] S. Backus, J. Peatross, C. P. Huang, M. M. Murnane, and H. C. Kapteyn. Ti-sapphire amplifier producing millijoule-level, 21-fs pulses at 1 khz. *Opt. Lett.*, 20(19):2000–2002, 1995.

[58] R. Trebino, K. W. DeLong, D. N. Fittinghoff, J. N. Sweetser, M. A. Krumbugel, B. A. Richman, and D. J. Kane. Measuring ultrashort laser pulses in the time-frequency domain using frequency-resolved optical gating. *Rev. Sci. Instrum.*, 68(9):3277–3295, 1997.

[59] C. Iaconis and I. A. Walmsley. Spectral phase interferometry for direct electric-field reconstruction of ultrashort optical pulses. *Opt. Lett.*, 23(10):792–794, 1998.

[60] Freek Kelkensberg. *Capturing Atomic and Electronic Motion with High Harmonic Generation Light Pulses*. Phd thesis, 2011, Radboud Universiteit Nijmegen.

[61] F. J. Furch, S. Birkner, F. Kelkensberg, A. Giree, A. Anderson, C. P. Schulz, and M. J. J. Vrakking. Carrier-envelope phase stable few-cycle pulses at 400 khz for electron-ion coincidence experiments. *Opt. Express*, 21(19):22671–22682, 2013.

[62] F. Shimizu. Frequency broadening in liquids by a short light pulse. *Phys. Rev. Lett.*, 19(19):1097–1100, 1967.

[63] M. Nisoli, S. DeSilvestri, and O. Svelto. Generation of high energy 10 fs pulses by a new pulse compression technique. *Appl. Phys. Lett.*, 68(20):2793–2795, 1996.

[64] C. P. Hauri, W. Kornelis, F. W. Helbing, A. Heinrich, A. Couairon, A. Mysyrowicz, J. Biegert, and U. Keller. Generation of intense, carrier-envelope phase-locked few-cycle laser pulses through filamentation. *Appl. Phys. B-Lasers Opt.*, 79(6):673–677, 2004.

[65] J. Tümmler, R. Jung, H. Stiel, P. V. Nickles, and W. Sandner. High-repetition-rate chirped-pulse-amplification thin-disk laser system with joule-level pulse energy. *Opt. Lett.*, 34(9):1378–1380, 2009.

[66] Robert W. Boyd. *Nonlinear Optics*. Academic Press, Burlington, San Diego, London, 3 edition, 2008.

[67] R. A. Baumgartner and R. L. Byer. Optical parametric amplification. *IEEE J. Quantum Electron.*, 15(6):432–444, 1979.

[68] J. Ullrich and H. Schmidt-Böcking. Time-of-flight spectrometer for the determination of microradian projectile scattering angles in atomic-collisions. *Physics Letters A*, 125 (4):193–196, 1987.

[69] R. Dörner, J. Ullrich, H. Schmidt-Böcking, and R. E. Olson. 3-body interactions in proton-helium angular scattering. *Phys. Rev. Lett.*, 63(2):147–150, 1989.

[70] W. Wu, J. P. Giese, Z. Chen, R. Ali, C. L. Cocke, P. Richard, and M. Stockli. Evidence for population of highly asymmetric states in double-electron capture by o(7,8+) and n(7+) colliding with he at low to intermediate velocities. *Phys. Rev. A*, 50(1):502–510, 1994.

[71] L. Pedemonte, G. Bracco, and R. Tatarek. Theoretical and experimental study of he free-jet expansions. *Phys. Rev. A*, 59(4):3084–3087, 1999.

[72] R. Moshammer, J. Ullrich, M. Unverzagt, W. Schmidt, P. Jardin, R. E. Olson, R. Mann, R. Dörner, V. Mergel, U. Buck, and H. Schmid-Böcking. Low-energy electrons and their dynamical correlation with recoil ions for single ionization of helium by fast, heavy-ion impact. *Phys. Rev. Lett.*, 73(25):3371–3374, 1994.

[73] R. Moshammer, M. Unverzagt, W. Schmitt, J. Ullrich, and H. Schmidt-Böcking. A 4 π recoil-ion electron momentum analyzer: A high-resolution "microscope" for the investigation of the dynamics of atomic, molecular and nuclear reactions. *Nucl. Instrum. Methods Phys. Res. Sect. B-Beam Interact. Mater. Atoms*, 108(4):425–445, 1996.

[74] J. Ullrich, R. Moshammer, A. Dorn, R. Dörner, L. P. H. Schmidt, and H. Schniidt-Böcking. Recoil-ion and electron momentum spectroscopy: reaction-microscopes. *Rep. Prog. Phys.*, 66(9):1463–1545, 2003.

[75] T. Weber, H. Giessen, M. Weckenbrock, G. Urbasch, A. Staudte, L. Spielberger, O. Jagutzki, V. Mergel, M. Vollmer, and R. Dörner. Correlated electron emission in multiphoton double ionization. *Nature*, 405(6787):658–661, 2000.

[76] Y. H. Jiang, A. Senftleben, A. Rudenko, M. E. Madjet, O. Vendrell, M. Kurka, K. Schnorr, L. Foucar, M. Kübel, O. Herrwerth, M. Lezius, M. F. Kling, J. van Tilborg, A. Belkacem, K. Ueda, S. Dsterer, R. Treusch, C. D. Schröter, R. Santra, J. Ullrich, and R. Moshammer. Watching the acetylene vinylidene intramolecular reaction in real time. *ArXiv*, 1402.4874, 2014.

[77] L. Ph. H. Schmidt, J. Lower, T. Jahnke, S. Schössler, M. S. Schöffler, A. Menssen, C. Leveque, N. Sisourat, R. Taïeb, H. Schmidt-Böcking, and R. Dörner. Momentum transfer to a free floating double slit: Realization of a thought experiment from the einstein-bohr debates. *Phys. Rev. Lett.*, 111(10), 2013.

[78] Max Wutz, Hermann Adam, and Wilhelm Walcher. *Handbuch Vakuumtechnik*. Vieweg+Teubner GWV Fachverlag GmbH, 2004.

[79] Giacinto Scoles. *Atomic and Molecular Beam Methods: Volume 1*. Oxford University Press, New York, 1988.

[80] S. Depaul, D. Pullman, and B. Friedrich. A pocket model of seeded supersonic beams. *Journal of Physical Chemistry*, 97(10):2167–2171, 1993.

[81] Charles Kittel. *Thermal physics*. Wiley, New York,, 1969. 72088609 illus. 25 cm. Bibliography: 13th-14th prelim. pages.

[82] H Ashkenas and Sherman F S. *Rarefied Gas Dynamics*. Academic Press, New York, 1966.

[83] W. C. Wiley and I. H. McLaren. Time-of-flight mass spectrometer with improved resolution. *Rev. Sci. Instrum.*, 26(12):1150–1157, 1955.

[84] B. A. Mamyrin, V. I. Karataev, D. V. Shmikk, and V. A. Zagulin. Mass-reflectron a new nonmagnetic time-of-flight high-resolution mass-spectrometer. *Zhurnal Eksperimentalnoi I Teoreticheskoi Fiziki*, 64(1):82–89, 1973.

[85] J. R. Barker. New coil systems for the production of uniform magnetic fields. *Journal of Scientific Instruments and of Physics in Industry*, 26(8):273–275, 1949.

[86] O. Jagutzki, A. Cerezo, A. Czasch, R. Dörner, M. Hattass, M. Huang, V. Mergel, U. Spillmann, K. Ullmann-Pfleger, T. Weber, H. Schmidt-Böcking, and G. D. W. Smith. Multiple hit readout of a microchannel plate detector with a three-layer delay-line anode. *Ieee Transactions on Nuclear Science*, 49(5):2477–2483, 2002.

[87] Dschwen. Constant fraction, 2006. `http://upload.wikimedia.org/wikipedia/commons/8/8f/Constant_fraction_1.svg`, Copyright information: Creative Commons Attribution-NonCommercial-ShareAlike 2.5 Generic (CC BY-SA 2.5).

[88] J. Christiansen. *HPTDC High Performance Time to Digital Converter*. CERN/EP - MIC, www.cern.ch, 2004.

[89] Roentdek GmbH. *Software for the RoentDek Hexanode*. Kelkheim, Germany, www.roentdek.com, 2011.

[90] William H. Press, Saul A. Teukolsky, William T. Vetterling, and Brian P. Flannery. *Numerical recipes in C : the art of scientific computing*. Cambridge University Press, Cambridge ; New York, 2nd edition, 1992. 94105607 William H. Press ... [et al.]. ill. ; 24 cm. Includes bibliographical references (p. 926-929) and index.

[91] Bastian Manschwetus. *Photoionisation von zweiatomigen Molekülen in hochintensiven Laserpulsen*. PhD thesis, 2010, Technische Universität Berlin.

[92] K. Klünder, P. Johnsson, M. Swoboda, A. L'Huillier, G. Sansone, M. Nisoli, M. J. J. Vrakking, K. J. Schafer, and J. Mauritsson. Reconstruction of attosecond electron wave packets using quantum state holography. *Phys. Rev. A*, 88(3), 2013.

[93] A. Giustisuzor, F. H. Mies, L. F. Dimauro, E. Charron, and B. Yang. Dynamics of h_2^+ in intense laser fields. *Journal of Physics B-Atomic Molecular and Optical Physics*, 28 (3):309–339, 1995.

[94] *CRC handbook of chemistry and physics*. CRC Press, Boca Raton, FL, 2005.

[95] D. G. Arbo, S. Yoshida, E. Persson, K. I. Dimitriou, and J. Burgdorfer. Interference oscillations in the angular distribution of laser-ionized electrons near ionization threshold. *Phys. Rev. Lett.*, 96(14), 2006.

[96] A. Rudenko, K. Zrost, C. D. Schröter, V. L. B. de Jesus, B. Feuerstein, R. Moshammer, and J. Ullrich. Resonant structures in the low-energy electron continuum for single ionization of atoms in the tunnelling regime. *Journal of Physics B-Atomic Molecular and Optical Physics*, 37(24):L407–L413, 2004.

[97] A. von Veltheim, B. Manschwetus, W. Quan, B. Borchers, G. Steinmeyer, H. Rottke, and W. Sandner. Frustrated tunnel ionization of noble gas dimers with rydberg-electron shakeoff by electron charge oscillation. *Phys. Rev. Lett.*, 110(2), 2013.

[98] F. Lindner, M. G. Schätzel, H. Walther, A. Baltuška, E. Goulielmakis, F. Krausz, D. B. Milošević, D. Bauer, W. Becker, and G. G. Paulus. Attosecond double-slit experiment. *Phys. Rev. Lett.*, 95(4), 2005.

[99] H. G. Muller and F. C. Kooiman. Bunching and focusing of tunneling wave packets in enhancement of high-order above-threshold ionization. *Phys. Rev. Lett.*, 81(6): 1207–1210, 1998.

[100] Charlotte E Moore. *Atomic Energy Levels ; Vol. I.* US Dep. of Commerce, NBS, 1949.

[101] H. G. Muller. An efficient propagation scheme for the time-dependent schrodinger equation in the velocity gauge. *Laser Physics*, 9(1):138–148, 1999.

[102] J. Crank and P. Nicolson. A practical method for numerical evaluation of solutions of partial differential equations of the heat-conduction type. *Proceedings of the Cambridge Philosophical Society*, 43(1):50–67, 1947.

[103] J. Mauritsson, T. Remetter, M. Swoboda, K. Klunder, A. l'Huillier, K. J. Schafer, O. Ghafur, F. Kelkensberg, W. Siu, P. Johnsson, M. J. J. Vrakking, I. Znakovskaya, T. Uphues, S. Zherebtsov, M. F. Kling, F. Lepine, E. Benedetti, F. Ferrari, G. Sansone, and M. Nisoli. Attosecond electron spectroscopy using a novel interferometric pump-probe technique. *Phys. Rev. Lett.*, 105(5), 2010.

[104] N. Camus, B. Fischer, M. Kremer, V. Sharma, A. Rudenko, B. Bergues, M. Kubel, N. G. Johnson, M. F. Kling, T. Pfeifer, J. Ullrich, and R. Moshammer. Attosecond correlated dynamics of two electrons passing through a transition state. *Phys. Rev. Lett.*, 108(7), 2012.

[105] A. Staudte, C. Ruiz, M. Schöffler, S. Schössler, D. Zeidler, T. Weber, M. Meckel, D. M. Villeneuve, P. B. Corkum, A. Becker, and R. Dörner. Binary and recoil collisions in strong field double ionization of helium. *Phys. Rev. Lett.*, 99(26), 2007.

[106] T. Shaaran, M. T. Nygren, and C. F. D. Faria. Laser-induced nonsequential double ionization at and above the recollision-excitation-tunneling threshold. *Phys. Rev. A*, 81(6), 2010.

[107] A. Rudenko, V. L. B. de Jesus, T. Ergler, K. Zrost, B. Feuerstein, C. D. Schröter, R. Moshammer, and J. Ullrich. Correlated two-electron momentum spectra for strong-field nonsequential double ionization of he at 800 nm. *Phys. Rev. Lett.*, 99(26), 2007.

[108] R. Moshammer, J. Ullrich, B. Feuerstein, D. Fischer, A. Dorn, C. D. Schröter, J. R. C. Lopez-Urrutia, C. Hohr, H. Rottke, C. Trump, M. Wittmann, G. Korn, K. Hoffmann, and W. Sandner. Strongly directed electron emission in non-sequential double ionization of ne by intense laser pulses. *Journal of Physics B-Atomic Molecular and Optical Physics*, 36(6):L113–L119, 2003.

[109] R. Wiehle and B. Witzel. Correlation between double and nonresonant single ionization. *Phys. Rev. Lett.*, 89(22), 2002.

[110] J. L. Chaloupka, J. Rudati, R. Lafon, P. Agostini, K. C. Kulander, and L. F. DiMauro. Observation of a transition in the dynamics of strong-field double ionization. *Phys. Rev. Lett.*, 90(3), 2003.

[111] G. Gingras, A. Tripathi, and B. Witzel. Wavelength and intensity dependence of short pulse laser xenon double ionization between 500 and 2300 nm. *Phys. Rev. Lett.*, 103 (17), 2009.

[112] M. Berglund and M. E. Wieser. Isotopic compositions of the elements 2009 (iupac technical report). *Pure and Applied Chemistry*, 83(2):397–410, 2011.

[113] X. F. Sun, M. Li, D. F. Ye, G. G. Xin, L. B. Fu, X. G. Xie, Y. K. Deng, C. Y. Wu, J. Liu, Q. H. Gong, and Y. Q. Liu. Mechanisms of strong-field double ionization of xe. *Phys. Rev. Lett.*, 113(10), 2014.

[114] B. K. McFarland, J. P. Farrell, P. H. Bucksbaum, and M. Guhr. High harmonic generation from multiple orbitals in n(2). *Science*, 322(5905):1232–1235, 2008.

[115] O. Smirnova, Y. Mairesse, S. Patchkovskii, N. Dudovich, D. Villeneuve, P. Corkum, and M. Y. Ivanov. High harmonic interferometry of multi-electron dynamics in molecules. *Nature*, 460(7258):972–977, 2009.

[116] A. E. Boguslavskiy, J. Mikosch, A. Gijsbertsen, M. Spanner, S. Patchkovskii, N. Gador, M. J. J. Vrakking, and A. Stolow. The multielectron ionization dynamics underlying attosecond strong-field spectroscopies. *Science*, 335(6074):1336–1340, 2012.

[117] J. Dannacher, J. P. Flamme, J. P. Stadelmann, and J. Vogt. Unimolecular fragmentations of internal energy selected 1,3-butadiene cations. *Chem. Phys.*, 51(1-2):189–195, 1980.

[118] W. A. Chupka and Berkowit.J. Photoionizaion of ethane, propane and n-butane with mass analysis. *J. Chem. Phys.*, 47(8):2921–2933, 1967.

[119] A. G. Brenton, R. P. Morgan, and J. H. Beynon. Unimolecular ion decomposition. *Annu. Rev. Phys. Chem.*, 30:51–78, 1979.

[120] James T. Yardley. *Introduction to molecular energy transfer*. Academic Press, New York, 1980.

[121] L. J. Frasinski, K. Codling, and P. A. Hatherly. Covariance mapping - a correlation method applied to multiphoton multiple ionization. *Science*, 246(4933):1029–1031, 1989.

[122] J. Mikosch and S. Patchkovskii. Coincidence and covariance data acquisition in photoelectron and -ion spectroscopy. ii. analysis and applications. *Journal of Modern Optics*, 60(17):1439–1451, 2013.

[123] M. Y. Ivanov, M. Spanner, and O. Smirnova. Anatomy of strong field ionization. *Journal of Modern Optics*, 52(2-3):165–184, 2005.

[124] H. L. Xu, T. Okino, K. Nakai, K. Yamanouchi, S. Roither, X. H. Xie, D. Kartashov, M. Schöffler, A. Baltuska, and M. Kitzler. Hydrogen migration and c-c bond breaking in 1,3-butadiene in intense laser fields studied by coincidence momentum imaging. *Chem. Phys. Lett.*, 484(4-6):119–123, 2010.

[125] J. Mikosch, A. E. Boguslavskiy, I. Wilkinson, M. Spanner, S. Patchkovskii, and A. Stolow. Channel- and angle-resolved above threshold ionization in the molecular frame. *Phys. Rev. Lett.*, 110(2), 2013.

[126] H. H. Ritze. *private communication*, 2. June 2015.

[127] B. Saha, M. Ehara, and H. Nakatsuji. Singly and doubly excited states of butadiene, acrolein, and glyoxal: Geometries and electronic spectra. *J. Chem. Phys.*, 125(1), 2006.

[128] M. A. L. Marques and E. K. U. Gross. Time-dependent density functional theory. *Annu. Rev. Phys. Chem.*, 55:427–455, 2004.

[129] Y. Huismans, A. Rouzee, A. Gijsbertsen, J. H. Jungmann, A. S. Smolkowska, Pswm Logman, F. Lepine, C. Cauchy, S. Zamith, T. Marchenko, J. M. Bakker, G. Berden, B. Redlich, A. F. G. van der Meer, H. G. Muller, W. Vermin, K. J. Schafer, M. Spanner, M. Y. Ivanov, O. Smirnova, D. Bauer, S. V. Popruzhenko, and M. J. J. Vrakking. Time-resolved holography with photoelectrons. *Science*, 331(6013):61–64, 2011.

[130] D. D. Hickstein, P. Ranitovic, S. Witte, X. M. Tong, Y. Huismans, P. Arpin, X. B. Zhou, K. E. Keister, C. W. Hogle, B. S. Zhang, C. Y. Ding, P. Johnsson, N. Toshima, M. J. J. Vrakking, M. M. Murnane, and H. C. Kapteyn. Direct visualization of laser-driven electron multiple scattering and tunneling distance in strong-field ionization. *Phys. Rev. Lett.*, 109(7), 2012.

[131] M. Lewenstein, P. Balcou, M. Y. Ivanov, A. Lhuillier, and P. B. Corkum. Theory of high-harmonic generation by low-frequency laser fields. *Phys. Rev. A*, 49(3):2117–2132, 1994.

[132] G. Bieri, F. Burger, E. Heilbronner, and J. P. Maier. Valence ionization energies of hydrocarbons. *Helv. Chim. Acta*, 60(7):2213–2233, 1977.

[133] M. G. Littman, M. M. Kash, and D. Kleppner. Field-ionization processes in excited atoms. *Phys. Rev. Lett.*, 41(2):103–107, 1978.

[134] F.B. Dunning and R.F. Stebbings. *Rydberg States of Atoms and Molecules*. Cambridge University Press, New York, 1983.

[135] C. I. Blaga, F. Catoire, P. Colosimo, G. G. Paulus, H. G. Muller, P. Agostini, and L. F. DiMauro. Strong-field photoionization revisited. *Nat. Phys.*, 5(5):335–338, 2009.

[136] C. Y. Wu, Y. D. Yang, Y. Q. Liu, Q. H. Gong, M. Wu, X. Liu, X. L. Hao, W. D. Li, X. T. He, and J. Chen. Characteristic spectrum of very low-energy photoelectron from above-threshold ionization in the tunneling regime. *Phys. Rev. Lett.*, 109(4), 2012.

[137] I. Shchatsinin, H. H. Ritze, C. P. Schulz, and I. V. Hertel. Multiphoton excitation and ionization by elliptically polarized, intense short laser pulses: Recognizing multielectron dynamics and doorway states in c-60 vs xe. *Phys. Rev. A*, 79(5), 2009.

[138] P. Russbueldt, T. Mans, G. Rotarius, J. Weitenberg, H. D. Hoffmann, and R. Poprawe. 400 w yb:yag innoslab fs-amplifier. *Opt. Express*, 17(15):12230–12245, 2009.

[139] E. Innerhofer, T. Südmeyer, F. Brunner, R. Häring, A. Aschwanden, R. Paschotta, C. Hönninger, M. Kumkar, and U. Keller. 60-w average power in 810-fs pulses from a thin-disk yb : Yag laser. *Opt. Lett.*, 28(5):367–369, 2003.

[140] A. T. J. B. Eppink and D. H. Parker. Velocity map imaging of ions and electrons using electrostatic lenses: Application in photoelectron and photofragment ion imaging of molecular oxygen. *Rev. Sci. Instrum.*, 68(9):3477–3484, 1997.

A Appendix

A.1 Atomic Units

In science, the most widely used system of units is the International System of Units (SI)[1]. However, the appearance of expressions in atomic physics can be greatly simplified by the introduction of atomic units. In the atomic units system quantities are related to properties of an electron in a hydrogen atom. The length is measured as a multiple of the Bohr radius a_0. The unit of energy is twice the ionization potential of an hydrogen atom. The velocity is measured in multiples of the velocity of an electron having a kinetic energy equal to the ionization potential of hydrogen. The unit of time is the time that an electron takes to travel the Bohr radius at this velocity.

As a consequence of these definitions in the atomic units system the electron mass m_e, the electron charge e_0, the reduced Planck's constant $\hbar$ and the Coulomb's constant $1/(4\pi\varepsilon_0)$ are equal to one.

Atomic units are noted with the unit *a.u.* independent of the physical quantity. This has to be deduced from the context. Table A.1 show the values of some basic and derived atomic units.

physical quantity	**definition**	**SI**
Electron charge e	1	$1.602176565(35) \times 10^{-19}\,\mathrm{C}$
Electron mass m_e	1	$9.10938291(40) \times 10^{-31}\ \mathrm{kg}$
reduced Plank's constant $\hbar$	1	$1.054571726(47) \times 10^{-34}\,\mathrm{J\,s}$
Length a_0	$\frac{4\pi\epsilon_0\hbar^2}{m_e e^2}$	$5.2917721092(17) \times 10^{-11}\,\mathrm{m}$
Energy E_h	$\frac{e^2}{4\pi\epsilon_0 a_0}$	$4.35974434(19) \times 10^{-18}\,\mathrm{J}$
Time	$\frac{\hbar}{E_\mathrm{h}}$	$2.418884326502(12) \times 10^{-17}\,\mathrm{s}$
Electric field	$\frac{E_\mathrm{h}}{e a_0}$	$5.14220652(11) \times 10^{11}\,\mathrm{V/m}$
Momentum	$\frac{\hbar}{a_0}$	$1.992851740(88) \times 10^{-24}\,\mathrm{kg\,m/s}$

Table A.1: Various quantities and their SI value corresponding to 1 a.u..

1 french: Le Système International d'Unités

A.2 Detection efficiency

This short section explains the calculation of the detector efficiencies from measured data as shown in table 3.1. For this calculation, one needs the numbers of detected ions n_i and electrons n_e, the number of coincidences n_{11} defined as events with one electron and one ion detected and the total number of laser pulses n_l. With these numbers, the probabilities of eq. 1.22 and eq. 1.24 are calculated:

$$w_i = \frac{n_i}{n_l}$$
$$w_e = \frac{n_e}{n_l}$$
$$w_{11} = \frac{n_{11}}{n_l}$$

Inserting eq. 1.22 solved for $\xi_{i,e}$ into eq. 1.24 one obtains a relation with only one unknown:

$$w_{11} = \frac{w_i w_e}{\bar{n}} \left[1 + \bar{n}\left(1 - \frac{w_i}{\bar{n}}\right)\left(1 - \frac{w_i}{\bar{n}}\right)\right] \exp\left[\frac{w_i w_e}{\bar{n}} - w_e - w_i\right] \tag{A.1}$$

It is not possible to solve this equation for $\bar{n}$ analytically. But one can subtract w_{11} on both sides and find the root numerically. With the $\bar{n}$, one can calculate $\xi_{i,e}$ immediately.

A.3 Technical Drawings

A.3.1 Anode Voltage Circuit

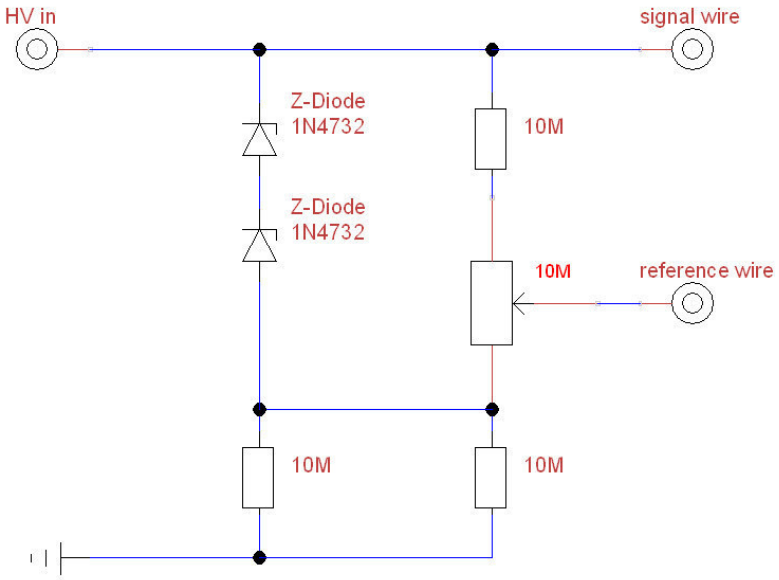

Figure A.1: Circuit for the supply of the anode voltages

A.3.2 Voltage Divider

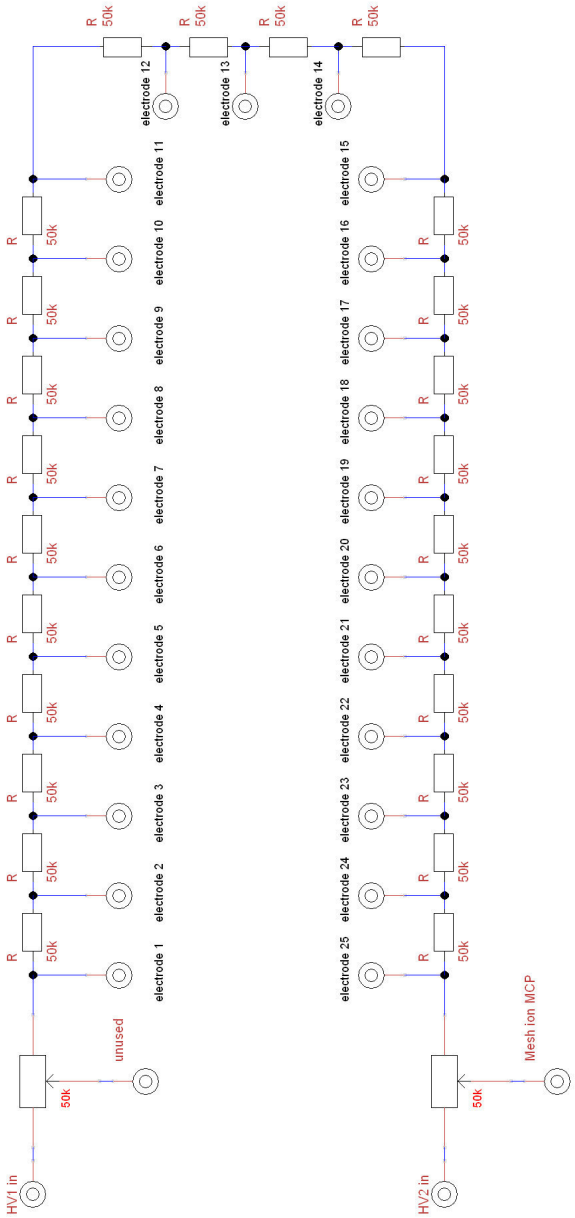

Figure A.2: Circuit for electrode voltages

A.4 Source Code of Storage File Format

This section presents the source code for the SLMA file type used to store the time information and position information of the raw data corrected by the CoBold software. It also explains briefly the structure of the file. When the CoBold software writes the data to the SLMA file, it starts with a header:

```
...
if (mode == 4) { // MHZ type header must be written
write_MHz_header();
} // END OF WRITING MHZ HEADER
...
```

where `write_MHz_header` is defined as

```
//////////////////////////////////////////////////////////
void Write_File::write_MHz_header()
//////////////////////////////////////////////////////////
{
const int MHzHeaderVersion = 20130514;

*File_Archive << MHzHeaderVersion;

*File_Archive << i_det_is_used;
*File_Archive << e_det_is_used;
}
```

This header contains a version number and the information if the ion detector and the electron detector are used.

Then Cobold starts to write information of each event to the file. It calls for each event the method `:WriteMHzData`:

```
//////////////////////////////////////////////////////////
void Write_File::WriteMHzData(__int64 eventc, double timestamp, double timelaser,
detector_parameters_class &det1, detector_parameters_class &det2)
//////////////////////////////////////////////////////////
{
int number_of_particles;

*File_Archive << eventc;
*File_Archive << timestamp;
*File_Archive << timelaser;

if (det1.use_this_detector){
number_of_particles = det1.number_of_particles;
*File_Archive << number_of_particles;
```

```
for (int i=0; i<number_of_particles; i++){
*File_Archive << det1.particle[i].TOF_s;
*File_Archive << det1.particle[i].x_m;
*File_Archive << det1.particle[i].y_m;
*File_Archive << det1.particle[i].reconstruction_method;
}
}

if (det2.use_this_detector){
number_of_particles = det2.number_of_particles;
*File_Archive << number_of_particles;

for (int i=0; i<number_of_particles; i++){
*File_Archive << det2.particle[i].TOF_s;
*File_Archive << det2.particle[i].x_m;
*File_Archive << det2.particle[i].y_m;
*File_Archive << det2.particle[i].reconstruction_method;
}
}
}
```

`:WriteMHzData` saves the event number `eventc`, the time stamp of this event `timestamp` and the first laser time `timelaser`. The time stamp is the time elapsed since the start of the measurement. With the laser time, the subsequent momentum calculation can check whether the detected electron that triggered the event is a real photoelectron or an secondary electron produced by the ion impact at ion detector. A photoelectron arrives in a time window of about a few hundred ns after the laser trigger.

After this, the method saves the information of the particle hits detected at each detector. It starts with ion detector (`det1`) and saves firstly the total number of hits `number_of_particles` at this detector. Then, the method goes through each hit and saves the time-of-flight `TOF.s`, the position on the detector in x-direction `x_m` and y-direction `y_m` and the reconstruction method `reconstruction_method` used by the software when sorting the raw data.

A.5 Reconstruction Methods

Table A.2 summarizes all possible sets of timing signals from which a particle hit can be reconstructed. Their reconstruction method number as assigned by the software [89] is given as well.

reconstruction method nr.	**U layer**	**V layer**	**W layer**	**MCP**	**comment**
0	2	2	2	1	
1	0	2	2	1	
2	2	0	2	1	
3	2	2	0	1	
4	1	2	2	1	2 permutations
5	2	1	2	1	2 permutations
6	2	2	1	1	2 permutations
7	2	2	2	0	
8	0	2	2	0	
9	2	0	2	0	
10	2	2	0	0	
11	1	2	2	0	2 permutations
12	2	1	2	0	2 permutations
13	2	2	1	0	2 permutations
14	1	2	1	1	4 permutations
	1	1	2	1	4 permutations
	2	1	0	1	2 permutations
	2	0	1	1	2 permutations
15*	1	2	0	1	2 permutations
	1	0	2	1	2 permutations
	0	2	1	1	2 permutations
	0	1	2	1	2 permutations
16*	1	1	1	1	8 permutations
	2	1	1	0	4 permutations
17*	1	2	1	0	4 permutations
	1	1	2	0	4 permutations
18*	1	1	1	0	8 permutations
	2	1	0	0	2 permutations
	2	0	1	0	2 permutations
19*	1	2	0	0	2 permutations
	1	0	2	0	2 permutations
	0	2	1	0	2 permutations
	0	1	2	0	2 permutations

Table A.2: Reconstruction methods. The methods marked by an asterix are risky methods. This methods cannot use any redundancy check due to the lack of enough signals. Therefore events reconstructed by these risky methods most probably do not correspond to real impacts.

Acknowledgements

Finally, I would like to say many thanks to all people who helped me and gave their support during the last years.

First of all I would like to thank my supervisor Prof. M.J.J. Vrakking for the opportunity, and infrastructure to pursue my thesis within his group at the Max Born Institute.

I am very grateful to my direct supervisor Dr. C.P. Schulz for many helpful discussions about physics beside all the technical aspects of the setup. His calm and serene way helped my a lot, especially in phases when nothing seemed to work.

Without the help of Federico Furch this work would not have been possible. He tamed the OPA system to deliver the light pulses needed in the experiments. Beside that, it was a pleasure to work with him together in the lab. His good mood is infectious and every time I was discouraged he managed to bring me back on track..

I also would like to thank Felipe Morales for his support on the TDSE calculations. His support helped to get familiar with the program in a very short time.

I am also grateful to Jochen Mikosch who spend time to discuss results of the strong field experiments on the hydrocarbon molecules, although he had his own project with a PhD student, that was not related to my experiments.

Since the work presented comprised a lot of construction, I relied on the support of the machine shop. Therefore, I would like to thank the entire team of the machine shop. Especially, I thank Roman Peslin and Armin Loudovici who showed me some secrets of machining. Due to their help, I was able to machine parts for the setup by myself, which saved a lot of time.

Many thanks to my colleagues, both past and present, from division A for their support. I sincerely thank Martin Eckstein, Christian Schröter, Sandra Höhm, Felix Braußе, Axel Hundertmark, Christian Neidel, Martin Galbraith, Alexandria Anderson, Achut Giree, Martin Flögel, Jesse Klei, Andea Lübcke for their assistance, nice discussions and the pleasant time we had together. (If someone thinks he is missing, please feel inserted.) I wish Felix Schell great success in his thesis with 'my' reaction microscope.

I thank also my parents for their support. My biggest thanks goes to my whole family: my wife Yvonne, my children Finja, Marla and Lars for their support throughout the years. They carried most of the burden caused by the thesis.

Kurzzusammenfassung

Die Kombination starker kurzer Laserimpulse von wenigen Zyklen mit einem Reaktionsmikroskops, welches die Impulsvektoren aller geladenen Teilchen, die aus einem Ionisations- oder Dissoziationsprozess stammen, koinzident detektieren kann, ermöglicht eine genaue und detaillierte Untersuchung von atomaren und molekularen Starkfeldprozessen. Experimente mit Reaktionsmikroskopen bedürfen jedoch eines niedrigen Verhältnisses zwischen Ereignisrate und Laserrate, um falsche Koinzidenzen zu vermeiden. Gewöhnliche Wiederholraten von Lasersystemen, die starke Laserimpulse mit wenigen Zyklen erzeugen, sind in der Größenordnung weniger kHz. Dies führt zur Messdauern von bis zu einigen Tagen für verlässliche Informationen über z.B. winkel- und energieaufgelöste Daten. Falls zusätzlich noch Laserparameter wie Polarisation oder der zeitliche Abstande zweier Laserimpulse variiert werden soll, kann die Dauer eines solchen Experimentes sogar noch größere Zeitskalen erreichen. Es ist sehr schwierig Experimente auf diesen Zeitskalen stabil zu halten. Deshalb sind die Möglichkeiten große Parameterräume zu durchsuchen stark eingeschränkt. Wir haben ein Reaktionsmikroskop mit einem NOPA-System kombiniert, das starke, kurze Laserimpulse von wenigen Zyklen mit einer Wiederholrate von 400 kHz erzeugt, um diese Einschränkung zu überwinden und Mehrelektronendynamiken in Starkfeldexperimenten zu untersuchen. Es wurden erste Experimente mit Starkfeldionisation an Argon durchgeführt, um den experimentellen Aufbau zu charakterisieren. Die Impulsverteilungen der Elektronen aus diesen Experimenten zeigten unerwartet scharfe Strukturen. TDSE (Time Dependent Schrödinger Equation) Berechnungen zeigten, dass diese Strukturen durch die zeitliche Form des Laserimpulses, der schwache Satellitenimpulse enthält, verursacht wurden. In diesem ungewollten pump-probe Schema ionisiert der starke Hauptimpuls nicht nur das Argonatom, sondern er bevölkert auch gleichzeitig Rydbergzustände des neutralen Atoms. Die Rydbergzustände werden durch einen späteren schwächeren Impuls ionisiert. Dies führt zu Interferenzen zwischen den direkt und indirekt erzeugten Photoelektronen sichtbar als scharfe Strukturen in den Elektronenspektren. Zusätzlich zeigte die TDSE-Berechnung, dass die relative Population und die initialen Phasen der Rydbergzustände, die durch die Starkfeldinteraktion bevölkert werden, aus den Photoelektronenspektren extrahiert werden können, wenn die Zeitabhängigkeit dieser Interferenzen durch ein Pump-Probe-Experiment untersucht wird.

In einem anderen Starkfeldexperiment an mehratomigen Molekülen wie Butadien und n-Butan untersuchten wir deren Fragmentation. Es wurden winkelaufgelösten Photoelektronenspektren für unterschiedliche Fragmentationskanäle aufgenommen. Diese Messungen zeigten, dass unterschiedliche ionische Zustände während einer Starkfeldionisation bevölkert werden. Dies deutet daraufhin, dass in mehratomigen Molekülen nicht nur das am schwächsten gebundene Elektron in Starkfeldionisationsprozessen teilnimmt.

Short Summary

The combination of strong few-cycle laser pulses with a reaction microscope, a spectrometer capable of detecting the momentum-vectors of all charged particles that emerge from ionization or dissociation processes in coincidence, enables precise and detailed investigations of strong field processes that occur in atoms and small molecules. However, to avoid false coincidences, experiments with a reaction microscope rely on a low ratio between event rate and laser rate. Common repetition rates of strong few cycle laser systems are on the order of a few kHz leading to long measurement duration up to several days to get reliable information e.g. on angular and energy resolved data. If, in addition, laser parameters such as pump probe delay or polarization have to be scanned, the duration for such experimental runs can extend even beyond this time scale. For such long time periods it is very difficult to maintain stable experimental conditions. Hence, the possibility to scan through large parameter sets is very limited. To overcome this limitation, we combined a reaction microscope with a 400 kHz high repetition rate NOPA-system delivering strong few-cycle laser pulses to study multi-electron dynamics in strong field ionization experiments.

First measurements on strong field ionization of argon were performed to characterize the setup. In these experiments unexpected sharp structures have been observed in the electron momentum distributions. With the help of TDSE (Time Dependent Schrödinger Equation) calculations, it was found that these sharp structures originate from the temporal shape of the laser pulses which contains weak post pulses. In this 'unwanted' pump probe scheme, the strong main pulse not only ionizes the argon atom but also populates Rydberg states in the neutral atom. A weaker post pulse ionizes the Rydberg states. This leads to interferences between the direct and the indirect created photo electrons and thus to sharp structures in the electron spectra. The TDSE calculation has shown that the relative population and initial phases of Rydberg states populated by the strong field interaction can be extracted when studying the time dependence of these interferences in a pump probe experiment.

In an experiment on strong field ionization of polyatomic molecules as Butadiene and n-Butane, we studied the fragmentation of these molecules. The angular-resolved electron spectra for different fragmentation channels have been retrieved. These measurements revealed that different ionic states are populated during the strong field ionization and hints towards a break-down of the single active electron approximation in polyatomic molecules.

List of Publications

1. F.J. Furch, S. Birkner, F. Kelkensberg, A. Giree, A. Anderson, C.P. Schulz and M.J.J. Vrakking: *Carrier-envelope phase stable few-cycle pulses at 400 kHz for electron-ion coincidence experiments.* Opt. Express, 21(19): 22671-22682, 2013.

2. F.J. Furch, S. Birkner, J.H. Jungmann, F. Kelkensberg, C.P. Schulz, A. Rouzee and M.J.J. Vrakking: *Photoelectron imaging of XUV photoionization of CO2 by 13-40 eV synchrotron radiation.* J. Chem. Phys., 139(12): 124309, 2013.